ABSTRACT

NEW APPROACHES TO SCALED-UP CARBON NANOTUBE SYNTHESIS AND NANOTUBE-BASED METAL COMPOSITES AND SENSORS

by
Amit Goyal

The first phase of the work presented in this dissertation is the development of a scaleable process for the cost-effective synthesis of single walled carbon nanotubes (SWNTs) by thermally-induced catalytic chemical vapor deposition (CVD). With the goal of understanding the growth mechanism and optimize the synthesis process, the effect of CVD and catalyst parameters on nanotube formation was investigated in detail. It was found that nucleation and growth of SWNTs occurred within a few seconds of the introduction of the carbon source, carbon monoxide, at temperatures above 675 °C over a Co-Mo/MgO catalyst/support system, resulting in the formation of high quality thinly bundled SWNTs with a narrow individual nanotube diameter distribution. A simple kinetic model is proposed to explain the observed growth and exit gas (CO_2) concentration data. A scaled up run using fluidized bed reactor is performed to demonstrate large SWNTs production.

In the second phase of the research performed some of the CVD parameters optimized for the synthesis of pure nanotubes were used to infiltrate SWNTs as well as multiwalled carbon nanotubes (MWNTs) into catalyst precursor filled iron and aluminum matrices, respectively, to directly fabricate metal-nanotube composites. Two carbon sources, carbon monoxide and acetylene were used for the synthesis of SWNTs and MWNTs, respectively. The yield strength of iron-carbon nanotube composites showed substantial enhancement of up to 45% and 36 % with ~ 1 wt % of infiltrated SWNTs and

MWNTs, respectively, relative to that of similarly treated pure iron samples of the same piece density without carbon nanotubes. Vickers hardness measurements showed an increase of 74% and 96% for iron composites filled with SWNTs and MWNTs, respectively. The use of a mixed feed of CO and acetylene resulted in carbide-free fabrication of the nanocomposites. A reaction mechanism supporting the observed carbide-free growth is also presented.

In the third phase of the research performed, a SWNT fabrication protocol using CVD growth or electrophoretic deposition was employed for integrating nanotubes as biosensor and chemical gas sensor probes. For biosensor probes, vertically aligned SWNTs were grown or deposited on metal interconnects (Cr/Co), at precise locations, which were patterned on quartz substrates using photo- and e-beam lithogrpahy to make electrical connections to each SWNT/bundle individually. Gas sensor probes were fabricated using individually suspended SWNTs contacted by Cr/Au pads as source and drain field effect transistor components for the monitoring of NO_2 vapors. The adsorption of an electron donating gas such as NO_2 on the SWNT sidewalls shifts the Fermi level of the p-type semiconducting nanotubes, consequently changing their electrical conductivity. Experimental results showed that sensor response to NO_2 (at 10-300 ppm levels) was of the order of a few seconds at 100 ppm, and was reversible and reproducible. Recovery of the sensor response was achieved by heating the sensors at 120 °C for a period of 10-12 hours indicating physisorption of the NO_2 molecules on the nanotube sidewalls.

NEW APPROACHES TO SCALED-UP CARBON NANOTUBE SYNTHESIS AND NANOTUBE-BASED METAL COMPOSITES AND SENSORS

by
Amit Goyal

A Dissertation
Submitted to the Faculty of
New Jersey Institute of Technology
in Partial Fulfillment of the Requirements for the Degree of
Doctor of Philosophy in Chemical Engineering

Otto H. York Department of Chemical Engineering

Aug 2007

APPROVAL PAGE

NEW APPROACHES TO SCALED-UP CARBON NANOTUBE SYNTHESIS AND NANOTUBE-BASED METAL COMPOSITES AND SENSORS

Amit Goyal

Dr. Zafar Iqbal, Dissertation Co-Advisor   Date
Research Professor of Chemistry and Environmental Science, NJIT

Dr. Joseph Bozzelli, Dissertation Co-Advisor   Date
Distinguished Professor of Chemistry and Environmental Science
and Chemical Engineering, NJIT

Dr. Laurent Simon, Committee Member   Date
Assistant Professor of Chemical Engineering, NJIT

Dr. Reginald Farrow, Committee Member   Date
Research Professor of Physics, NJIT

Dr. Frank Owens, Committee Member   Date
Senior Research Scientist
Armament Research, Development and Engineering Center, Picatinny, New Jersey

---

Dr. Jing Wu, Committee Member   Date
Assistant Professor of Chemical Engineering, NJIT

BIOGRAPHICAL SKETCH

Author: Amit Goyal

Degree: Doctor of Philosophy

Date: Aug 2007

Undergraduate and Graduate Education:

- Doctor of Philosophy in Chemical Engineering,
  New Jersey Institute of Technology, Newark, NJ, 2007

- Master of Science in Chemical Engineering,
  New Jersey Institute of Technology, Newark, NJ, 2003

- Bachelor of Engineering in Chemical Engineering,
  Manipal Institute of Technology, Manipal, Karnataka, India, 2000

Major: Chemical Engineering

Awards and Honors

Schering-Plough Science and Innovation award, 2007

Publications and Presentations:

Goyal, A., Iqbal, Z., Fetter, L., Liu, S., and Farrow, R. (2007). The single particle nanoscopic lens. Manuscript in preparation to be submitted to Applied Physics letters.

Goyal, A. and Iqbal, Z. Scalable production of single wall carbon nanotubes Manuscript submitted to Nanotechnology

Goyal, A., Wiegand, D.A., Owens, F.J., and Iqbal, Z. (2007). Directly synthesized, carbide-free iron multiwall carbon nanotube composite with enhanced mechanical properties. *Chemical Physics Letters*, 442, Pages 365-371.

Helbling, T., Pohle, R., Stampfer, C., Durrer, L., Goyal, A., Fleischer, M. and Hierold, C. (2007). NO_2 gas sensors based on individual suspended single-walled carbon nanotubes. (EA 0679), Transducer 2007: The 14th International conference on

Solid-State Sensors, Actuators and Microsystems. Lyon, France, June 10-14.

Goyal, A., Mandapuram, S., Michniak, B. and Simon, L. (2007). Application of orthogonal collocation and regression techniques for recovering parameters of a two-pathway transdermal drug-delivery model, *Computers & Chemical Engineering*, 31, Pages 107-120.

Maschmann, M. R., Amama, P. B., Goyal, A., Iqbal, Z. and Fisher,T .S. (2006). Freestanding vertically oriented single-walled carbon nanotubes synthesized using microwave plasma-enhanced CVD, *Carbon*, 44 (13), 2758-2763.

Goyal, A., Wiegand, D. A., Owens, F. J. and Iqbal, Z. (2006). Enhanced yield strength in iron nanocomposite with in-situ grown single wall carbon nanotubes, *Journal of Materials Research*, 21 (2), 522-528.

Maschmann, M. R., Amama, P. B., Goyal, A., Iqbal, Z., Gat, R. and Fisher, T. S. (2006). Parametric study of synthesis conditions in plasma-enhanced CVD of high-quality single-walled carbon nanotubes, *Carbon*, 44 (1), 10-18.

Goyal, A., Wiegand, D. A., Owens, F. J. and Iqbal, Z. (2006). Enhanced yield strength in iron nanocomposite with in-situ grown single wall carbon nanotubes, Presented at 14th International Conference on Composites/Nano Engineering, July 2-8, 2006, Boulder, Colorado.

Iqbal, Z. and Goyal, A. (2005) Carbon nanotubes/nanofibers and carbon fibers in *Functional Fillers for Plastics*, (ed. Xanthos, M.) Ch 10 (WILEY-VCH Verlag GmbH & Co., Wienheim 2005).

Goyal, A., Simon, L. and Iqbal, Z. (2005), Kinetic investigations of CO disproportionation on Co-Mo/MgO bimetallic catalyst for single wall carbon nanotubes production, Presented at AICHE annual meeting, Cincinnati, Ohio, Oct 20 – Nov 4, 2005

Gat, R., Maschmann, M.M., Goyal, A., Iqbal, Z. and Fisher, T. S. (2005). Single and Multiwall Carbon Nanotube Deposition using Dedicated Microwave CVD System, Presented at 2005 NSTI Nanotechnology Conference and Trade Show, Nanotech 2005. May 8-12, 2005

Goyal, A. and Iqbal, Z. (2004), Novel In-Situ Grown Carbon-Iron Nanotube Composites: Synthesis and Properties. Poster Presentation at 2005 MRS Spring Meeting in San Francisco. March 28-April1 2005.

Maschmann, M.M., Goyal, A., Iqbal, Z., Fisher, T. S. and Gat, R. (2004). Single wall Carbon nanotube by microwave plasma CVD, Presented at MRS Fall 2004 Conference in Boston. 29th Nov. 2004.

Goyal, A. and Iqbal, Z. (2004). Scaleable cost-effective synthesis and self-assembly of single wall carbon nanotubes, Presented at ASM Fall 2004 Conference and show held in Columbus, Ohio. 18th Oct. 2004.

Goyal, A. (2003). Role of Catalyst and Substrate in Synthesis of Single Wall Carbon Nanotubes, *M.S. Thesis*, New Jersey Institute of Technology, Newark, NJ.

Goyal, A. (2000), Devil in Diesel on concerns of sulphur concentration and quantities in emissions from diesel engines, Article in annual magazine for Chemical Engineering Association (CHEA)

This thesis is dedicated to my family
for their unending love and encouragement

ACKNOWLEDGMENT

TABLE OF CONTENTS

TABLE OF CONTENTS
(Continued)

LIST OF TABLES

LIST OF FIGURES

CHAPTER 1

INTRODUCTION

"Since their discovery in 1991, carbon nanotubes have attracted a great deal of attention". Most of the literature on carbon nanotubes opens with a sentence like this one. It sounds very encouraging but fails to capture the excitement that carbon nanotubes and nanotechnology has generated among scientists and even among the general public. The wealth of exciting properties of carbon nanotubes makes one wonder where one should begin when talking about them. One obvious starting point would be to talk about their relationship to graphite, which is made from carbon the most versatile element on earth. Starting from the mid-1980s, however, new forms of carbon, the buckminster fullerenes, were discovered leading to new ideas on the structural physics and chemistry of caged clusters at the frontier between a molecule and a three-dimensional crystal.

The result of research on the fullerenes then led to hollow carbon structures comprised of rolled up sheets of graphite, now widely known as carbon nanotubes. Their exceptional mechanical strength that exceeds that of steel, and electronic properties that range from those of one dimensional metals to one dimensional semiconductors, have attracted a great deal of attention. This has led to extensive research in these materials pointing to potential applications that range from scanning probe microscopy tips, hydrogen storage for fuel cells, field-emitting flat panel displays, high strength composites, field effect transistors and sensors. Applications relying on growth or deposition of aligned nanotube and mechanical strength in the area of flat panel displays and polymer nanocomposites have shown the most success. However, a complete

1

understanding of the formation of nanotubes and the design of a facile and cost-effective process for scale up to production is still in the research phase. Moreover, the use of nanotubes to fabricate high strength and lighter weight metal nanocomposites is still in its infancy because of high temperature processing challenges. One of the most difficult of all applications is the incorporation of single wall nanotubes in micro- and nano-electronic devices. This requires precision and control to make working devices with a single type (in terms of chirality and diameter) of nanotube so as to have a detailed understanding of the devices electronic properties. With these challenges in mind the work performed for this thesis was centered around bulk synthesis by catalytic chemical vapor deposition (CVD) of carbon nanotubes and the use of some aspects of the synthesis technologies developed to fabricate high strength nanocomposites and novel nanotube-based bio- and gas-sensors.

Following this brief introduction, Chapter 2 will provide a review of the basic knowledge about carbon nanotubes that has emerged so far from published research. It will cover structural studies and especially techniques used for the characterization of single walled carbon nanotubes (SWNTs). Chapter 3 will review various CVD methods for bulk production of single wall nanotubes and the results presented in this chapter will provide an optimized method and a reaction mechanism that can be scaled up for the production of high quality SWNTs with minimal post processing for purification. Chapter 4 will turn to the experimental CVD method to infiltrate single and multiple wall carbon nanotubes into metal (iron and aluminum) matrices. The composites formed are characterized to determine if metal carbide phases are present. The findings will yield information on increase in yield strength and hardness with selective incorporation of

nanotubes as a filler material. Chapter 5 will focus on methods to directly grow or electrophoretically deposit carbon nanotubes as part of a process to fabricate a bio-sensor or bio-probe device. The use of pre-synthesized SWNTs in the fabrication of gas sensors and their testing under various gas environments will also be discussed in Chapter 5. Detailed conclusions are drawn in Chapter 6 and the future work in Chapter 7.

CHAPTER 2

CARBON NANOTUBES

2.1 Overview

It is the chemical genius of carbon that it can bond in different ways to create structures with entirely different properties. This variety comes from the bonding configuration of carbon atoms. Carbon has six electrons, i.e. $1s^2$, or inner shell electrons which do not take part in the hybridization and the remaining four in $2s$ and $2p$ which can hybrid to form sp, sp^2 and sp^3 structures. Diamond and graphite are the two well-known forms of crystalline carbon. Diamond has four coordinated sp^3 carbon atoms forming an extended three-dimensional network, whose motif is the chair conformation of cyclohexane. Graphite has three coordinated sp^2 carbons forming planar sheets, whose motif is the flat six-membered benzene ring. The latter sp^2 type of bonding builds a layered structure with strong in-plane bonds and weak out-of-plane bonding of the van der Waals type. Graphite is thus a soft material, which slides along the planes. The story of *fullerenes* and *nanotubes* belongs to the architecture of sp^2- bonded carbon and the subtlety of certain group of topological defects that can create unique, closed shell structures out of planar graphite sheets.

Graphite is the thermodynamically stable bulk phase of carbon up to very high temperature in the normal range of pressure. This is not true when there are only finite numbers of carbon atoms; it is because of the high density of dangling bonds when the size of graphite crystallites becomes smaller (i.e., nanosize). At small sizes, the structure does well energetically by closing onto itself and removing all the dangling bonds. Thus, with few hundred-carbon atoms, the structure formed corresponds to linear chain, rings,

and closed shells. The closed shell carbon atoms with even number of atoms are called *Fullerenes*.

To form curved structures from a planar fragment of hexagonal graphite lattice, certain topological defects have to be included in the structure. To produce a convex structure, positive curvature has to be introduced into the planar hexagonal graphite lattice. Creating pentagons does this; one needs exactly twelve pentagons to provide topological curvature necessary to completely close the hexagonal lattice, which strictly follows Euler's principle. One can thus imagine that a greatly elongated fullerene can be produced with exactly twelve pentagons and millions of hexagons. This would correspond to a *Carbon Nanotube*.

Iijima first observed in 1991 that multi-walled carbon nanotubes (MWNTs) (Figure. 2.1 a) of graphite were deposited on the negative electrode during the direct current arcing of graphite used for the preparations of fullerenes (Iijima, 1991). This followed by the discovery of single-walled carbon nanotubes (SWNTs) (Figure. 2.1 b) (Iijima, 1993; Bethune, 1993) lead to a new era of research in nanotechnology. The unique one dimensional structure and cylindrical symmetry of SWNTs leads to appealing mechanical and electrical properties which have received a great deal of attention and investigation. A wide range of potential applications has been proposed for carbon nanotubes due to their extraordinary properties. Applications include but are not limited to conductive high-strength composites, field effect transistors, gas- and bio-sensors, field emission displays, semiconductor devices, and energy storage.
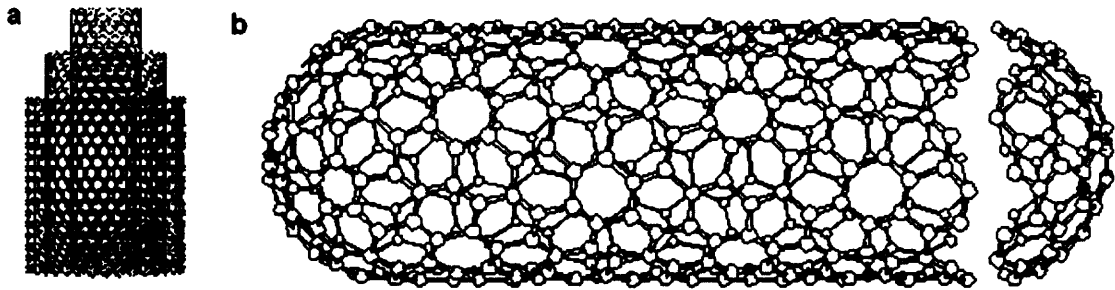
Figureure 2.1 (a) Multi-walled carbon nanotube (MWNT) consisting of concentric cylinders formed by wrapping of graphene sheets. **(b)** Single-walled carbon nanotube (SWNT).
[Source: Iijima 1993, Bethune 1993].

SWNTs and MWNTs have been mainly utilized in three areas of research both academically as well as industrially, namely: field effect transistors for sensors, flat panel display emitters and conductive high strength composites. Nanoelectronic devices using carbon nanotubes will be useful in downsizing the circuit dimensions, thus, following Moore's law computational power can be increased with shrinkage of circuits by orders of magnitude (Moore 1965). In addition, SWNTs are ballistic conductors and can conduct electricity at room temperature without significant scattering from the atoms and defects. Therefore, electrons encounter very little resistance and dissipate minimal thermal energy in the SWNTs (Tans, 1997). In addition to shrinkage of electronic devices, the ballistic conducting properties arising due to quantum wire like structure make them useful in novel devices such as spin transport medium for spintronics. Experimental results show that metallic SWNTs can carry currents up to 10^9 A/cm^2, and since nanotubes are completely covalently bonded with sp^2 configuration there is no electromigration as in case of metals due to atomic diffusion. This property makes it useful in high power electronics (Liang, 2001; Yao, 2000). The electronic structure of a nanotube is dependent

on the diameter and chirality (this will be discussed in detail in a later section on band structure of the tubes), resulting in both metallic and semiconducting tubes. The semiconducting tubes when contacted between two metal electrodes can be used as a field effect transistor (FETs). Semiconducting tubes can be converted from conducting to insulating state by modulating the gate field (Tans, 1998). Transistors using an individual SWNT can be fabricated by identifying the position of the nanotube on a surface by means of markers and atomic force microscope (AFM) scans (Helbling, 2007), by dragging nanotubes on pre-defined electrodes using AFM tips (Martel, 1998; Bachtold, 2001), or by drop casting solutions on the substrates and contacting with metal electrodes (Tans, 1998). Although promising results have been reported using individual SWNTs, several inherent properties such as diameter and chirality variations in typical samples, make it challenging to obtain reproducible devices. Therefore efforts are underway to find alternative ways of incorporating SWNTs in conventional CMOS schemes to fabricate reproducible devices. This will be discussed in Chapter 5 which discusses the fabrication of individual SWNT based gas sensors.

Nanocomposites utilizing carbon nanotubes are the second-most promising direction in nanotechnology. With the discovery of near molecular scale carbon nanotubes and advances in understanding their mechanical and electrical properties over the past decade, new nanocomposites based on these novel materials are possible. Experimental estimates of SWNT strength are in the range of 13-52 GPa and tensile modulus is of the order of 1 T Pa (Yu, 2000; Walters, 1999; Gere 1990), values much higher than those of carbon fibers. Electrical resistivity and thermal conductivity measurements along the length of a bundle of SWNTs indicate values approximately 10^{-4}

Ωcm and 200 Wm^{-1}K^{-1}, respectively (Hone, 2000). Two main issues to be addressed for the effective use of nanotubes and the translation of their extraordinary mechanical properties to a composite are alignment and uniform dispersion in the polymer/ceramic/metal matrix. Jia, 1999 et al. used an in-situ process for the fabrication of a PMMA/MWNT composite. An initiator was used to open up the π bonds of the MWNTs in order to increase the linkage with PMMA. The formation of C-C bonds result in a strong interface between the nanotubes and the PMMA. Haggenmueller, 2003 et al. used a method of repetitive film forming and mixing at high temperature and pressure, this resulted in uniform dispersion. The first commercial application of MWNTs has been their use as electrically conducting components in polymer composites. Nanofiber morphology with high aspect ratio leads to low loading levels of the MWNTs that allow sufficient conductivity for originally insulating plastics. Promising results have been reported for polymer-nanotube composites; however, not enough improvement in mechanical properties has been achieved in metal composites, which can be attributed to bundling of nanotubes. This part will be discussed in detail in the Chapter 4.

In addition to electronic and mechanical applications, MWNTs have been shown to outperform commercial silicon AFM tips (Dai, 1996; Nishijima, 1999). The use of MWNTS as AFM tips has a number of advantages, which result from their high aspect ratio and small diameter. Mechanical robustness of MWNTs and the low buckling force dramatically increases the probe life and minimize sample damage. Also, deep and narrow structures can be easily accessed and imaged. Furthermore, functionalization with different chemical groups is used to investigate the local chemistry of the surface being probed (Wong, 1998).

Another area of interest is the functionalization of carbon nanotubes. Functionalization of nanotubes imparts new chemical and electrical properties different from those of pristine nanotubes (Chen, 1998; Mickelson, 1998). New properties arise from the attachment of chemical species to the sidewalls or ends of carbon nanotubes which is used to tailor the interaction nanotubes with other entities, such as solvents (Wang, 2005), a polymer matrix (Ramanathan, 2005), or other nanotubes (Chiu, 2002). Functionalization can be obtained through chemical or physical means. Chemical modification includes sidewall functionalization by desired molecular groups whereas physical modification is deposition of suitable species on the surface of nanotubes. Carbon nanotube caps and defects are more active than the sidewalls and prone to oxidation. Most of the functionalization process starts with prolonged acid treatments to add carboxylic, nitrate, and chlorine groups. Synthesized single-walled carbon nanotubes (SWNTs) are a mixture of metallic and semiconducting tubes, functionalization aides in dispersing (Chen, 2001) and separating the tubes on the basis of electronic properties (Zheng, 2003).

2.2 Structure and Types

An ideal single-walled carbon nanotube can be thought of as a hexagonal network of carbon atoms that has been rolled up to make a seamless cylinder. Just a nanometer across, the cylinder can be tens of microns long and each end is capped with half a fullerene molecule. Generally, nanotubes form in two categories. The first form is called multiple walled carbon nanotubes (MWNTs Figure 2.1 b). They are made of concentric cylinders placed around a common central tube, with spacings between the layers close to

that of the interlayer distance in graphite of 0.34 nm. Their external diameters are on the

order of 4-50 nm. The MWNTs can be grown using catalytic chemical vapor deposition,

so that by patterning the catalyst and applying an electric field or plasma during growth,

it is possible to obtain the vertically aligned and patterned nanotubes shown in Figure. 2.2

a. The smallest possible MWNT is the double wall carbon nanotube as shown in Figure

2.2 b.
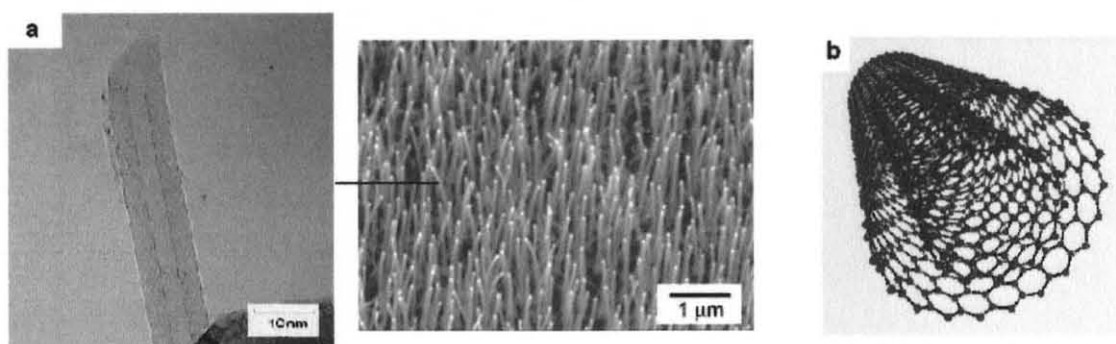
Figureure 2.2 (a) Transmission electron microscope image of a MWNT and aligned
MWNTs. **(b)** Double wall carbon nanotube.
[Source: Harris, 1999].

The electrical properties of MWNTs are found to be less interesting because electron

conduction in MWNTs occurs through the outer shell. Since the diameter of the nanotube

shell is relatively large, the band gap (ca. 3.4 eV) and semi-metallic band structure

approaches that of graphite (Bachtold, 1999). Layers can be removed via oxidation and it

has been observed that each layer has its own electronic structure (Collins, 2001).

The second form of nanotubes are called single walled carbon nanotubes (SWNTs

Figure 2.1 b), which are close to fullerenes in diameter and comprise of a single cylinder.

They possess uniform diameters (0.4 - 2 nm) and can be several micrometers long

(Collins, 2001; Qin, 2000; Zheng, 2004). They also assemble via van der Waals interactions to form hexagonally aligned bundles of individual SWNTs (Thess, 1996).

The structure of carbon nanotubes is distinct from that of all previously known carbon fibers and filaments. A SWNT can be thought of as a graphene sheet rolled up to from a cylinder, such that open edges meet to form a tube with the ends closed. The pentagons nucleate to initiate the closure mechanism. The rolling of the graphene sheet can be done in various ways, satisfying the criterion that the dangling bonds present at both the edges are matched. Any translational shift along the edges before fitting the dangling bonds will lead to a different orientation of the lattice with respect to an arbitrary tube axis. Thus, in general, the hexagonal arrays of carbon atom winds around in a helical fashion, introducing helicity to the structure. In the mapping of a graphene plane into a cylinder, the boundary conditions around the cylinder can be satisfied only if one of the Bravais lattice vectors (defined in terms of two primitive lattice vectors and a pair of integers (m, n)) of the graphene sheet maps to a whole circumference of the cylinder. This scheme is very important in characterizing the types of single wall nanotubes (see below) and the essential symmetry of the nanotube structure.
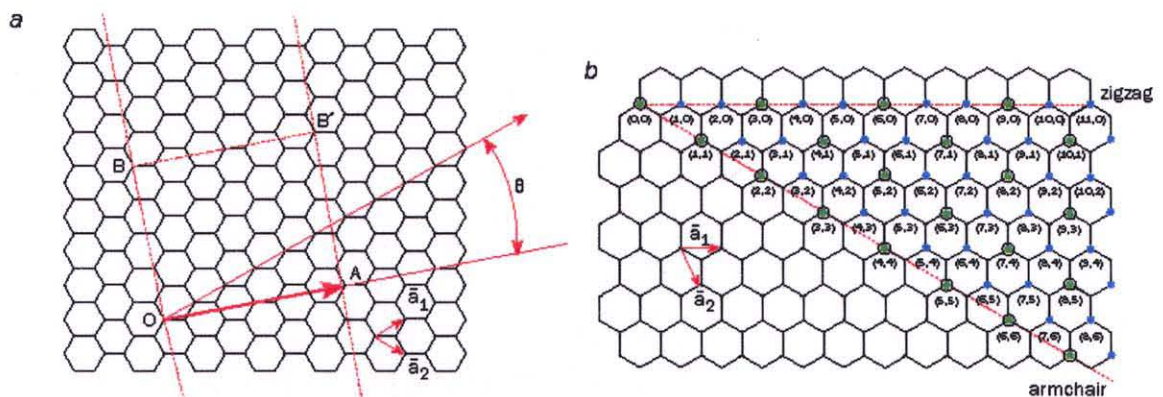
Figure 2.3 A carbon nanotube is based on a two-dimensional graphene sheet. **(a)** The chiral vector is defined on the hexagonal lattice as $C_h = n\bar{a}_1 + m\bar{a}_2$, where $\bar{a}_1$ and $\bar{a}_2$ are unit vectors, and n and m are integers. The unit cell of this nanotube is bounded by OAB'B. To form the nanotube, imagine that this cell is rolled up so that O meets A and B meets B', and the two ends are capped with half of a fullerene molecule. Different types of carbon nanotubes have different values of n and m. **(b)** Zigzag nanotubes correspond to $(n, 0)$ or $(0, m)$ and have a chiral angle of $0°$, armchair nanotubes have (n, n) and a chiral angle of $30°$, while chiral nanotubes have general (n, m) values and a chiral angle of between $0°$ and $30°$. Nanotubes can either be metallic (dots enclosed in circles) or semi-conducting (dots).
[Source: Dresselhaus, 2001].

The circumference of any SWNT is characterized by the chiral vector, which is defined by:

$$C_h = na_1 + ma_2 \qquad (2.1)$$

where a_1 and a_2 are the unit vectors in the hexagonal lattice and n and m are the integers as shown in Figure. 2.3 a. n and m indices fully identify the SWNTs. Nanotubes made from lattice translational indices of the form $(n, 0)$ or (n, n) will have two helical symmetry operations while all other sets of nanotubes will have the three equivalent operations. The $(n, 0)$ type of nanotubes are in general called *Zig-Zag* nanotubes, whereas the (n, n) and m-$n = 3\ X$ (where X is an integer) types are called *Armchair* nanotubes; all others are called *Helical or Chiral* nanotubes (Figure. 2.4 a-c). Armchair SWNTs are all metallic whereas zig-zag and helical tubes are either metallic or semi-conducting (Dresselhaus, 2001). Electronic properties of the nanotubes are dictated by the diameter and chirality. Chiral vector basically forms the circumference of the SWNT and the diameter is the circumference divided by π. It is also related to the chiral indices by the following relationship.

$$d_t = \frac{\sqrt{3}a_{c-c}(m^2 + mn + n^2)^{1/2}}{\pi} = \frac{C_h}{\pi} \qquad (2.2)$$

Where $a_{c\text{-}c}$ is the distance between neighboring carbon atoms. The chiral angle θ is given by

$$\theta = \tan^{-1}[\sqrt{3}n/(2m+n)] \qquad (2.3)$$
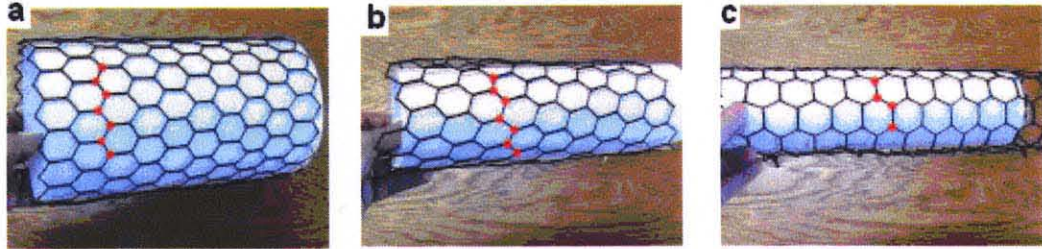
Figure 2.4 (a) Zig-Zag nanotube, **(b)** Chiral nanotube, **(c)** Armchair nanotube.

SWNT bundles can be characterized by using Raman spectroscopy and scanning electron microscopy (SEM) while individual nanotubes can be characterized by scanning tunneling microscopy (STM) and transmission electron microscopy (TEM). Some of the above mentioned structural properties of the nanotubes are given below in Table 2.1.

Table 2.1 Structural Parameters for Carbon Nanotubes
[Source: Charlier, 2000]

Symbol Name	Formula	Value
"a" Length of unit vector	a= √3a $_{c\text{-}c}$ = 2.49 A	a $_{c\text{-}c}$ = 1.44 Å
"$\bar{a}_1$, $\bar{a}_2$" unit vectors	(√3/2, 1/2) a, (√3/2 , 1/2) a	x,y coordinate
"b_1, b_2" reciprocal lattice vectors	(1/√3, 1) 2π/a, (1/√3, 1) 2π/a	x,y coordinate
"C_h" chiral vector	$C_h = na_1 + ma_2 \equiv$ (n, m)	(0≤ |m | ≤ n)
"L" length of C_h	L = |C_h| = a√(n^2 + m^2 + nm)	
"d_t" diameter	d_t = L/π	
"θ" chiral angle	sin θ = √3m/(2√(n^2 + m^2 + nm)) cos θ = (2n +m)/ /(2√(n^2 + m^2 + nm)) tan θ = √3m/(2n +m)	(0≤ |θ | ≤ π/6)

2.3 Band Structure of SWNTs

As mentioned in the last section, graphene and carbon nanotubes are closely related according to their atomic scale structure and this relationship also holds true for the electronic structure and properties (Saito, 1992). In graphene, three of the four valence electrons of carbon are hybridized in sp^2 orbitals forming covalent σ bonds to neighboring atoms, and the one remaining electron populates a p orbital. The half filled p orbital forms a valence bond with one bonding π and one antibonding π* orbital with the neighboring atoms. The bonding π orbital is filled, while the antibonding π* orbital is empty. Since all the atoms contribute an electron in a p orbital, the electron in the π orbital are delocalized over the entire atomic plane. This situation is very similar to the delocalized electrons in conjugate double bonds, e.g. in benzene. But in contrast to benzene, where the electrons are restricted to the limited geometry of the benzene ring, in graphene the electrons can move in the plane with momentum. This leads to the band structure of graphene.

The band structure is usually presented in the first Brillouin zone of the reciprocal lattice, which is shown in Figure. 2.5 for graphene. The band structure of graphene can be obtained by following dispersion relation (Saito, 1992).

$$E_{graphene} = \pm\gamma_0\left\{1 + 4\cos\left(\frac{\sqrt{3}k_y a}{2}\right)\cos\left(\frac{k_x a}{2}\right) + 4\cos^2\left(\frac{k_x a}{2}\right)\right\}^{1/2} \quad (2.4)$$

Where γ_0 is the C-C tight bonding overlap energy, a is the lattice constant ($a = \sqrt{3}\ a_0$), where a_0 denotes the nearest neighbor distance with the value of 1.42 Å. In the Figure 2.5, b_1 and b_2 are base vectors.

Reciprocal lattice vector

Bravais Lattice
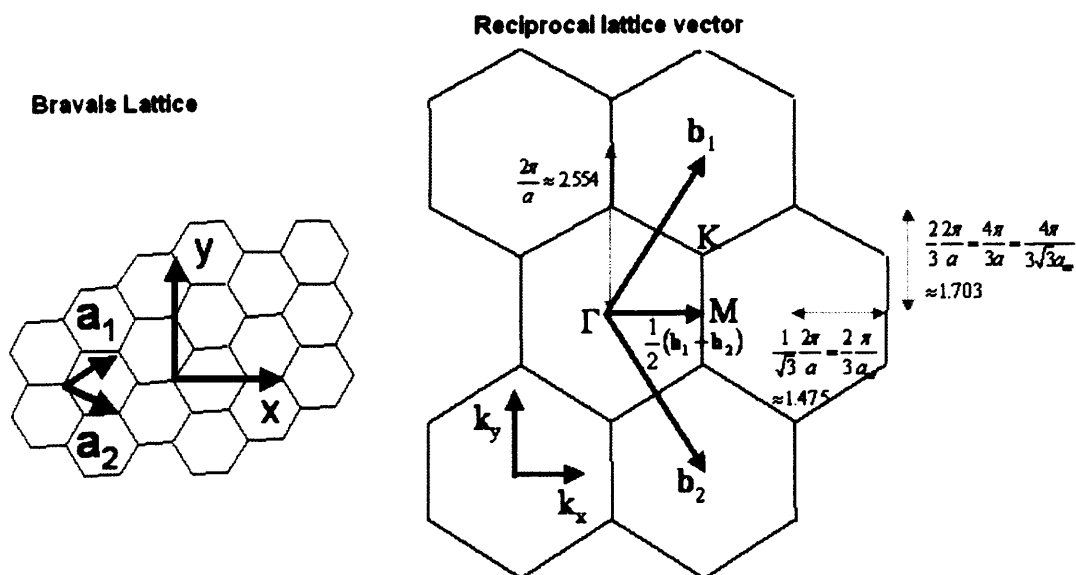
Figureure 2.5 Bravais lattice and corresponding reciprocal lattice vector for a graphene sheet.
[Source: http://www.photon.t.u-tokyo.ac.jp/~maruyama/kataura/discussions.html]

As mentioned before the bonding π orbital is filled and the antibonding π^* orbital is empty, thus the Fermi level is located between these bands. The π and π^* bands touch at K points, that is in the corners of the Brillouin zone, the density of states vanish at the Fermi level and graphene is a zero gap semiconductor. In graphite, the weak interaction between the graphene planes results in the small overlap between π and π^* bands, hence a small but finite density of states at the Fermi level is populated with electrons and holes, which makes graphite a semimetal (Cracknell, 1973; Samuelson, 1980). Since electronic transport is dominated by the electronic states near the Fermi level, the K points are the most interesting ones in the Brillouin zone.
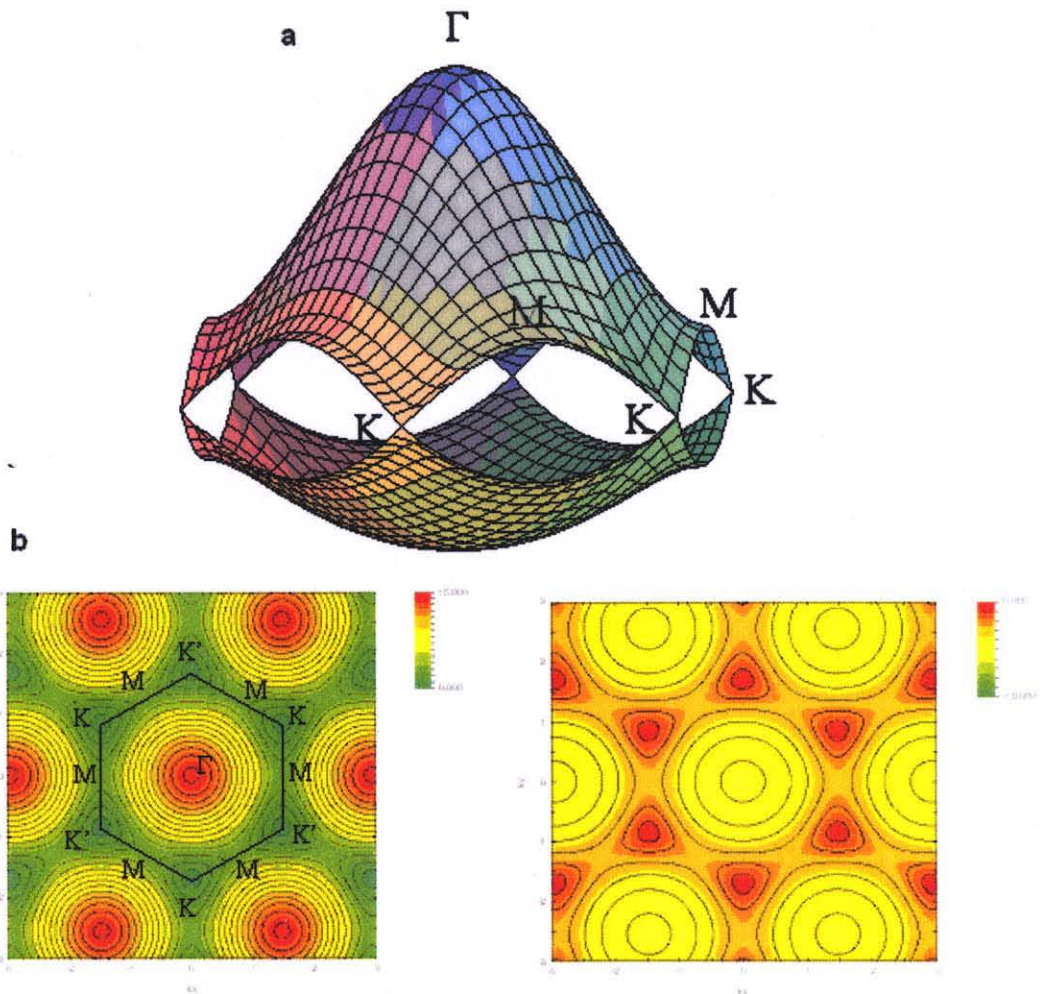
Figureure 2.6 (a) Band structure of graphene. The valence and conduction band touch at the six Fermi points in k space called K points. **(b)** Contour plot of graphene valence states for a SWNT with zero chiral angle. Lower energies are marked with yellow and higher with red (right hand side). The circular contours around six K points (left hand side) defines the graphene unit cell in k space, beyond this the unit cell repeats itself. [Source: Saito, 2000]

Now the band structure of a SWNT can be derived from the band structure of graphene (Saito, 1992; Hamada 1992). The electronic properties of SWNTs arise from their quasi-one dimensional nature, which leads to quantum confinement of the electrons in the circumferential direction. All the electronic states of the tube have to match this

periodicity around the circumference and thus their momentum $k_\perp$ has to fulfill (Saito, 1992) the following equation:

$$k_\perp C_h = 2\pi i \tag{2.5}$$

Where i is an integer and C_h is the chiral vector. Thus, when the graphene sheet is rolled up to form a nanotube each band of graphene splits into a number of subbands labeled by the subband index i, according to their quantization condition, the momentum k is directed along the tube axis. The emphasized lines in the Figure. 2.7 a- b are the subbands of the π and π^* bands of graphene. One dimensional dispersion relation is then given by (Saito, 1992)

$$E_{1D} = \pm\gamma_0 \left\{ 1 + 4\cos\left(\frac{q\pi}{n}\right)\cos\left(\frac{k_x a}{2}\right) + 4\cos^2\left(\frac{k_x a}{2}\right) \right\}^{1/2} \tag{2.6}$$

a   **b**
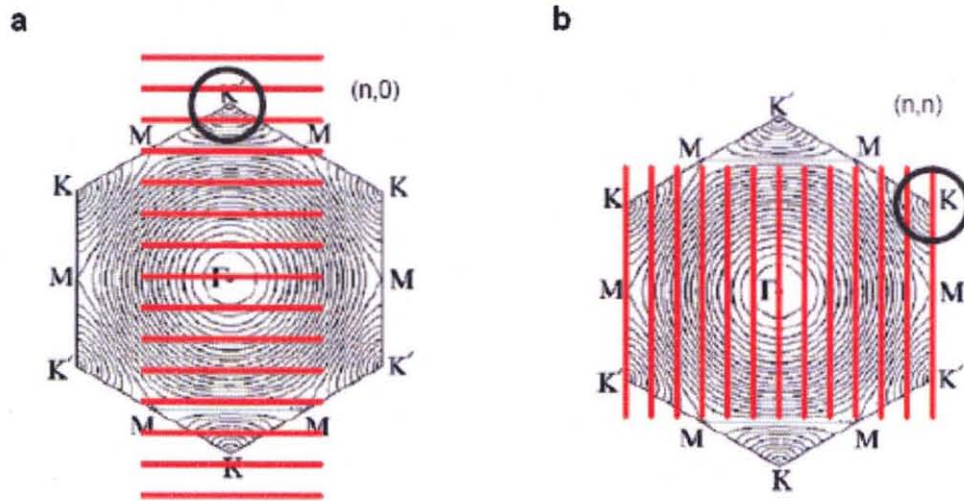
Figureure 2.7 Illustrations of orientation of the allowed k lines for zig-zag (n, 0) (a) and armchair (n, n) (b) tubes, respectively, superimposed on the graphene unit cell and contours of the electronic dispersion for the π^* electron.
[Source: Dresselhaus, 1992]

The allowed set of k values depends on the diameter and chirality of the SWNT as shown in Figure. 2.7 a-b. Exact alignment of the k points with the K points of graphene

determines the electrical properties of the SWNT. If the allowed k values are aligned with the special corner K points of the Brillouin zone, the SWNT behaves as a metal with a non-zero density of states at the Fermi level, as shown in Figure. 2.7 b. The reason for this is that now an electron has a path through an allowed state and then a Fermi point which allows it to enter the conduction band without additional energy. It is also possible that none of the allowed k values align with the K points. In this case, the SWNT will behave as a semiconducting tube (Liu, 2001). The energy gap is inversely proportional to its diameter (Dresselhaus, 1992), as shown in Figure. 2.7 a. Thus, electronic properties are diameter and chirality dependent and follow the selection rules as described in the structural section (2.2) of this chapter, i.e. metallic if $n - m = 3i$ and if $n = m$; semiconducting if $n - m \neq 3i$, where n, m and i are integers.

2.4 Characterization and Measurement Techniques for SWNTs and MWNTs

In this section various techniques that were used in this work to characterize as prepared catalyst, as prepared SWNTs/MWNTs and purified SWNTs/MWNTs are discussed briefly. A brief overview of measurement of mechanical and electrical properties of nanotube based composites and sensors are also discussed. These techniques will be also be discussed in detail in Chapter 4 and Chapter 5, respectively.

2.4.1 Raman Spectroscopy

Raman spectroscopy is the most powerful and widely used characterization technique for SWNTs. Raman scattering is the inelastic scattering of light, i.e. scattering of light in which the scattered photon gains or loses energy. A monochromatic beam of light is incident on the sample and the spectrum of the scattered light is examined. The elastic

scattered light (Rayleigh scattering) dominates the spectrum with an intense peak at the energy of the incoming photons. However, additional peaks are observed at energies different from the excitation energy and these peaks are known as Raman peaks after the Indian physicist Sir C.V. Raman who first observed the effect in 1928 (Raman, 1928). Thus, in the scattering process photons lose (Stokes) or gain (anti-Stokes) energy corresponding to the frequency shift. In solids Raman scattering excited in the ultraviolet to the infrared range occurs via the creation or annihilation of lattice vibrations or phonons, which either subtracts or adds energy to that of the incident photons. Lattice dynamics is intimately related to the solid state electronic and crystal structure and has been widely used as an indirect probe of atomic order in inorganic and organic crystals, and particularly in carbon allotropes, such as graphite, diamond, fullerenes and nanotubes (Dresselhaus, 2000; Schwan, 1996; Wagner, 1991). The observation of Raman spectra from very low concentrations of single wall nanotubes is possible because of the very large density of one-dimensional electronic states that occurs at well-specified energies referred to as van Hove singularities dependent on the unique geometric structure of each SWNT. When the incident photon energy is in resonance with the electronic transition energy between the valence band and conduction band at van Hove singularities or very special energy states, $E_{ii}(d_t)$, the Raman signal becomes very large as a result of the strong electron-phonon coupling which occurs between the electrons and phonons of the nanotube under these resonance conditions. Note that resonance enhancement occurs only in SWNTs due their quasi-one-dimensional structure. Multiwall nanotubes on the other hand are more two-dimensional and hence their electronic band structures have no van Hove singularities and therefore no resonance enhancement of the Raman spectrum.

The so-called Kataura plot is obtained when calculated transition energies between the van Hove singularities in the valence and conduction bands $E_{ii}(d_t)$, for all chiral SWNTs (n, m) are plotted versus the SWNT diameters (Kataura, 1999). The Kataura plot has been widely used to interpret the Raman spectra using different laser excitation energies from currently-produced SWNT samples which contain a mixture of nanotube diameters and chiralities. The plot is shown in Figure 2.8. To create the plot Kataura et al. measured the optical absorption spectra of SWNTs and correlated them with band structure calculations using the zone-folding method with the correlation given in Equation 2.4. Scanning tunneling microscopy studies (Wilder, 1998) and tunable wavelength Raman spectroscopy studies together with fluorescence measurements (Bachilo, 2002), showed that the theoretical Kataura plot agreed with the experimental data
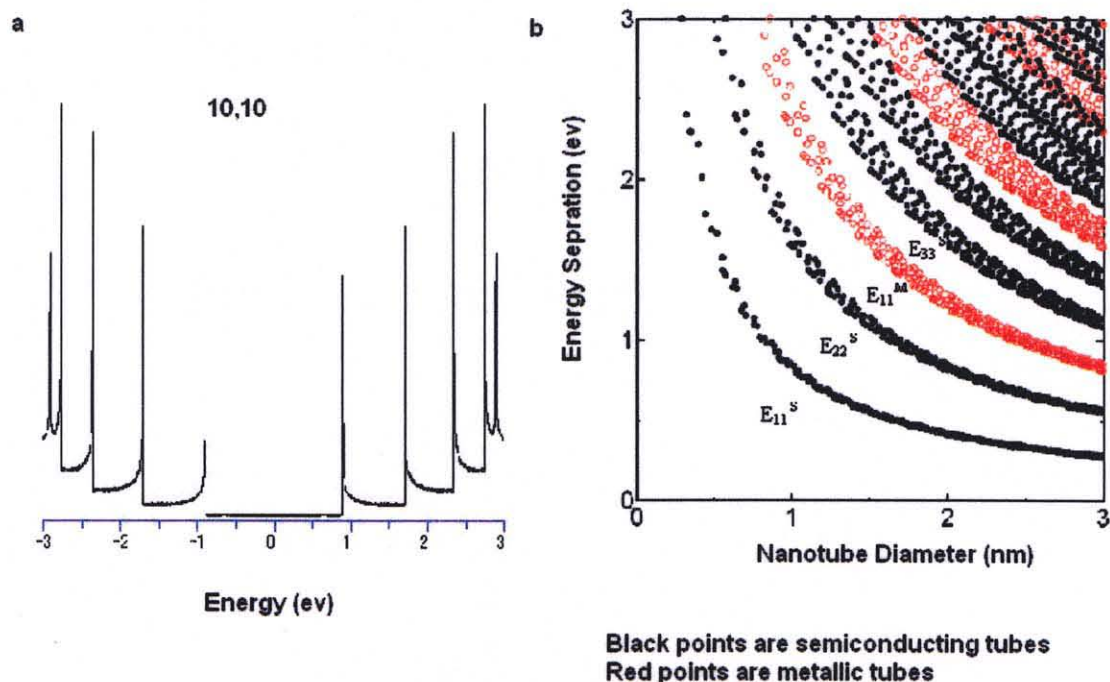
Figureure 2.8 (a) Electronic 1D density of states per unit cell for a metallic armchair SWNT (10, 10). Van Hove singularities are the peaks and the gap between valence and conduction band is shown. **(b)** Kataura plot for all (n, m) SWNTs, each circle denotes one chirality. [Source: Kataura, 1999]

Thus it can be inferred from the Kataura plot, that at an excitation of 632.8 nm (1.95 eV)

brings into resonance both semiconducting and metallic tubes in a typical SWNT sample.

In the spectrum, smaller diameter semiconducting SWNTs with resonant transition $E_{22}{}^{S}$

and larger metallic SWNTs with resonant transition $E_{11}{}^{M}$ will be apparent. (In this work,

mostly 632.8 nm excitation is used).

Raman-active modes can be predicted by group theory for specified lattice

structure and symmetry, although, group theory selection rules indicate that there should

be fifteen to sixteen Raman-active modes in a single wall carbon nanotube, only six or

seven lines are experimentally observed because some of the lines have small scattering

cross-sections. A typical Raman spectrum for SWNTs is shown in Figure 2.9. The

spectrum has three important features namely, low frequency lines assigned to radial

breathing modes (RBM) of the nanotubes, intermediate frequency disorder-induced mode

due to defects and/or amorphous carbon on the nanotube sidewalls (D-peak), and a higher

energy tangential mode (G-peak). One should note that in G-peak region there is shoulder

also labeled as the G⁻ peak due to the breakdown of the degeneracy of the G mode in

graphite via roll-up of the graphene sheet. The Raman lineshapes are Lorentzian except

for the G⁻ peak in metallic, which has a Breit-Wigner-Fano lineshape due to electron-

phonon coupling.
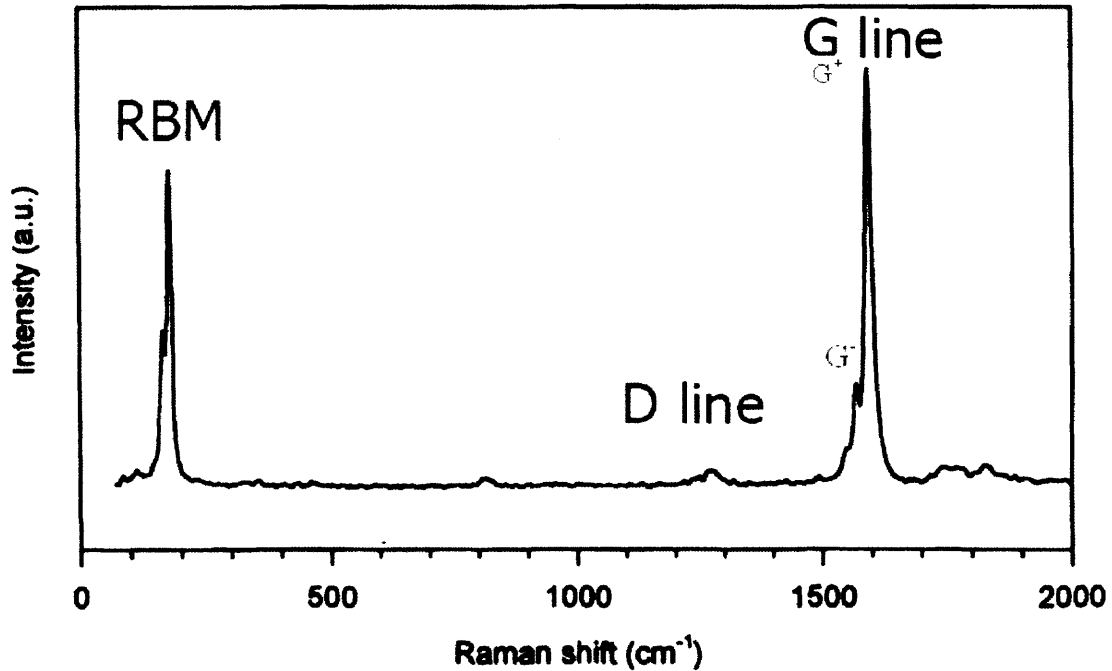
Figure 2.9 Raman spectrum for SWNTs showing RBM, D-peak and G-peaks.

The RBM lines usually appear in the low frequency region, between 120 – 280 cm^{-1} and correspond to the atomic vibrations of the carbon atoms in the tube's radial direction. RBM line frequencies are diameter-dependent and can be use to determine the average individual SWNT diameters following the relationship in Equation 2.7 (Rao, 1997).

$$d_t = (238 / \omega_{RBM})^{1.075} \tag{2.7}$$

where ω_{RBM} (cm^{-1}) indicates the RBM peak position and d_t (nm) is the diameter of the nanotube. The D line is the second important feature. It indicates the disorder-induced, defect bands at $\sim$ 1300 cm^{-1} for 632.8 nm laser excitation. Although it is usually referred to as the disorder line no definitive studies have concluded that these features can be attributed to kinks, heptagons and other defects on the tube walls. However, by empirical observation between the D - peak and G - peak intensity ratio one can monitor the quality of the SWNT sidewalls (Kataura, 2000). The G$^+$ line similar in frequency to the main line

in graphite is also referred to as the tangential mode because its C-C stretching eigenvector is parallel to the tube axis. As pointed out earlier, a second lower frequency G^- component is observed in SWNTs due to curvature-induced softening and removal of the degeneracy of the C-C graphene mode.

2.4.2 Scanning Electron Microscopy (SEM)

Scanning Electron Microscopy (SEM) is one of the most versatile techniques available for the characterization of carbon nanotubes. The primary reason for the usefulness is the high spatial resolution that can be obtained. For typical scanning electron microscopes, resolution on the order of 2 to 5 nm are possible, while advanced research instruments have resolution less than 1 nm in the range where individual SWNTs can be resolved. One of the important features of the SEM is the three-dimensional appearance of the specimen image, a direct result of the larger depth of field, as well as the shadow relief effect of the secondary and backscattered electron contrast. In the case of SWNTs, it is a good technique to check bulk yields as SWNTs form in bundles with diameters of about 15 nm. Alignment of nanotubes can also be studied using tilted SEM images. In this work a LEO (Carl Zeiss) 1530 VP microscope was used at the Material Characterization Laboratory of NJIT. Throughout the thesis SEM is extensively used to image catalyst deposition and dispersion, as-prepared and purified tubes, tubes formed in-situ in metal composites and on quartz template structures.

2.4.3 Transmission Electron Microscopy (TEM)

TEM provides cross-sectional information of the sample with at near-atomic scale resolution. In TEM a high energy monochromatic electron beam is accelerated towards a thinned down, electron transparent sample and the transmitted portion of the electrons and electron diffraction pattern are projected on to a phosphor screen. While in SEM mainly topographical information is revealed, TEM is able to provide much detailed information like number of sidewalls, defects such as kinks, density of catalyst particles, bundles in case of SWNTs, different forms of carbon and information about the growth mechanism if growth is performed in-situ in an environmental chamber (Sharma and Iqbal, 2004). We also used TEM to image the interface between the metal grains and the nanotubes in metal-carbon nanotube composites. Most of the measurements were performed using the TEM at NJIT [LEO 922 Omega EF-TEM]. For nanocomposites the TEM observations were made at Rutgers University using a TOPCON 002B ultra-high resolution TEM operated at 200 kV. The sample preparation varies and depends on the physical state of sample. For bulk nanotubes, samples are typically sonicated in ethanol or methanol and deposited on copper TEM grids with a holey-carbon layer. In case of metal-nanocomposites the sample preparations are more complex and time-consuming, and will be described in detail in Chapter 4.

2.4.4 X-Ray Diffraction

X-Ray diffraction (XRD) studies were performed to characterize the average structure of the SWNTs and to determine the presence or absence of impurity phases in the SWNT preparations and metal nanocomposites. The XRD patterns of purified SWNTs show only the (hk0) and (00l) reflections but no general (hkl) reflection was observed. Special

studies have been suggested to study the (hk0) reflection; such studies support the electron microscopy data of Murakami (1993). In this thesis, XRD studies were performed to find the level of purity of the SWNT samples, particularly to determine if the MgO catalyst support being used is washed away using dilute HCl after synthesis. In the case of the metal-nanocomposites XRD was used to determine if different phases of metal and carbon were formed during the growth of the SWNTs and MWNTs. All XRD measurements were made using a Philips XRD diffractometer [PW3040, in the Materials Characterization Laboratory at NJIT].
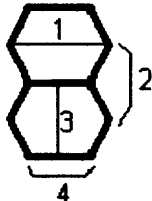
2.4.5 Mechanical Measurements

Information about enhanced mechanical properties for a composite reinforced with nanotubes was obtained by making two kinds of investigations. Firstly, the Vickers hardness measurements were conducted using a LECO micro-hardness tester (LM 700, LECO Corp.). A load of 10 kgf (kilogram force) at ambient temperature with a dwell time of 5 seconds was selected and an optical image of the indentation sites using a fine pixel camera attached to the LM 700 micro hardness tester was obtained before and after indentation. Secondly, stress-strain data were taken with an MTS servo hydraulic system operated at a constant displacement rate so as to give a strain rate of about 0.00004/sec (Wiegand, 1991). The data were taken in simple compression along the cylindrical sample axis. Flow stress and work hardening coefficients were obtained from stress-strain curves for the nanotube-iron composites and compared with similar data obtained from the pristine reference iron pellets.

2.4.6 Electrical Measurements:

It is important to understand the electrical properties of SWNTs that are subsequently employed in devices. Understanding the conduction mechanism is also important in order to obtain the desired properties of the fabricated device. As mentioned in previous sections, the as-prepared bulk SWNTs are a mixture of metallic and semiconducting tubes, thus, this investigation becomes more important. In the case of transistors made for gas-sensing applications, we contact each tube with gold metal electrodes using e-beam evaporated Cr/Au metal pads followed by current-voltage (I-V) measurements using a LabView controlled set up. The measurement set up consisted of a current amplifier: Keithley 428 (0.01 nA to 10µA), two multimeters: Keithley 2000 (-100 mV to 100 mV), and two voltage sources Keithley 2400 meters (-20V to 20V). The details about the laboratory-scale gas test set up and different types of electrical measurements will be discussed in Chapter 5.

Table 2.2 Compilation of Properties. All Values are for Single Wall Carbon Nanotubes Unless Otherwise Stated

Equilibrium Structure

Average Diameter of SWNT's	1.2 -1.4 nm
Distance from opposite Carbon Atoms (Line 1)	2.83 Å
Analogous Carbon Atom Separation (Line 2)	2.456 Å
Parallel Carbon Bond Separation (Line 3)	2.45 Å
Carbon Bond Length (Line 4)	1.42 Å

C - C Tight Bonding Overlap Energy	~ 2.5 eV
Group Symmetry (10, 10)	C_{5v}
Lattice: Bundles of Ropes of Nanotubes	Triangular Lattice (2D)
Lattice Constant	17 Å

Lattice Parameter:

(10, 10) Armchair	16.78 Å
(17, 0) Zigzag	16.52 Å
(12, 6) Chiral	16.52 Å

Density:

(10, 10) Armchair	1.33 g/cm³
(17, 0) Zigzag	1.34 g/cm³
(12, 6) Chiral	1.40 g/cm³

Interlayer Spacing:

(n, n) Armchair	3.38 Å
(n, 0) Zigzag	3.41 Å
(2n, n) Chiral	3.39 Å

Optical Properties
Fundamental Gap:

For (n, m); n-m is divisible by 3 [Metallic]	0 eV
For (n, m); n-m is not divisible by 3 [Semi-Conducting]	~ 0.5 eV

Electrical Transport

Conductance Quantization	$(12.9 \text{ k}\Omega)^{-1}$
Resistivity	10^{-4} Ω-cm
Maximum Current Density	10^{13} A/m²

Thermal Transport

Thermal Conductivity	~ 2000 W/m/K
Phonon Mean Free Path	~ 100 nm
Relaxation Time	~ 10^{-11} s

Elastic Behavior

Young's Modulus (SWNT)	~ 1 TPa
Young's Modulus (MWNT)	1.28 TPa
Maximum Tensile Strength	~ 100 GPa

CHAPTER 3

SYNTHESIS OF CARBON NANOTUBES USING THERMAL CATALYTIC CHEMICAL VAPOR DEPOSITION

3.1 Abstract

The primary objective of the work described in this chapter is the synthesis of single walled carbon nanotubes (SWNTs). Thermally-induced catalytic chemical vapor deposition (CVD) was utilized as a simple and cost-effective approach for producing high quality SWNTs. The effect of growth parameters in a CVD system was investigated in order to optimize the process. As-grown and purified SWNTs were characterized using Raman spectroscopy, field emission scanning electron microscopy (FE-SEM), X-ray diffraction (XRD), and transmission electron microscopy (TEM) to obtain structural and purity information. It was found that nucleation and growth of SWNTs occurred within a few seconds of the introduction of the carbon source, carbon monoxide, resulting in the formation of high quality SWNTs with a narrow diameter distribution in thin bundles. The SWNTs synthesized comprised of only small amounts of amorphous carbon and were grown using cobalt nitrate (as the active catalyst precursor) mixed with molybdenum nitrate (the promoter precursor) and magnesium oxide as catalyst support, at a temperature above 675 °C. These studies together with data on exit gas concentrations of CO_2 formed during SWNT synthesis allowed the determination of a simple kinetic model. This served as the basis for a large scale method for production of SWNTs using thermal CVD in a fluidized bed reactor.

3.2 Background on SWNT Synthesis

SWNTs can be synthesized using four methods, namely, arc-discharge (Bethune, 1993; Iijima, 1993; Journet, 1997; Ebbesen, 1992), laser ablation (Thess, 1996; Guo, 1995; Yudaska, 1997), plasma-enhanced chemical vapor deposition (PECVD) and thermal chemical vapor deposition (CVD) (Endo, 1995; Kong, 1998; Cassell, 1999; Hafner, 1998). The growth of carbon nanotubes takes place by a vapor-liquid-solid growth mechanism. Carbon vapor generated from the carbon precursor diffuses into the catalytic metal particles, leads to a liquification of the nanoparticles as indicated by the metal-carbon binary phase diagram and finally the precipitation of a graphitic filament occurs at saturation. In arc-discharge and laser ablation methods carbon precursors are generated from graphite rod, whereas for CVD the carbon source is gaseous carbon monoxide, ethanol vapor or a hydrocarbon gas, such as methane.

3.2.1 Synthesis of SWNTs by Arc Discharge

In the arc discharge method, carbon atoms are evaporated in plasma of helium gas when an arc is ignited between the graphite anode and cathode as shown in Figure 3.1. C_{60} fullerene is synthesized by a similar method, and Iijima (1991) was the first to show that multiwall carbon nanotubes (MWNTs) form on the cathode. Ebbesen and Ajayan (1992) demonstrated the synthesis of bulk quantities of MWNTs by this method. The as-grown MWNTs were shown to have few defects such as heptagons and pentagons on the side walls of nanotubes. Relatively large quantities of disordered carbons that form during synthesis by this method can be removed by controlled oxidation; nevertheless the oxidation process also removes a considerable amount of the nanotubes formed. For the growth of SWNTs small amounts of catalytic metals (such as, cobalt and nickel) were

placed inside holes machined into the graphite electrodes. Growth of SWNTs was demonstrated for the first time by Iijima (Iijima, 1993) and Bethune et al (Bethune, 1993) using cobalt as catalyst in the graphite rods. Later Journet et al (Journet, 1997) optimized the arc-growth of SWNTs by utilizing 1 at % of yttrium and 4.2 at % of Ni as the catalyst. Significant amounts of SWNTs were found in the web-like soot material produced. The structure of these arc-grown SWNTs were found to be similar to that of the laser-grown (see below) tubes which been shown to have a hexagonally close packed bundled structure where the individual SWNTs are held together by van der Waals interactions.
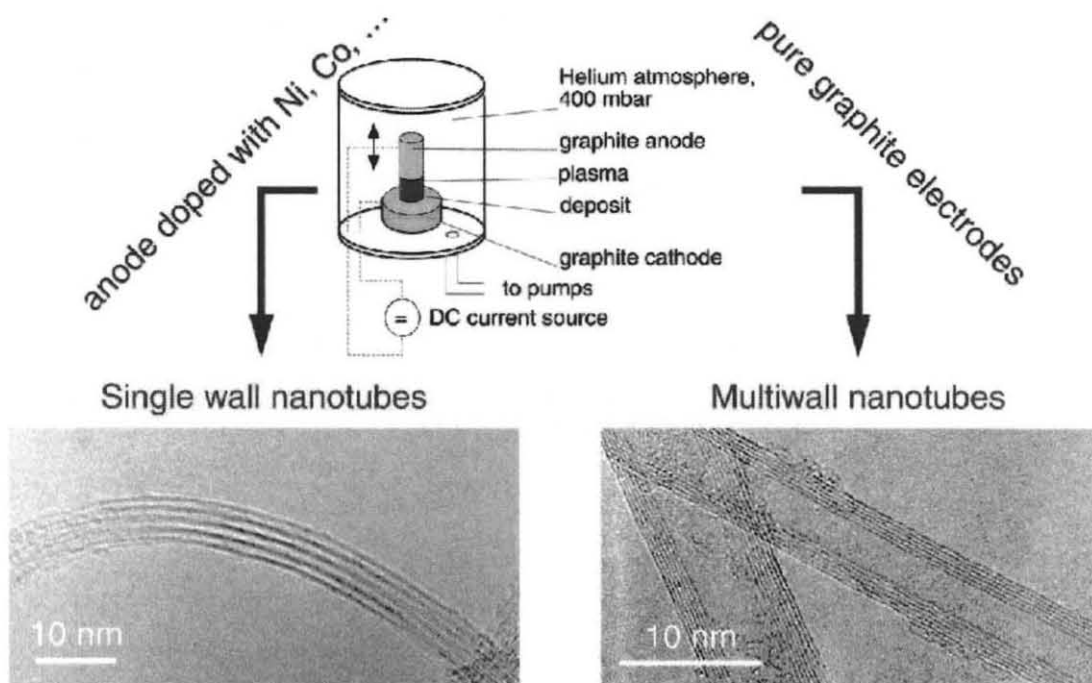
Figure 3.1 Schematic of arc discharge apparatus used for nanotube growth. TEM cross-sectional images for bundled SWNTs and 5-wall MWNTs grown using this method. [Source: Iijima, 1993].

3.2.2 Synthesis of SWNTs using Laser Ablation

In 1997 Smalley and coworkers demonstrated an alternative method for growth of SWNTs at the gram scale. The laser ablation method (Figure 3.2) utilizes intense laser pulses from typically two lasers impinging on the carbon target containing 0.5 at % of nickel and cobalt. The target is placed in a furnace heated at 1200 °C. A flow of inert gas (Argon) is introduced to carry the nanotubes grown to be collected on a cold finger located downstream. The SWNTs produced were mostly in the form of hexagonally-packed bundles or ropes consisting of tens of nanotubes. Around 70% SWNTs compared to about 50% SWNTs for the arc-method are produced by the laser process. By-products of this process are similar to that of the arc-process and consist of graphitic polyhedrons with enclosed catalyst metal particles, and small amounts of disordered carbon on the SWNT sidewalls.
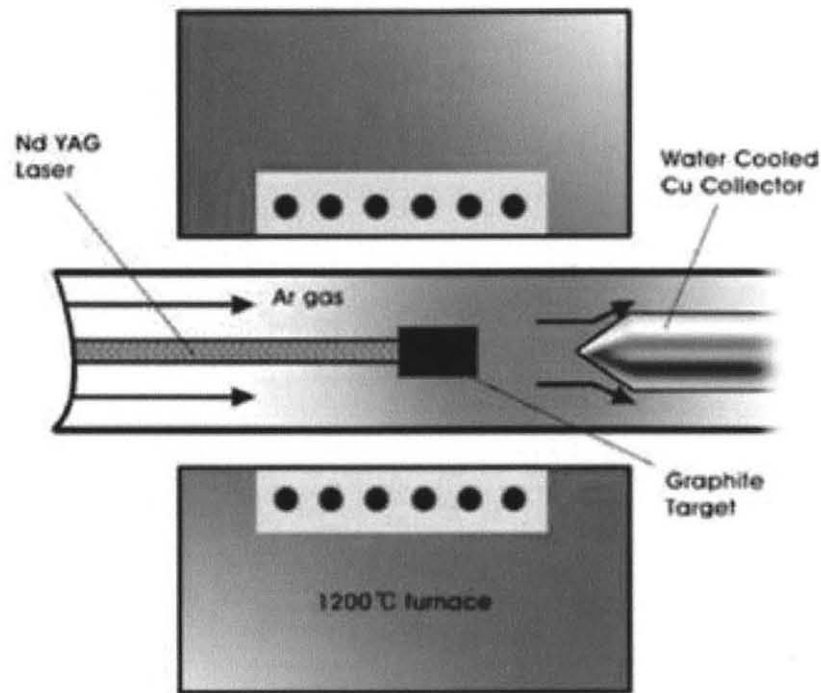
Figure 3.2 Laser ablation method to grow single walled carbon nanotubes.
[Source: Smalley, 1997].

Both arc discharge and laser ablation involve the condensation of carbon atoms generated by evaporation of graphite. The temperatures during growth are close to 3000 - 4000 °C and therefore these methods cannot be used to grow nanotubes directly on device structures or allow the growth of arrayed nanotubes. Moreover, the volume fraction of disordered carbon grown is rather high and scaled up production costs would therefore be prohibitive. However, attractive features of both arc- and laser- grown SWNTs due to their high growth temperatures, are the high degree of structural perfection of their sidewalls and relatively narrow distribution of tube diameters.

3.2.3 Synthesis of SWNTs by Chemical Vapor Deposition (CVD)

The above-mentioned two methods have long been the principal techniques used for the synthesis of SWNT. They both rely on evaporating carbon atoms from graphite at $\geq$ 3000 °C, for short reaction times of the order of a few micro- to milli-seconds. The CVD method on the other hand is a moderate temperature (700 - 1200° C) technique involving relatively long reaction times, which can typically run from minutes to hours. Arc discharge and laser ablation produce carbon nanotubes in the form of powders, whereas CVD can be used to make nanotubes both on the flat substrates (Kong, 1998; Franklin, 2001; Homma, 2002, Seidel, 2003) as well as in powder form (Lacerda, 2004; Dai, 1996). It is a more versatile process, allowing control of length and orientation (Zhang, 2001; Huang, 2003), together with a limited control on diameter of the nanotubes (Li, 2001; Bachilo, 2003). Various CVD methods are available for nanotube growth, the prominent methods include decomposition of carbon monoxide at high pressure widely known as the HiPCO method (Nikolaev, 1999; Bronikowski, 2001), disproportionation of carbon monoxide (Alvarez, 2001; Kitiyanan, 2000; Zheng, 2002), and a new method that

is becoming prominent involving the use of alcohol CVD (Maruyama, 2002; Murakami, 2003). The CVD method can be used to make MWNTs (Delpeux, 2002) as well as SWNTs, by varying the carbon source and growth conditions. Typically metal catalyst particles such as Fe, Ni, Co, or Mo in powder form of their nitrate, acetate and molybdate salts or on as coating on a substrate are heated to high temperatures under hydrogen and a carbon feedstock in gaseous form is introduced into the reactor at 1 atm. for nanotube growth. The experimental setup and the schematic for the CVD method used in this work is shown in Figures 3.3 a and b. The parameters that greatly influence the growth and quality of the nanotubes produced are the choice of carbon feedstock, particle size and dispersion of catalysts, growth temperature and pressure, and the gas flow rate.
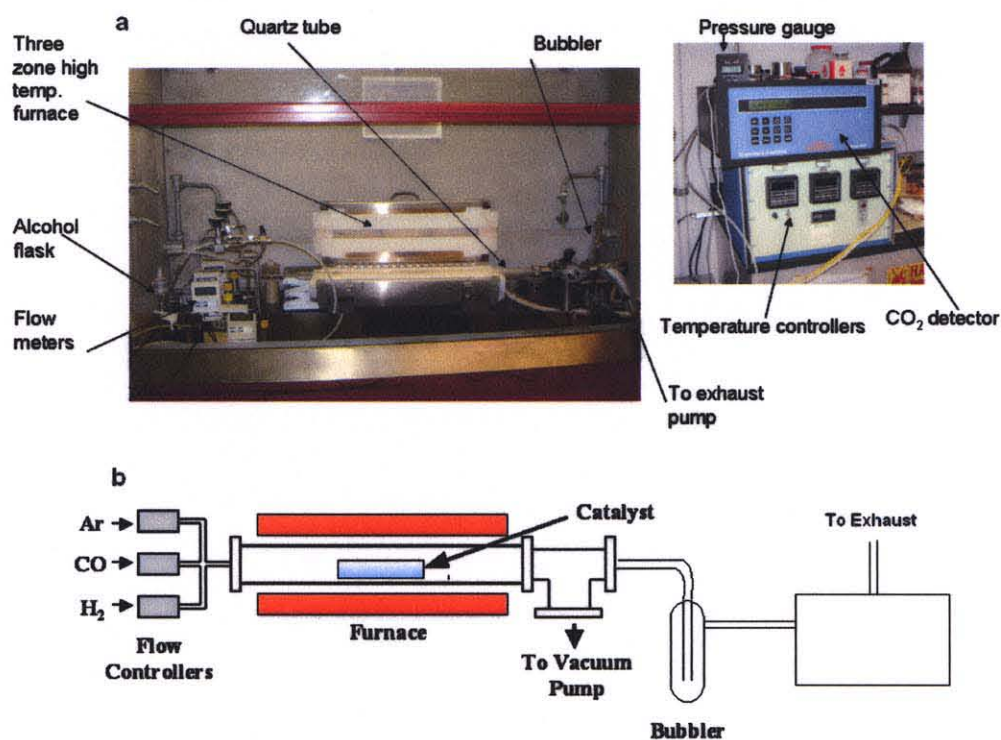
Figure 3.3 Experimental setup: a) photograph of the CVD setup used in this work, and b) schematic for growth of SWNTs.

Unsaturated hydrocarbon feedstocks, such as acetylene and ethylene have been reported to give higher yields and decomposition rates compared to methane, CO and alcohol. In addition, the latter gases give more ordered SWNT sidewalls. CO is also known to give more ordered MWNTs with fewer walls. Therefore, gases like methane and CO are mainly used for SWNT synthesis, whereas unsaturated hydrocarbon gases like acetylene and ethylene are used for the production of MWNTs. MWNTs can be grown at significantly lower temperatures of around 500-700 °C since the carbon feedstock for MWNTs dissociate at these temperatures and less stringent conditions are required for catalyst particle size. A major disadvantage of CVD grown MWNTs is their high defect densities, most likely arising due to low temperature growth conditions, which do not provide sufficient thermal energy to anneal out defects on the sidewalls. SEM images of CVD grown SWNTs and MWNTs from the literature are shown in Figure 3.4
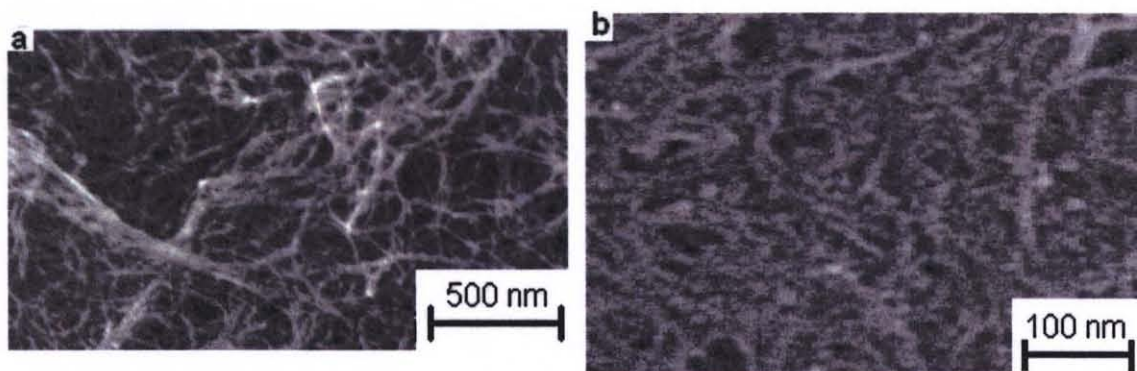
Figure 3.4 SEM images from literature a) HiPCO b) CoMoCat.

3.3 Growth Mechanism for Carbon Nanotubes

The model originally proposed for the growth of carbon fibers (Baker, 1972) and silicon whiskers (Wagner, 1964), widely known as the vapor-liquid-solid (VLS) model, has been extended to understand the growth mechanism of carbon nanotubes (Saito, 1995). The

VLS model schematically shown in Figure 3.5 can be explained in terms of the dissociation of the carbon precursor molecule under the catalytic conditions provided by transition metals. The metal nanoparticles provide the liquid phase by dissolution of carbon, which decreases their melting points. The transition metal catalysts are chosen because of the moderate solubility of carbon in the metals in the synthesis temperature range. The dissolved carbon precipitates out of the metal particle as a tube after the metal particle-carbon liquid is super-saturated. Nucleation and precipitation in the form of sp^2-bonded tubules occur in the colder regions of the particles. Tubule formation is favored over that of other forms of carbon such as graphitic sheets with open edges, because the energy gained by forming the closed tubular structure saturates the dangling bonds at the edges of graphene sheets initially formed. SWNT growth ceases after the catalyst particle is covered with amorphous or graphitic carbon layers, this prevents the diffusion of carbon into the metal and also leaves no further nucleation sites. The catalyst size is also an important factor. In the case of arc discharge and laser ablation methods the catalyst particles are fragmented in the carbon plasma and therefore the growth conditions, such as temperature, pressure and noble gas flow rate govern the particle size. Except for methods like HiPCO involving floating catalyst growth, in most CVD methods the catalyst particles are pre-synthesized from their precursor salts before nanotube growth. The size depends on the ability of the metal particles to disperse on the support material. For flat surfaces such as silicon and quartz wafers, it is highly desirable to use dispersing and immobilizing agents like polymers to create uniform and monodisperse catalyst layers. The Therefore the ability of transition metal catalysts to form nanotubes depends

on several factors, such as their binary phase diagram with carbon, formation of metastable metal carbides and interaction of the catalyst with the support material.
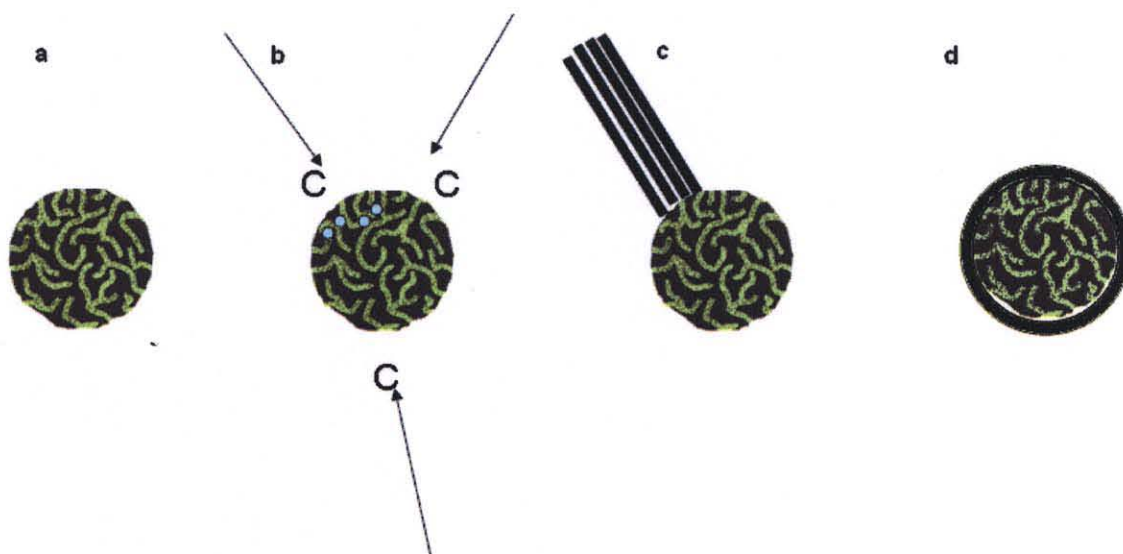
Figure 3.5 VLS model for carbon nanotube growth: a) porous support particle with embedded catalytic metal nanoparticles, b) carbon diffusion resulting in nucleation sites, c) carbon precipitates as nanotubes at super-saturation, and d) poisoned catalyst particle covered with graphitic carbon layers cutting off nanotube growth.

Two mechanisms have been observed for the growth of carbon nanotubes as shown in Figure 3.6. One mechanism involves bottom growth, where the catalyst particle is at the bottom of the tube and attached to the support material. In the second mechanism (referred to as tip growth) the catalyst particle is lifted up by the growing nanotube and attached to the tip while nanotube growth continues from the tip down. The type of growth involved is governed by the interaction between the metal catalyst particle and support material. Contact angles between the particle and support determine the strength of the interaction. For example, a large contact angle between the two results in a weak interaction and tip growth is favored, whereas small contact angles result in strong interaction and leads to bottom growth. In most cases bottom growth has been observed

for SWNT synthesis by CVD although tip growth has also been reported. MWNTs have been found to grow by similar mechanisms.

For bulk growth of SWNTs in the powder form a greater interaction of metal particle with the support material is desirable. A high surface area and large pore volumes are required specifically for the support material to contain sufficiently large numbers of well-dispersed catalyst nanoparticles. In addition, the metal particles must remain immobilized within the pores of the support material in order to withstand high temperatures without significantly growing in size by Ostwald ripening. The agglomeration and growth of the catalytic metal particles generally lead to the formation of MWNTs and in some cases large bundles of SWNTs. The most commonly used support materials are silica, alumina, zeolites and magnesium oxide. Substrates used for nanotube growth are: Si wafers, silica and quartz wafers.
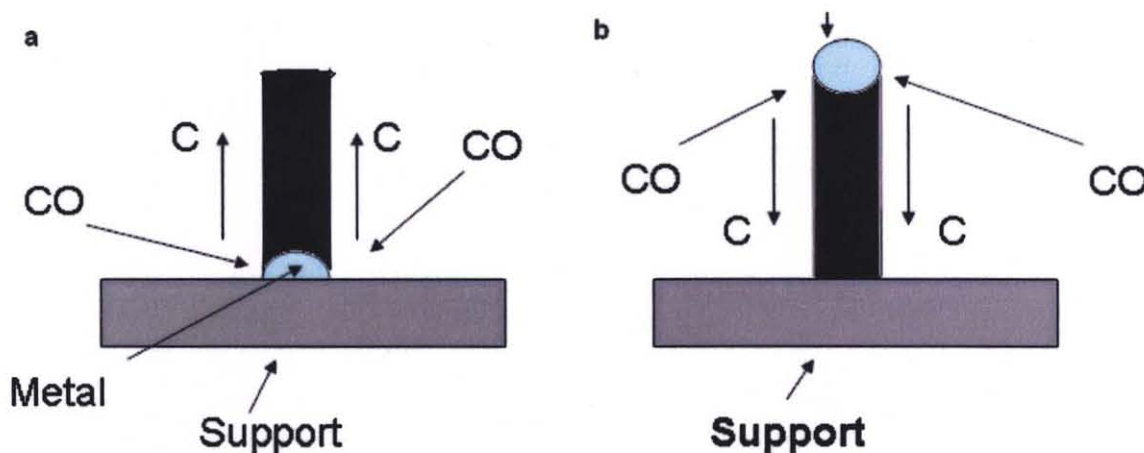
Figure 3.6 Schematic of the two mechanisms for the growth of SWNTs; a) base growth, where carbon atoms or carbon dimers deposit at the support, and b) tip growth where carbon atoms or dimers deposit from the tip down.

3.4 Comparison of Key CVD Methods for Bulk SWNT Production

3.4.1 High Pressure Carbon Monoxide (HiPCO) Synthesis of SWNTs

Commercially viable quantities of SWNTs using the high pressure catalytic decomposition of carbon monoxide referred to as the HiPCO method was developed at Rice University by Smalley's group (Zheng, 2002; Nikolaev, 1999). Iron pentacarbonyl [Fe(CO)$_5$] an organometallic precursor that decomposes at high temperatures in the gas phase to iron particles is used to catalyze the synthesis. SWNTs then grow by the disproportionation of carbon monoxide to carbon via the following reaction which is also known as the Boudouard reaction:

$$2CO \text{ (g)} \leftrightarrow C \text{ (s)} + CO_2 \text{ (g)}$$
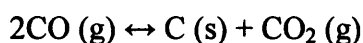
Since the reaction is reversible it is driven to the right by higher pressures (~30-100 atm). Also relatively high temperatures (near ~1050 °C) are used. Gas-phase iron pentacarbonyl decomposes rapidly above 300 °C (Nichllos, 1973) whereas the disproportionation reaction occurs at a significant rate only at temperatures above 500 °C (Renshaw, 1970). Thus, the rate at which the gas mixture is heated through the temperature range of 300–500 °C determines the outcome of this process. In addition, CO and Fe(CO)$_5$ are initially kept at a low temperature using a water-assisted injector and allowed to heat up rapidly on introduction into the reaction chamber. Carbon monoxide as a carbon source is more stable than unsaturated hydrocarbons. It also produces very little disordered carbon at the growth temperatures used. This also limits the overall conversion rate to carbon and as mentioned above the reaction rate is increased by high temperature and pressure. Using this method a SWNT growth rate upto ~450 mg/hour with a purity of about 75~80 %, can be achieved. A TEM image of SWNTs grown using

this method is shown in Figure 3.7. Because of the need to remove large amounts of catalyst metals, the price of SWNTs synthesized by this method is relatively high. SWNTs produced and purified by Carbon Nanotechnologies Inc of Houston, TX can be currently obtained at a price of $500/gm.
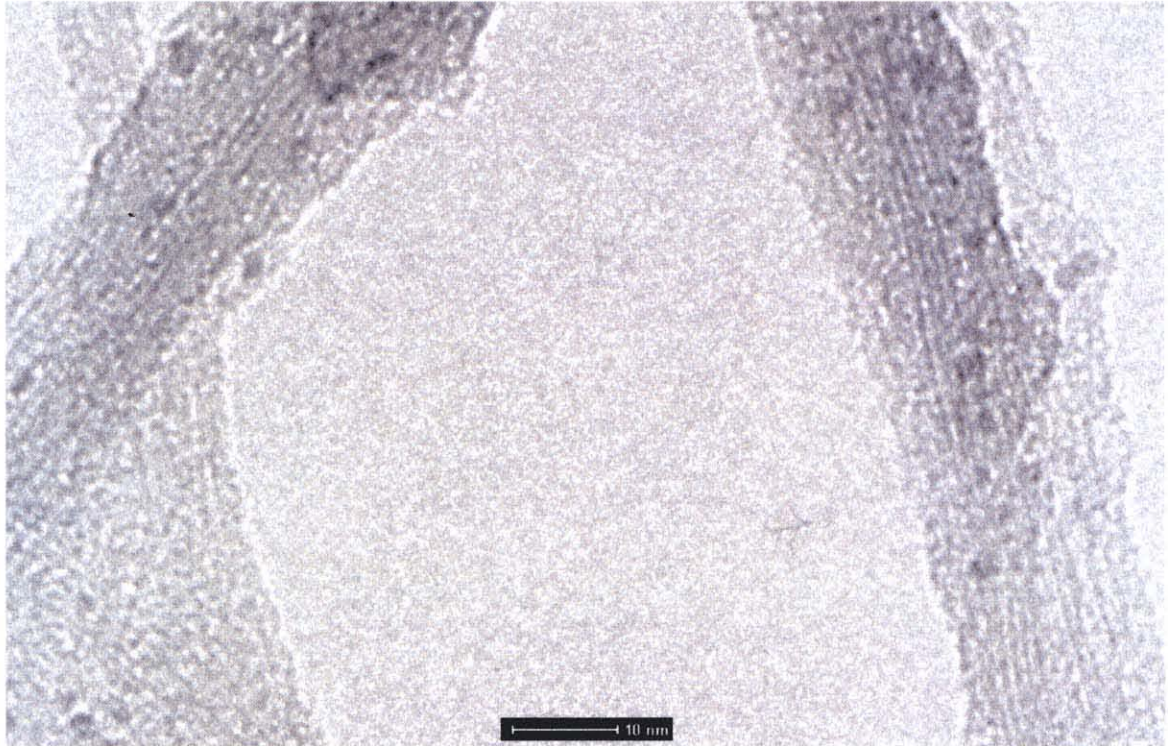
Figure 3.7 TEM image for a bundle of SWNT synthesized using the HiPCO method [Ref: sample obtained from CNI and observed at NJIT, TEM facility].

3.4.2 Cobalt Molybdenum Catalytic Chemical Vapor Deposition (CoMoCat) Method using Carbon Monoxide for Synthesis of SWNTs

CoMoCat is a chemical vapor deposition method developed by Resasco et al. (Alvarez, 2001; Kitiyanan, 2000) for the synthesis of SWNTs. A bimetallic Co-Mo catalyst embedded in SiO_2 (silica gel) support was used. The catalyst was prepared using a wet method which involved soaking the support material with solutions of cobalt nitrate and ammonium heptamolybdate to achieve the desired atomic ratio of the catalytic metals. Carbon monoxide was used as the carbon source and the synthesis was carried out at a

temperature range of 600-800 °C and the pressure between 1 atm and 5 atm. This method is relatively more economical than the HiPCO method; however, the use of silica support makes its removal more difficult. This method can also be used to grow SWNTs on silicon wafers, quartz and zeolites. Both randomly oriented tubes and vertically aligned tubes have been grown using this method on flat silicon wafers. High flow rates are necessary to grow the vertically aligned SWNTs. In addition to the work of Resasco et al, growth of SWNTs by carbon monoxide CVD using different substrates have also been reported by other groups (Dai, 1996; Plöjnes, 2002; Zheng, 2002).

3.4.3 Carbon Monoxide Chemical Vapor Deposition (CO-CVD) Method for Synthesis of SWNTs

This method was developed and optimized in the course of this work. Here SWNTs were synthesized in powder form using carbon monoxide as the carbon source and MgO as the catalyst support material. A detailed parametric study of the various factors influencing the growth of the SWNTs was performed. Specifically the effects of catalyst type, bimetallic catalyst composition, growth temperature, and flow rate and partial pressure of the carbon source, were investigated. The growth process consisted of three stages, namely: catalyst preparation, catalyst calcination and reduction, and finally, SWNT growth.

Catalyst preparation: The catalysts were prepared by a wet mixing and combustion synthesis method (Patil, 1993; Tang, 2001). Magnesium nitrate hexahydrate [$Mg(NO_3).6H_2O$], cobalt nitrate hexahydrate [$Co(NO_3).6H_2O$], ammonium heptamolybdate [$(NH_4)_6Mo_7O_{24}.4H_2O$] and citric acid (all from Sigma Aldrich) were mixed with enough distilled water to form a clear solution. Part of the solution was

poured into quartz or ceramic boats and fired for 5-10 min. at a temperature of 550-560 °C in a pre- heated furnace resulting in a fine creamy powder which was ground further using a mortar and pestle. Catalyst/support oxides in different atomic ratios $MgO_{(1-x-y)}Co_xMo_y$ were obtained. In a second approach to obtain larger quantities of catalyst for fluidization experiments, a simpler protocol for making the catalyst/support combinations were used. An aqueous solution of Co:Mo in a 1:4 ratio was mixed with magnesium oxide (MgO) (Sigma Aldrich) powder of 20 µm size and citric acid, followed by calcination at a temperature of 150 °C in large ceramic trays. The powder was then sieved using a 500 µm mesh and further annealed to remove moisture because water can act as a weak oxidant.

Calcination and reduction: The calcination and reduction of the catalyst was performed using a microprocessor controlled three-zone (Applied Tests Systems Inc.), horizontal tube furnace, Desired amount of catalyst/support precursors were placed in quartz boats and covered with Toray® carbon paper. The catalyst was calcined by heating to 500 °C for a period of 30 min. under ambient pressure. This step converted the nitrate and molybdate salts into their respective oxides. The setup was pumped (GE, ¼ HP) to 10^{-2} torr before the reduction step and backfilled with hydrogen (Spectra Gases Inc, research grade) to atmospheric pressure. The temperature was maintained at 500 °C for a period of 35 min. and a flow rate of 100 sccm (standard cubic centimeters per minute). For the fluidized bed experiments less than 5 % H_2 mixed with nitrogen (N_2) (Matheson, ultra high purity) was used for safety reasons as the reduction gas. Hydrogen is known to form a combustible mixture with air in the 4% to 74 % range with an auto-ignition

temperature of 571 °C. These experiments should be conducted with great care and approval from the Safety Department of the institution should be obtained.

Nanotube growth: After pumping out the hydrogen in the last stage, the temperature was raised to 600-850 °C and the system was backfilled with flowing CO (Matheson, 99.9 % research grade) at atmospheric pressure and flow rates between 100-1000 sccm. The growth conditions were maintained for a period of 1-30 min. System was then filled with flowing argon (Matheson, research grade) and allowed to cool after each run.

Purification: As-prepared samples were treated with 4-6 M HCl (Sigma Aldrich, 36 % by vol.) and mixed well using a magnetic stirrer for 45 min. to 1 hour in order to remove the MgO support and catalytic metals. The solution was then vacuum-filtered and the solids deposited on the filter paper (Millipore, PTFE 47 mm dia, 0.1 μm pore size) was allowed to dry and used for further analysis. In addition, the nanotubes obtained from the filter paper were suspended in water using a non ionic surfactant, Triton-X100 (Supelco) and again vacuum-filtered. After drying in ambient conditions a free standing nanotube sheet or paper was obtained. In order to remove the amorphous carbon remaining after the acid treatment a limited oxidation step was carried out using water vapor as oxidant. A small amount of water was placed in the first zone of the furnace and argon was used as the carrier gas. The nanotube paper or powder sample was placed in third zone and oxidation was performed at 450 °C. TGA (Hata, 2004) data have shown that the oxidation temperature of SWNTs takes place well above 450 °C while for amorphous carbon is removed in the 300 – 450 °C temperature range.

3.5 Results and Discussion

3.5.1 Effect of Catalyst Composition

A total of six different compositions were used to grow SWNTs while keeping all other variables, such as synthesis temperature, flow rates, carbon source and growth time, constant. As described in the experimental section the catalyst was prepared in various atomic percent combinations with MgO as the common support material. All the calculations were performed based on a starting material comprised of 3 gms of $MgNO_3$. Six combinations were used: 1) $Mo_{0.05}MgO_{0.95}$, 2) $Co_{0.05}MgO_{0.95}$, 3) $Co_{0.01}Mo_{0.01}MgO_{0.98}$, 4) $Co_{0.01}Mo_{0.02}MgO_{0.97}$, 5) $Co_{0.01}Mo_{0.04}MgO_{0.95}$, and 6) $Co_{0.05}Mo_{0.01}MgO_{0.94}$. The Raman spectra displayed here are divided into the radial breathing mode (RBM) region below 1000 cm^{-1} and the tangential mode (TM) region around 1600 cm^{-1} for the above-mentioned catalysts and are shown in Figures. 3.8 (a-f) and 3.9 (a-f), respectively.
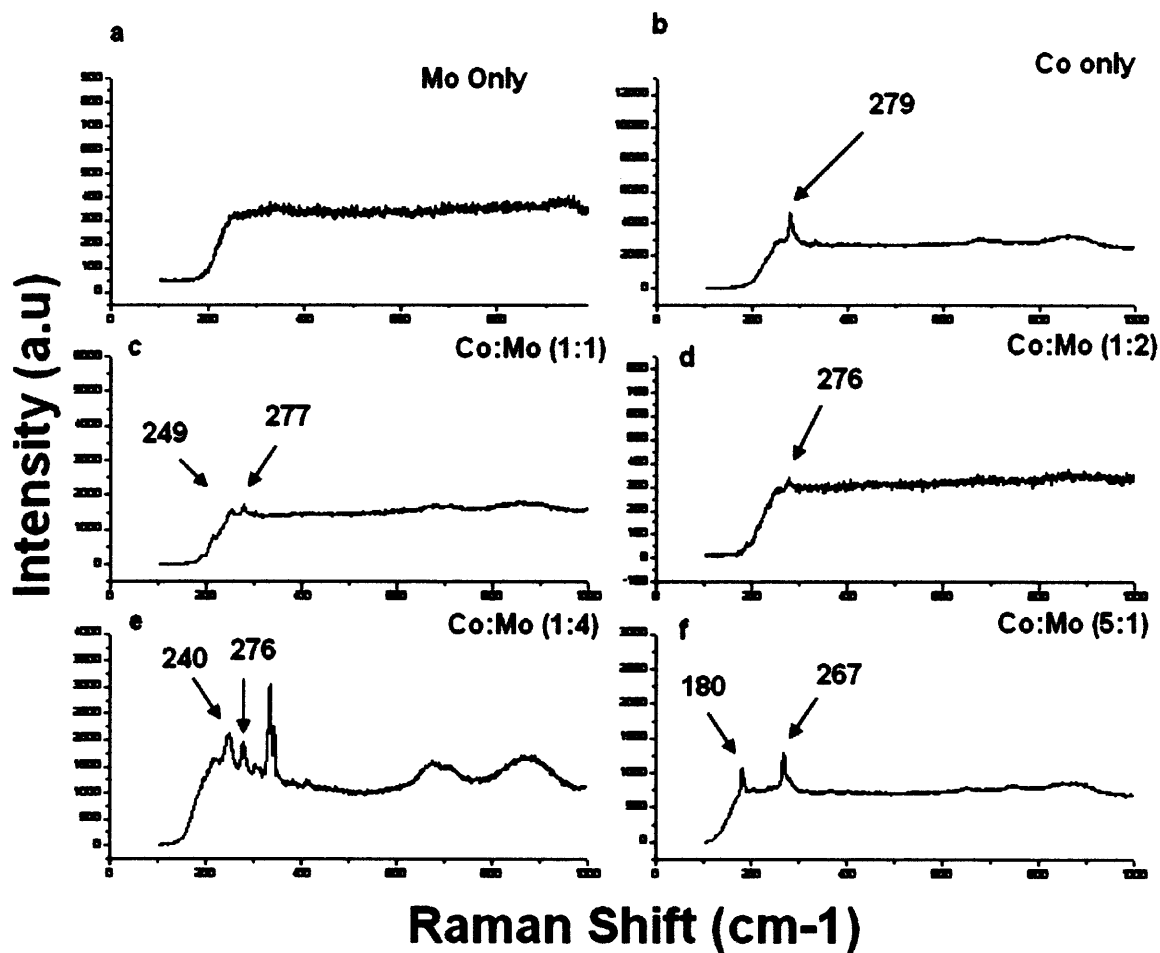
Figure 3.8 Raman spectra using 632.8 nm laser excitation in the radial breathing mode region for nanotubes prepared using catalyst compositions: a) Mo only, b) Co only, c) Co:Mo 1:1, d) Co:Mo 1:2, e) Co:Mo 1:4, and f) Co:Mo 5:1.
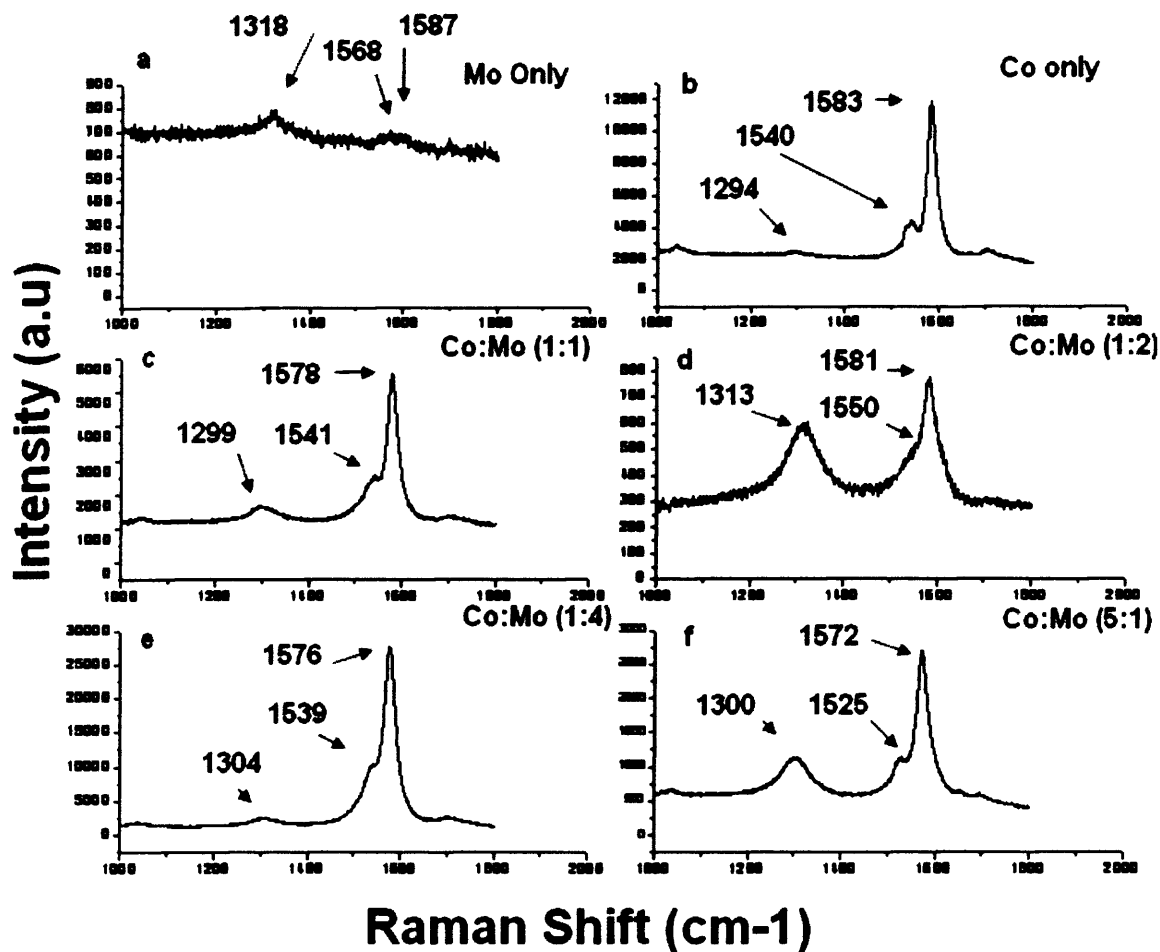
Figure 3.9 Raman spectra using 632.8 nm laser excitation in the disorder and tangential mode region for catalyst compositions: a) Mo only, b) Co only, c) Co:Mo 1:1, d) Co:Mo 1:2, e) Co:Mo 1:4, f) Co:Mo 5:1.

The SEM images of the samples prepared using the above-mentioned catalyst combinations are shown in Figure 3.10.

From the Raman spectra in Figures 3.8 (a) and 3.9 (a) for samples prepared using just Mo as catalyst, no RBM and TM features are observed indicating that SWNTs are not formed. The Raman spectra in Figures 3.8 (b) and 3.9 (b) for samples prepared using Co alone as catalyst indicate significant growth of SWNTs. The observed RBM line at 279 cm^{-1} corresponds to the presence of SWNTs with an average individual tube diameter of

0.84 nm (calculated using Equation 2.7). SWNT-specific TM features at 1545 cm^{-1} (G^{-} peak) and 1581 cm^{-1} (G^{+} peak) are also clearly observed. The presence of relative few RBM lines indicates a narrow diameter distribution of the SWNTs formed using Co alone as catalyst. However, the monometallic cobalt catalyst particles have no regular shape as evident from the SEM image in Figure 3.10 (b), where a random distribution with irregular shape and size of the metal particles can be observed. As molybdenum is mixed with cobalt to form bimetallic catalysts; the Raman spectra shown in Figures 3.8 (c-f) and Figures 3.9 (c-f) for ratios 1:1, 1:2, 1:4, 5:1 show clear features of SWNTs in both the RBM and TM frequency regions, respectively. The peak positions for each catalyst combination, calculated diameters from the RBM peaks and the ratio of intensity of the D to the G^{+} peak are listed in Table 3.1. The SEM images in Figures 3.10 (c-e) show monodispersed catalyst particles when molybdenum is equal to or in excess of cobalt metal, for example, in the 1:1, 1:2, 1:4 Co:Mo ratios, respectively. However, when cobalt metal is in excess as in case of 5:1 Co:Mo ratio, the catalyst shape and size become random. In addition, from Figure 3.11, a plot of the ratio of the intensities of the disorder line (D) and tangential mode (G^{+}) line ~ I(D)/I(G^{+}) gives an indication of the purity (and hence the quality) of the SWNTs prepared. The lower the value of this ratio the better is the average quality of the nanotubes synthesized. The lowest value of I(D)/I(G^{+}) = 0.090 is observed in case of samples prepared using a Co:Mo ratio of 1:4 indicating that this catalyst combination has the highest selectivity towards SWNT growth. Based on the Raman data, it is concluded that molybdenum acts as a promoter and cobalt acts as the active catalyst for SWNT growth. In addition, introduction of molybdenum makes the

bimetallic catalyst particles spherical and monodisperse, and thus more ideal for engineering studies related to scaled SWNT production.

Table 3.1 Raman Peak Positions, Calculated SWNT Diameters and Ratio of D/G$^+$ Line Intensities

Co:Mo	RBM Peaks (cm⁻¹)	SWNT Diameter (nm)	D peak (cm⁻¹)	TM peaks (cm⁻¹)		D peak intensity (a.u)	G$^+$ peak intensity (a.u)	I(D)/I(G$^+$)	Yield
				G$^-$	G$^+$				
0:1	No peak	N/A	1318	1568	1587	790	691	1.143	0
1:0	279	0.84	1294	1540	1583	2497	11712	0.213	11
1:1	249	0.95	1299	1541	1578	1653	5573	0.297	6.3
	277	0.85							
1:2	276	0.85	1313	1550	1581	594	768	0.773	7.5
1:4	240	0.99	1304	1539	1576	2497	27775	0.090	10
	276	0.85							
5:1	180	1.35	1300	1525	1572	1110	2691	0.412	12 to 18
	267	0.88							

The yields defined in terms of the weight of carbon deposited (after purification) to the total weight of starting catalyst for the various combination ratios, are listed in Table 3.1. However, one must note that this yield corresponds to the total carbon deposited and not only just SWNTs. Later in this study it will be shown using a simple EDX image analysis how different forms of carbon segregate. In addition, from the binary phase diagrams shown in Figure 3.12 for C-Co and Co-Mo the catalyst phase favorable for SWNT growth and the carbon adsorbed by the active cobalt catalyst can be determined. From Figure 3.12 (a) it can be seen that carbon dissolves in the α-phase of Co metal in the 700° -1000 °C temperature range. It is also observed from Figure 3.12 (b) that the Co present in the catalyst composition at a temperature of 550-560 °C is in the β

phase. However, at the nanotube growth temperature of around 700 °C, β-Co converts to α-Co in the presence of Mo. Under these conditions around 10 % (atomic) ~ 10 % (by weight) Mo is dissolved in cobalt whereas, around 1 % (atomic) ~ 0.17 % (weight) of carbon can dissolve in cobalt under the same conditions. This concentration of carbon in cobalt can be considered to be supersaturated - it represents the concentration at which carbon begins to precipitate out in the form of SWNTs. Elemental analyses by EDX was performed in order to confirm the distribution of catalyst over the support. In Figure 3.13, the ratio of Co:Mo agrees well with the composition desired over the entire surface scanned as shown in Figure 3.13. The table at the bottom left of Figure 3.13 lists the elemental weight and atomic percentages.
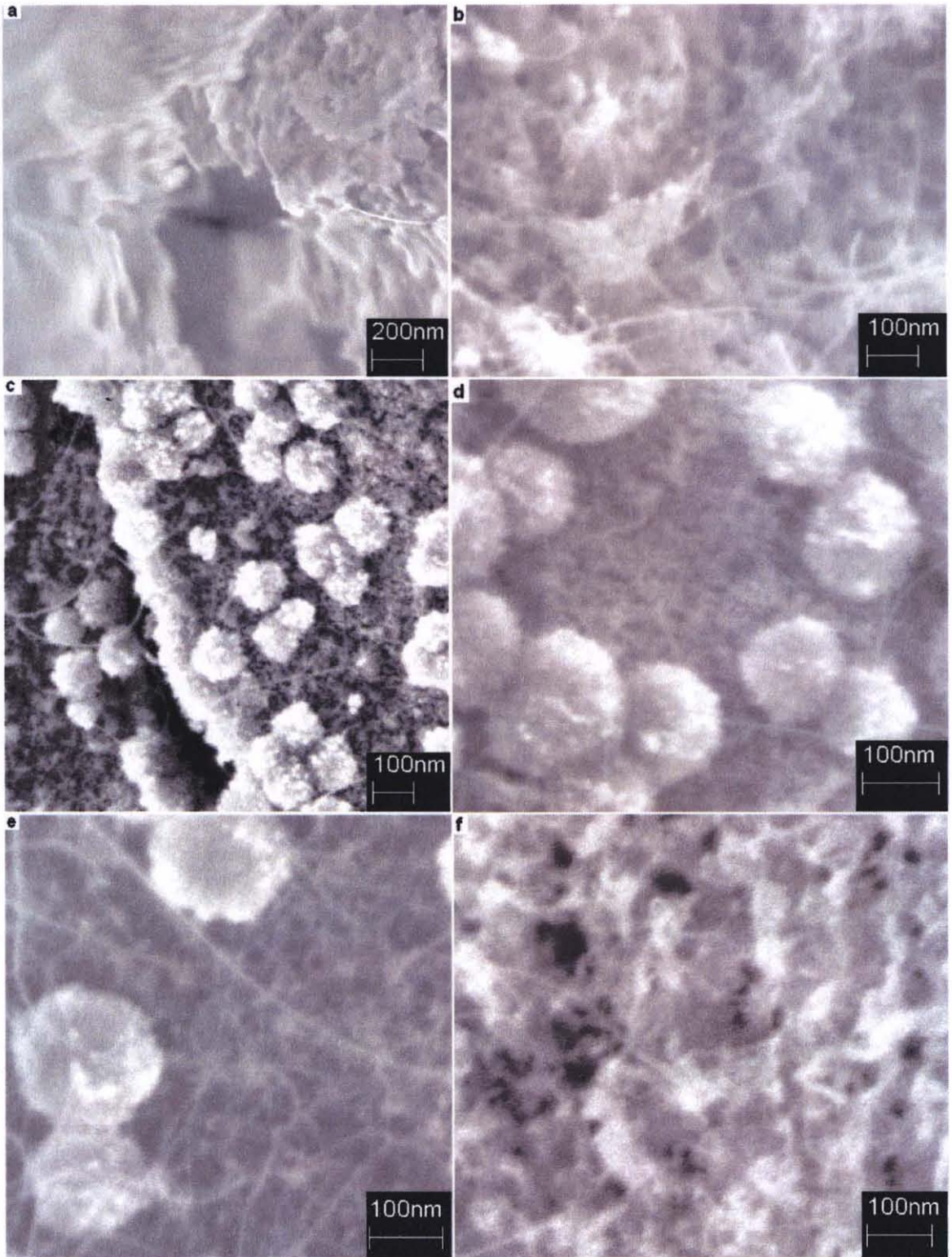
Figure 3.10 SEM images for as-prepared SWNT samples prepared over different catalysts: a) Mo only, b) Co only, c) Co:Mo 1:1, d) Co:Mo 1:2, e) Co:Mo 1:4, and f) Co:Mo 5:1.
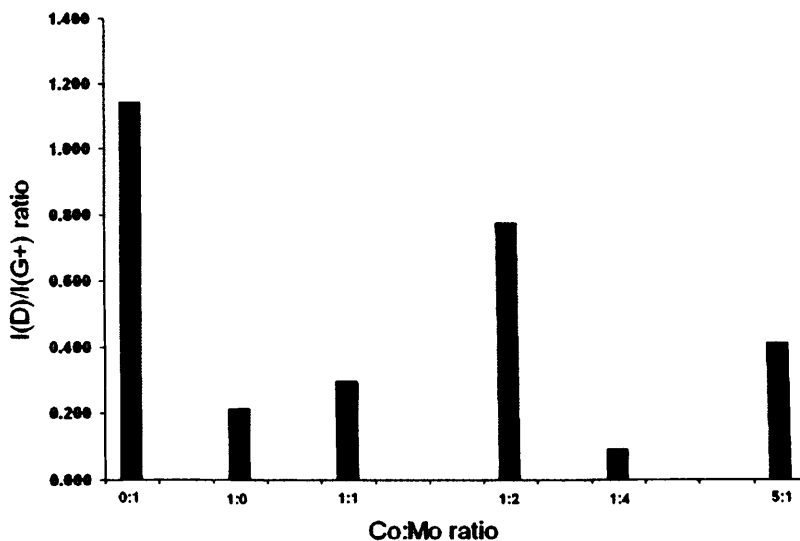
Figure 3.11 Ratio of disorder (D) to tangential mode (G⁺) Raman line intensities for SWNTs synthesized versus catalyst compositions used.
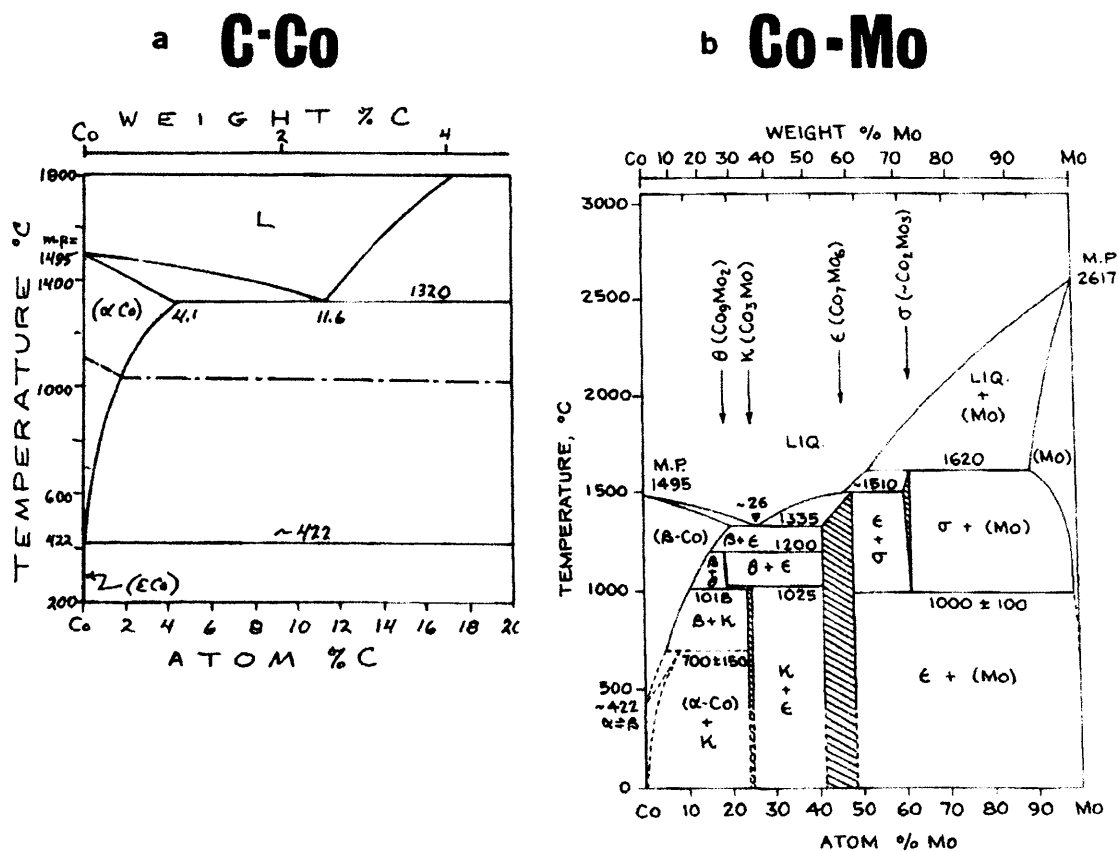
Figure 3.12 Binary phase diagrams: a) C-Co [Source: Ishida, 1991], and b) Co-Mo. [Source: Brewer, 1980].

Element	Weight%	Atomic%
C K	3.01	5.06
O K	47.49	59.94
Mg K	39.11	32.48
Co L	2.46	0.84
Mo L	7.93	1.67
Totals	100.00	
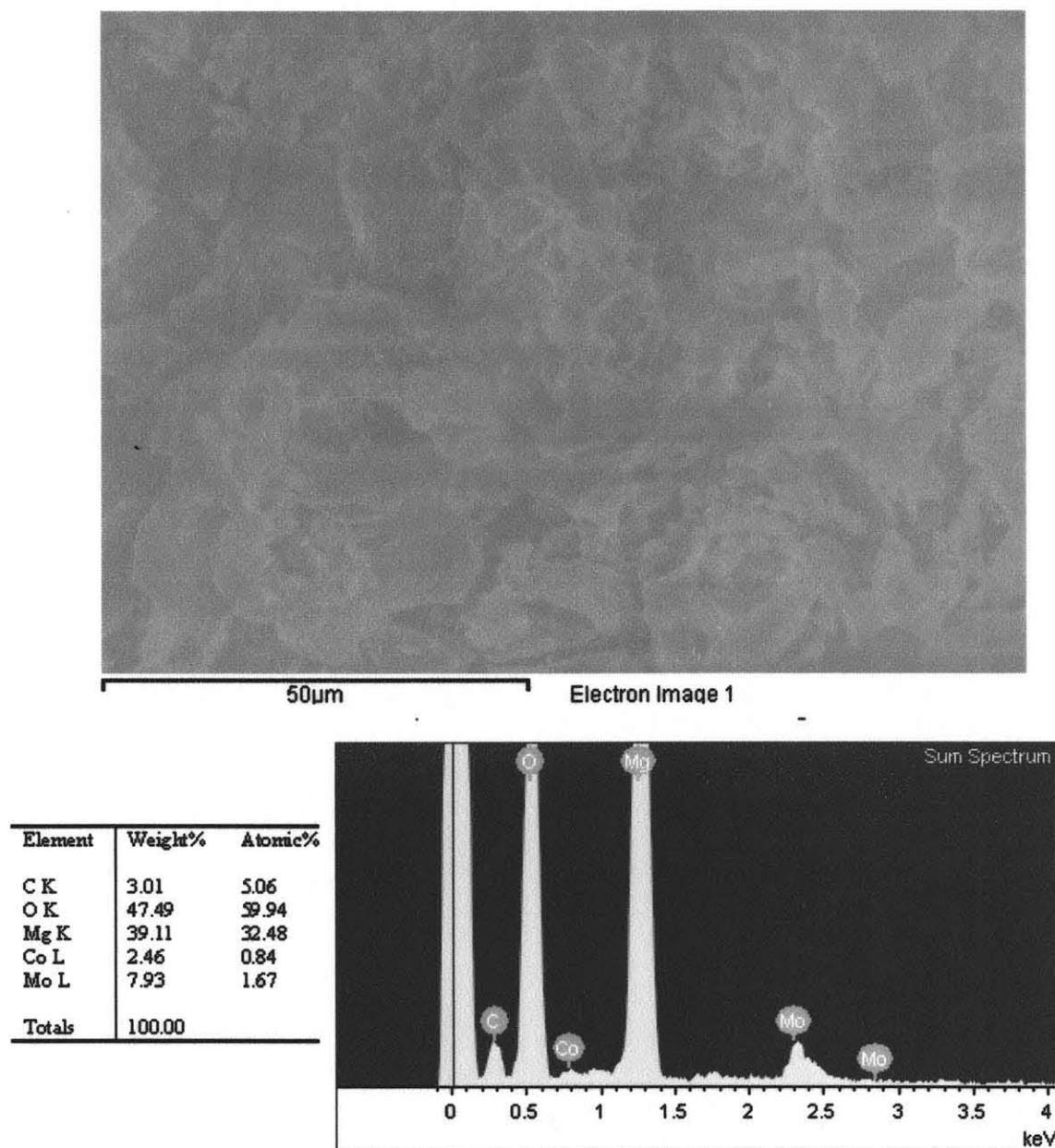
Figure 3.13 SEM image and EDX elemental analysis for the Co:Mo 1:4 catalyst.

3.5.2 Effect of Growth Temperature

Nanotubes were grown at five different temperatures while keeping all other variables such as, catalyst composition, carbon source, CO flow rate, and growth time constant. The Co:Mo catalyst in ratio of 1:4 shown in Figure 3.13.was used to study the effect of

temperature. Key experimental conditions listed below were maintained at constant values in order to avoid deviation from experiment to experiment.

- Constant total flow rate of reactant gases was maintained at 500 sccm.

- Constant amount equal to 0.03 gm of catalyst was used in every run.

- Catalyst used throughout the studies was prepared in a single large batch (for example, a master batch of 3-5 gms of Co:Mo 1:4 catalyst was prepared for the studies reported here).

The optimum flow rate required for the CO_2 sensor (Rosemount Analytical model 880A) is 500 sccm (controlled using a CO mass flow meter: Sierra Instruments range 0- 2 L/min) as described in the manufacturer's manual. 0.030 gm of catalyst was found to grow enough nanotubes for Raman, SEM and TEM analyses. For XRD measurements single nanotube synthesis experiments were conducted to obtain the 500 mg of nanotubes needed. The CO_2 sensor which was equipped with a 2-point calibration system, it was calibrated with CO_2 gas diluted with argon. Figure 3.14 shows the exit concentration of CO_2 at different deposition temperatures collected over 30 minutes. It can be observed that as the deposition temperature is increased the CO_2 formation increases and consequently the formation of carbon deposited also increases following the Boudouard reaction [$2CO$ (g) $\leftrightarrow$ C (s) + CO_2 (g)]. The Raman spectra shown in Figure 3.15 for samples prepared at 650, 700 and 750 °C clearly show that the most optimum temperature for nanotube formation is 700 °C. Nanotube growth probably begins at 650 °C since very weak Raman scattering can be observed with no distinct peaks in RBM mode region. However, as the temperature is raised to 700 °C, RBM lines with peaks at 214 and 222 cm^{-1} corresponding to 1.12 and 1.08 nm diameter SWNTs can be observed. As the temperature is raised further to 750 °C, the RBM line intensities decrease but it is

not clear whether a majority of the tubes formed are single-or multi-walled. Another possibility is that at higher growth temperatures the smaller diameter SWNTs are destroyed, and the RBM lines of the larger diameter nanotubes remaining lie at frequencies below the approximately 150 cm^{-1} lower limit of the Raman system used in this study. At lower temperatures the Raman line near 1300 cm^{-1} associated with disordered carbon is more intense due to the formation of amorphous carbon and/or defects on the nanotube sidewalls. With increasing growth temperature the intensity of the 1300 cm^{-1} line decreases due to the greater crystallinity of the nanotube sidewalls. The $I(D)/I(G^{+})$ ratio values for samples prepared at 650, 700 and 750 °C are 0.539, 0.160, 0.129, respectively. The carbon yield calculated on a weight basis as defined earlier matches well with the exit gas concentration measurements. A representative calculation for 700 °C is shown in Table 3.3. Cumulative amounts of carbon deposited (Cc) in moles at the end of 30 minutes is 0.00026775 mol, which is equivalent to 0.00321 gms of carbon deposited with 10.7% of starting catalyst/support material (0.030 gm). The amount of carbon recovered after acid purification is about 0.0030 gm which is 10 % of the starting catalyst/support material (shown in Table 3.2 for 700 °C, where the balance used could measure the weight only to 3 decimal places - more accurate values would be measurable with a more sensitive balance).
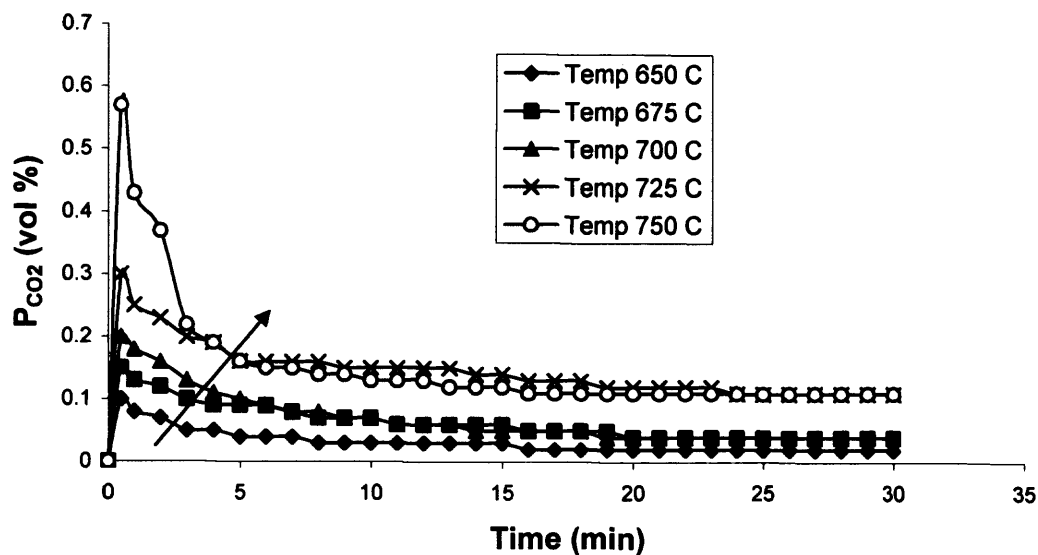
Figure 3.14 Exit CO_2 gas concentration at different SWNT deposition temperatures.

Table 3.2 Raman Peak Positions, Calculated SWNT Diameters and Ratio of D/G^+ Intensities at Different Growth Temperatures

Temperature °C	RBM Peaks (cm⁻¹)	SWNT Diameter (nm)	D peak (cm⁻¹)	TM peaks (cm⁻¹) G⁻	G⁺	D peak intensity (a.u)	G⁺ peak intensity (a.u)	I(D)/I(G⁺)	Yield
650	No peak	N/A	1301	1543	1581	1373	2547	0.539	6
700	214	1.12	1305	1550	1580	805	5019	0.160	10
	222	1.08							
750	210	1.14	1317	1542	1580	451	3504	0.129	13.33
	230	1.04							
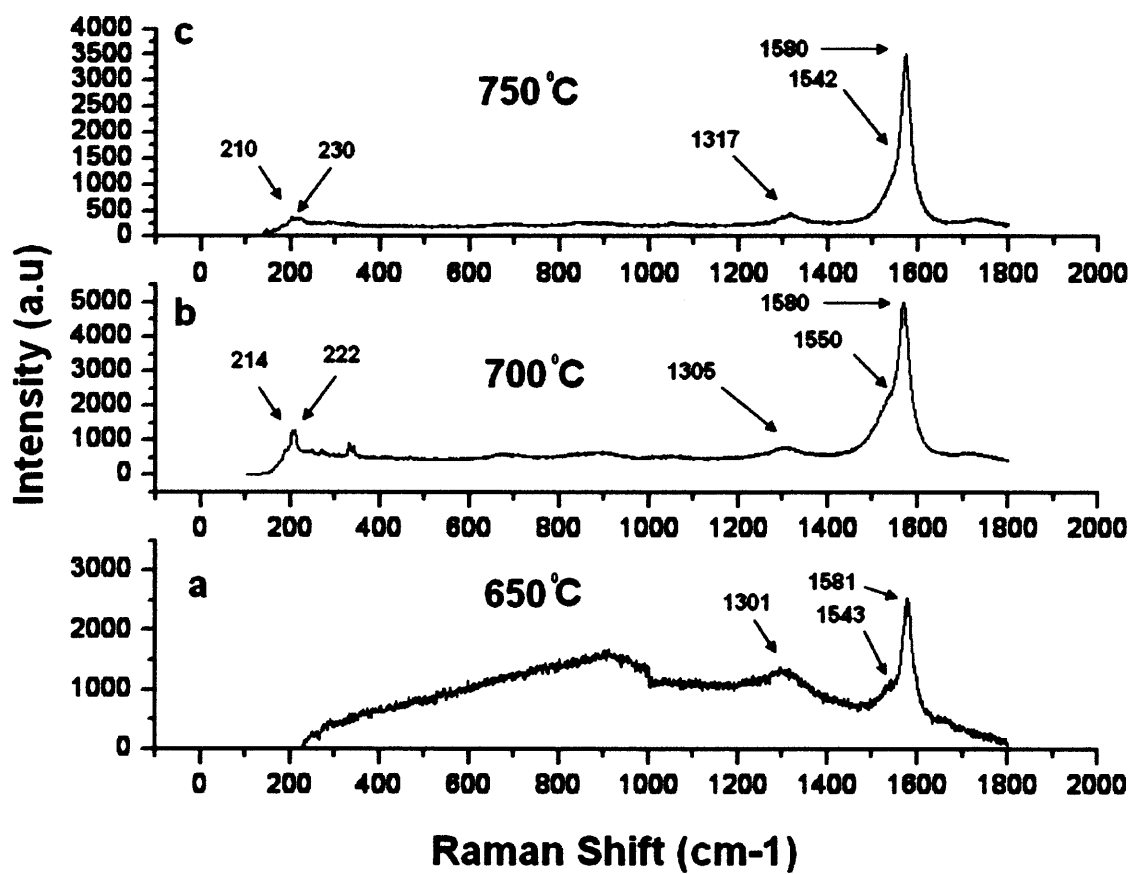
Figure 3.15 Raman spectra with 632.8 nm excitation for SWNTs prepared using Co:Mo 1:4 catalyst at: a) 650 °C, b) 700 °C, and c) 750 °C.

Table 3.3 Estimates of Carbon Deposition using CO_2 Exit Gas Concentrations at 700 °C

Temp 700 °C

Time (min)	Conc. vol % CO_2	P_{CO_2}(atm)	P_{CO}(atm)	X	X*vol%CO_2	Cc (mol/time)	Cc (mol)
0	0	0	1		0	0	0
0.5	0.2	0.00998	0.99002	499.002	0.998003992	4.45537E-05	2.22769E-05
1	0.18	0.008984	0.991016	499.1016	0.898382911	4.01064E-05	4.01064E-05
2	0.16	0.007987	0.992013	499.2013	0.798722045	3.56572E-05	7.13145E-05
3	0.13	0.006492	0.993508	499.3508	0.649156097	2.89802E-05	8.69405E-05
4	0.11	0.005494	0.994506	499.4506	0.549395665	2.45266E-05	9.81064E-05
5	0.1	0.004995	0.995005	499.5005	0.4995005	2.22991E-05	0.000111496
6	0.09	0.004496	0.995504	499.5504	0.449595364	2.00712E-05	0.000120427
7	0.08	0.003997	0.996003	499.6003	0.399680256	1.78429E-05	0.0001249
8	0.08	0.003997	0.996003	499.6003	0.399680256	1.78429E-05	0.000142743
9	0.07	0.003498	0.996502	499.6502	0.349755171	1.56141E-05	0.000140527
10	0.07	0.003498	0.996502	499.6502	0.349755171	1.56141E-05	0.000156141
11	0.06	0.002998	0.997002	499.7002	0.299820108	1.33848E-05	0.000147233
12	0.06	0.002998	0.997002	499.7002	0.299820108	1.33848E-05	0.000160618
13	0.06	0.002998	0.997002	499.7002	0.299820108	1.33848E-05	0.000174003
14	0.05	0.002499	0.997501	499.7501	0.249875062	1.11551E-05	0.000156172
15	0.05	0.002499	0.997501	499.7501	0.249875062	1.11551E-05	0.000167327
16	0.05	0.002499	0.997501	499.7501	0.249875062	1.11551E-05	0.000178482
17	0.05	0.002499	0.997501	499.7501	0.249875062	1.11551E-05	0.000189637
18	0.05	0.002499	0.997501	499.7501	0.249875062	1.11551E-05	0.000200792
19	0.04	0.001999	0.998001	499.8001	0.199920032	8.925E-06	0.000169575
20	0.04	0.001999	0.998001	499.8001	0.199920032	8.925E-06	0.0001785
21	0.04	0.001999	0.998001	499.8001	0.199920032	8.925E-06	0.000187425
22	0.04	0.001999	0.998001	499.8001	0.199920032	8.925E-06	0.00019635
23	0.04	0.001999	0.998001	499.8001	0.199920032	8.925E-06	0.000205275
24	0.04	0.001999	0.998001	499.8001	0.199920032	8.925E-06	0.0002142
25	0.04	0.001999	0.998001	499.8001	0.199920032	8.925E-06	0.000223125
26	0.04	0.001999	0.998001	499.8001	0.199920032	8.925E-06	0.00023205
27	0.04	0.001999	0.998001	499.8001	0.199920032	8.925E-06	0.000240975
28	0.04	0.001999	0.998001	499.8001	0.199920032	8.925E-06	0.0002499
29	0.04	0.001999	0.998001	499.8001	0.199920032	8.925E-06	0.000258825
30	0.04	0.001999	0.998001	499.8001	0.199920032	8.925E-06	**0.00026775**

SEM images for the SWNTs deposited at 650-750 °C are shown in Figure 3.16 a-f, respectively. No nanotubes were found in the sample grown at 650°C and only sparse growth was observed for a sample prepared at 675 °C. 700 °C was found to be the optimum temperature both with regard to nanotube growth and stability of catalyst particle size. As the growth temperature was further increased to 725 °C and 750 °C, the

SEM images from the samples show significant growth of nanotubes but the catalyst particles appear to be randomly oriented. In addition, the Raman spectra show low RBM line intensities for samples grown at higher temperatures suggesting that the nanotubes are bundles of thin MWNTs and not SWNTs.
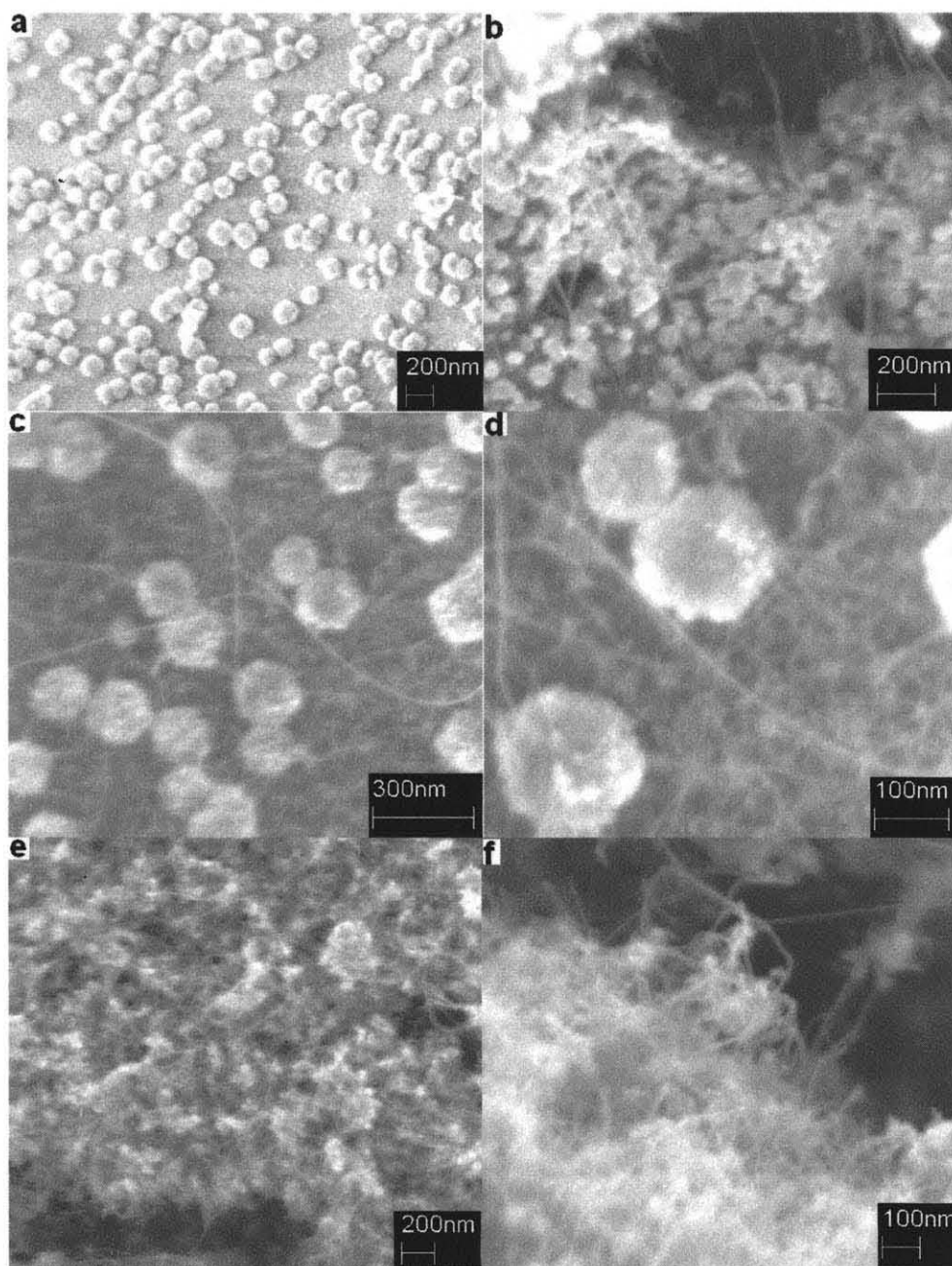
Figure 3.16 SEM images of as-prepared SWNTs at different temperatures: a) 650 °C, b) 675 °C, c) 700 °C, d) 700 °C, e) 725 °C, and f) 750 °C.

3.5.3 Effect of CO Flow Rate

In order to investigate the influence of the carbon monoxide flow rate on the SWNT yield and purity, the flow rates were varied within the range of 500 sccm to 1000 sccm. The flow rate was controlled using a Sierra Instruments mass flow meter, with a range of 0-2 L/min. Once again all other conditions such as, 100 % CO as carbon source, 0.030 gms of Co:Mo (1:4) catalyst, growth temperature of 700 °C, deposition time of 30 minutes, and atmospheric pressure, were maintained constant. Figure 3.17 shows typical Raman spectra obtained from the as-prepared SWNTs for flow rates of 500, 600, 700, 800, and 1000 sccm. The Raman spectra of the SWNTs indicate no shift or change in peak positions as a function of CO flow rate. Also, the ratio for D to G^+ line intensities remains essentially the same for all the flow rates. However, it can be observed that the SWNT line intensities are highest for a flow rate of 700 sccm and is consistent with the exit CO_2 gas concentration data shown in Figure 3.18. The peak positions of 213 and 251 cm^{-1} correspond to average SWNT diameters of 1.13 and 0.94 nm, respectively.
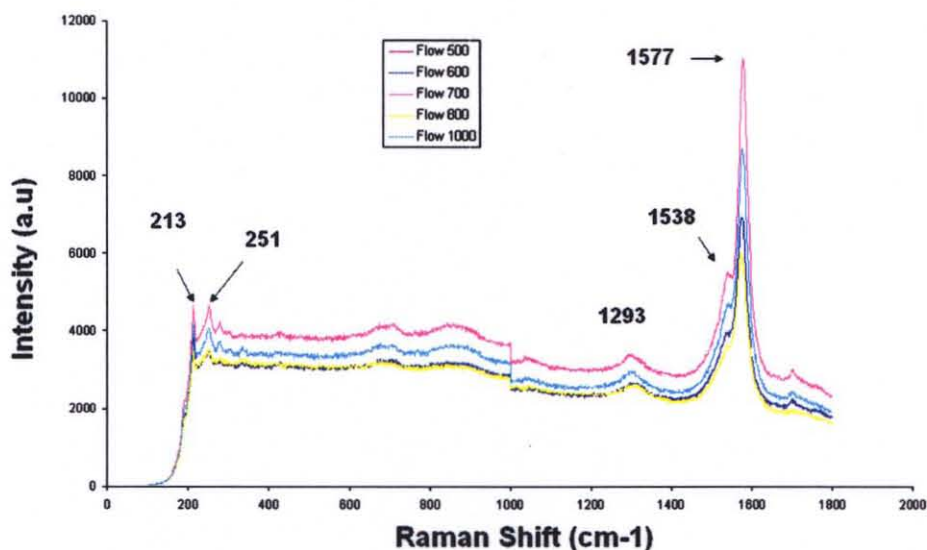
Figure 3.17 Raman spectra obtained with 632.8 nm laser excitation of as-prepared SWNTs using different flow rates.

There is no observable change in the RBM peak positions at flow rates between 500 to 1000 sccm suggesting that at higher flow rates the SWNT diameters can be controlled within a narrow range. As discussed earlier, low flow rates produce SWNTs with smaller diameters corresponding to RBM peaks at 240 and 276 cm^{-1} for the same growth conditions. From Figure 3.18, the exit CO_2 gas concentrations are almost the same for CO flow rates of 700, 800 and 1000 sccm. There is a shift in the equilibrium concentration from 0.03-0.04 vol% to 0.16-0.17 vol% when the CO flow rates are changed from 600 to 700 sccm. This can be attributed to the increase in rate of removal of carbon dioxide at higher flow rates; therefore the reverse Boudouard reaction slows down and leads to a shift in the equilibrium. This suggests that at higher flow rates a higher conversion of CO to SWNTs can be obtained. From the experimental data shown in Figure 3.18 and following the calculation shown in Table 3.3, the carbon yields after 30 minutes on a weight basis for different flow rates of 500, 600, 700, 800 and 1000 sccm at a temperature of 700 °C are 10.7, 48.14, 59.90, 68.46, 80.23 %, respectively.
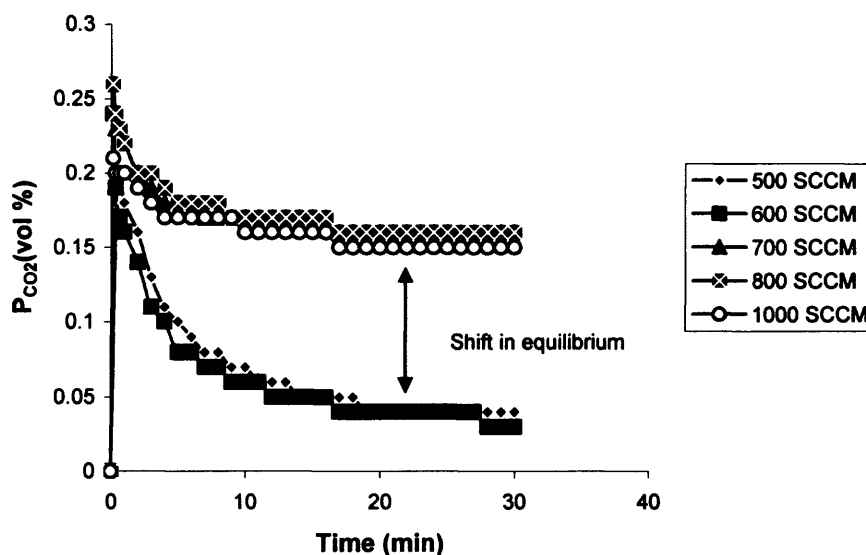
Figure 3.18 Exit CO_2 gas concentration data at different flow rates.

3.5.4 Effect of Initial Partial Pressure of CO

In order to investigate the effect of a diluted carbon precursor feed. Experiments were conducted by maintaining all other parameters constant while changing the volumetric flow ratio of carbon monoxide to argon, so as to have initial partial pressures of CO (P_{CO}) of 0.2, 0.4, 0.6, 0.8 and 1 atm. Figure 3.19 (a-e) show representative Raman spectra for as prepared SWNTs after a growth time of 30 minutes under these conditions. From Figure 3.19 (a) at P_{CO} = 0.2 atm, SWNT growth is observed as indicated by the appearance of weak RBM lines. For samples prepared at P_{CO} of 0.4 atm and above, relatively intense RBM and TM lines as shown in Figure 3.19 (b-e).
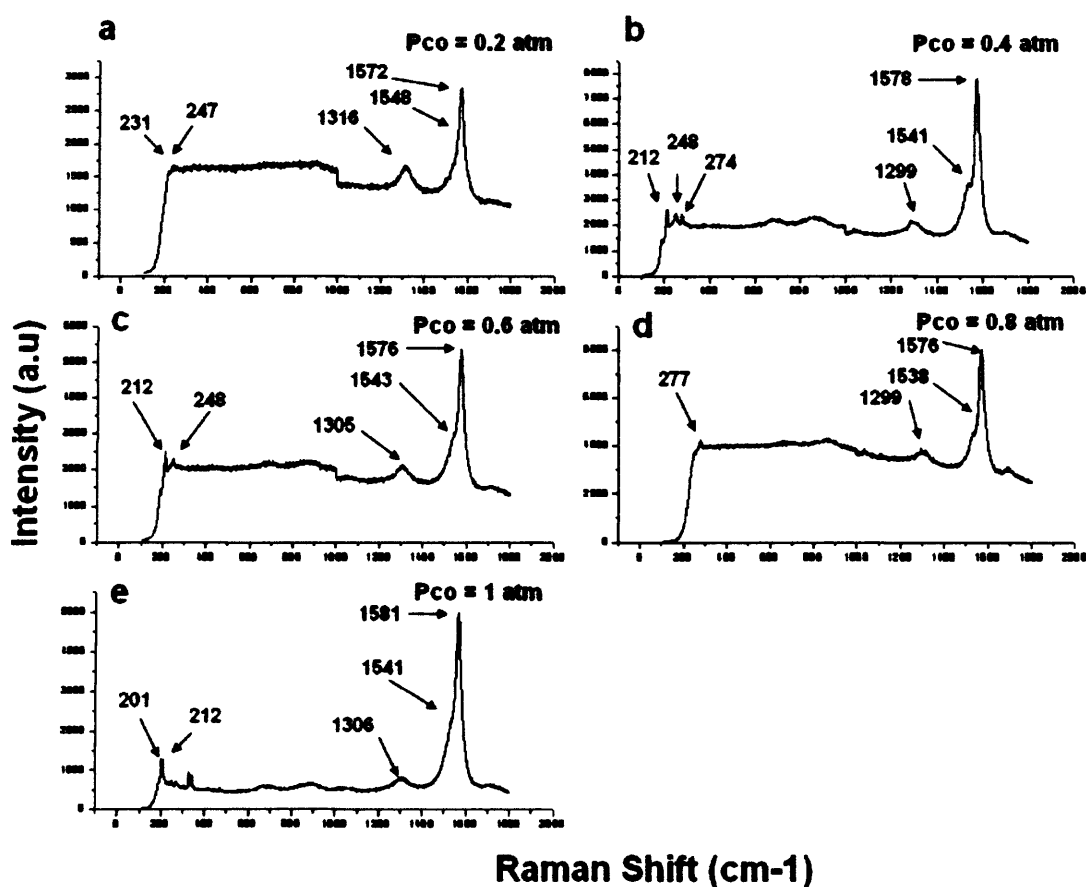
Figure 3.19 Raman spectra using 632.8nm excitation at different initial partial pressures of carbon monoxide: a) 0.2 atm, b) 0.4 atm, c) 0.6 atm, d) 0.8 atm, and e) 1 atm.

As the CO pressure is increased the peak position of RBM line varies indicating changes in the SWNT diameters. This was not the case when SWNTs were prepared as a function of the CO flow rate. The RBM line peaking at 210-214 cm^{-1} corresponding to a SWNT diameter of ~ 1.1 nm was found consistently in most of the samples. XRD and TEM studies discussed in section 3.5.5 below reveal a similar diameter distribution. An EDX study (Figure 3.20) was also conducted to find the number of active catalytic sites (cobalt) occupied by the carbonaceous species after deposition. The maps for cobalt and carbon on the samples are shown in Figure 3.20. The EDX measurement conditions: working distance of 9 mm, constant area and time for scan of 300 sec and energy of 6 keV, were kept constant. The statistical quantitative analyses data from the images obtained are listed in Table 3.4. Irrespective of the change in partial pressure from 0.2 atm to 1 atm of CO, the catalyst sites occupied was found to be in the range of 80-85%. These two observations are critical for the scale up, as non-diluted higher flow rates of CO would not be safe to use. In the fluidized bed scheme for the same reaction, the H_2 and CO feed is diluted with N_2 both in the reduction and deposition stages, respectively.

Table 3.4 An Estimate of Catalytic Site Occupation as a Function of Inlet CO Pressure from Corresponding Images Shown in Figure 3.20

Initial CO pressure P_{co} (atm)	Total no. of catalytic sites (green color dots)	Sites Occupied (green dots covered by red dots)	Percentage occupation
0.2	46	38	80.00
0.4	71	58	83.33
0.6	6	5	81.70
0.8	45	36	82.61
1.0	148	126	85.13
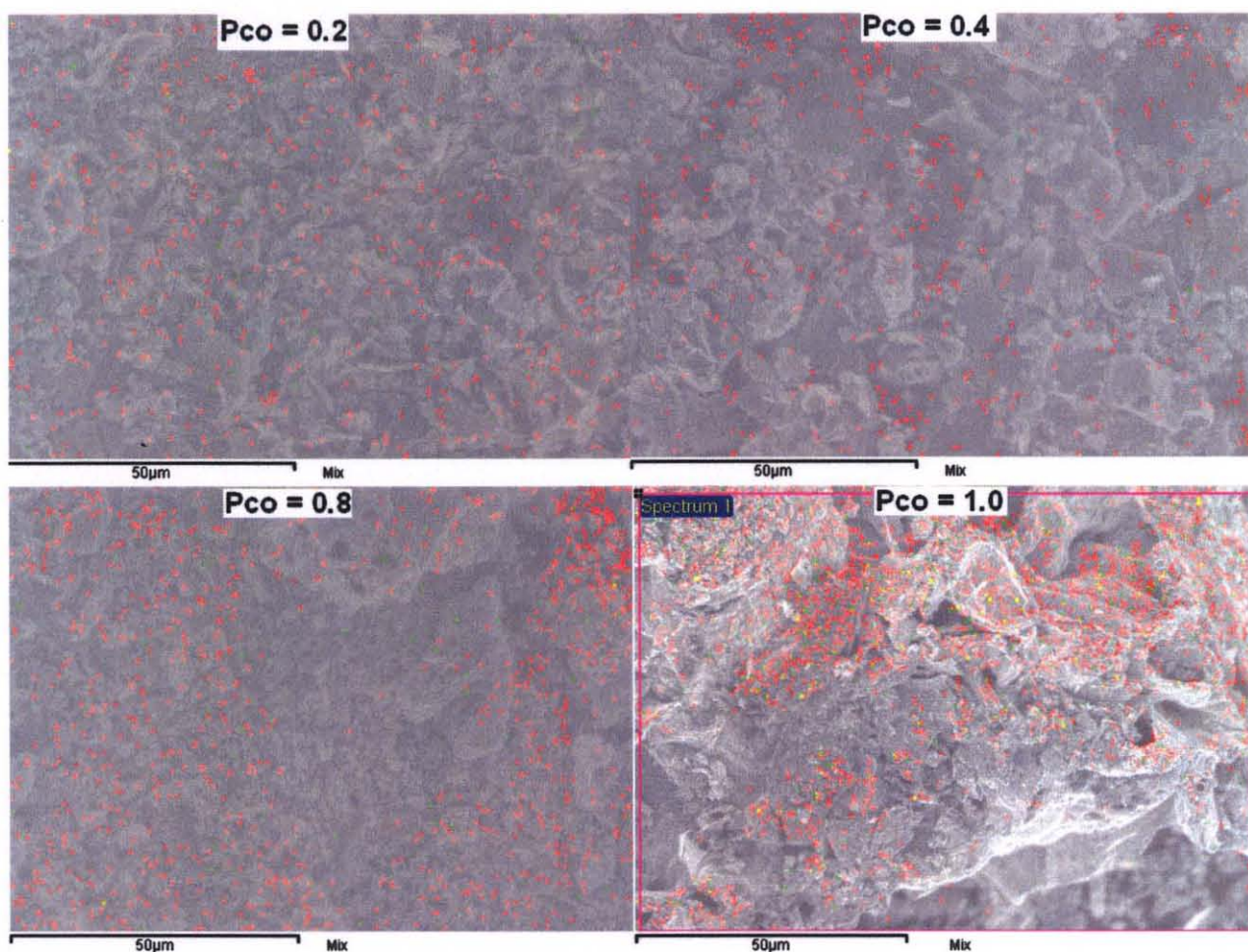
Figure 3.20 EDX maps showing distribution of cobalt catalyst (green dots) and carbon (red dots) at different inlet pressures of carbon monoxide used.

3.5.5 Purification

An XRD study was done primarily to investigate the efficiency of the purification method used to remove the support/catalyst (MgO/Co-Mo) from as-prepared SWNTs. The diffractograms (Figure 3.21) are plotted both as x-ray intensity versus 2θ and Q (Å^{-1}) $= 4\pi Sin\theta/\lambda$ and shown for as-prepared and purified samples. The data show that MgO reflections are not observed for the purified sample (Swanson, 1953). In addition, from the XRD patterns for the purified samples in the region below Q $< 2\text{Å}^{-1}$ four peaks at 0.98, 1.18, 1.3, and 1.8 Å^{-1} are observed consistent with the 2D triangular lattice of SWNT

bundles as reported in earlier studies (Thess, 1996). A small, sharp peak at 1.85 Å^{-1} is close to the graphite (002) position. The reflection at Q = 0.43 Å^{-1} could not be observed since the diffractometer used cannot resolve small angle reflections. Also, from the (110) reflection at 2θ = 77.25° (Figure 3.21) d_{11} = 12.4 nm can be calculated using Bragg's equation. Therefore for a bundle of 10 SWNTs arranged in a hexagonal packing, an individual SWNT diameter of 1.1 nm can be estimated (Bandow, 1997) which is consistent with the average individual tube diameter obtained from the Raman and TEM data.

The TEM images of as-prepared and purified SWNTs grown on MgO are shown in Figure 3.22. From the TEM image in Figure 3.22(a) it can be seen that only small amounts of amorphous carbon are present. The support material MgO can be seen at the top left and bottom of the image while catalyst particles are dispersed on the nanotube bundles and MgO. The image in Figure 3.22 (b) shows that HCl purification has removed all the MgO support consistent with the XRD data in Figure 3.21; however, small amounts of amorphous carbon and catalyst particles attached to the SWNTs still remain. The TEM images therefore show that these purified samples are comprised of thin bundles of SWNTs compared to HiPCO SWNTs, which form larger bundles of 20-100 nanotubes (see Figure 3.7). In order to remove residual amorphous carbon that cannot dissolve in HCl, a partial oxidation procedure was conducted. TGA data show that SWNT oxidation occurs at 600 °C in air (Hata, 2004). SWNTs were therefore partially oxidized using water (a weak oxidant) through which flowing argon at 300 sccm was bubbled over SWNTs maintained at a temperature of 450 °C. Amorphous carbon has been reported to oxidize in air at 300 °C. The TEM image from a weakly oxidized sample

shown in Figure 3.22 (c) indicate defect free walls with very few catalyst particles attached mainly to the tips. The average diameter of the SWNTs is ~1.1 nm, consistent with the Raman and XRD data discussed earlier. Figure 3.23 shows an over all comparison of SWNTs obtained by CO-CVD, CoMoCat, and the HiPCO processes based on TEM images and Raman spectra taken from corresponding samples.
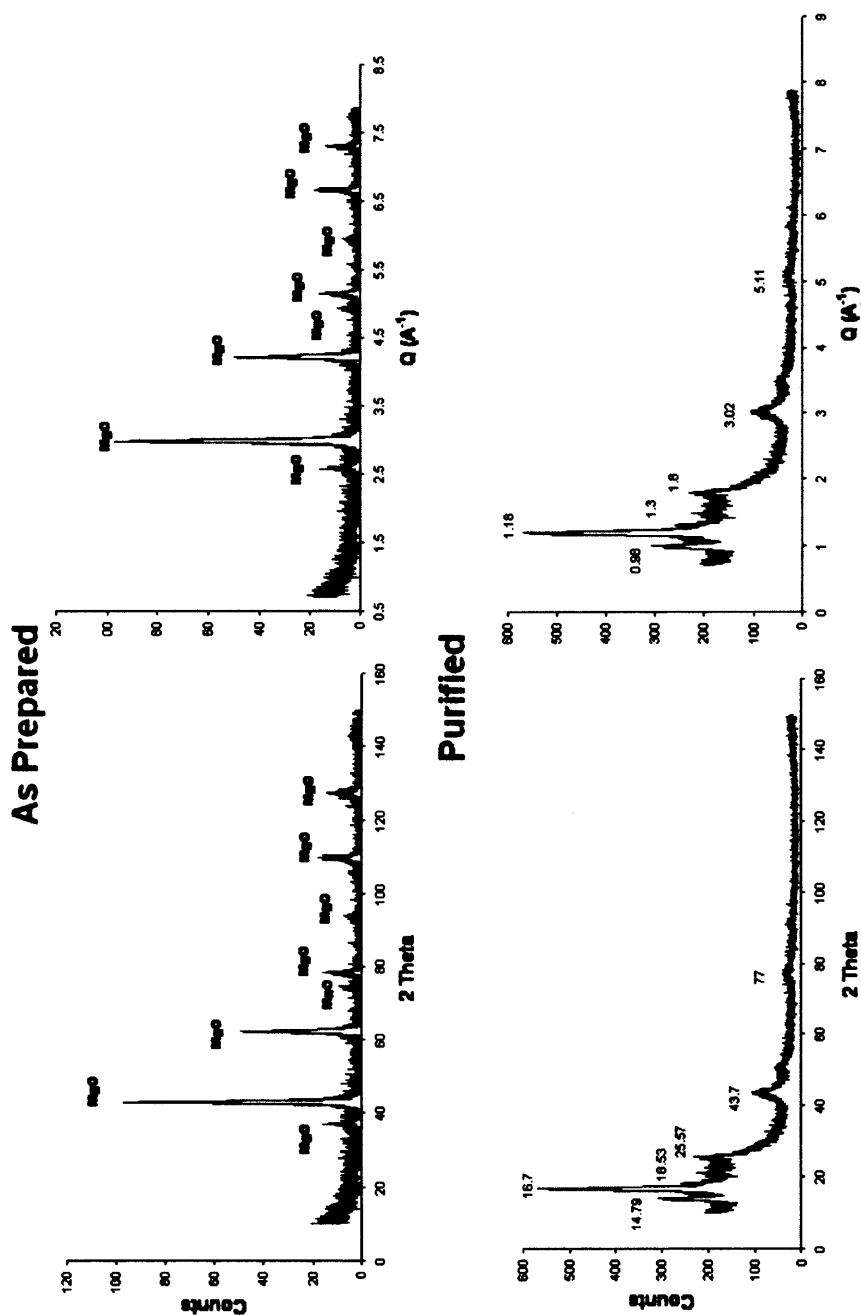
Figure 3.21 XRD diffractograms: on top as prepared SWNTs with catalyst and support, bottom purified samples with 4-6M HCl
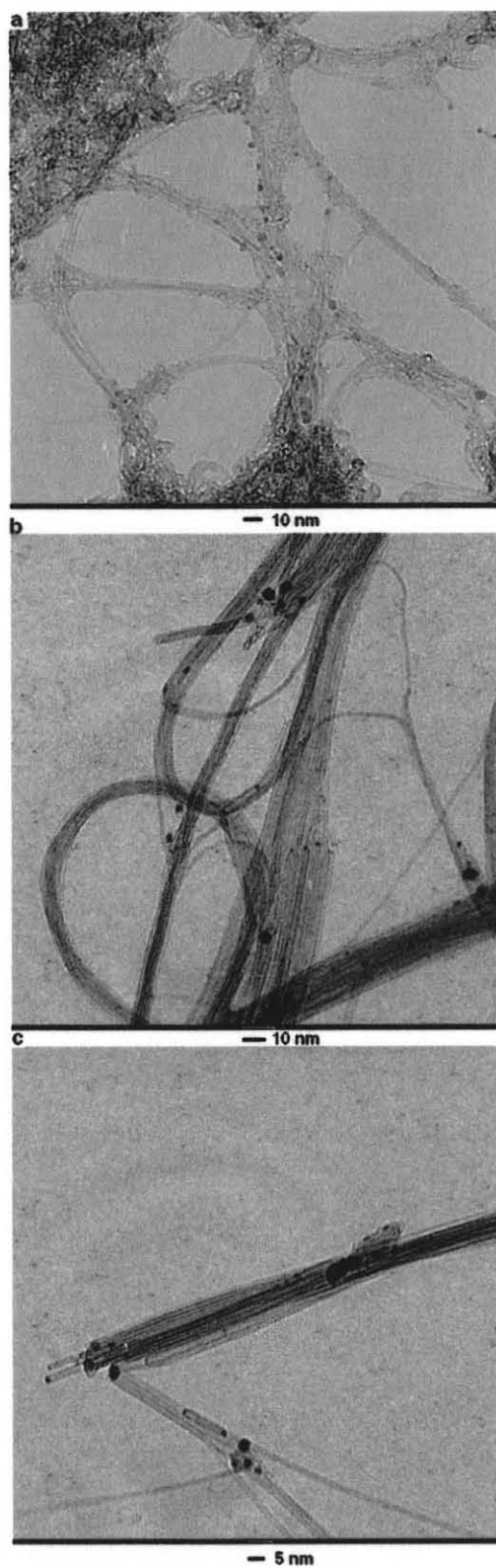
Figure 3.22 TEM images of SWNTs: a) as-prepared with catalyst and support, b) after HCl acid purification, and c) after partial oxidation.
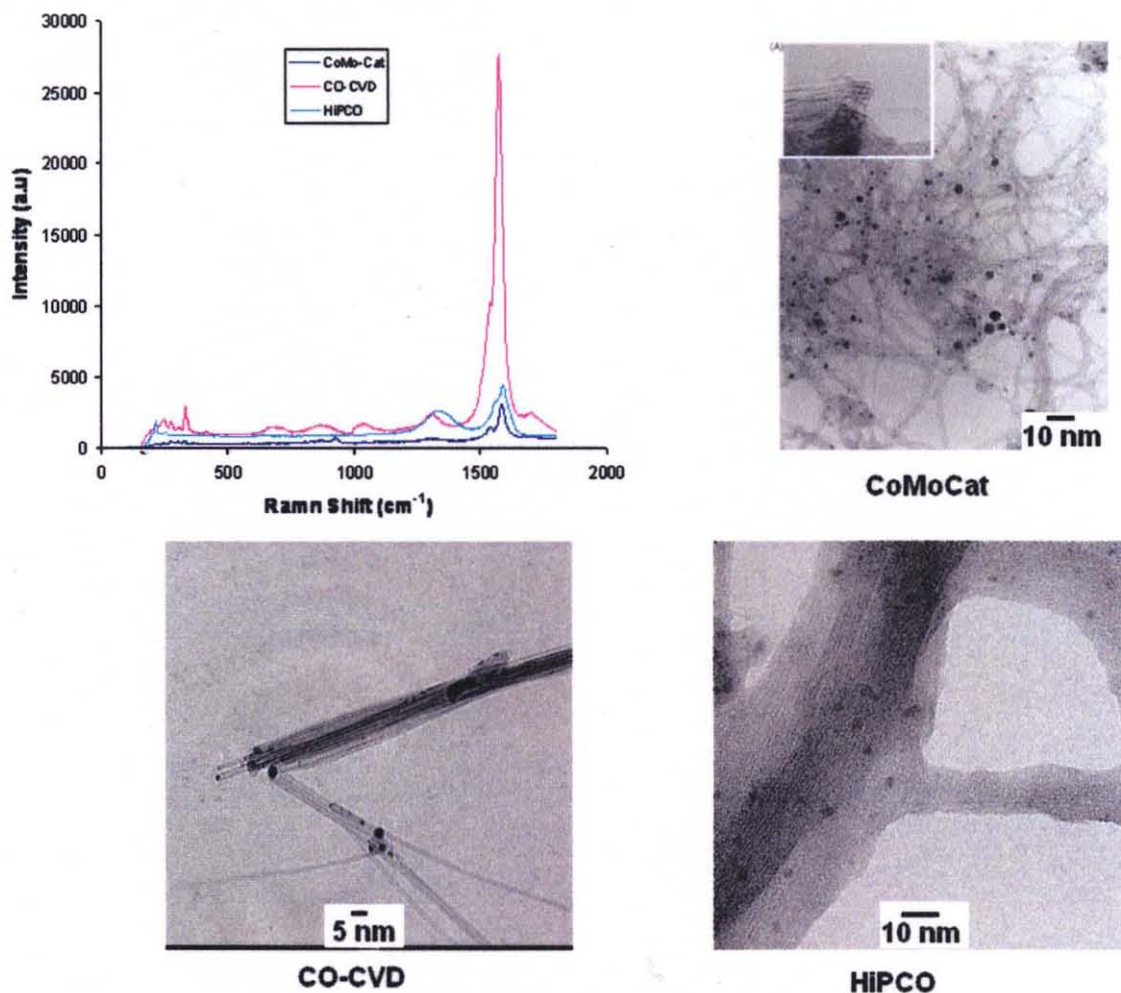
Figure 3.23 Comparison of TEM images and Raman data for purified CO-CVD, CoMoCat [Source: Kitiyanan, 2002], and HiPCO [from Carbon Nanotechnologies Inc] processes.

3.5.6 Kinetic Model for SWNT Deposition

Chemical vapor deposition (CVD) is a critical process in the microelectronics industry since one of the key steps in chip-making is the deposition of different semiconductors and metals on the surface of a chip. This step is typically achieved by CVD. In this section the CVD reaction mechanism for SWNT deposition will therefore be discussed in some detail. A number of CVD reactors have been studied in the past, such as barrel reactors, boat reactors, and horizontal and vertical reactors, to study reaction kinetics. In

this study a boat reactor is used where a small amount of catalyst is placed in ceramic or quartz boats inside the reaction chamber. A model to develop the rate law of the catalytic reaction that is not diffusion-limited is presented. Since, at low pressures there is a large increase in the diffusion coefficients, surface reactions are more likely to be rate-controlling than the mass transfer.

The reaction of interest is the Boudouard reaction involving the decomposition of two molecules of gaseous CO to form one molecule of gaseous CO_2 and a carbon atom in solid C.

The overall Boudouard reaction is:

$$2CO(g) \rightleftharpoons C(s) + CO_2(g) \tag{3.1}$$
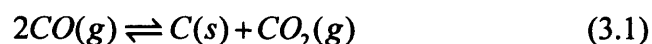
A model depicting the sequence of steps in the cobalt-catalyzed Boudouard reaction is shown in Figure 3.24 below.
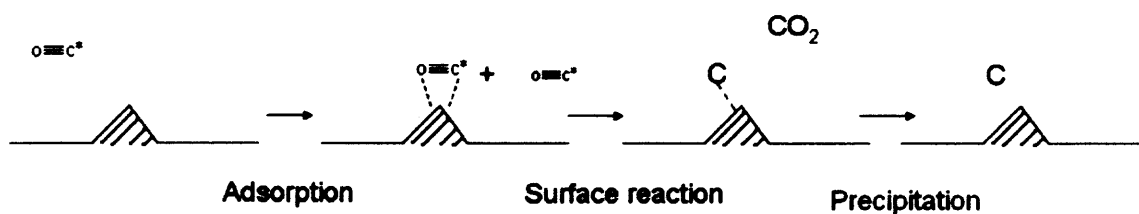
Figure 3.24 Schematic showing the sequence of steps in reaction-limited catalytic deposition of SWNTs.

In Figure 3.24 the dashed lines show the formation of a complex with the catalytic site, whereas solid lines show the bonding of a molecule to the catalytic site. The model can be represented by the following reaction steps:

$$CO(g) + S \underset{k_2}{\overset{k_1}{\rightleftharpoons}} CO.S \qquad \text{Adsorption of carbon monoxide on the cobalt surface} \tag{3.2}$$

$$CO.S + CO(g) \underset{k_4}{\overset{k_3}{\rightleftharpoons}} C.S + CO_2 \qquad \text{Surface reaction to form adsorbed carbon and carbon dioxide in the gas phase} \tag{3.3}$$

$$C.S \xrightarrow{k_5} C(s) + S \qquad \text{Precipitation of carbon out of the cobalt surface} \qquad (3.4)$$
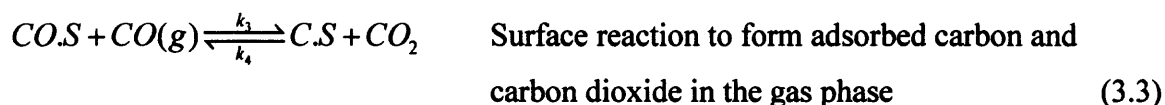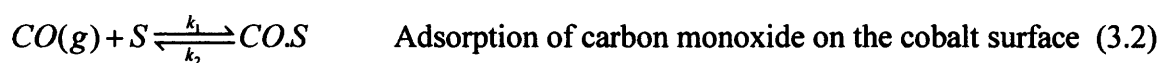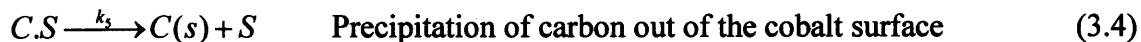
where, k_1 is the rate of the forward adsorption reaction
k_2 is the rate of the backward adsorption reaction
k_3 is the rate of the surface reaction
k_4 is the rate of the forward precipitation reaction
k_5 is the rate of the backward precipitation reaction

Units for reaction constants (mole/atm min)

The proposed mechanism is based on the following assumptions:
1. The adsorption and surface reaction which leads to desorption of CO_2 reactions rapidly approach equilibrium.
2. Precipitation of carbon is rate-limiting. This is the classic Eiley-Rideal mechanism where reaction between an adsorbed molecule and a gas phase molecule takes place.

Therefore,

$$R_{ads} = k_1 P_{CO}[S] - k_2[CO.S] = 0 \qquad (3.5)$$

$$R_{sur} = k_3 P_{CO}[CO.S] - k_4[C.S]P_{CO_2} = 0 \qquad (3.6)$$

$$R_{pre} = k_5[C.S] \qquad (3.7)$$

Or,

$$K_{ads} = \frac{k_1}{k_2} = \frac{[CO.S]}{P_{CO}[S]} \qquad (3.8)$$

And

$$K_{sur} = \frac{k_3}{k_4} = \frac{[C.S]P_{CO_2}}{[CO.S]P_{CO}} \qquad (3.9)$$

The site balance is given by:

$$S_o = [S] + [CO.S] + [C.S] \qquad (3.10)$$

where, S_o = Total number of initial catalytic sites
S = Available sites for reaction at any given time
$CO.S$ = Sites occupied by CO to form an intermediate complex
$C.S$ = Sites occupied by C atoms to form a complex

The rate-limiting is the precipitation reaction

Therefore,

$$R_{pre} = R_c = \frac{dC_c}{dt} = \frac{k_5 K_{sur} K_{ads} P_{CO}^2}{P_{CO_2}} \left[\frac{S_0}{1 + K_{ads} P_{CO} + K_{sur} K_{ads} \dfrac{P_{CO}^2}{P_{CO_2}}} \right] \qquad (3.11)$$

Where, R_{pre} is the rate of precipitation and is equivalent to rate of formation of carbon R_c.

K_{ads} and K_{sur} decreases with increasing temperatures. Therefore at high temperatures it is

a good approximation that $1 \gg K_{ads} P_{CO} + K_{sur} K_{ads} \dfrac{P_{CO}^2}{P_{CO_2}}$

Therefore,

$$R_{pre} = R_c = \frac{dC_c}{dt} = \frac{K_{reaction} P_{CO}^2 S_o}{(P_{COinitial} - P_{CO})} \qquad (3.12)$$

Considering that the total number of initial sites is equal to 100 % or 1 in the beginning

$$R_{pre} = R_c = \frac{dC_c}{dt} = \frac{K_{reaction} P_{CO}^2}{(P_{COinitial} - P_{CO})} \qquad (3.13)$$

Therefore,

$$C_c = \int_0^t K_{reaction} \frac{P_{CO}^2}{(P_{COinitial} - P_{CO})} dt \qquad (3.14)$$

Thus, carbon deposited is first order with respect to the concentration of carbon monoxide.

The experimental data agrees well with the above model as shown by the linear dependence of the plot of the carbon deposited (C_c) against time (t) in Figure 3.25. In Figure 3.26 the carbon deposited (C_c) is plotted against $(P_{CO}^2/(P_{COinitial} - P_{CO})) \times t$, at different initial carbon monoxide partial pressures ($P_{COinital}$).
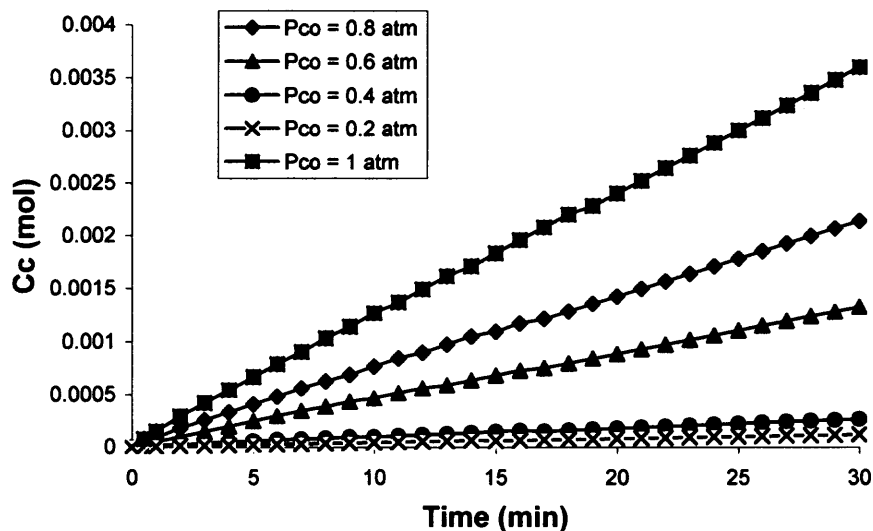
Figure 3.25 Plot of carbon deposited (C_c) vs time (t).
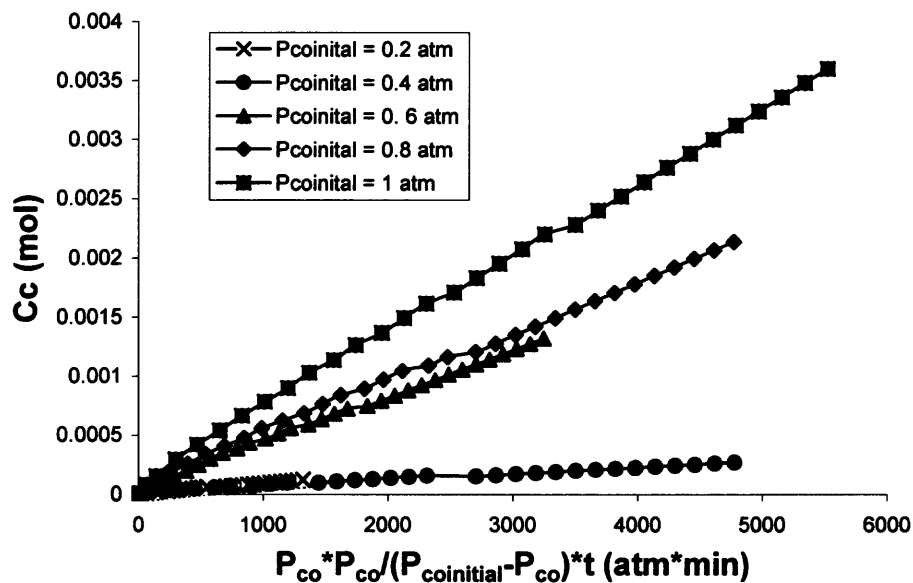
Figure 3.26 Determination of $K_{reaction}$ by plotting the carbon deposited (C_c) vs $(P_{CO}^2/(P_{COinitial} - P_{CO}) \times t$.

From Figure 3.26 the $K_{reaction}$ values at different $P_{COinital}$ can be determined as slopes of the plots after linear regression. The $K_{reaction}$ values are listed in Table 3.5.

Table 3.5 Kinetic Coefficients at Different Inlet Carbon Monoxide Pressures

$P_{cointial}$ (atm)	$K_{reaction}$ (mole/atm×min)	I(D)/I(G$^+$)
0.2	9E-08	0.584
0.4	6E-08	0.279
0.6	4E-07	0.395
0.8	5E-07	0.475
1	7E-07	0.159

It is important to note that so far the model reports the formation of carbon and as well as SWNTs. In order to segregate the amorphous carbon to form SWNTs, the reaction equation can be multiplied by the I(D)/I(G$^+$) ratio which is a measure of the selectivity towards nanotube formation. The I(D)/I(G+) ratios of intensities obtained from the Raman data (Figure 3.19) are listed in Table 3.5. It was already noted from earlier observations that the number of catalyst sites occupied by the carbonaceous species is independent of the initial partial pressure of CO. Therefore if fresh catalyst is fed into the reactor, the kinetics does not depend on past history and can be treated separately, where a decay or selectivity coefficient can be multiplied by the rate equation.

Therefore,

$$C_c = \frac{1}{I(D)/I(G^+)} \int_0^t K_{reaction} \frac{P_{CO}^2}{(P_{COinitial} - P_{CO})} dt \qquad (3.15)$$

3.6 Fluidization Bed Reactor for Scale up of SWNTs

In the previous sections it was concluded that SWNTs can be selectively synthesized with the diameter controlled in a narrow range of flow rates using Co:Mo (1:4) catalyst supported on MgO at 1 atm of pure CO feed at a temperature of 700 ° C. It was also observed that as the CO feed is diluted with an inert gas the rate of formation of nanotubes decreases with a minimum at a CO partial pressure ($P_{COinitial}$) of 0.2 atm. This

condition is not favorable for the production of SWNTs. However, for safety reasons pure CO cannot be used at high flow rates in a typical laboratory environment. In this section, an initial study using some of the findings from the small scale reactor will be used to demonstrate the formation of a large batch of nanotubes in a cost effective manner. As mentioned earlier in the experimental section, the catalyst/support preparation procedure was somewhat modified in order to make the larger quantities required to achieve the required depth of the bed.

There are very few reports in the literature regarding the use of a fluidized bed system to synthesize carbon nanotubes and most are limited to MWNTs (Wang, 2002; Weizhong, 2004; Mauron, 2002). Production of fine particles such as carbon nanotubes is a challenging task in the field of powder technology research. Initial experiments in this study were carried out on the MgO powder of -325 mesh, which is equivalent to 44 μm and below. Before choosing the size of the MgO particles, the particle size distribution of the optimized catalyst was carried out using a Beckman Coulter LS series particle size analyzer in order to understand the relative size distribution of the catalyst that is largely constituted of MgO ($\geq$ 95 %). Figure 3.27 shows that the particle size distribution of the MgO support varies from 2 μm to 1000 μm with the highest volume fraction of particles having sizes of 20 and 300 μm. The mean particle size observed is 143 μm. The large variation in particle size indicates the formation of agglomerates. It is very important to understand catalyst/support particle size distributions scale up issues. Since all the calculations for fluidizing the bed depends on a nominal particle size, the loss of particles due to entrainment can be estimated by knowing the volume fraction of particles smaller than the mean size present in the bulk catalyst/support powder. In addition formation of

agglomerates is favorable for reduction in loss due to entrainment, at the same time it increases the difficulty of fluidizing the whole bed uniformly.
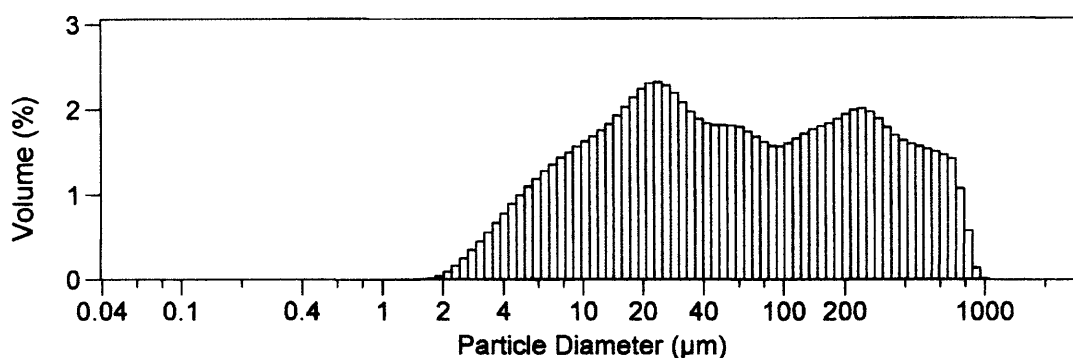
Figure 3.27 Particle size distribution of Co:Mo/MgO catalyst/support in ratio of 1:4 Co:Mo/MgO.

The -325 mesh MgO powder was further sieved using 500 µm pore sieve (35 mesh) to retain all the agglomerates and remove larger chunks of particles. A 2 inch quartz tube with a ceramic gas distributor (pore size 40 µm) at the bottom was used to determine the minimum fluidization velocity required. Figure 3.28 shows a plot of the pressure drop versus the flow of N_2. The experimental minimum fluidization velocity was found to be between 0.033 m/sec, which is equivalent to 4 liters/min with tube cross section area of 0.00202 m^2.
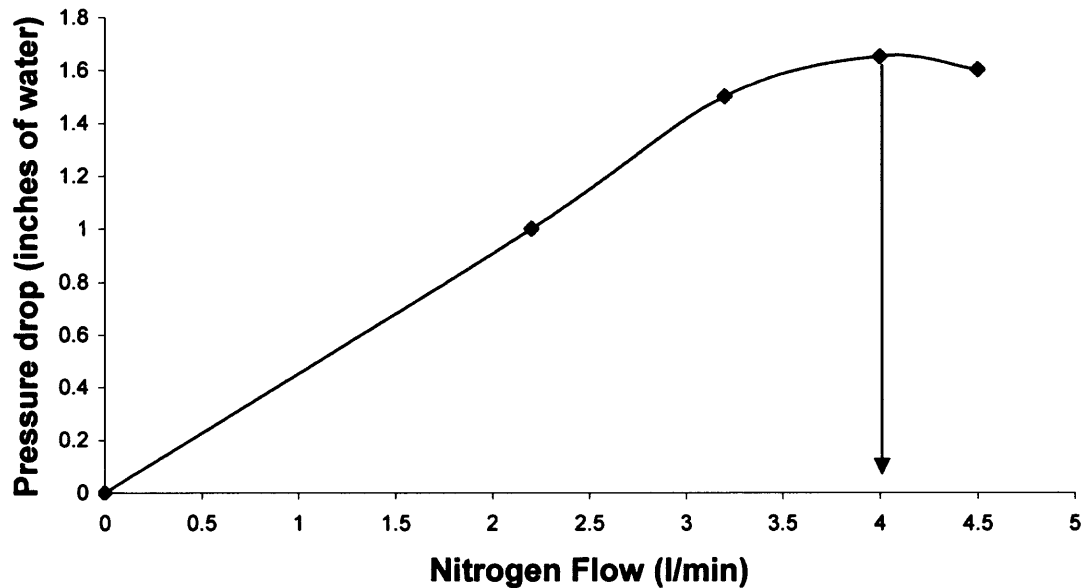
Figure 3.28 Plot of pressure drop versus nitrogen flow.

Calculation for minimum fluidization velocity

Using the Ergun equation for pressure drop in packed beds (McCabe, 5th ed. 1993)

$$\frac{\Delta P g_c}{L} = \frac{150 \mu \overline{V}_0 (1 - \varepsilon^{2)}}{\phi_s^2 D_P^2 \varepsilon^3} + \frac{1.75 \rho \overline{V}_0^2 (1 - \varepsilon)}{\phi_s D_P \varepsilon^3}$$ (3.16)

where,
ΔP is the pressure drop
g_c is the acceleration due to gravity
μ is the viscosity of gas phase
D_p is the particle diameter
V_o is the superficial velocity
ε is the void fraction
ρ is the density of gas phase
ρ_P is the density of particle,
all in SI units.

In the case of incipient fluidization a quadratic equation is obtained:

$$\frac{150 \mu \overline{V}_{0M} (1 - \varepsilon_M)}{\phi_s^2 D_P^2 \varepsilon_M^3} + \frac{1.75 \overline{V}_{0M}^2}{\phi_s D_P \varepsilon_M^3} = g(\rho_P - \rho)$$ (3.17)

where the subscript M refers to a minimum value. For very small particles, only the laminar flow term of the Ergun equation is significant. Also for spherical particles the void fraction ε_M is 0.40. Therefore, for particle Reynolds number, $N_{Re,P} < 1$, the above equation reduces to

$$\overline{V}_{0M} \approx \frac{g(\rho_P - \rho)\varepsilon_M^{\;3}}{150\mu(1-\varepsilon_M)}\phi_s^{\;2}D_P^{\;2} \tag{3.18}$$

For a particle size of 143 μm, 4 liter/min of volumetric flow rate (experimental data), nitrogen gas density of 1.256 Kg/m^3, and viscosity of 0.0180, $N_{Re,P}$ is equal to 0.33 using the following equation:

$$N_{Re,P} = \frac{D_P V \rho}{\mu} \tag{3.19}$$

Therefore minimum fluidization velocity ($\overline{V}_{0M}$) for this case using Equation 3.18 is 0.028m/sec.

The velocity equivalent of the volumetric flow rate of 4 liter/min with the cross section area of the tube = 0.002025 m^2, is 0.032 m/sec. Therefore, the experimentally observed velocity (0.032 m/sec) is slightly higher than the calculated velocity of 0.028 m/sec. It suggests that the particulate forms bigger agglomerates than that indicated by the particle size distribution. This is possible because MgO is known to be hygroscopic at ambient conditions. In addition, while determining size the particle size distribution the particles are sonicated resulting in de-segregation. Figure 3.29a shows a photograph of the fluidized bed experimental setup used in this work and Figure 3.29b shows a schematic of the scale up process.
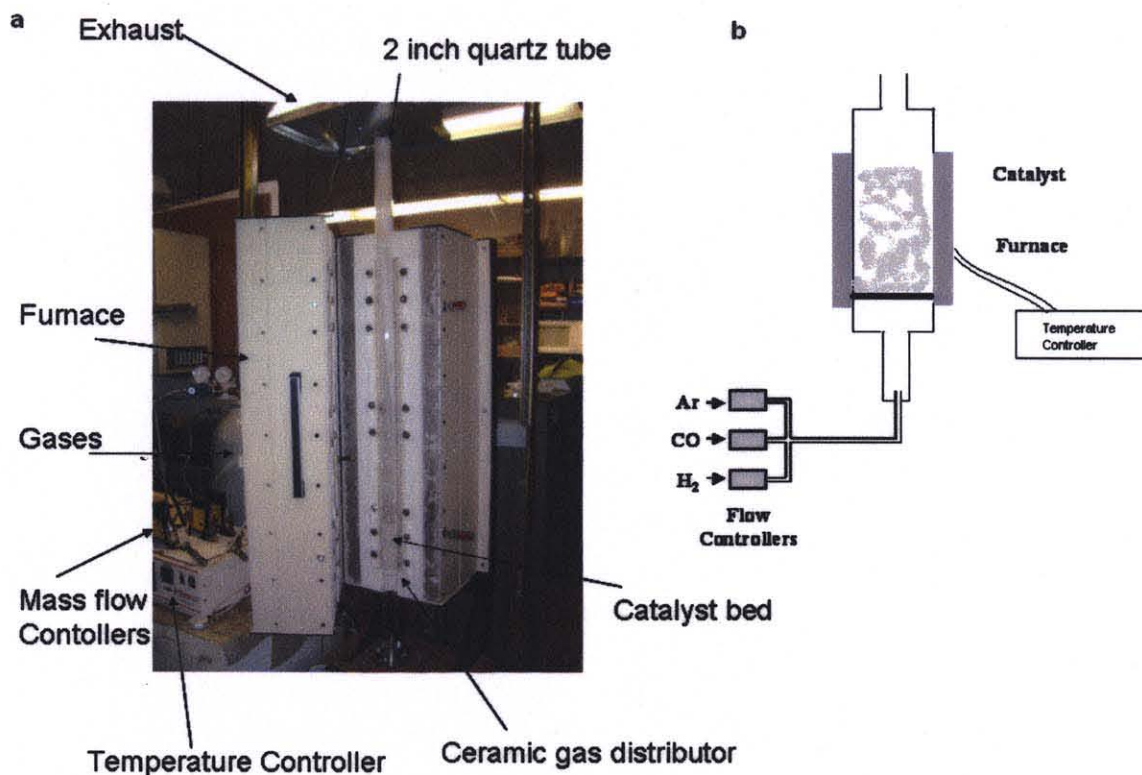
Figure 3.29 Experimental setup for scaled-up SWNT synthesis: a) photograph of the fluidized CVD setup used in this work. Note color of the catalyst/support bed which is white, and b) schematic for growth of SWNTs using fluidized bed CVD.

For the experiment carried out a 110 gm batch of catalyst/support was introduced into the reactor tube resulting in a bed height of 10.5 cm. The bed fluidized uniformly to a height of 13.5 cm and a bubbling type of fluidization was observed. As the gas flow was increased the bed height remained uniform suggesting that the expansion of the bed comes from the space occupied by gas bubbles. Photographs of the fluidized bed experiment are shown in Figure 3.30.
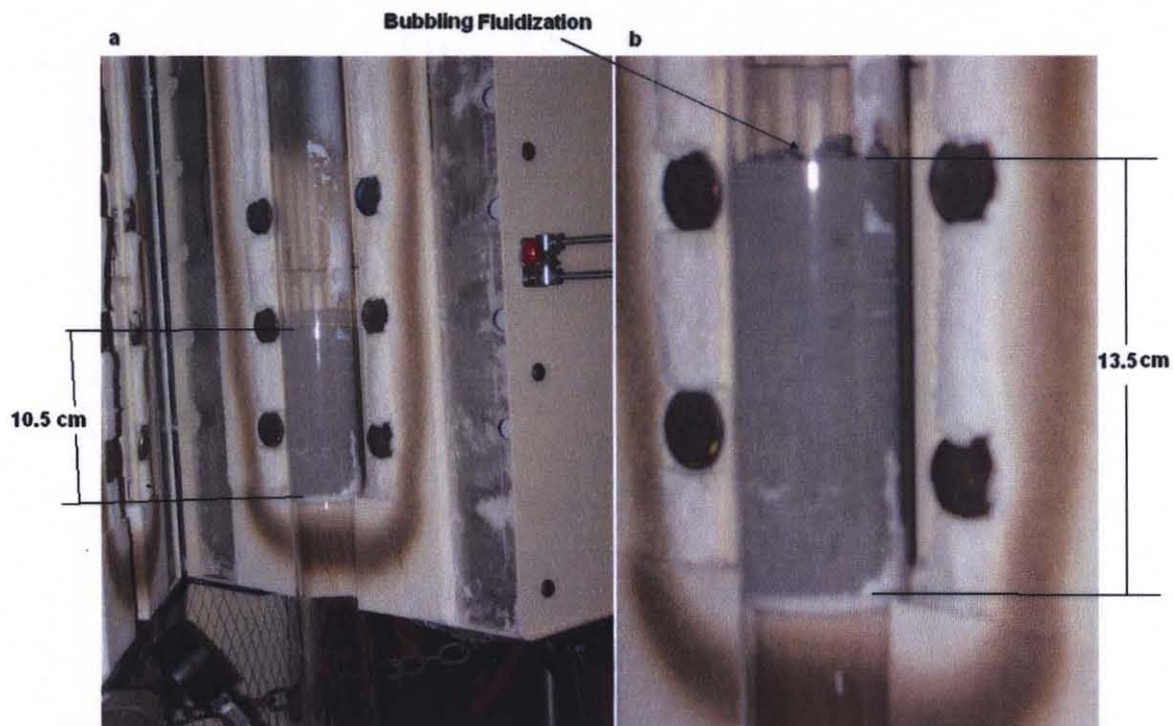
Figure 3.30 Photographs of fluidized bed during a run; a) before flow of gases bed height is 10.5 cm; and b) after gas flow bed height is 13.5 cm. Note darkening of catalyst/support bed due to carbon deposition.

SEM and Raman analysis were conducted on the samples after fluidized CVD deposition clearly indicating the formation of SWNTs but at low yields. It is likely that the low yields are due to the lowered concentrations of CO used in this run due to safety considerations and use of a reducing gas environment with low H_2 concentrations. Figure 3.31 (a) is a representative SEM image obtained from the as prepared sample and Figure 3.31 (b) is from a purified sample. Due to the relatively large amount of MgO and low SWNT yield, it was very difficult to observe SWNTs in the as prepared sample. However, after briefly cleaning (1 hr) with 4M HCl, SWNTs were easily visible. A Raman spectrum from the purified tubes is shown in Figure 3.32, where features for the SWNTs can be clearly observed in the RBM and TM regions of the spectrum.
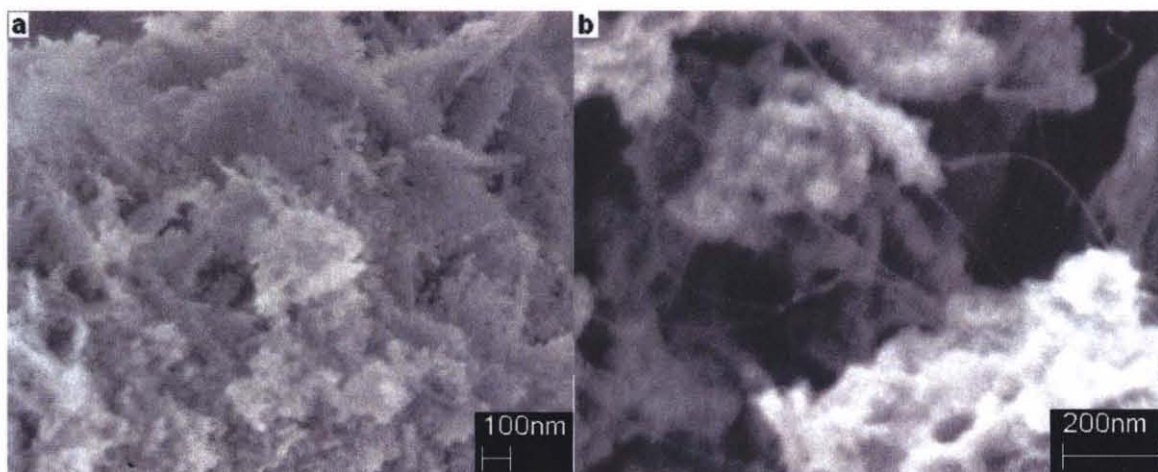
Figure 3.31 SEM images of SWNTs from fluidized CVD run: a) as prepared SWNTs, b) Acid purified SWNTs.
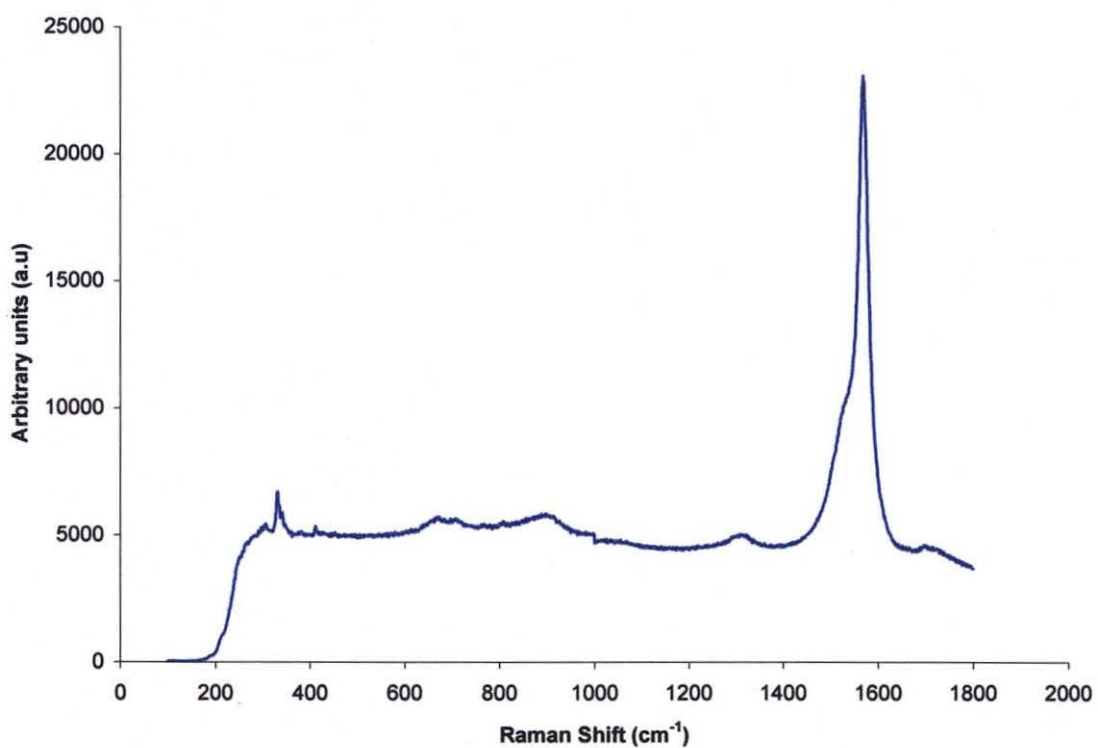
Figure 3.32 Raman spectrum obtained with 632.8 nm laser excitation for purified SWNTs synthesized using a fluidized bed reactor.

3.7 Conclusions

The carbon monoxide chemical vapor deposition (CO-CVD) method was developed and optimized for the production of SWNTs in a scalable manner. Two furnaces, one a horizontal furnace with a small scale boat type reactor and another, a large-scale vertical furnace with a fluidized bed reactor, were set up and characterized for nanotube growth. A Co-Mo/MgO catalyst/support system was studied and it was found that Co is the effective catalyst while Mo acts as co-catalyst or promoter for nanotube growth. It was also observed that if Co, is present in excess of Mo, the catalyst becomes random in shape and size. Spherical monodisperse catalyst of composition Co:Mo in the ratio of 1:4 with the remaining comprised of MgO as catalyst support, was found to be most effective for nanotube growth. The optimum conditions for growth of SWNTs using the small scale reactor were determined in this study. It was observed that nanotube growth initiates at a temperature of 675 °C and above, and the most optimum temperature is around 700 °C. The $I(D)/I(G^+)$ ratios associated with the intensities of the disorder and graphitic lines of the SWNTs, respectively, determined from the Raman data, confirmed this observation. From Co-Mo-carbon phase diagram it was inferred that the Co catalyst converts from the β to the α-phase at the nanotube growth temperature in the presence of Mo, and 1.7 wt % carbon is needed to supersaturate the catalyst metals. Purification of SWNTs was carried out using 4-6 M HCl and thin bundles of very high quality SWNTs were observed with transmission electron microscopy. XRD data revealed complete removal of MgO support after HCl purification. Yields of 10% by weight of SWNTs were obtained in these small scale experiments. As the flow rate was increased the exit CO_2 gas concentration data revealed a shift in equilibrium suggesting that higher yields

can be obtained with increasing flow rates. It was found that the partial pressure of CO above 0.2 atm is needed for nanotube growth; however, the percentage occupation of catalyst sites did not vary with the partial pressure of CO. A rate limited kinetic model with precipitation as the rate limiting step in conjunction with the observed experimental growth was proposed and fitted well with the experimental data. The SWNT formation reaction was observed to follow first order kinetics. An initial scaled up experiment carried out in a fluidized bed using the large-scale vertical furnace showed the formation of SWNTs but at low yields probably due to the relatively low concentration of CO used due to safety considerations. More detailed optimization of the scaled up process would therefore be necessary and will be carried out later in the group using a safer experimental set up.

CHAPTER 4

METAL-CARBON NANOTUBE COMPOSITES

4.1 Abstract

The primary objective of the work described in this chapter is the fabrication of metal-nanotube composites. Catalytic chemical vapor deposition method is used to infiltrate metal pellets with SWNTs/MWNTs. Two carbon precursors namely, carbon monoxide and acetylene are used for the synthesis of SWNTs and MWNTS, respectively inside the metals. Catalysts used in this study are acetates and nitrates of cobalt, iron, and molybdenum. Either individual metals or and in some cases bimetallic mixes of the above mentioned metals are used. To monitor the growth of nanotubes and metal-carbon phases the composites are characterized using Raman spectroscopy, FE-SEM, TEM, XRD, and EDX. Vickers hardness numbers and stress-strain curves are obtained to characterize the mechanical properties of the composites formed. We found that the yield strength of iron-carbon nanotube composites shows substantial enhancement up to 45% with ~ 1 wt % of infiltrated SWNTs, relative to that of similarly treated pure iron samples without carbon nanotubes of the same piece density. The work hardening coefficient and the Vickers hardness coefficient (74% and 96% for the SWNT- and MWNT- reinforced composites, respectively) are also significantly increased in these composites relative to the reference samples. In order to avoid the formation of iron carbide, a carbon feed comprised of a mixture of acetylene and carbon monoxide is used. A reaction mechanism supporting the observed carbide-free growth of nanotubes is also presented in this chapter. The same fabrication-infiltration technique was extended to other metal matrices, such as copper and aluminum.

4.2 Overview of Composites

Many technologies require materials with unusual combinations of properties that cannot be provided by conventional single phase metal alloys, ceramics and polymers. This is needed more so in the case of aerospace, underwater, construction and transportation industries. A composite in the currently understood context, is a multiphase material that is artificially fabricated in contrast to thermodynamically stable single phase metals or alloys. In addition, the constituent phases must be chemically dissimilar and separated by a distinct interface. Metallic alloys and ceramics are single phase structures and therefore do not fit this definition. Composites are fabricated made by various combinations of metals, ceramics and polymers. Examples are ceramic-polymer and ceramic-metal composites. Most composites are fabricated to create improvement in properties, such as stiffness, toughness, ambient and high temperature strength, and thermal and electrical conductivity. A composite material is composed of at least two phases: one is referred to as the matrix, which is continuous and surrounds the other phase, often called the dispersed phase. The resultant properties are a function of concentration of constituent phases, structural alignment of the dispersed phase and the interface between the two phases.

Composites can be classified based on the matrix material, the dispersed phase used, and the composite properties. A simple classification based on the architecture of the dispersed phase is discussed below and presented in Figure 4.1. The three main branches of this classification are particle-reinforced, fiber-reinforced and structural composites. Each branch can be subdivided further into two categories. In particle-reinforced composites, dispersion strengthening can be achieved if the dispersed phase is

equiaxed (i.e., the particle dimensions are approximately the same in all directions); in continuous fiber-reinforced composites alignment is determined by the aspect ratio α (ratio of the length to diameter) of the fiber. Structural composites involve combinations of homogeneous and composite materials into arrayed architectures.
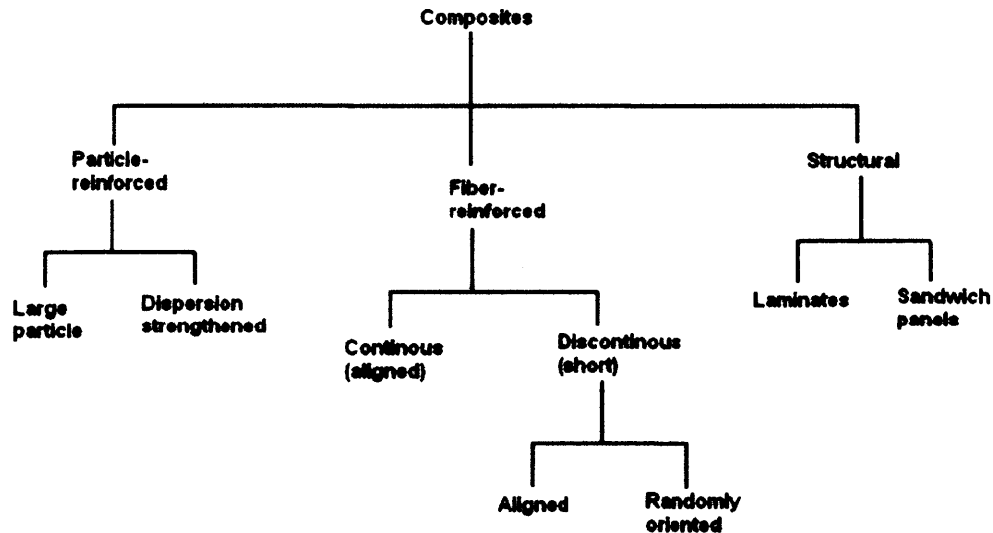
Figure 4.1 A classification scheme for the various composite types on the basis of the geometry of the dispersed phase.

The present work is based on reinforcing a metal matrix with carbon nanotubes, which can be perceived as long fibers with very small diameters as discussed in the Introduction. In addition, technologically, the most important composites are those in which the dispersed phase is in the form of a fiber. As can be noticed from the classification in Figure 4.1 fiber-reinforced composites can be divided into two categories on the basis of fiber length. The mechanical properties of such composites depend mainly on two characteristics other than the properties of the fiber itself. Firstly, the length to diameter ratio of the fiber, and secondly the orientation and concentration of the fibers dispersed in the matrix. The degree to which an applied load is transmitted to the fiber

also depends on the interfacial bond between the fiber and matrix and for this purpose a critical fiber length is necessary for effective strengthening and stiffening of the composite material. This critical length l_c is dependent on the fiber diameter d and its ultimate (or tensile) strength σ^*_f and on the fiber matrix bond strength τ_c (or the shear yield strength of the matrix, whichever is smaller) given by the Equation:

$$l_c = \frac{\sigma^*_f d}{2\tau_c}$$ (4.1)

For glass and carbon fiber-matrix combinations, this critical length is on the order of 1 mm, which is between 20 to 150 times the fiber diameter. When a stress equal to σ^*_f is applied to fiber with critical length l_c, the stress position profile is as shown in Figure 4.2 a, i.e., maximum fiber load is achieved at the center of the fiber length. As the fiber length increases the fiber reinforcement becomes more effective; this is demonstrated in Figure 4. 2 b, where $l > l_c$ and the applied stress is equal to the fiber strength. In the case of $l < l_c$, the resultant stress position profile is shown in Figure 4.2 c. A fiber with $l >> l_c$, normally $15l_c$, is referred to as continuous, and is discontinuous when the fiber length is smaller than this. Discontinuous fibers mainly constitute particle-reinforced fibers.

Table 4.1 Common Fillers and their Respective Aspect Ratios

Form	Size		Fabrication route	Examples
	d	l		
Monofilaments	100-150 μm	∞	CVD	SiC, Boron
Multi-filaments	7-30 μm	∞	Precursor stretching, Pyrolysing: melt spinning	Carbon, Glass, Nicalon™, Kevlar™
Short Fibers	1-10 μm	50-5000 μm	Spinning of slurries or solutions, heat treatment	Saffil™, Kaowool, Fiberfrax™
Whiskers	0.1-1 μm	5-100 μm	Vapor phase growth/reaction	SiC, Al$_2$O$_3$
Particulates	5-20 μm	5-20 μm	Steel making byproduct: refined ore; sol-gel processing etc.	SiC, Al$_2$O$_3$, B$_4$C, TiB$_2$
Carbon Nanotubes	1-100 nm	∞	CVD; Arc-discharge: Laser ablation	SWNTs, MWNTs
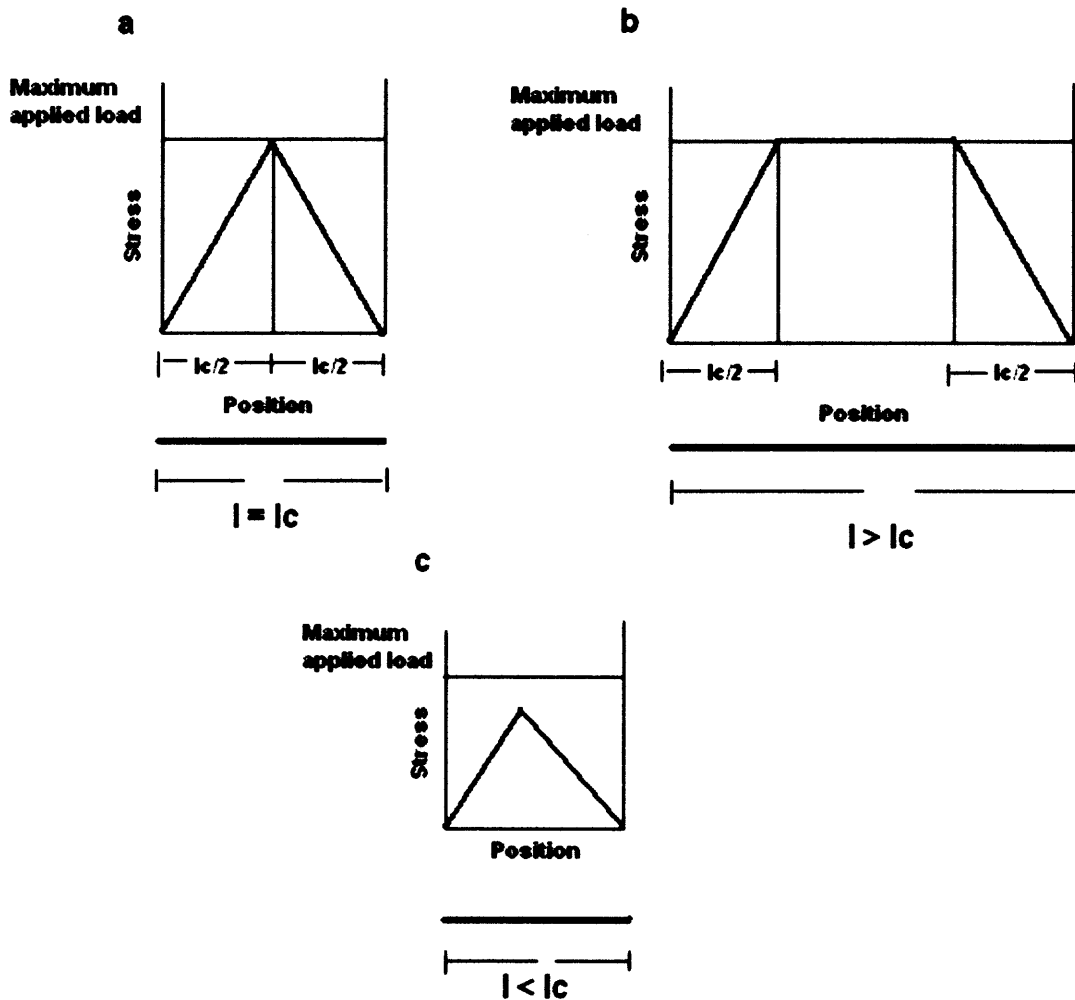
Figure 4.2 Stress position profiles when fiber length (a) l is equal to critical length l_c, (b) l is greater then critical length l_c and (c) l is less than the critical length l_c that is subjected to a tensile stress equal to the fiber tensile strength σ^*_f.

[Source: Callister, (2002). Materials Science and Engineering an Introduction, 6th Ed. John Wiley & Sons, Inc. New York, pp. 536]

For spheres, which have minimal reinforcing capacity, the aspect ratio α equals to unity. In designing new composites with reinforcing fillers, the process aim is to have fillers with high aspect ratio, improved compatibility and interfacial adhesion. A useful parameter to characterize the effectiveness of filler is to relate the area to volume ratio

(A/V) with the aspect ratio. Thus, maximizing A/V and particle-matrix interaction through the interface requires $\alpha >> 1$ for fibers and $1/\alpha << 1$ for platelets as shown in Figure 4.3.
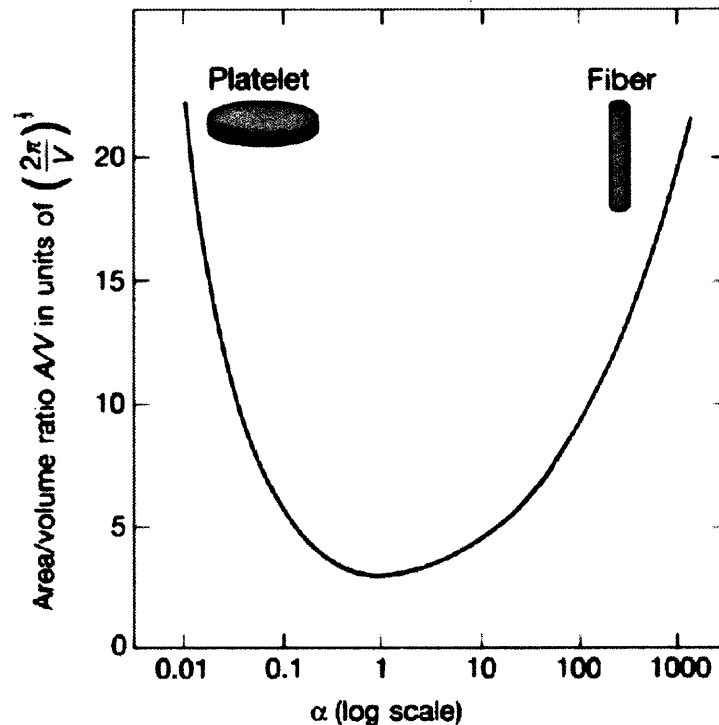
Figure 4.3 Surface area to volume ratio, A/V, of a cylindrical particle versus aspect ratio $\alpha = l/d$.

[Source: McCrum, (1997). Principles of Polymer engineering, 2nd Ed. Oxford University Press, New York, pp. 242-245]

The orientation or arrangement of fibers within the matrix and relative to each other is another important factor in determining bulk mechanical properties. With respect to orientation two extremes are possible: (1) A parallel alignment of the longitudinal axis of the fibers in a single direction; and (2) Randomly oriented fibers throughout the matrix. In the case of metal- carbon nanotube composites, we will mainly focus on the second type i.e., randomly oriented nanotubes (dispersed phase) in the metal (matrix phase) because in this work we were able only to fabricate composites of this type. Figure 4.4 illustrates the direction and dispersion of carbon nanotubes within the matrix.

Longitudnal Direction

a   b

Metal Pellet

Transverse Direction

Carbon Nanotubes (fibers)
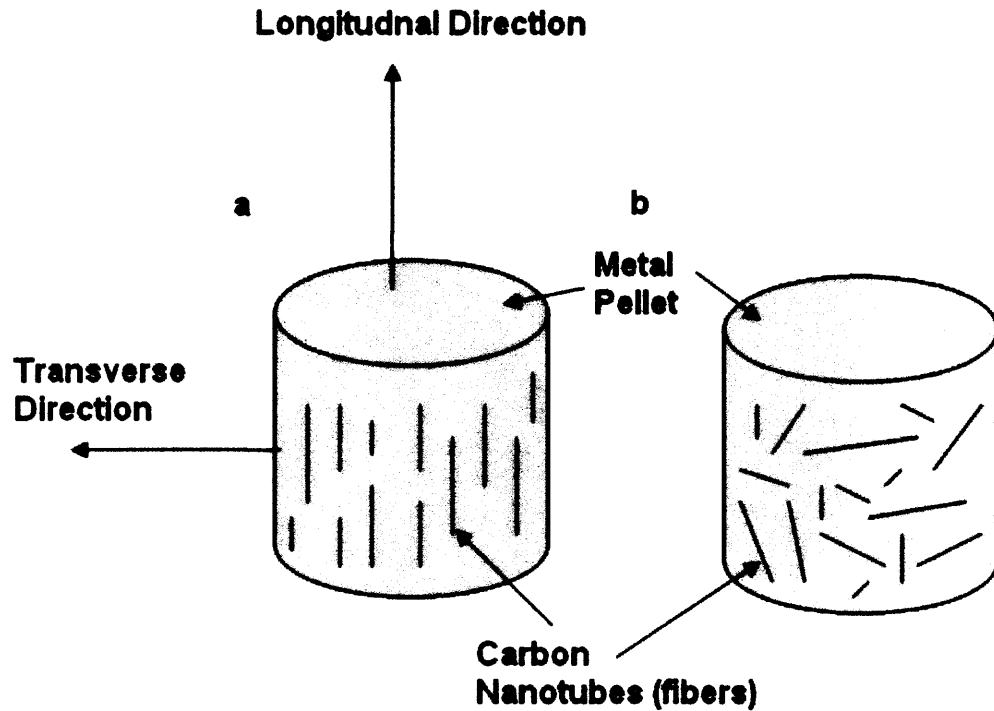
Figure 4.4 (a) Parallel aligned continuous fibers in a metal matrix **(b)** randomly oriented fibers in a metal matrix.

4.3 Background for Metal-Carbon Nanotube Composites

Carbon nanotubes, which have high length to diameter ratios, are capable of imparting toughness and strength to polymer, ceramic and metallic composites (Curtin, 2004; Iqbal & Goyal, 2005). Theoretical modeling (Lier, 2000; Sanchez-Portal, 1999; Hernandez, 1998; Lu, 1997; Yakobson, 1997) and experimental measurements (Treacy, 2002; Wong, 1997; Salevtat, 1999; Krishnan, 1998) have demonstrated that carbon nanotubes have high stiffness and strength, high electrical and thermal conductivity, and are capable of sustaining high elastic strain. Carbon nanotubes have been incorporated in polymer and ceramic matrices (Flahaut, 2000; Siegel, 2001; An, 2003; Balázsi, 2003; Zhan, 2003; Zhan, Kuntz, & Garay 2003; Wang, 2004) to provide improved mechanical properties.

However, only sparse results are available for carbon nanotube-metal composites, with no improvement in mechanical properties reported so far. Unfortunately, materials fabrication difficulties have limited research on carbon metal-carbon nanotube reinforced composites. One of the key issues is to achieve uniform dispersion of nanotubes in the matrix without damaging or destroying the crystalline structure owing to the high temperatures and highly reactive environments needed for the production of metal matrices. Mainly powder processing methods have been used to form ceramic and metal composites (Flahaut, 2000; Siegel, 2001; An, 2003; An & Lim, 2002; Balázsi, 2003; Zhan, 2003; Zhan, Kuntz, & Garay 2003; Yang, 2004; Wang, 2004). The large aspect ratio of the tubes makes it difficult to obtain a good dispersion between the two phases before subjecting the mixture to sintering or hot pressing. However, some progress has been made in achieving dispersion of small amounts of nanotubes in metals by utilizing conventional milling techniques. Kuzumaki et al. (1998) fabricated aluminum composites using 5 and 10% by volume of pre-synthesized arc-grown multi-wall carbon nanotubes (MWNTs) by hot press and hot extrusion methods. TEM observations revealed no formation of carbides along the interface of metal and nanotubes after annealing at temperatures of 873-983 K. However, there was no significant change observed in mechanical strength. Yang and Schaller (2004) prepared MWNT/magnesium composites by gas pressure infiltration of liquid magnesium into a porous array of nanotubes and investigated their damping characteristics; but no improvement relative to damping characteristics of conventional metal matrix materials was observed. However, a 20 % increase in shear modulus at high temperatures was reported for a magnesium composite reinforced with 25 %-SAFIL® (a short synthetic polyglycolic acid fiber) coated with

nanotubes and compared to magnesium reinforced with 25 %-SAFIL® fibers. This suggests the possibility of weak bonding between the magnesium matrix and the carbon nanotubes. When SAFIL® fibers along with small amount of carbon nanotubes are used the shear modulus at high temperatures is further enhanced because of increased bond strength between magnesium and the carbon nanotubes. Flahaut *et al.* (2000) fabricated carbon nanotube-iron-Al_2O_3 composites by hot-pressing *in-situ* formed carbon nanotubes using a H_2-CH_4 mixture as the carbon source. A very good dispersion of nanotubes can be achieved by in-situ growth of the nanotubes on the powder. However, the carbon nanotubes made using this process are damaged during the high temperature (1500-1600° C) processing step used and disordered carbon layers precipitate at the grain boundaries. The nanotubes therefore do not provide an increase in mechanical strength. Goh et al. (2006) also used a powder metallurgy technique to reinforce a magnesium matrix with 0.3 wt % carbon nanotubes. The results show improved thermal stability and an increase of 0.2 % in yield strength, ductility and work of fracture (point of rupture for composite under compression or tensile load, expressed as integral under the stress-strain curve).

Aluminum-carbon nanotube composites have also been studied both for improvement in mechanical [George, 2005; Zhong, 2002; Tang, 2004;] and electrical properties (Xu, 1999). In all the methods mentioned above powder metallurgy techniques have been used to mix pre-synthesized carbon nanotubes in various volume percentages with metals or ceramics. George at al. used ball milling to mix the nanotubes with aluminum powder of 200 mesh size and compacting it at a load of 120 kiloNewtons. The billets formed were then sintered at a temperature of 580 °C and finally extruded at about the same temperature. An increase in Young's modulus of 12-23 % for 0.5 % to 2 %

MWNT loading, respectively was reported. However, no observations were made for carbide formations in this study. Zhong et al. (2002) also utilized a powder mixing method to form nano-aluminum/carbon nanotube composites by compacting at 1.50 GPa at room temperatures followed by consolidation at a pressure of 1 GPa at $280 - 460\ ^{\circ}$ C. They reported an increase in hardness at $380\ ^{\circ}$ C of about 178 %. Utilizing a method similar to that of Zhong et al. (2002), Tang et al. (2004) reported a decrease in coefficient of thermal expansion by as much as 65 % with 15 vol % addition of nanotubes to aluminum. Xu et al. (1999) reported a slight increase in electrical resistivity with increasing amount of nanotubes by hot pressing a mixture of nanotubes and aluminum powder; however, the process used resulted in the formation of an aluminum carbide phase.

The above-mentioned observations of the lack of substantial increases in mechanical strength in metal composites with nanotube loading are probably related to the use of methods involving physical incorporation of pre-synthesized nanotubes into the metal matrix, which results in very little bonding of the nanotubes to the metal matrix required to mechanically support the structure. Also, the formation of different metal-carbon phases in optimal quantities may be required to impart further improvement in mechanical properties. In this study we report on a fabrication strategy to directly grow the nanotubes inside the metal matrices by chemical vapor infiltration in pellet forms of metals. The nanocomposites investigated in this work are: iron-SWNT, iron-MWNT, and aluminum-MWNT.

Table 4.2 Mechanical Properties of Commonly Used Filler Materials: Comparison with Carbon Nanotubes [Source: Askeland, 1989]

Material	Density (g/cm^3)	Tensile strength (GPa)	Modulus of elasticity (GPa)	Ductility $(\%)$	Melting temp. $(°C)$	Specific modulus $(10^6\,m)$	Specific strength $(10^4\,m)$
E-glass	2.55	3.4	72.4	4.7	<1 725	2.90	14
S-glass	2.50	4.5	86.9	5.2	<1 725	3.56	18
SiO_2	2.19	5.9	72.4	8.1	1 728	3.38	27.4
Al_2O_3	3.95	2.1	380	0.55	2 015	9.86	5.3
ZrO_2	4.84	2.1	340	0.62	2 677	7.26	4.3
Carbon (high-strength)	1.50	5.7	280	2.0	3 700	18.8	19
Carbon (high-modulus)	1.50	1.9	530	0.36	3 700	36.3	13
BN	1.90	1.4	90	1.6	2 730	4.78	7.4
Boron	2.36	3.4	380	0.89	2 030	16.4	12
B_4C	2.36	2.3	480	0.48	2 450	20.9	9.9
SiC	4.09	2.1	480	0.44	2 700	12.0	5.1
TiB_2	4.48	0.10	510	0.02	2 980	11.6	0.3
Be	1.83	1.28	300	0.4	1 277	19.7	7.1
W	19.4	4.0	410	0.98	3 410	2.2	2
Polyethylene	0.97	2.59	120	2.2	147	12.4	27.4
Kevlar	1.44	4.5	120	3.8	500	8.81	25.7
Al_2O_3 whiskers	3.96	21	430	4.9	1 982	11.0	53.3
BeO whiskers	2.85	13	340	3.8	2 550	12.3	47.0
B_4C whiskers	2.52	14	480	2.9	2 450	19.5	56.1
SiC whiskers	3.18	21	480	4.4	2 700	15.4	66.5
Si_3N_4 whiskers	3.18	14	380	3.7	—	12.1	44.5
Graphite whiskers	1.66	21	703	3.0	3 700	43	128
Cr whiskers	7.2	8.90	240	3.7	1 890	3.40	12
SWNT	1.33-1.40	13-52	1 TPa	—	400-450	—	—
MWNT	1.33-1.40		1.28 TPa	—	350-400	—	—

Note: In the category Melting Point the temperatures given for nanotubes are the respective oxidation temperatures.

Table 4.3 Mechanical Properties of Metal Matrices that can Potentially be Reinforced with Carbon Nanotubes

Material Type	Density (g/cm^3)	Youngs Modulus (Gpa)	Tensile Strength (Mpa)
Steel	7.6	210	676
Titanium	4.5	83	241
Aluminum	2.8	70	468
CFRP	1.5	140	2500
CNT	1.3	1,200	50,000

4.4 In-situ Synthesis of Metal-Carbon Nanotube Composites

A detailed study for the various factors influencing the growth of carbon nanotubes in a metal matrix to form a composite has been performed. Specifically, the effects of carbon precursor, type of catalysts, bimetallic-catalyst ratio, pelletization pressure, time for growth, and powder or pellet from of metal matrix has been investigated. The growth process mainly consists of three main stages: firstly, catalyst precursor preparation and loading in a metal matrix, secondly reduction of precursor to metal under hydrogen environment, and thirdly nanotube growth using different carbon sources. The metal matrix pellets with carbon nanotubes were characterized using Raman spectroscopy, field emission-scanning electron microscopy (FE-SEM), energy dispersive X-ray analysis (EDX), X-Ray diffraction (XRD) and high-resolution transmission electron microscopy (HRTEM).

The nanotubes were grown using chemical vapor deposition method using a 2.54 cm quartz tube reactor placed in a high temperature furnace controlled externally by a three point microprocessor controlled temperature unit (Applied Systems Inc. three point temperature controller). The high temperature furnace is capable of reaching 1200 °C, a mechanical pump by manufactured by GE with ¾ horse power was used to attain a vacuum of 10^{-3} Torr. Carbon monoxide (Matheson, 99.9 % research grade), acetylene (99.6%) and ethanol vapors (100% purity especially from Fischer) were used as the carbon source. Iron acetate (Aldrich, 99.995%), iron/cobalt acetate (Aldrich, 99.995%), iron/molybdenum acetate (98%), iron pthalocyanine (Aldrich ~90%), ferrocene (Fluka, >98%), and nanosized iron powder, were used as catalysts or catalyst precursors. Metal matrices were formed from: iron powder (Sigma-Aldrich, 99.9 + %) of -325 mesh size

corresponding to 20 µm particles, aluminum powder (Sigma-Aldrich ~99%) particle size of ~ 20 µm, 20-50 nm size coated aluminum powder was obtained from ARDEC, Picatinny and an alloy of aluminum 1060 A (Reade Advanced Materials) with 0.01% of iron content were used in this study.

4.4.1 Catalyst Loading

The nanotube growth process depends on the type of catalyst used. Below is the list of methods used for introducing catalyst or catalyst precursors into the metal matrices:

1) **Acetates:** 0.01 – 0.03 wt % iron acetate, cobalt acetate and molybdenum acetate were dissolved in ethanol.. Typically in 15 ml of ethanol solution weighing about 14 gms, 0.00135 – 0.00405 gms of acetates were added and sonicated. Three different catalyst precursor solutions were obtained in this manner: iron acetate, iron-cobalt acetate (1:1 ratio), and cobalt-molybdenum acetate (1:1 ratio) all dissolved in ethanol. Few drops of the solution were used to soak either the metal powder or a pellet formed from the metal powder.

2) **Ferrocene:** Ferrocene powder was mixed with iron powder of 20 µm size and compressed to form pellets. In this method during the high temperature synthesis of nanotubes ferrocene pyrolyzed above 300°C and contaminated the whole growth chamber. A second method, using the two heating zones in the furnace at different temperatures to pyrolyze ferrocene on to the metal powder was conducted and a third method involving introduction of ferrocene (0.2 wt %) mixed with ethanol using a micro syringe (1 ml soln.) in the last stage of nanotube growth at 700 °C was also utilized.

3) **Iron Pthalocyanine:** Iron pthalocyanine in powder formed was mixed with iron powder of 20 μm size and pellets were formed.

4) **Nanosized iron powder (50 nm):** Nano sized iron powder was used to synthesize nanotubes in two ways: powder used as-obtained and reduced for one hour under hydrogen at 500 °C, and secondly, powder covered with hexane and heated in argon (70 °C) to remove hexane followed by reduction under hydrogen.

5) **Iron-Co-Mo/MgO:** A mixture of Co-Mo (1:4) with MgO as support was mixed with iron powder of 20 μm size. Experiments were carried with 0.25 to 1 gm of the catalyst mixed with 3-4 gms of iron powder.

4.4.2 Synthesis Processes for Carbon Nanotubes

In this section the processes for synthesis of carbon nanotubes after catalyst loading are described. The section is divided in two parts: SWNT and MWNT synthesis.

4.4.2.1 In-situ Single Wall Carbon Nanotube (SWNT) Synthesis.

Typically 3-5 gms of micron-sized iron powder was soaked in catalyst precursor solution, dried overnight in a hood and pressed into cylindrical pellets under an applied load of 5000 kg to give piece densities in the range of 5.67 to 5.81 gm/cc. The pellets formed were 13 mm in diameter and between 4 and 5 mm in thickness using a stainless steel die obtained from International Crystal Laboratories. The density of both the reference pellets without nanotubes and the pellets with nanotubes were 72-74.5% of the pure iron density (7.8 gm/cc). Therefore, the average porosities of all the samples used in the mechanical measurements were the same. The catalyst loading in our samples was very low as described in the catalyst loading section above – 0.01 weight % of metal acetate

precursor was dissolved in 15-20 ml of ethanol to make the master solution. From this only about 2-3 ml was used to soak the starting iron pellet or powder. After heat treatment to decompose the precursor to oxides followed by reduction in hydrogen to metal, the amount of catalyst metal in the iron matrix was estimated to be about 0.003 weight % of the total weight of the pellet.

The pellets or powders were placed in a quartz boat in a horizontal quartz tube reactor in a microprocessor-controlled high temperature furnace. The quartz tube was pumped down to about 10^{-3} torr and heated to 500°C to decompose the acetate precursors to oxides under argon. The reactor was back-filled with flowing pure hydrogen for 30 minutes to an hour to reduce the oxides to metals. The hydrogen was then pumped out, the reactor temperature was raised to 700°C and the carbon source, carbon monoxide (CO), was introduced into the reactor at a flow rate of 100 standard cubic centimeters per minute (sccm) for 30 minutes to about 1 hour to deposit SWNTs within the matrix as determined by micro-Raman spectroscopy and field emission-scanning electron microscopy (FE-SEM). After completion of the deposition, the system was pumped down, back-filled with argon and allowed to cool to room temperature under 100 sccm of flowing argon. The pellets were either taken out at this point for characterization or in some cases annealed at 900°C under 100 sccm flowing argon followed by cooling to ambient temperature before removal. The growth process differed from the above-mentioned method depending on the type of catalyst used and will be described as and when necessary in the Results and Discussion section.

4.4.2.2 In-situ Multiwalled Carbon Nanotube (MWNT) Synthesis. The catalyst precursors and promoters, cobalt acetate (0.01 weight %) and molybdenum acetate (0.01 weight %), respectively, were dissolved in ethanol. Typically 3-4 gms of micron-sized iron powder was soaked in this solution, dried overnight in a hood and pressed into thin cylindrical pellets under an applied load of 5000 Kg. The pellets were 13 mm in diameter and between 4 and 5 mm in thickness. The pellets were typically made with an applied load of 5 MTs (metric tones) to give piece densities in the range of 6.10 gm/cc.

The pellets were placed in a quartz boat in a horizontal quartz tube reactor in a three-zone, microprocessor-controlled high temperature furnace. The quartz tube was pumped down to about 10^{-3} torr, a single step protocol involving heating to 800°C under flowing argon followed by switching to either **a)** a mixed feed of acetylene and argon with flow rates of 6 to 7 sccm and 300 sccm, respectively or **b)** a mixed feed of acetylene, CO and argon with flow rates of 6, 100 and 300 sccm, respectively, at atmospheric pressure, followed by cooling under argon atmosphere.

4.4.2.3 Reference Pellets of Metals. Reference pellets were prepared with the same weight of metal powder (but without catalyst precursor; see discussion about catalyst content above) and applied load, followed by heating under argon under the same temperature cycles and time used to grow the nanotubes. The density of the reference samples is also kept the same as the samples containing nanotubes.

4.5 Characterization of Metal-Carbon Nanotube Composites

The characterization of the composites was conducted by micro-Raman spectroscopy, x-ray diffraction (XRD), field-emission scanning electron microscopy (FE-SEM) and energy dispersive x-ray (EDX) analysis. A confocal micro-Raman spectrometer (LabRam, Jobin Yvon/Horiba, Metuchen, New Jersey USA) was used with the laser light source at a wavelength of 632.8 nm. For FE-SEM (LEO microscope, Carl-Zeiss) imaging the pellets were placed on sample holders with carbon tape as support, and the microscope was operated at an applied electric field of 2 keV. Samples were fractured after all other measurements were made to investigate the dispersion of carbon nanotubes within the whole matrix. EDX measurements were performed at 6 keV and a working distance larger than 9 mm. A clear FE-SEM image was obtained before an area was selected for point EDX measurements. XRD measurements were performed using a PAN Analytical Diffractometer employing Cu-Kα radiation (wavelength λ = 1.5405 Å) from 2θ = 20 to 110 degrees at a count rate of 2.8 sec per step of 0.02 degrees.

A transmission electron microscope (TOPCON 002B ultra-high resolution TEM) operated at 200kV was used to obtain the TEM images. In order to thin down the sample for TEM imaging a protocol based on the method of Laub et al (from a Lab Manual method from EPFL-CIME, 1015 Lausanne Switzerland method developed by Anderson *et al*) was used. Briefly, two 10 mm × 3 mm × 1 μm slices of metal were cut and then mounted on a tripod with epoxy glue. The metal strips were polished using diamond lapping films from 30 μm to 3 μm pore size in that order. A film is replaced by smaller size when there are striation marks on the whole film and it seems to be used up by visual observation. The thumb rule is that the sample can be thinned down as much as 3 times

the pore size of the lapping film. The objective to use a lapping film from higher to lower size is to decrease the surface roughness. This process can obtain a sample as thin as 50-100 μm, but it is not thin enough to conduct a TEM investigation. Following that the sample was electropolished using a Fischione electropolisher with 50%chromic acid/50%acetic acid by volume as electrolyte and 27V applied voltage. The final step involved ion milling at three different angles of 6, 12, 15 degrees for 3 hrs each with an electric field of 3 KV and current of 5 mA on each side at same time.

Stress-strain data were taken with an MTS servo hydraulic system operated at a constant displacement rate so as to give a strain rate of about 0.00004/sec (Wiegand, 1991). The data were taken in simple compression along the cylindrical sample axis. A flow stress and a work hardening coefficient were obtained from stress-strain curves for the nanotube-iron composites and compared with similar data obtained from the pristine reference iron pellets. Vickers hardness measurements were conducted using a LECO micro-hardness tester (LM 700, LECO Corp.). A load of 10 kgf (kilogram force) at ambient temperature with a dwell time of 5 seconds was selected and an optical image of the indentation sites using a fine pixel camera attached to the LM 700 micro hardness tester was obtained before and after indentation. Each specimen was indented at several locations. Three to five measurements were made with clear indentations and an average value of the hardness is reported.

4.6 Results and Discussions

4.6.1 Influence of Catalyst on SWNT Growth

Iron (Cassell, 1999; Li, 2001), cobalt (Kathyanini, 2004; Lan, 2003), iron-cobalt (Kathyanini, 2004), cobalt-molybdenum (Kitiyanan, 2000; Tang, 2001), ferrocene (Schintzler, 2003), and iron pthalocyanine (Harutyunyan, 2003) have been successfully used as catalysts or catalyst/carbon precursors to grow carbon nanotubes. It is well-known that iron is an excellent catalyst for carbon nanotube growth and can partially dissolve and bond to carbon to provide supporting bridges at the cavities. Bonding might also occur at nano-sized iron particles embedded in the larger iron particles of the matrix. Our first observation of the growth of multiwall carbon nanotubes using iron as catalyst motivated us to perform this study with related catalysts and precursors. In the process development phase we identified the above- mentioned catalysts and precursors to be suitable in order to introduce minimum amount of a third phase (catalyst particles) i.e. other than metal matrix and carbon nanotubes. The primary goal was to achieve uniformly dispersed catalysts, which results in the growth of carbon nanotubes with low amounts of amorphous carbon. Presence of amorphous carbon at grain boundaries affects the mechanical strength of nanocomposites adversely (Flahaut, 2000). Figure 4.5 shows the Raman-active RBM modes for the SWNTs synthesized using different catalysts used in this study. Figure 4.6 shows the tangential modes and the corresponding SEM images for the samples are shown in Figure 4.7. The RBM modes are key features used to determine the diameter distribution of single wall carbon nanotubes formed in the sample. The RBM lines appear in the low frequency region $120 - 280$ cm^{-1} and correspond to the atomic vibrations of the carbon atoms in the tube's radial direction.

Nanotubes were grown on eight different catalysts; in case of ferrocene three different methods were used to incorporate the catalyst within the matrix. From Figure 4.5 it can be noticed that in the case of iron and iron-cobalt powder there is growth of single wall nanotubes and the corresponding RBM peaks are at 191.6 cm^{-1} and 214.5, 276.4 cm^{-1}, respectively. However, these samples did not show the G peak (shoulder or G$^-$ peak) signatures for single wall tubes. The G line similar in frequency to the primary line in graphite is also referred to as the tangential mode. As pointed out earlier, a second lower frequency G$^-$ component is observed in SWNTs due to curvature-induced softening and removal of the degeneracy of the C-C graphene mode. SEM images of the nanotubes grown on iron and iron-cobalt powder as shown in Figures 4.7 a-b reveal that a low density of nanotubes is formed on the iron pellet surface. For the sample prepared using nanosized iron particles, Fig 4.6 shows a high intensity D–peak located at 1317.5 cm^{-1}, which is attributed to disorder arising due to the formation of amorphous carbon and defects on the tube walls. Although, SWNTs appeared to have formed since both RBM and TM features were observed for this sample, the process was not pursued further due to overall experimental difficulties. Two methods were used to prepare SWNTs using nanosized iron particles. In the first method the nanosized particle mixed with micron sized iron particles were used to directly grow the nanotubes after initial reduction in hydrogen. This method resulted in sizable oxidation of the iron particles due to their large surface area and even long reduction times of up to 3 hours under pure hydrogen at 500 °C did not increase the yield of nanotubes. In order to reduce oxidation, a second method was used where a small amount of nanosized iron particles was immersed under hexane and slowly heated to 70 °C under argon atmosphere to avoid oxidation. A

mixture of two sizes of iron powders was then compressed to form pellets after SWNTs were grown on them.

Ferrocene was used in three different ways, first by mixing with iron powder, second by subliming at 300 °C and third by injecting a ferrocene solution during the SWNT growth at 900 °C. As mentioned earlier, the method of incorporation of catalyst and nanotube growth varies according to the catalyst used and will be discussed in the Results section. Therefore a short overview of the experimental observations is provided in this section. Ferrocene dissociates at a much lower temperature (~300 °C) than that required for nanotube growth. In the first method, ferrocene and iron powders are initially mixed together and a protocol similar to that described in the experimental section for SWNT growth was used with the exception of growth was performed at a temperature of 900 °C. The growth of MWNTs can be seen in Figs. 4.5 and 4.6; however, the images showed the formation of a black layer of soot on the entire surface of the pellet possibly due to the rapid dissociation of ferrocene. This also led to contamination of the entire experimental set up with soot. To avoid this, ferrocene was placed in the first zone of the furnace and the pellets were placed in the third zone. The first zone was heated slowly to 300 °C under flowing argon. The sublimed ferrocene was then carried on to the pellets which were kept at the nanotube growth temperature. This, however, did not completely prevent contamination of the growth apparatus, and therefore a third method was used where ferrocene was introduced at the nanotube growth temperature by injecting an alcohol solution of ferrocene into the reaction zone. There was no indication of RBM modes in the Raman spectra of samples prepared by the second process and this was confirmed by SEM images which showed no single wall

nanotubes (Figure 4.7 e). In samples prepared using injected ferrocene a new feature at 667 cm^{-1} was observed in the Raman spectrum which is associated with the formation of magnetite (Cao, 2000) in the sample. The G^- peak (shoulder on the lower frequency side of the G peak) was not observed and the disorder mode is relatively intense when injected ferrocene was used to prepare the composite pellets. The use of ethanol also caused a black soot coating to be formed on the surface of the pellet as confirmed by performing a study with ethanol as carbon source, which showed the formation of a large amount of nanotubes together with amorphous carbon soot that would make it difficult to perform mechanical property measurements on the samples. The use of iron pthalocyanine also resulted in the formation of the magnetite phase, and with no indication of RBM and tangential mode features in the Raman spectra shown in Fig 4.4 and Figure 4.6, respectively. We also used the Co-Mo/MgO catalyst discussed in the previous chapter. Here, although the growth of SWNTs was very good as confirmed by Raman spectroscopy, larger amounts of catalyst of the order of 0.5 to 1 gm per pellet was required to achieve uniform growth. Large catalyst loadings are undesirable for composite applications. It also makes it difficult to judge changes in mechanical properties with nanotube loading due to catalyst particle size variation between the metal matrix and the nanotube phase.

Finally, two catalysts made from iron acetate and iron-cobalt acetates were used and showed the most promising results. The remainder of the discussion will be on SWNT-iron composites prepared using these two catalysts. As is evident from Figs. 4.5 and 4.6, both RBM and tangential mode features associated with SWNTs are clearly observed with high intensities in the Raman spectra taken from these samples. The

SEM images shown in Fig 4.7 also confirm the presence of SWNTs throughout the

matrix.
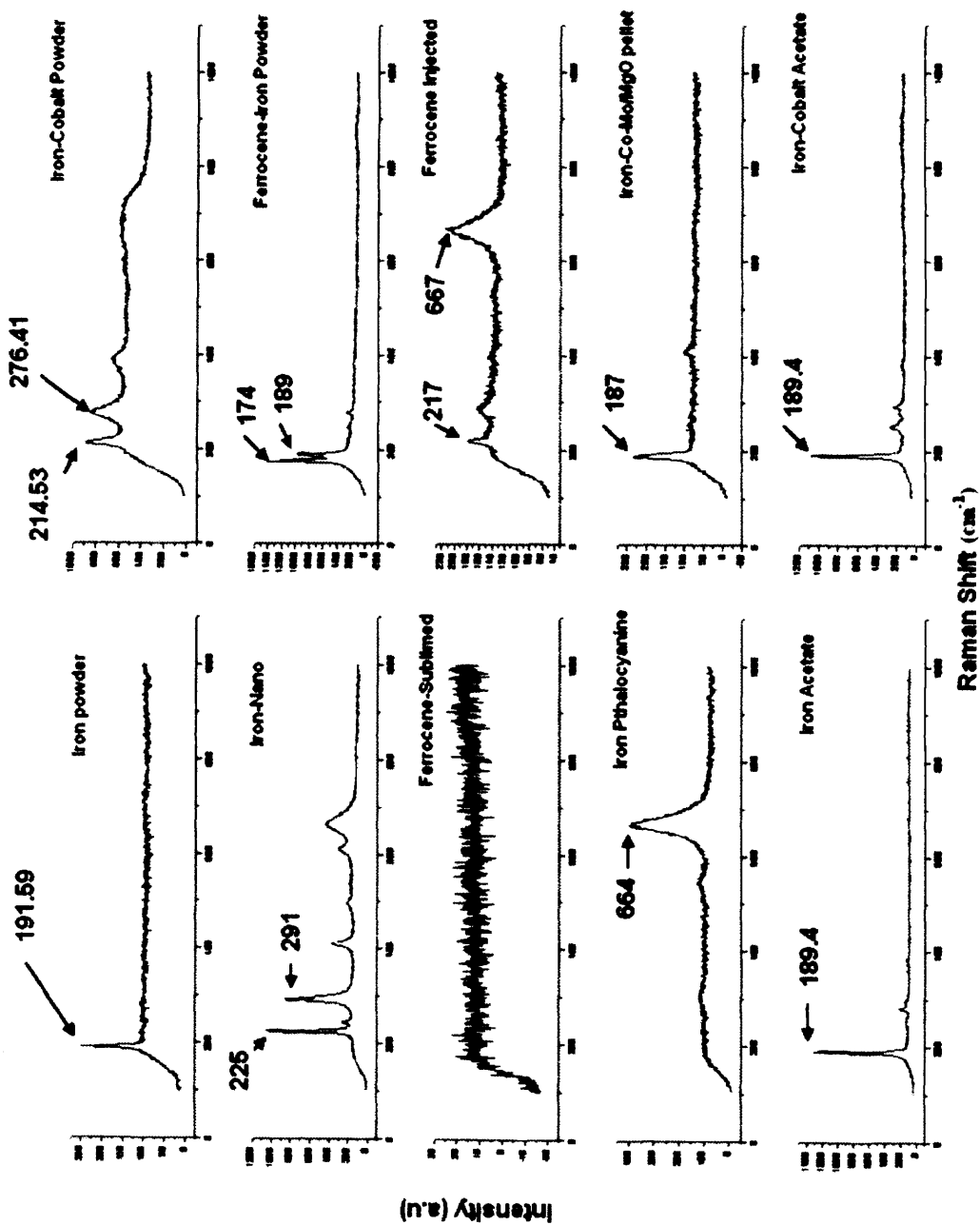
Figure 4.5 Raman spectra with 632.8 nm excitation in radial breathing mode region for iron-carbon nanotube composites prepared with different catalysts.
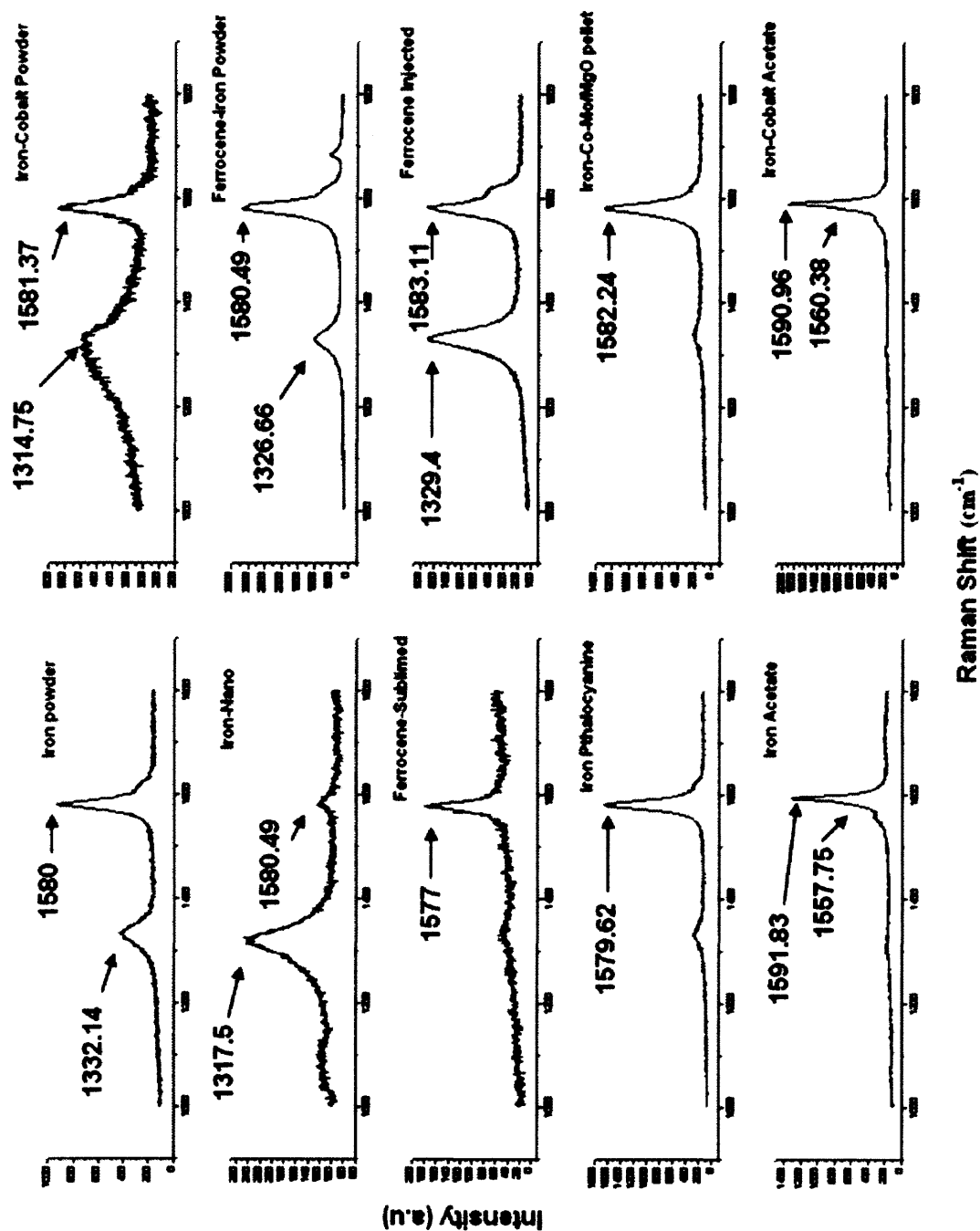
Figure 4.6 Raman spectra with 632.8 nm excitation in the tangential and disorder mode region for iron–carbon nanotube composites prepared with different catalysts.
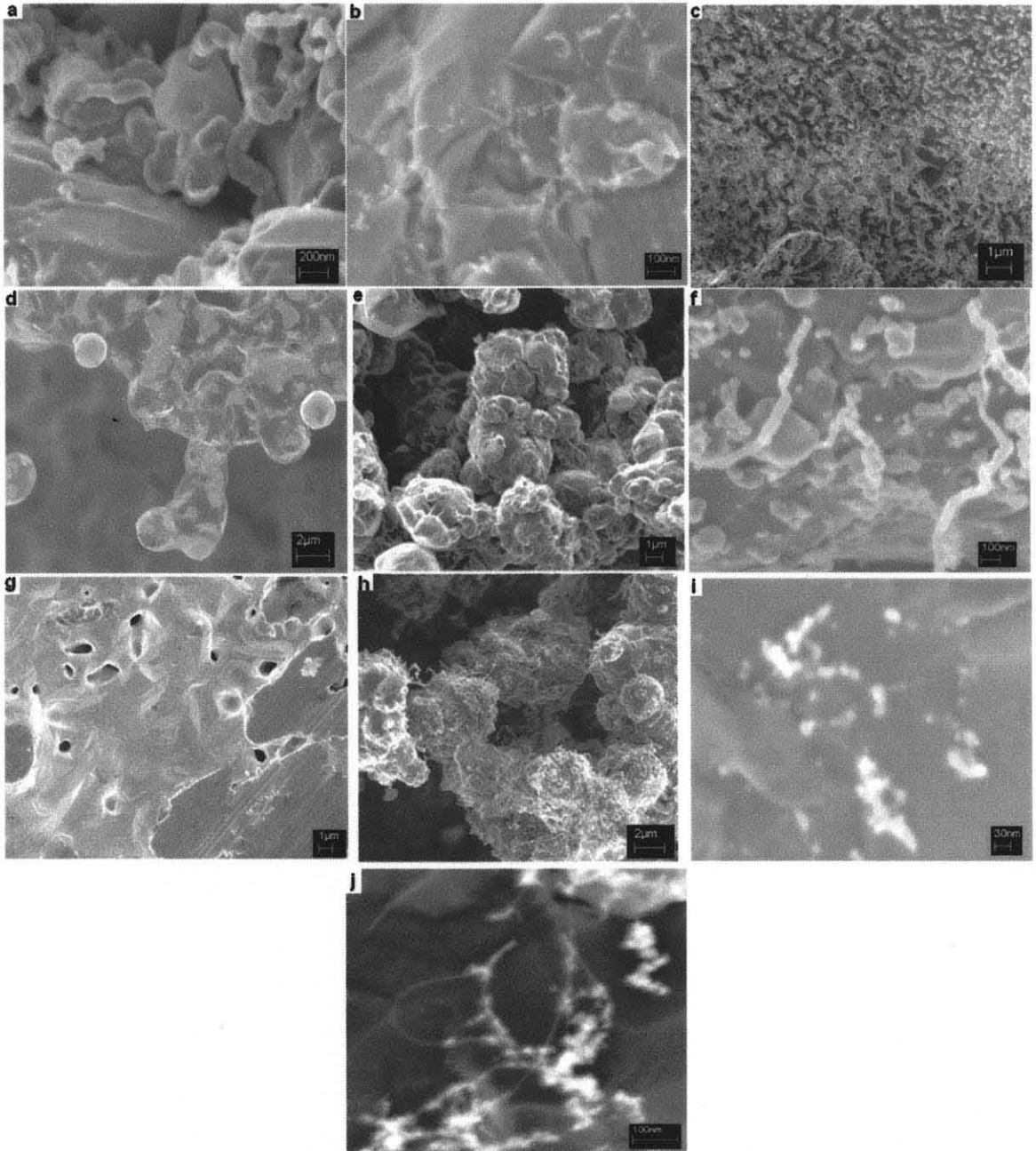
Figure 4.7 SEM images for iron-carbon nanotube composites prepared using different catalysts or catalyst precursors. (a) iron powder, (b) iron-cobalt powder, (c) iron nanoparticles, (d) ferrocene-iron powder, (e) sublimed ferrocene, (f) injected ferrocene solution, (g) iron pthalocyanine, (h) iron-Co-Mo/MgO pellet, (i) iron acetate, and (j) iron-cobalt acetate.

The Raman spectra from samples prepared using iron and iron-cobalt catalysts are replotted in Fig 4.8 for clarity and to obtain a better understanding of the spectral details.

Clear evidence for the formation of SWNTs is provided by the appearance of the characteristic SWNT lines associated with the carbon-carbon bond tangential modes near frequencies of 1591 cm^{-1} and 1552 cm^{-1} (the latter appearing as a well-defined shoulder in the spectrum), and the lines at 190, 247, 259 and 279 cm^{-1} due to the radial breathing modes (RBMs) of individual tubes of different diameters (Rao, 1997). The line observed at 293 cm^{-1} is likely to be associated with Fe_2O_3 present as an impurity in the iron matrix (Cao, 2000). The diameters (d, nm) of the individual SWNTs can be determined from the RBM frequency ω. For bundled SWNTs: $d = (238/\omega)^{1.075}$ (Alvarez, 2001). Therefore, the RBM mode frequencies at 190, 247, 259 and 279 cm^{-1} correspond to individual SWNT diameters of 1.27, 0.96, 0.91 and 0.84 nm, respectively, in the sample. The broad line at 1327 cm^{-1} assigned to defects and amorphous carbon was found to be relatively weak. This indicated that rather defect-free SWNTs are formed with relatively little amorphous carbon present. Figure 4.8 b is a representative Raman spectrum obtained from a composite prepared using CO with only iron acetate as the catalyst precursor; it shows features similar to that of the spectrum in Figure4.8 a, consistent with the formation of SWNTs, except that the defect and amorphous carbon content is even lower than that for the sample in Figure 4.8 b, as indicated by the lower intensity of the broad line at 1302 cm^{-1}.

Further nanoscale characterization of the SWNTs and their distribution in the iron matrix was performed by FE-SEM imaging. Figs. 4.9 a-b show low and high-resolution FE-SEM images, respectively of the SWNT-iron composites. The lighter spots, some of which are marked by black circles on the micrograph in Figure 4.9 a, represent some of the locations of high SWNT density in the composite. The SWNTs appear to be well

appear to be well dispersed in the matrix and growth is significant as evident from the

higher magnification image shown in Figure 4.9 b. Diameters of 10 to 20 nm estimated

from the FE-SEM images are an order of magnitude larger than the individual SWNT

diameters obtained from the RBM Raman frequencies, indicating that the SWNTs formed

are bundled into "ropes". The images also show that the nanotube bundles are decorated

with unused catalyst and catalyst sub-oxide particles, and that they span the cavities

(darker regions in the FE-SEM images) in the metal matrix. The individual iron particles

are therefore likely to be anchored in place by the nanotube bridges. It is estimated from

the measured increase in weight after nanotube deposition that typically 1 weight % or

2.2 volume % of SWNTs are incorporated into the starting iron matrix.
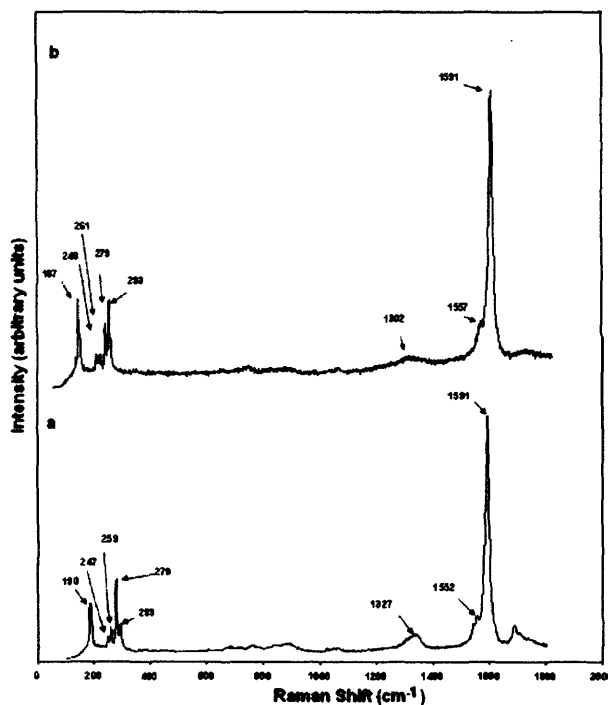
Figure 4.8 Raman spectra for representative iron-nanotube composites using 632.8 nm laser excitation. (a) Shows spectrum for composite fabricated with iron and cobalt acetate catalyst precursors and pure carbon monoxide (CO) as the carbon source at 700°C followed by annealing at 900°C under argon; and (b) Shows spectrum for composite fabricated with only iron acetate catalyst precursor, using a similar protocol to that used for the sample in spectrum (a).
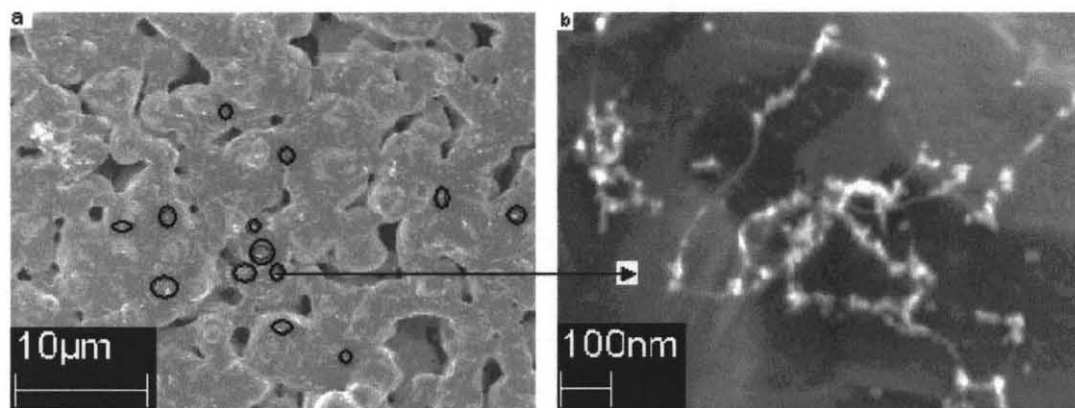
Figure 4.9 Field-emission scanning electron microscope images of an iron-SWNT nanocomposite: **(a)** Low magnification image of iron-SWNT nanocomposite surface showing well dispersed nanotubes as lighter contrast dots, some of them indicated by small circles. The iron particle surfaces are gray and the cavities between them are dark in the image shown; and **(b)** Higher magnification image obtained by zooming in on one of the circled regions in (a) showing SWNT bundles decorated by catalyst particles bridging the darker cavities between the gray iron particles of approximate dimensions of 10 microns or greater. The catalyst particles on the SWNT bundles appear to be charging possibly due to the presence of metal sub-oxides formed during the deposition process.

4.6.2 Influence of Pelletization Pressure and Growth Time

In order to increase the carbon nanotube loading during the growth process an experimental study was conducted as a function of pelletization pressure and growth time. Three different pressures of 3, 4 and 5 metric tons were applied to form equal weights of iron powders into pellets. Three pellets for each load were prepared with the same Fe-Co catalyst. Note that this catalyst had provided the best results in terms of SWNT growth (also refer to previously described methods used to load the catalyst precursors into the Fe matrix). Three different growth times of 30, 45 and 60 minutes were used to form the nanotube-iron composites. The results shown in Figure 4.10 indicate that as the porosity and growth time increases, the amount of carbon deposited also increases. However, Raman observations on these samples show that most of the

carbon formed after 40-45 minutes was amorphous and not carbon nanotubes as evident from the increase in the intensity of the D peak in the Raman spectra.
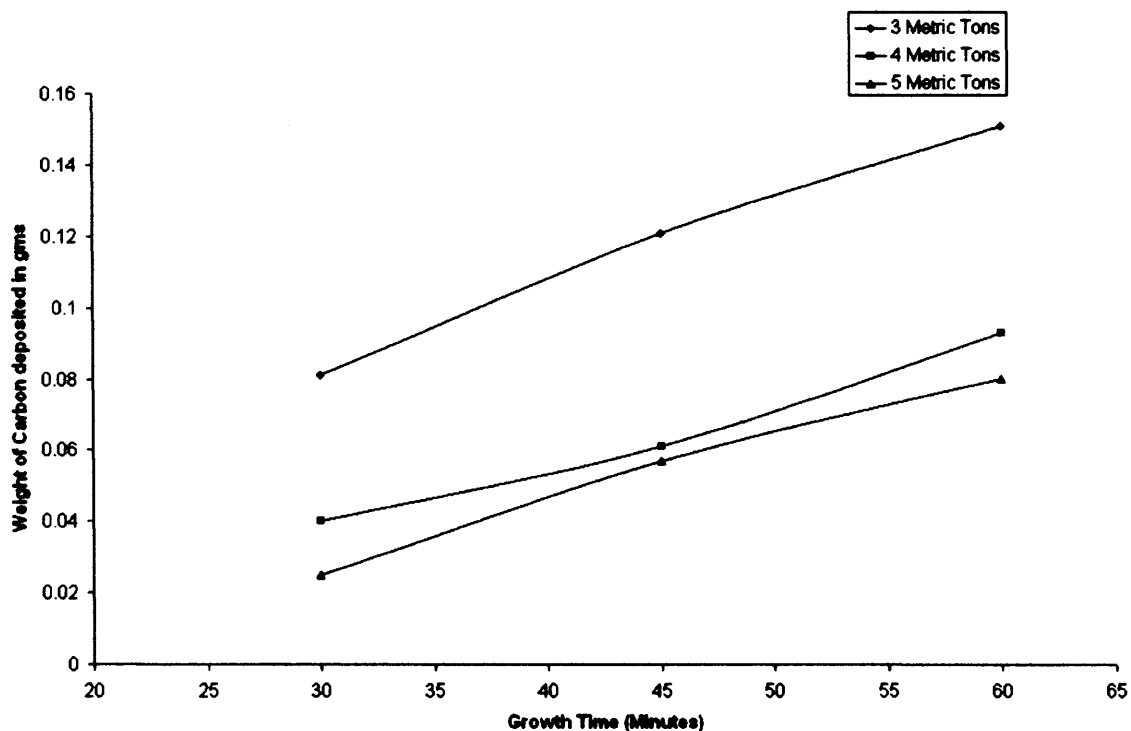
Figure 4.10 Pelletization pressure and growth time to observe increase in carbon filler.

4.6.3 Identification of Structural Phases in the Iron-Nanotube Composites

XRD measurements (Figure 4.11) showed the presence of pure iron as indicated by reflections at 2θ values of 45, 65, 83, and 99 degrees. XRD reflections from SWNTs are not detected due to the relatively low weight % (0.5-1) loading of SWNTs in the nanocomposites. Reflections associated with the iron-rich cementite Fe_3C phase were clearly absent. An XRD line at a 2θ value of 26 degrees was observed near the expected (001) reflection of graphite, but its intensity is too high for it to be attributed to a carbon

phase. This reflection is tentatively assigned to an iron sub-oxide formed in the iron matrix under our fabrication conditions.
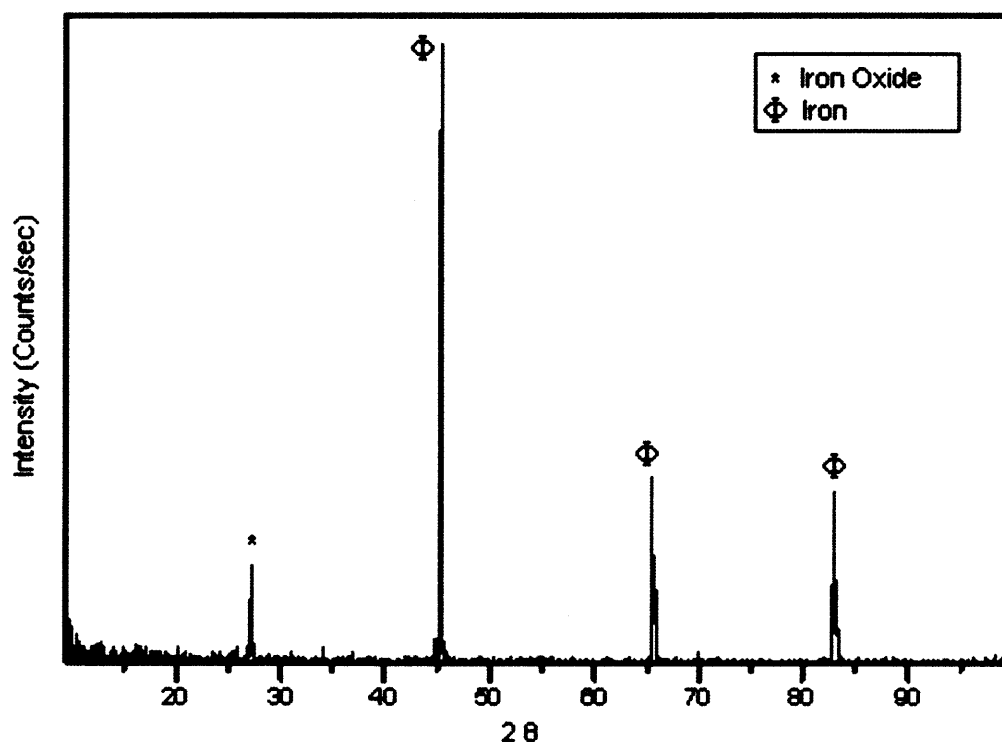
Figure 4.11 X-ray diffraction pattern using Cu-Kα radiation with wavelength λ = 1.5405 Å from an iron-SWNT composite prepared using CO, and iron-cobalt acetate catalyst precursors.

EDX data taken from nano-sized spots from the composite surface together with corresponding FE-SEM images (Figure 4.12) showed the carbon content to be higher (observed 32-77 %) than the 6.7 weight % predicted for Fe_3C, and is consistent with these spots being comprised largely of SWNTs. Such measurements were carried out at many locations on the pellet surface with the beam size in EDX at approximately 1μm ×1 μm at 6 keV. Therefore, the measurements made are likely to represent the properties of the bulk phase.
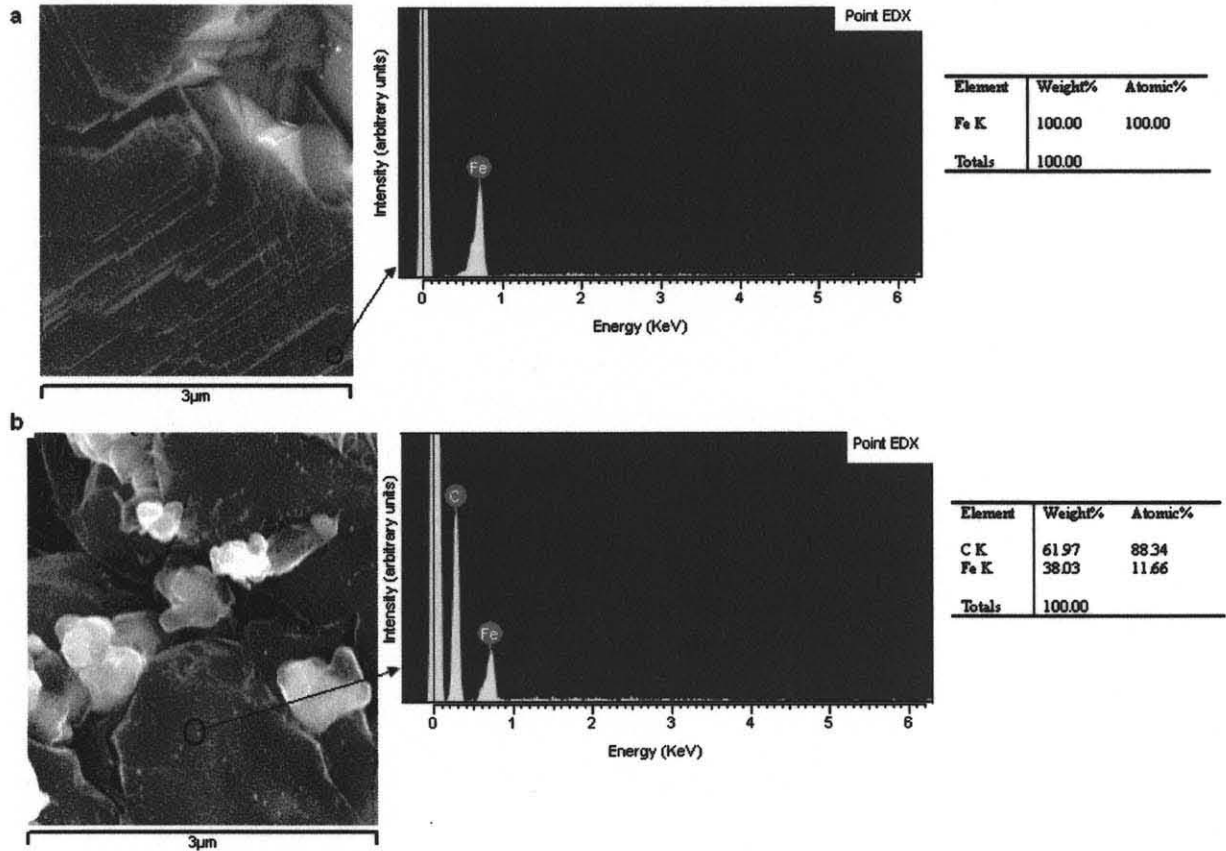
Figure 4.12 Energy dispersive x-ray spectroscopic data (right panel) and corresponding SEM images (left panel): (a) For reference iron matrix with no carbon nanotubes where only the line due to iron is observed, (b) For region around and including carbon nanotubes in iron-SWNT composite. Carbon line corresponds to 61.97 weight %, much higher than that expected for the Fe_3C carbide phase.

The SWNTs are largely concentrated in cavities in the matrix as indicated by the FE-SEM images shown in Figure 4.9b. The TEM image in Figure 4.13 shows a SWNT bundle spanning a cavity. The nanotube sidewalls appear to have suffered some damage from the extensive sample preparation process required. This confirmed the concept of pinning of the particles in the iron matrix by the nanotubes. This observation is important since SEM imaging does not clearly indicate the interface between the nanotubes and the metal matrix. Due to the rigorous sample preparation involved, successful TEM observations were possible only on a limited number of samples.
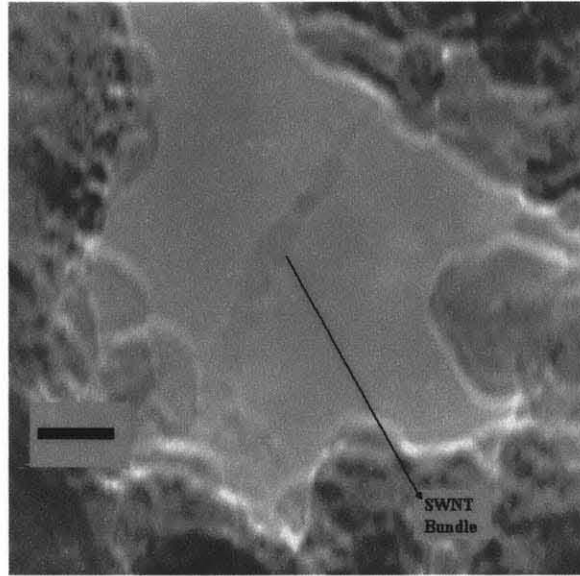
Figure 4.13 Transmission electron microscope image in the neighborhood of a pore in an iron-SWNT composite. The image shows a SWNT bundle with somewhat corrugated walls caused by the sample thinning methods employed. The image shows that the SWNT bundle is pinned to the iron matrix at both the ends, and bridges the pore in the matrix. Scale bar is 10 nm.

4.6.4 Mechanical Properties

4.6.4.1 Vickers Hardness Measurements.

The Vickers hardness test method (Figure 4.14) consists of indenting the test material with a diamond indenter in the form of a right pyramid with a square base and an angle of 136 degrees between opposite faces subjected to a load of 1 to 100 kgf (kilogram force). The full load is normally applied for 5 to 15 seconds. The two diagonals of the indentation left on the surface of the material after removal of the load are measured using a microscope and their average is calculated. The area of the sloping surface of the indentation is calculated, and the Vickers hardness (HV) given by Equation 4.1 below is the quotient obtained by dividing the kgf load by the square of the indentation area in mm^2.
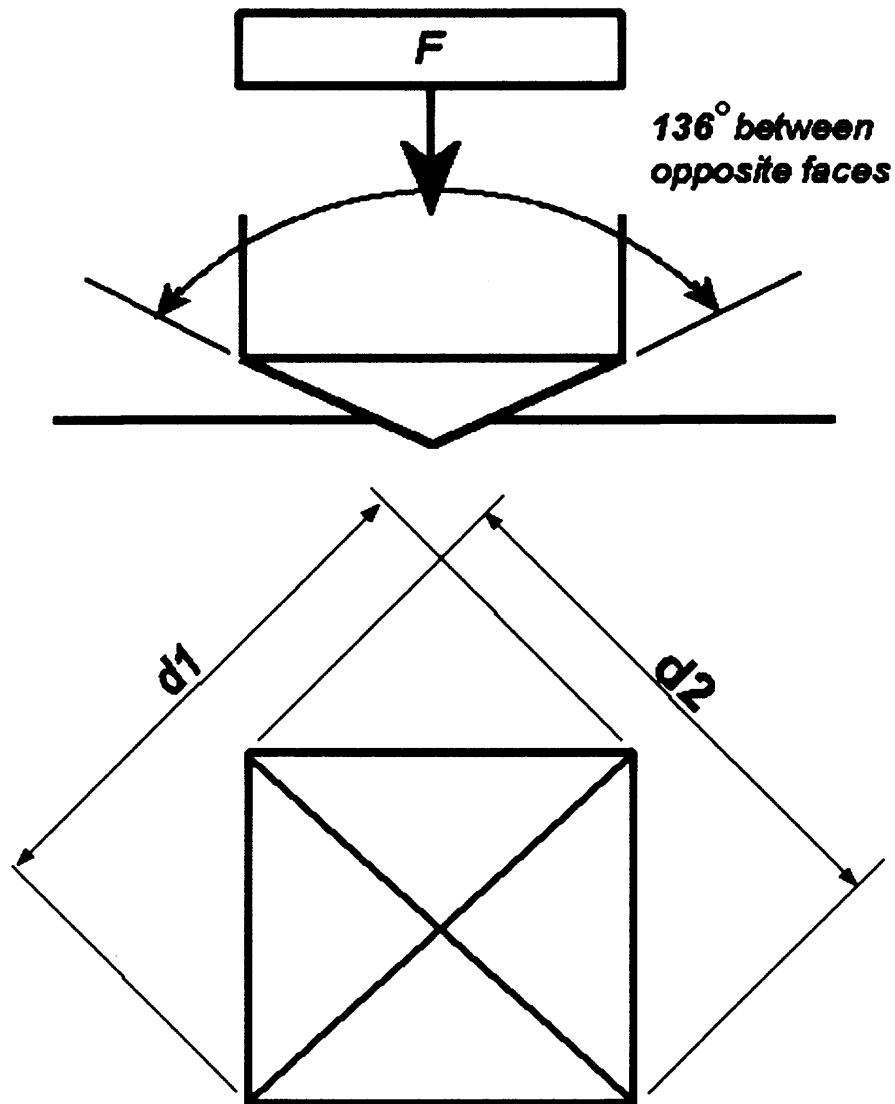
Figure 4.14 Vickers hardness measurements: Indentation marks observed after subjected loads, the diagonal dimensions are used to calculate hardness numbers.

$$HV = \frac{F\sin\dfrac{136^o}{2}}{d^2} \therefore HV = 1.854\frac{F}{d^2}$$ (4.2)

Where,
F = Load in kilogram-force (kgf)
d = Arithmetic mean of the two diagonals, d_1 and d_2 in mm in Figure 4.13
HV = Vickers hardness

When the mean diagonal of the indentation has been determined, the Vickers hardness can be calculated from Equation 4.2, but it is more convenient to use conversion tables. The Vickers hardness is reported for example as: 800 HV/10, which signifies a Vickers hardness of 800 obtained using a 10 kgf force. Several different pressure settings give practically identical hardness numbers on a uniform material. This is much better than the arbitrary changing of scales used in other hardness testing methods. The advantages of the Vickers hardness test are that extremely accurate readings can be taken, and just one indenter type is used for all types of metals and surface treatments.

Vickers hardness indices, which correlate with the tensile strength and fatigue resistance (Callister, 2003), were measured on these nanocomposites and compared with measurements on pristine reference pellets prepared under the same conditions but with no nanotubes in them. A load of 10 kgf was applied and a clear diamond-shaped indentation was observed. In a typical measurement, at least 3-5 points on the composite surface were chosen for better statistics. Typical average values of the Vickers hardness (HV) indices HV/10 (with 10 kgf) of 95.2 for the reference sample and 135.7 for an iron-SWNT composite sample showed an increase in the hardness index by 74 % relative to that of a reference sample for a representative iron-SWNT nanocomposite prepared using CO as the carbon source and iron and cobalt acetate as catalyst precursors. A list of the Vickers Hardness numbers obtained is given in Table 4.4. The metal micrographs for the samples before and after indentation that show significant change in hardness are depicted in Figure 4.15. As indicated earlier, the use of large amounts of catalysts is undesirable. Although dense growth of nanotubes is observed for iron-Co-Mo/MgO pellets with high catalyst loadings, the Vickers hardness number shows a decrease due to

the relatively weak mechanical properties of MgO, distribution of particle sizes and weak interfaces between the MgO and iron particles. In addition, hardness is related to tensile strength, or in other words it is a measure of resistance to plastic deformation. Consequently they are roughly proportional, as shown in Figure 4.16 for tensile strength as a function of Brinell's hardness number for cast iron, steel and brass. However, the same proportionality does not hold good for all the metals. We will make use of cast iron and steel as reference to obtain theoretical values for ultimate tensile strength. Since in experimental observation we could not apply loads up to ultimate tensile failure. We will use the extrapolation of available data and literature to estimate the same. Vickers hardness numbers can be converted to Brinell's hardness. The equivalent Brinell 500 Kg numbers from the available Vickers data are found and the tensile strengths obtained from the Figure 4.16 are compared. The results are shown in Table 4.4. From the compression measurement on extrapolation the trend matches well with both reference and pellets reinforced with carbon nanotubes.

Table 4.4 Vickers Hardness Numbers and Tensile Strengths for Iron-SWNT Composite Samples

Sample Description	Vickers Hardness Number = HV/10	SI units (MPa) (HV/10 × 9.807)	% Change after SWNT in-situ synthesis	Brinell's Hardness Number (500 Kg)	Tensile Strength (MPa) from Figure 4.16	Comments
All the samples below were heat-treated at 900 °C						
Reference iron pellet	57.75	566.35				Control sample
Pure iron pellet	73.67	722.48	27.57			
Iron-Cobalt powder precursor infiltrated iron pellet	96.87	949.97	67.74			
Ferrocene infiltrated iron pellet	79.45	779.16	37.58			

(CONTINUED)						
All the samples below were heat-treated at 700 °C						
Reference iron pellet	95.20	933.63		79	250	Control Sample
Iron acetate catalyst precursor infiltrated iron pellet	124.62	1222.12	30.90	110	360	
Iron-Cobalt catalyst infiltrated iron pellet	135.67	1330.52	42.51	120	380	
Iron-Co-Mo catalyst precursor/MgO iron pellet	44.45	435.92	53.3			Significant amount of catalyst used
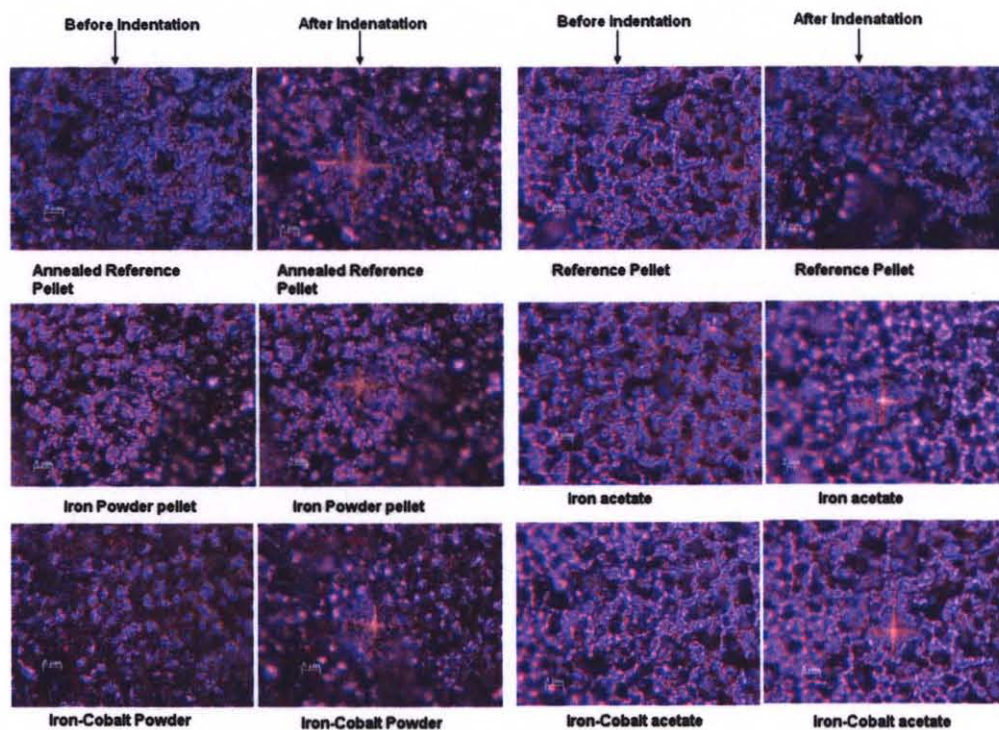
Figure 4.15 Micrographs of Vickers indentation marks for the samples listed in Table 4.4.

Rockwell hardness

60 70 80 90   100 HRB
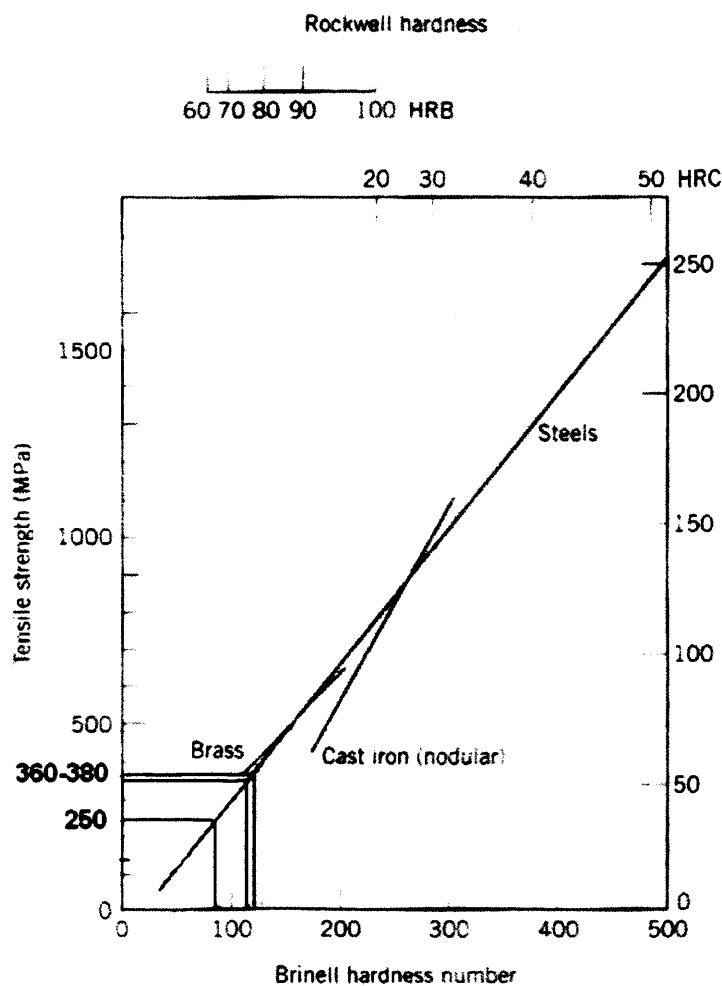
Figure 4. 16 Relationships between hardness and tensile strength for steel, brass, and cast iron. [Data taken from *Metals Handbook: Properties and Selection: Irons and Steels*, Vol. 1, 9th edition, B. Bardes (Editor). American Society for Metals, 1978, pp. 36 and 461; and *Metals Handbook: Properties and Selection: Nonferrous Alloys and Pure Metals*, Vol. 2, 9th edition, H. Baker (Managing Editor). American Society for Metals, 1979, p. 327.]

4.6.4.2 Compression Test Measurements. Compressive stress-strain curves were measured on samples containing SWNTs and compared with stress-strain curves measured for pure, similarly heat- and pressure- treated iron reference samples. The data from two representative samples displayed in Figure 4.17(a) shows significant differences between the nanocomposite and pure iron reference samples. The flow stress, the stress for significant plastic flow, is taken at the intersection of a straight line passing through the initial linear part of the stress-strain curve at low strains and a straight line passing through the linear work hardening part of the curve at larger strains. For the data

in Figure 4.17(a), the flow stress is about 45% higher for the sample containing the SWNTs compared to the value for the reference iron sample. This flow stress is numerically equivalent to a yield stress obtained by a 0.4% strain offset technique. In addition, the work hardening coefficient, the slope in the latter linear part of the stress-strain curve at larger strains, is greater by a factor of about 3.4 (a 240% increase) for the sample containing the SWNTs relative to the reference sample. Thus, the mechanical strength of the sample containing the SWNTs is significantly increased and much greater work is required to deform this sample plastically in the work hardening range compared to the reference sample. Since mechanical properties depend on porosity, it is important to emphasize that the porosity of the reference sample and the sample with SWNTs is the same and therefore differences in porosity cannot account for the enhanced mechanical strength. The initial linear slopes of the stress-strain curves of Figure 4.17(a) are influenced by instrumental effects and are not considered here.

One sample containing SWNTs was recompressed after the initial stress-strain curve was measured, and the results indicate that the flow stress increased by an amount consistent with the work hardening during the first compression. After this recompression both flat end surfaces of this sample were ground so as to reduce the sample length or pellet thickness by 370 μm. A stress-strain curve taken after grinding again indicates that the flow stress increased by an amount consistent with the work hardening during the initial compressions. Thus, the removal of the thin surface layers containing the highest population densities of SWNTs had a minimal effect on the flow stress. These results indicate that the higher flow stresses observed in the samples containing the SWNTs are due to bulk effects and that the SWNTs are distributed throughout the sample

thicknesses of the order of 0.6 cm. After an initial compression a reference sample was also ground on both flat end surfaces to remove 175 µm from each side of the sample thickness. A stress-strain curve taken after grinding also indicates that the flow stress increased by an amount consistent with the work hardening during the first compression. Enhanced yield strengths were observed for a number of similarly prepared composites; data for some of these composites are shown by the stress-strain curves in Figure 4.17(b). To the first approximation, the theoretical values predicted by the rule of mixtures fit well with the experimental data. Although many mechanical models are available to predict the metal composite properties, parameters such as the Burgers vector, thermal strain, and Poisson's ratio have not been calculated or experimentally determined for carbon nanotubes. Therefore, values of the tensile strength for a bundle of SWNTs and for an individual MWNT obtained from the literature were used. The rule of mixtures is given by the Equation:

$$\sigma_c = \sigma_m V_m + \sigma_{cnt} V_{cnt} \qquad (4.3)$$

where σ_c, σ_m and σ_{cnt} are the tensile strengths of the metal-SWNT composite, SWNT bundle and metal, respectively; and V_m and V_{cnt}, respectively represent the volumes of the metal and the nanotubes in the composite.

The pellets are porous and the densities used to calculate the volumes do not correspond to the true density of the matrix material. The tensile strength of the pellet is smaller than that of the matrix material and can be estimated by normalizing the pellet density with the true density of the matrix material using the Equation below:

$$\sigma_c = \sigma_m V_m (0.72) + \sigma_{cnt} V_{cnt} \qquad (4.4)$$

Taking $\sigma_{cnt} = 3$ GPa [Ref..] for a SWNT bundle, $V_{cnt} = 2.2$ vol % and $\sigma_m = 200$ MPa for iron and $V_m = 97.8$ %, Equation 4.4 yields $\sigma_c = 206.83$ MPa, which is very close to the experimentally observed value of 205 MPa from Figure 4.17a.
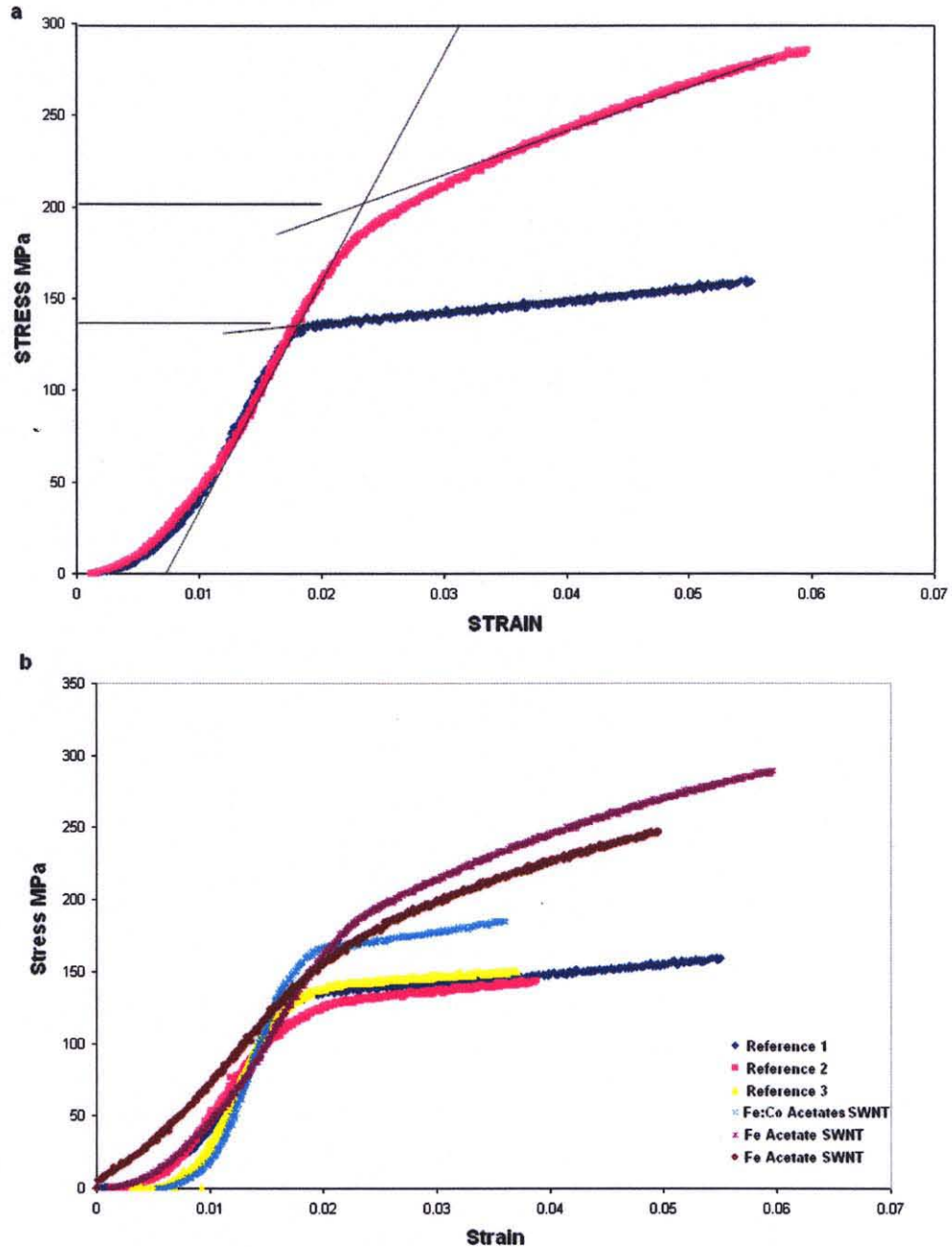
Figure 4.17 Stress versus strain curves for iron-SWNT samples made with metal acetates as catalyst precursor and iron reference samples. **(a)** Lower curve for an iron reference sample, upper curve for a sample prepared with iron acetate as catalyst precursor. **(b)** Lower three curves are for iron reference samples and the upper three curves are for iron–SWNT composite samples. The top two curves were taken from iron-SWNT composites prepared using iron acetate as the catalyst precursor, and the third curve from the top was taken from an iron-SWNT composite prepared with Co and Fe acetate precursors. Sample descriptions are also given by the color markers on the bottom right of the figure.

4.6.5 In-Situ Metal-MWNT Composites

In this section a discussion on the process parameters that influence growth of MWNTs for synthesis in iron and aluminum composites is presented. The carbon precursors used are carbon monoxide and acetylene. Catalyst precursors used are acetates and nitrates of iron, cobalt and molybdenum. The temperatures required for MWNT synthesis are relatively low and growth can be carried for longer times unlike for SWNTs. The optimization required is therefore discussed briefly and there is more focus on composite characterization and mechanical properties.

Acetylene at low partial pressures has been used for the growth of both SWNTs (Liu, 2004; Sharma & Iqbal, 2004) as well as MWNTs (Delpeux, 2002), but under the present growth conditions only MWNT formation in the metal matrix was expected. The iron-MWNT composites were prepared using acetates of cobalt and molybdenum as catalyst and promoter precursors, respectively, and a mixture of acetylene and CO diluted with argon as the carbon source at flow rates ranging from 6 to 300 standard cubic centimeters (sccm). A representative micro-Raman spectrum of composites with nanotubes grown *in-situ* from acetylene or acetylene and CO, in both cases diluted with argon are shown in Figure 4.18 a-b, respectively. The spectrum does not show the relatively sharp RBM lines that are indicative of SWNTs. The features at 1323 cm^{-1} and 1581 cm^{-1} for samples prepared with acetylene-CO and at 1332 cm^{-1} and 1583 cm^{-1} for samples prepared with acetylene alone represent the disordered (D) carbon and graphite (G) peaks, respectively, suggesting the formation of primarily MWNTs. Also, in the tangential mode frequency region spectral features near 1590 cm^{-1} associated with the rolling up of a single grapheme sheet are not observed, indicating the absence of SWNTs

in a majority the sample. The Raman spectra therefore suggest the formation of MWNTs, although the presence of small amounts of SWNTs in the composite cannot be ruled out since very weak scattering in the RBM region is evident in Figure 4.18. Growth of iron carbide also takes place when acetylene is used as the carbon feed – this aspect will be covered in more detail later in the discussion of the XRD results. The line widths of the D and G bands and the D/G ratios are related to the crystallinity of the carbon phases formed. The D/G ratio in the case of iron carbide formation is higher with broader G bands. The intensity of the D peak depends on in-plane carbon atom displacements, which leads to a loss of the hexagonal symmetry of the two- dimensional graphene planes. From Figure 4.18a D/G = 0.579 and from Figure 4.18b D/G = 0.247. It can also be seen that the G lines are relatively narrow and the D line is reduced in intensity with the introduction of CO mixed with acetylene (D/G = 0.247). In addition, for iron carbide to be a major component, the D/G ratio should be of the order of 1.5 according to observations in most coke formations (Zeng, 2002). This suggests that even with an acetylene feed where D/G = 0.579, the formation of iron carbide is partial and most of the carbon atoms form MWNTs. This observation was confirmed by SEM images discussed below. However, XRD data show characteristic iron carbide peaks for such samples.
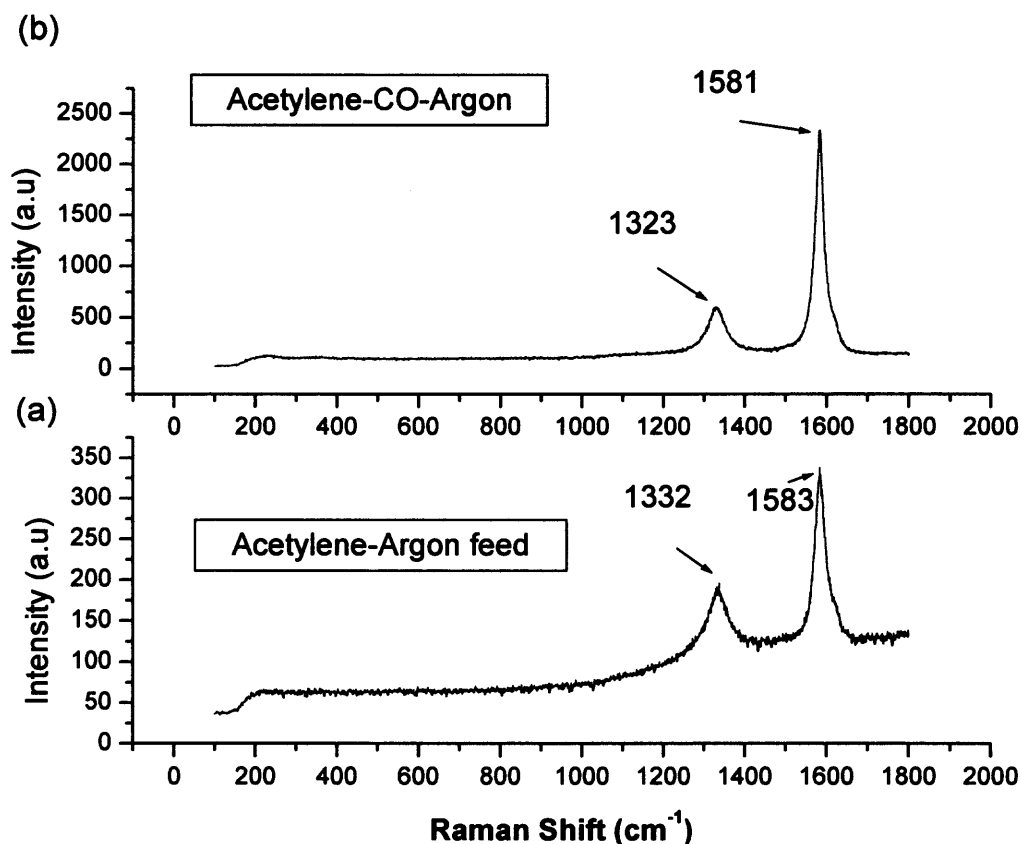
Figure 4.18 Raman spectra of composites fabricated at 800 °C using (a) acetylene and argon, (b) acetylene-CO mixed with argon. Cobalt and molybdenum acetate are used as catalyst and promoter precursors in the starting iron matrices.

FE-SEM images are consistent with largely MWNT formation and the images shown in Figure 4.19 a-b indicate somewhat denser growth of MWNTs in the iron matrix. FE-SEMs were obtained from the cross-section of a piece cut from an iron-MWNT composite and examined for evidence of infiltration of the nanotubes deep inside the porous metal matrix. Figure 4.19c depicts a low magnification image showing sizable MWNT penetration to a depth of 150 to 160 μm. A lower concentration of nanotubes is evident below 160 μm and through the approximately 0.5 mm thickness of

the piece. A high magnification image taken from a region about 160 μm from the top surface of the composite showing dense growth of MWNTs is displayed in Figure 4.19d. Measured weight changes indicate a MWNT loading of up to 1 weight % in the optimized iron-MWNT composites, which is similar to that obtained for the iron-SWNT composites. However, up to 5 weight % MWNTs can be grown using iron matrices of smaller piece density prepared at lower pelletization pressures. These pellets can be subsequently consolidated to higher densities by hot isostatic pressing techniques for use in structural and related applications.
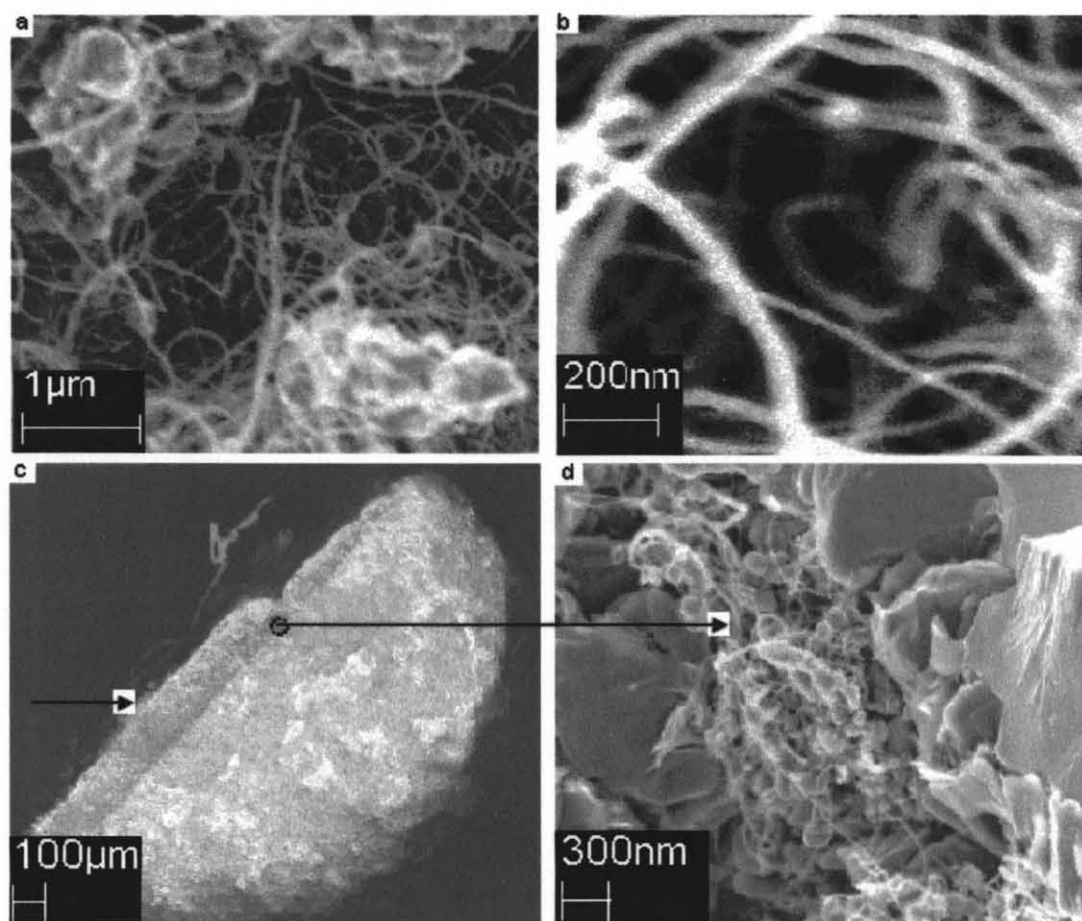
Figure 4.19 (a) Image showing dense growth of MWNTs on composite prepared using acetylene mixed with CO in argon as the carbon source. **(b)** Higher magnification image showing MWNTs in a dense network within interstitial spaces of the iron matrix. **(c),** Low magnification cross sectional view of a piece from an iron-MWNT composite. The

edge of the top surface of the composite (arrow) is on the left side of the image. Dark-grey regions show penetration of carbon nanotubes down to 150-160 μm. Somewhat lighter regions can be seen further down inside the matrix. **(d)** Higher magnification image taken from the circled region of the image in panel (c) showing extensive growth of nanotubes.

Vickers hardness measurements of the iron-MWNT composites showed enhancement in average hardness by 180% for an iron-MWNT composite prepared with acetylene and argon (Table 4.5), but the XRD pattern from this sample clearly showed the presence of iron carbide (Fe_3C) (Figure 4.20). The composite prepared by combining CO with acetylene, however, showed an enhancement in hardness by 97.5%, substantially higher than that of a similarly loaded iron-SWNT composite (Goyal, 2006) with no evidence for Fe_3C phase formation from XRD measurements (Figure 4.20), clearly indicating that the hardness increase is entirely due to nanotube infiltration. MWNTs formed in the iron-MWNT composites appear to be longer than the corresponding SWNTs in the iron-SWNT composites and may therefore provide more efficient and therefore stronger interparticle bridging than the SWNTs.

In order to understand why iron carbides are not formed when acetylene is mixed with CO, we propose the following sequence of reactions during *in-situ* growth with acetylene. The Fe_3C impurity phase is formed by reaction 1 below:

$$3Fe_2O_3 + 8H_2 + C_2H_2 \rightarrow 2Fe_3C + 9H_2O \tag{1}$$
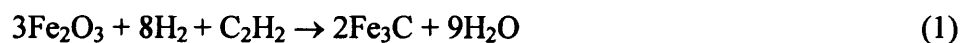
It involves the reduction of Fe_2O_3 present in the iron matrix by hydrogen (formed by the initial dissociation of acetylene) followed by adsorption of carbon from acetylene decomposition. The dissociation of acetylene is further enhanced by the presence of iron as catalyst. Iron is supersaturated with carbon and leads to the formation of iron carbide. However, this phase is unstable at high temperatures and decomposes to iron and

amorphous or disordered carbon soot. Introducing CO initiates occurrence of concurrent reactions 2 and 3 below. The presence of CO results in the formation of carbon nanotubes and CO_2 following the disproportionation reaction 2 in presence of catalysts and reaction 3. In addition to that, reaction 3 scavenges hydrogen to form carbon nanotubes and prevents the reduction of Fe_2O_3 to Fe_3C via reaction 1.

$$2CO \rightarrow C + CO_2 \tag{2}$$

$$CO + H_2 \rightarrow C + H_2O \tag{3}$$
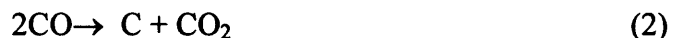
The above reaction sequence is consistent with the XRD data, which shows no evidence for the formation of the Fe_3C phase when CO is introduced into the carbon precursor feed. Figure 4.20 a-b show XRD patterns for composites made using acetylene and argon, and a mixture of acetylene, CO and argon, respectively. Further confirmation that the phase is Fe_3C is shown by the fact that a composite containing this phase is decomposed to Fe by heat treatment in hydrogen at 850°C for 2 hours (Park, 2001) (Figure 4.20c). Furthermore, the XRD data for the composites also do not show the presence of austentite and martensite carbide structures, which would show reflections at 2θ values of 41, 47 and 63 degrees due to austenite and values of 44, 51 and 82 degrees due to martensite, respectively (De, 2004). The formation of austenite by carburizing gases generally occurs in the temperature range of 850-950 °C where the high solubility of carbon at such temperatures results in the formation of a stable crystal structure. The presence of the austenite phase increases the hardness of metals because the structure comprises of a low carbon core and outer layers with high carbon content. Thus it is important to differentiate between various phases formed during nanotube growth in metal matrices. The temperature used for nanotube growth is therefore chosen to be 800

°C which is substantially lower the austenite forming temperature. Martensite, which is a very hard but brittle phase, is formed during quenching of metal pellets containing the austenite phase. The crystal structures of martensite and austenite are different and thus it is easy to determine the relative amounts of each phase from XRD data.
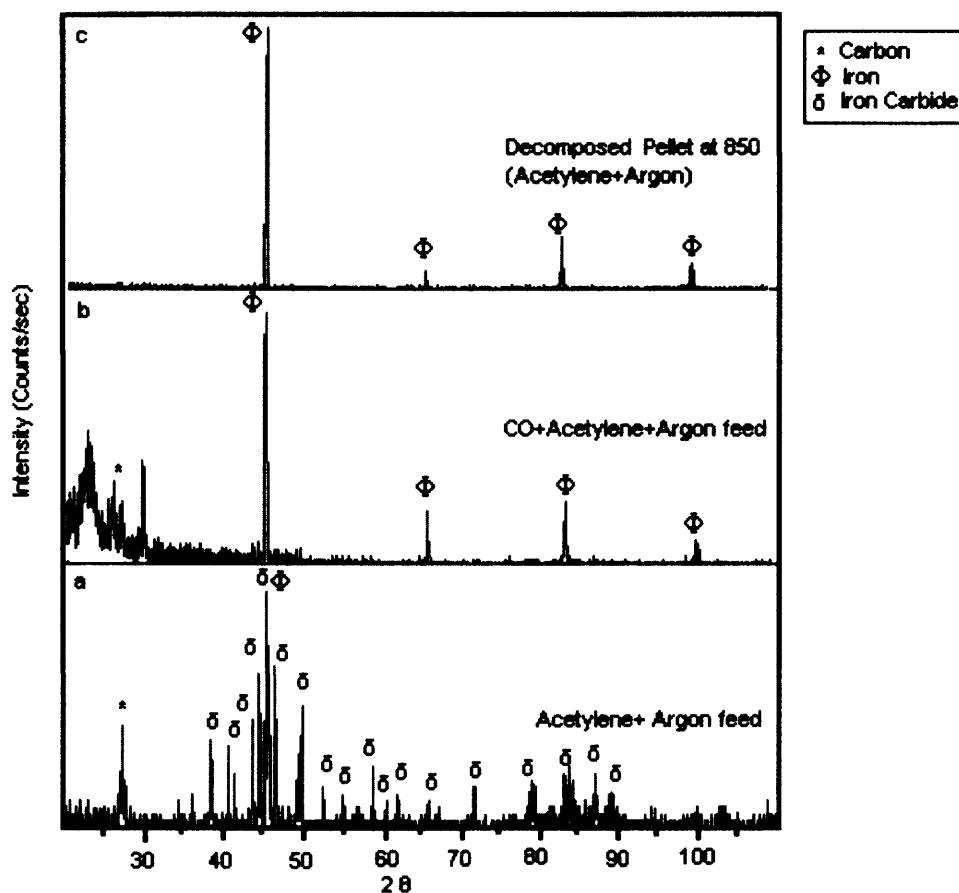
Figure 4.20 X-Ray diffraction (XRD) patterns using Cu-Kα radiation with wavelength λ = 1.5405 Å from various iron-MWNT composites. **a)** XRD from composite prepared using an acetylene-argon feed shows reflections indicating formation of iron carbide phase. **b)** XRD from iron-MWNT composite prepared using a carbon source comprising of CO and acetylene mixed with argon, which shows only carbon and iron peaks. **c)** XRD from iron-MWNT composite containing Fe₃C heat treated at 850°C for 2 hrs in hydrogen shows decomposition of the carbide phase. Only iron reflections are clearly evident in the diffraction pattern.

Table 4.5 Vickers Hardness Values for MWNT-Iron Composites

Sample Description	HV/10 numbers	SI units (MPa) (HV/10 × 9.807)	% Change	Comments
All the samples below are treated at 800 °C, with the same heat treatment time cycles.				
Annealed Reference pellet	77.6	761.0		Control sample
Acetylene-Argon feed	217.6	2134.3	180.4	Iron carbide formed as shown by XRD
CO-Acetylene-Argon feed (4.48 vol % MWNTs)	153.3	1503.1	97.5	No iron carbide formed; confirmed by XRD

Compression test measurements performed on iron-MWNT composites show similar yield stress enhancement as in the case of iron-SWNT composites. The increase in upper and lower yield strength is 36 and 43%, respectively as shown in Figure 4.21. The lower yield point for the reference sample is at 179 MPa and for the iron-MWNT sample it is at 255 MPa. The upper yield point for the reference sample is at 200 MPa and at 276 MPa for the iron-MWNT composite. The observed increase in strength of the iron-nanotube composites can be attributed to the mechanical support provided to the cavities by the carbon nanotubes. The theoretical values predicted by the rule of mixtures (Callister, 2003) fit well with the experimental data. The theoretically predicted upper yield point using the rule of mixtures (Equation 4.3) is 283 MPa which is in good agreement with the observed value of 276 MPa.
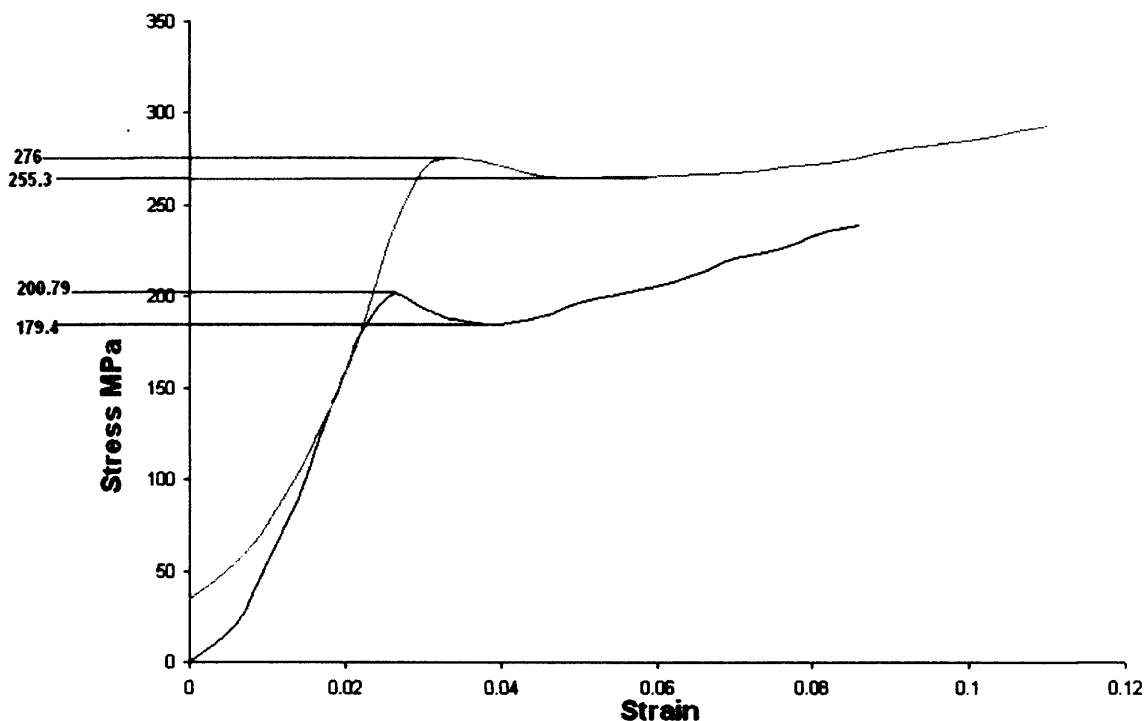
Figure 4.21 Stress versus strain plots for iron-MWNT composite sample prepared with cobalt-molybdenum acetate as catalyst precursor (top curve) and iron reference sample (lower curve).

4.6.6 Aluminum-MWNT Composites

A preliminary study was performed with aluminum as the metal matrix to confirm the results for mechanical property enhancement in iron due to pinning of nanotubes. In addition, aluminum is a widely used metal in the aerospace and defense industry and there is an emerging need to obtain aluminum composites with enhanced mechanical properties. In this section a discussion on the effect of the particle size on aluminum pellet formation and the results on composites fabricated with aluminum alloys, containing small amounts of iron which can function as catalyst for nanotube growth are presented.

The catalyst preparation methods are the same as those used for SWNT growth and discussed in Section 4.4.1. The melting point for aluminum is 650 °C and this limited

us only to the synthesis of MWNTs, the temperatures required for SWNTs by thermal chemical vapor deposition are in the range of 700°-950 °C. Therefore nanotube synthesis in aluminum to form aluminum-nanotube composites was carried out at 600 °C.

Initially a passivated aluminum nanosized particles obtained from ARDEC, Picatinny Arsenal were used, the particle size range was observed using SEM (Figure 4.24) and it was found to be uniformly between 60-80 nm. The powder was soaked in catalyst solution and dried overnight and formed into pellets with an applied load of 4 metric tons. XRD data (Figure 4.22 a-b) showed that the powder consisted of pure aluminum.
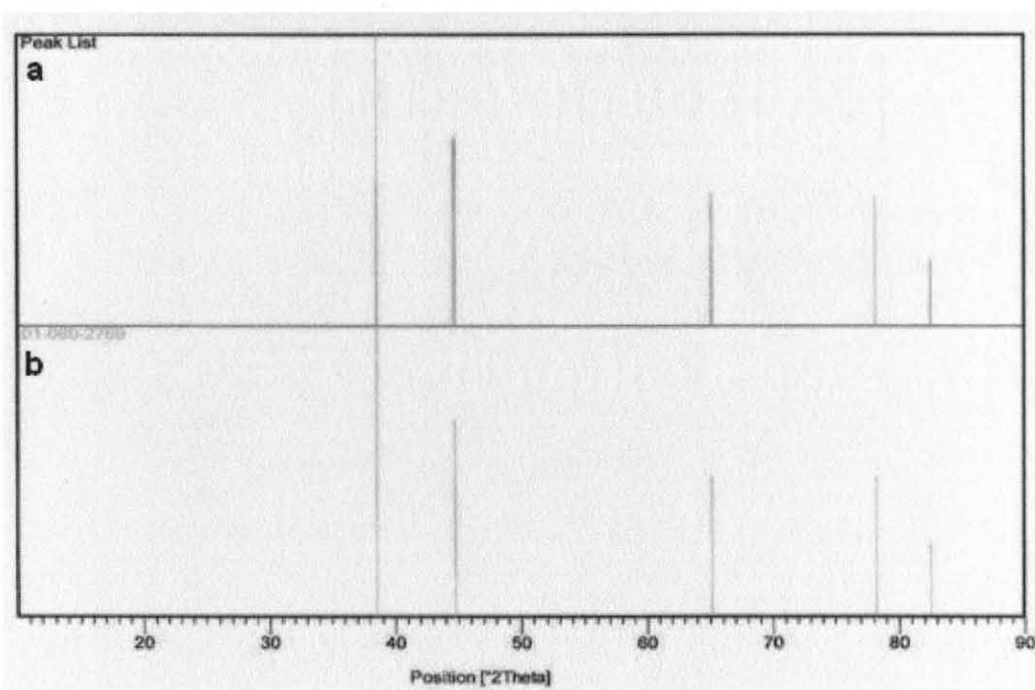
Figure 4.22 XRD diffractograms a) peak list from aluminum nanosized powder, b) pure aluminum reference peak list from XRD data base (01-089-2769).

Three types of experiments were performed in this study, first using above-mentioned aluminum nanosized powder, second using mixture of aluminum nanosized powder and

325 (~20 µm) mesh aluminum particles and third using aluminum alloy 1060 with a composition of 99.8 % Al containing 0.10 % Fe with an average particle size of 16.5 µm.

Using the experience gained from the synthesis of iron-MWNT composites, we first synthesized nanotubes with acetylene diluted with an argon gas feed. Significant amounts of MWNTs were formed as evident from the Raman data (Figure 4.23 a) and SEM images (Figure 4.24). The XRD results (Figure 4.25) on this sample, however, showed the formation of aluminum carbide. The D/G ratio from Raman also indicates higher values confirming this observation as discussed above for the iron-MWNT composite containing iron carbide.

Therefore, CO mixed with acetylene and diluted with argon was used. No carbide formation was observed in the XRD pattern and lower D/G ratios were seen in the Raman spectra (Figure 4.23 b-d). These results also confirm the reaction mechanism proposed in the earlier (Section 4.6.5) involving the formation of the nanotube phase with elimination of the carbide phase. However, one must note that the yield of MWNTs does not increase significantly by changing the carbon precursor feeds.
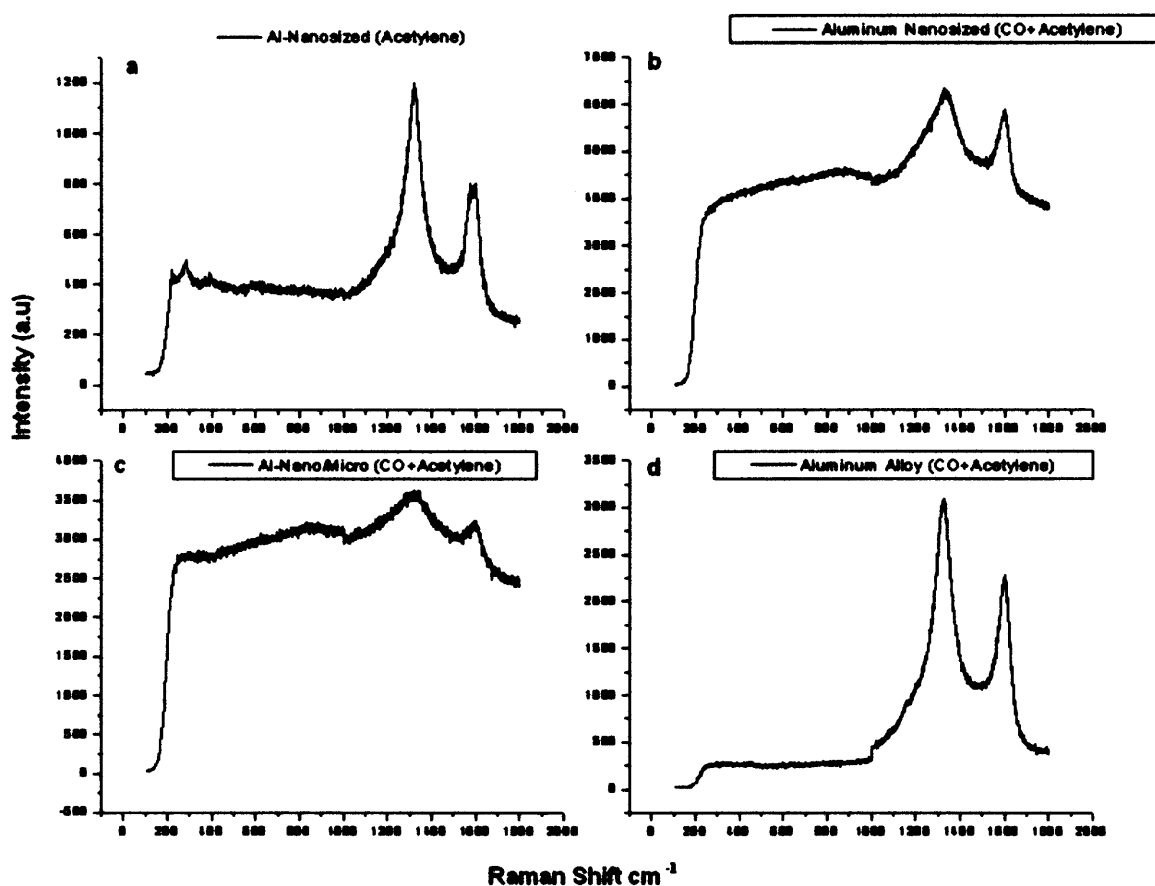
Figure 4.23 Raman spectra from Al-MWNT samples a) Al-nanosized using acetylene-argon feed, b) Al-nanosized using CO-acetylene and argon feed, c) Al-nano- and micron-sized mixed powders with CO-acetylene and argon feed, d) aluminum alloy 1060 with CO-acetylene and argon feed.
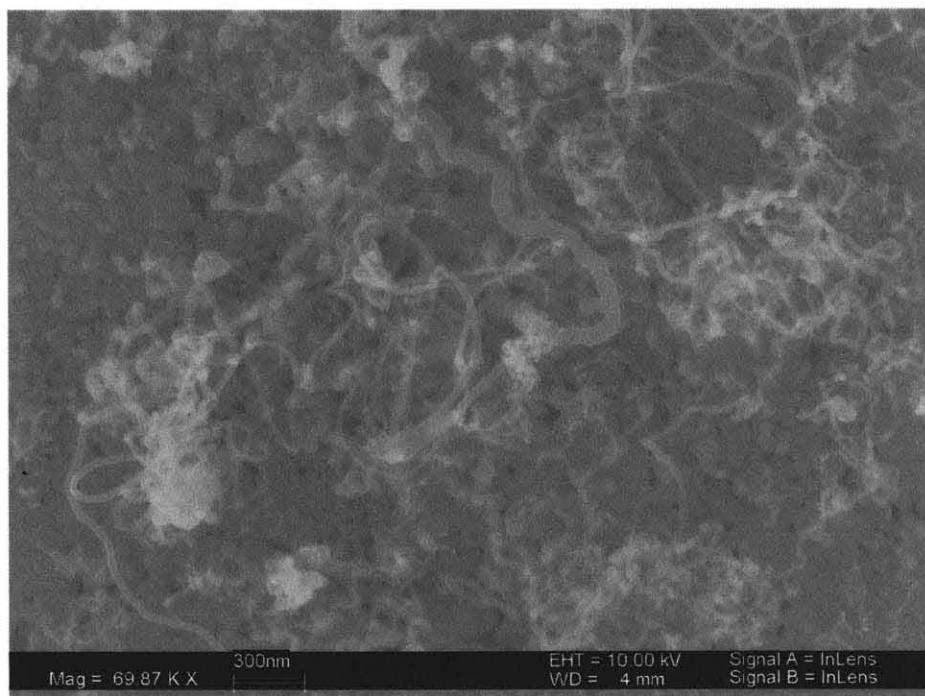
Figure 4.24 SEM image from surface of Al-nanosized powder-MWNT composite.
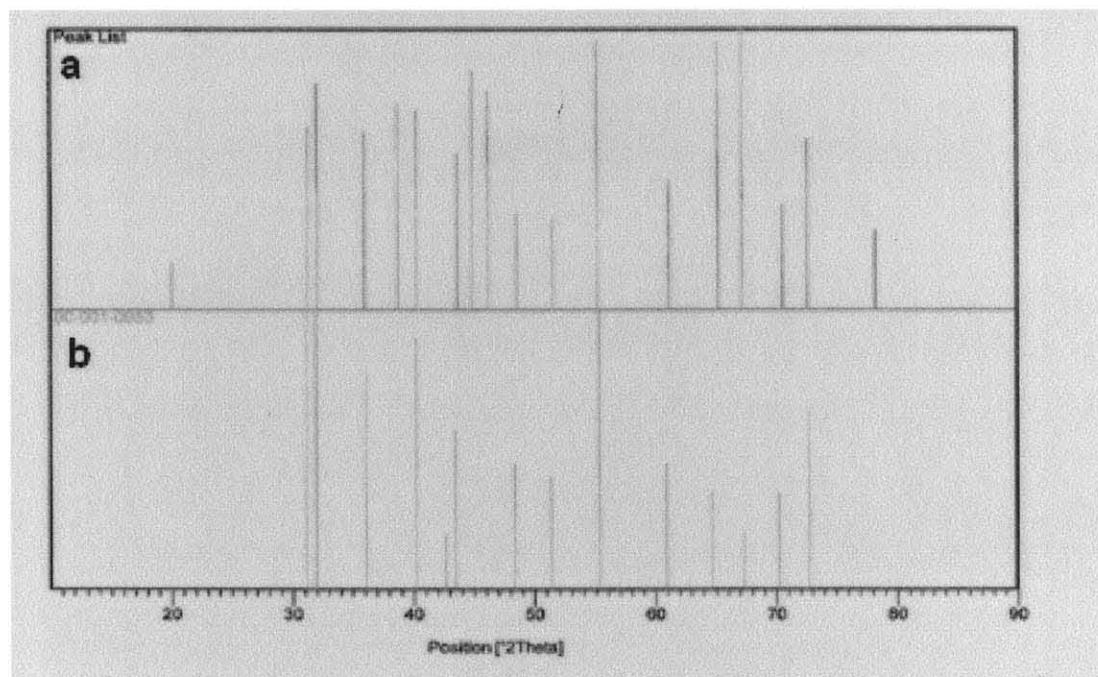
Figure 4.25 XRD patterns of: a) Al-nanosized powder sample after MWNT synthesis, and b) Aluminum carbide peaks from reference XRD data base (00-001-0953).

After the initial results for carbide formation using an acetylene feed, CO-acetylene feeds were used for all the subsequent experiments. In the above experiments it was observed that the formation of pellets using Al powder with nanosize was very difficult. The pellets would fragment into many pieces as soon as they were taken out of the die and could therefore not be used for mechanical property measurements, such as compression tests. Therefore two size distributions of aluminum powders were used to form pellets. 1.5 gms of 20 μm size aluminum powder was mixed with 0.100 gms of 60-80 nm sized powder to fill the die and compressed at 4 MT. These pellets showed improved consolidation and only broke into two pieces. One piece was therefore used as reference and the other piece for nanotube infiltration. From the Raman spectra shown in Figure 4.23 c it can be noticed that both the D and G peak indicating formation of amorphous carbon along with graphitic carbon are present. The D/G ratio is of the order of 1.12 which is lower than 1.5, which is usually the case when iron carbide is formed. Figure 4.26 a- b show representative SEM images obtained from the surface of the pellet before and after nanotube synthesis. From the images it can be clearly observed that there is a mixture of two particle sizes and that the nanotubes emerge from the particles of smaller size containing small amounts of iron-cobalt catalyst obtained from the acetate precursors added before synthesis. Representative XRD patterns from these samples are shown in Figure 4.27 a-c. The diffraction pattern in Fig 4.27a shows the diffraction peaks from the composite sample after nanotube synthesis which can be compared with those for pure aluminum in Figure 4.27b and for aluminum carbide in Figure 4.27c. It can be clearly observed that the aluminum phase remains unchanged after nanotube synthesis and there no evidence for the presence of aluminum carbide phase.
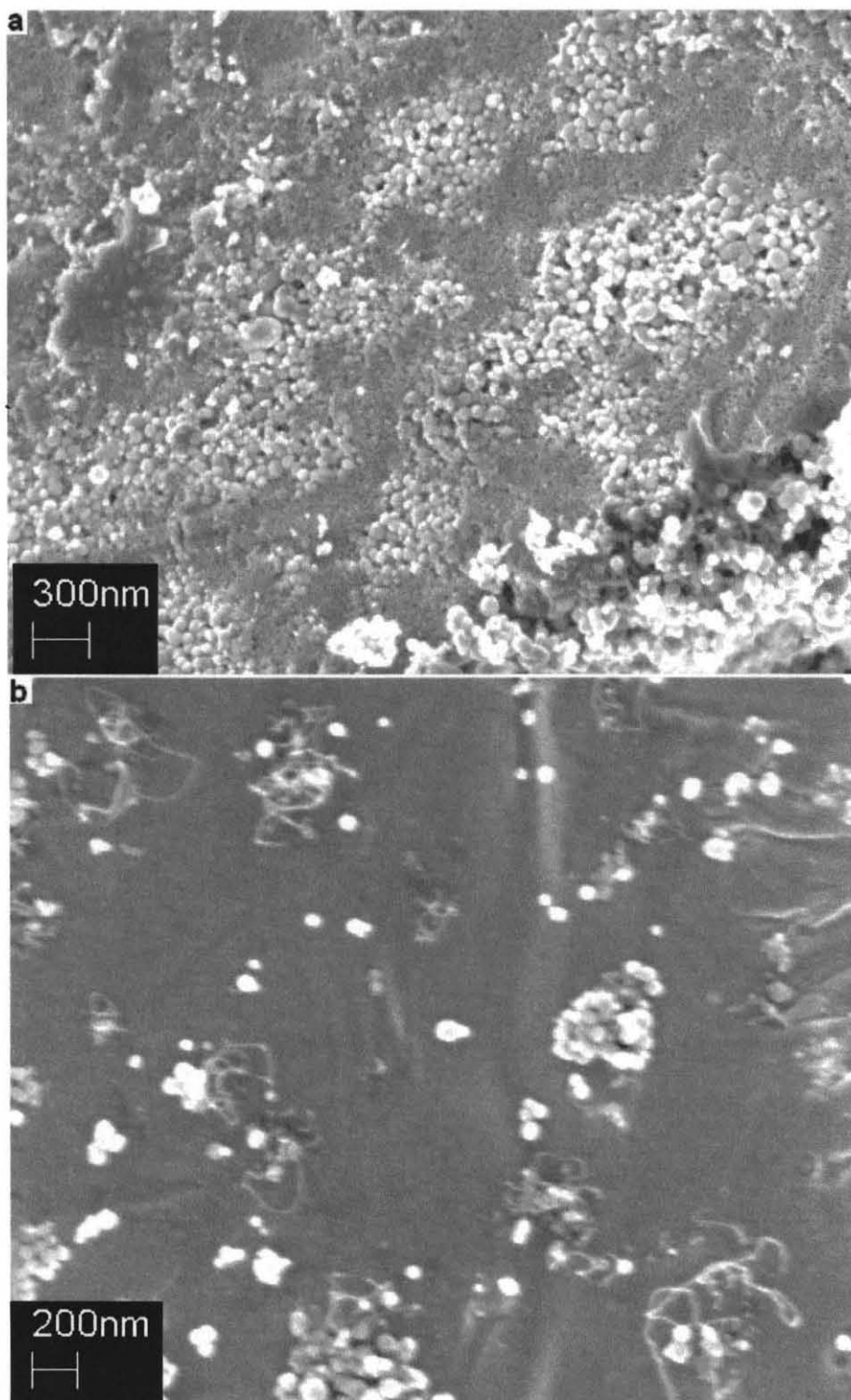
Figure 4.26 SEM images taken from the surface of nano- and micron-sized mixed aluminum powders: a) before MWNT synthesis and infiltration, and b) after MWNT synthesis and infiltration. It can be noticed from image (b) that the formation of nanotubes is from the smaller aluminum particles. The size distribution of the aluminum particles is clearly evident in image (a).
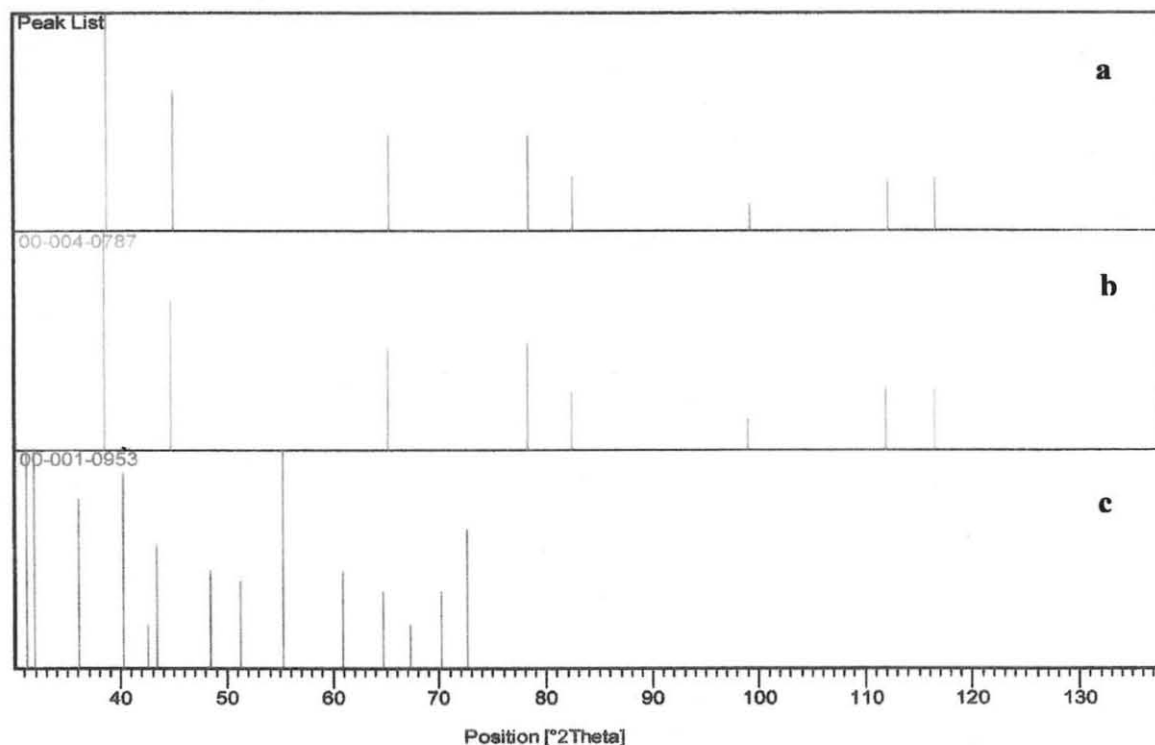
Figure 4.27 XRD line positions from sample surface and from databases. (a) Composite sample surface fabricated with aluminum nano- and micron- sized powders after MWNT synthesis, b) Peak positions for aluminum taken from XRD database (00-004-0787), and c) Peak position for aluminum carbide taken from XRD database (00-001-0953). It can be clearly observed that in (a) the aluminum phase is unchanged after nanotube synthesis and no carbide formation has occurred.

Vickers hardness measurements were carried out to see the change in hardness for all the samples relative to the control samples. A list of hardness numbers is shown in Table 4.6. In the case of composites prepared with aluminum nanosized powders, the increase in hardness is very large because of aluminum carbide formation. This is analogous to results obtained for iron-MWNT composites. The increase in hardness that occurs due to formation of MWNTs with no carbides present as indicated by XRD results is 67.32%. We could not use these pellets any further for compression tests due to fragmentation. We report the hardness numbers and compression tests on pellets prepared using aluminum powders with two particle sizes (Table 4.6). The compression data showed

(Figure 4.28) that the yield point is substantially decreased relative to that of the reference sample probably due to the absence of bonding of the MWNTs with the aluminum matrix, although the slope of the stress vs strain curve which corresponds to the Young's modulus increases with MWNT loading. Further mechanical property measurements on an aluminum alloy containing a small fraction of iron to provide pinning sites for the nanotubes therefore needs to be performed to understand the behavior of aluminum-MWNT composites.

With this goal in mind, aluminum-iron alloy-MWNT composites without carbide formation have been prepared and their Vickers hardness numbers measured. These numbers given in Table 4.6 show an increase in hardness of the composites by 58.70% relative to a pure aluminum alloy reference sample. This increase in hardness is, however, similar to that observed for a pure nano-sized aluminum matrix with in-situ grown MWNTs, although uniform and dense growth of nanotubes is evident from the SEM images (Figure 4.29). In order to obtain enhanced yield strength in aluminum-nanotube composites it may therefore be necessary to use alloys with higher concentration of iron pinning sites.
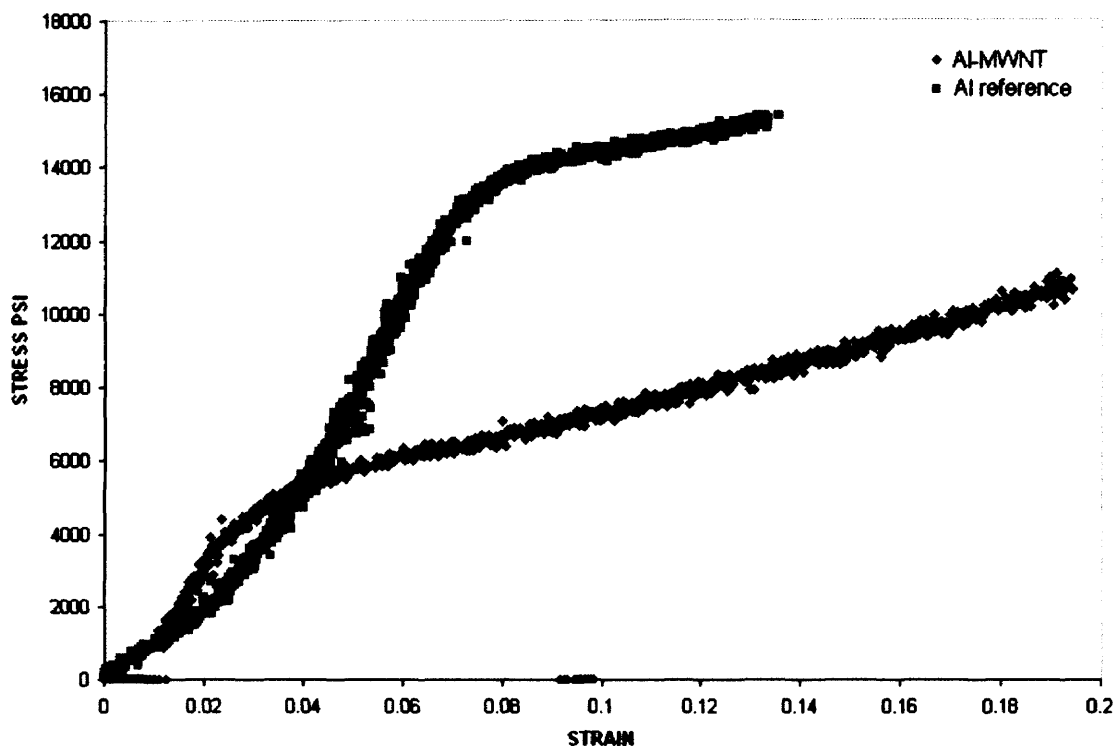
Figure 4.28 Stress versus strain curves for Al-MWNT samples made with metal acetates as catalyst precursor and Al reference samples. Lower curve for an Al-MWNT sample prepared with cobalt-molybdenum acetate as catalyst precursor, upper curve for an Al reference sample.

Table 4.6 Vickers Hardness Numbers for Aluminum-MWNT Composites

Sample Description	HV/10 numbers	SI units (MPa) (HV/10 × 9.807)	Change	Comments
All the samples below are treated at 600 °C, with same heat treatment time cycles.				
Starting metal matrix from Aluminum nanosized powder				
Annealed reference pellet	35.74	350.50		Control sample
Acetylene-argon feed	154.27	1512.93	331.65%	aluminum carbide formed
CO-acetylene-argon feed	59.8	586.46	67.32%	No iron carbide formed; confirmed by XRD
Starting metal matrix from Aluminum nano/micron sized mixed powders				
Annealed reference pellet				Control sample
CO-acetylene-argon feed				No aluminum carbide formed; confirmed by XRD
Starting metal matrix from Aluminum alloy 1060				
Annealed reference pellet	25.22	247.33		Control sample
CO-acetylene-argon feed	40.03	392.53	58.70%	No aluminum carbide formation: confirmed by XRD
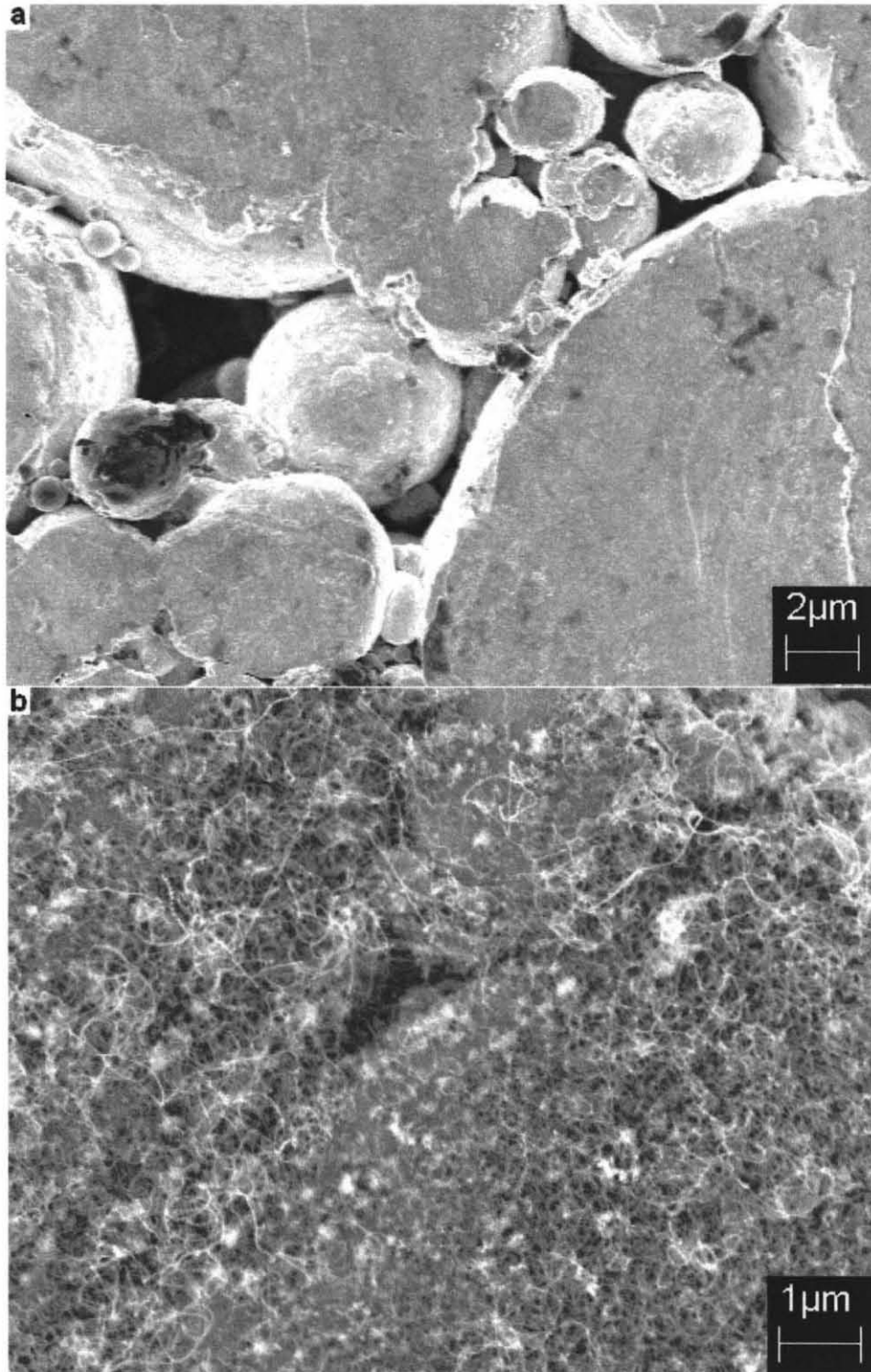
Figure 4.29 SEM images taken from: (a) The surface of aluminum alloy 1060 before MWNT synthesis, and b) After MWNT synthesis. Dense and uniform growth of MWNTs can be observed over the whole surface and inside crevices.

4.7 Conclusions

In this chapter, an *in-situ* CVD method for metal-carbon nanotube composite developed during the course of this work, is discussed. The results indicate that acetates of iron and cobalt supported on the metal matrix particles are ideal catalyst precursors for nanotube synthesis. Several other catalysts studied also indicated the formation of nanotubes, but a layer of carbonaceous material also formed on the surface of the pellets making it difficult to conduct studies of the mechanical properties of the composite formed. Characterization by XRD revealed that no other phases of iron and carbon were formed during SWNT synthesis with CO as the carbon source. MWNT synthesis with acetylene as the carbon source on the other hand resulted in the formation of an iron carbide impurity phase. By mixing acetylene with CO as the carbon source, iron carbide formation was prevented. A mechanism for the reaction involved is proposed in this chapter and confirmed by XRD measurements. Iron-SWNT and iron-MWNT composites prepared were found to have substantially enhanced compressive yield strength and hardness relative to specimens of similarly treated iron matrices without nanotubes. Increases of yield strength up to 45% and 36 % with ~ 1 wt % of infiltrated SWNTs and MWNTs, respectively, relative to that of similarly treated pure iron samples without carbon nanotubes of the same piece density was observed and Vickers hardness showed an increase of 74% and 96%, respectively. Iron being a very effective catalyst for carbon nanotube growth anchors the nanotube tips to the metal surfaces and creates supporting bridges in the cavities of the metal matrix as shown particularly by transmission electron microscopy. These bridges offset in part the weakening of the composites due to the presence of the cavities or pores in the matrix structure, resulting in higher mechanical

strength. The enhanced mechanical strength raises the possibility of using of these nanocomposites in structural and engineering applications. It is expected that further mechanical strength enhancement and weight reduction can be achieved by increased nanotube loading using a more optimized deposition process and by controlling the porosity of the iron matrix.

CHAPTER 5

CARBON NANOTUBE- BASED BIOCHEMICAL AND CHEMICAL SENSORS

5.1 Abstract

Single wall carbon nanotubes (SWNTs) have many attractive properties that can be exploited to develop the next generation of sensors. Here the use of directly grown or electrophoretically deposited carbon nanotubes to fabricate a bio-sensor or bio-probe device, and the use of pre-synthesized nanotubes in the fabrication and testing of gas sensors, are described. Vertically aligned SWNTs were grown on metal interconnects (Cr/Co), which were patterned on quartz substrates using photolithography to make electrical connections to each SWNT individually. This fabrication was conducted using processes that are also used for complementary metal oxide semiconductor (CMOS) processing. The insulating layer was comprised of silicon nitride, which is robust to the ionic liquids used in biological cell cultures. Electron-beam lithography was used to define the locations (5 nm-100 nm holes) for SWNT growth, which was performed using thermal chemical vapor deposition and electrophoretic deposition. A second application of gas sensors involved individually suspended SWNTs contacted by Cr/Au pads as source and drain field effect transistor components for the monitoring of various gases (NO_2, NH_3, CH_4, H_2, CO, CO_2, ethyl acetate, acetone vapor, and a mixture of hydrocarbon vapors, and H_2O). The adsorption of different electron donating gases on the SWNT backbone shifts the Fermi level of the p-type semiconducting nanotubes, consequently changing their electrical conductivity. Experimental results showed that sensor response to NO_2 (at 10-300 ppm levels) was in the range of a few seconds for 100 ppm, and was reversible and reproducible. Recovery of sensor response was achieved by

heating the sensors at 120 °C for a period of 10-12 hours. Reversible electrical response indicated physisorption of NO_2 molecules on the nanotube sidewalls. Other gases did not show a significant increase or decrease in the source drain current. Although a change in threshold voltage was observed for a negative gate bias, the results were not reproducible. The experiments for all the gases were conducted in dry gas (N_2 80% and O_2 20%) and humid gas (35% relative humidity) environments enabling compatibility of the sensors with real time applications, such as monitoring of low concentrations of gases in residential, industrial, medical, and automotive environments.

5.2 Overview of Nanotube-Based Sensors

Sensors are devices that detect or measure physical and chemical quantities such as pressure, temperature, concentration, pH, sound, and chemical structure-induced changes. The measurands are converted into electrical signals. A good sensor features high sensitivity, fast response, reversibility, reproducibility, low operating and manufacturing costs, and high volume production. The application of carbon nanotube as a sensing element in the sensor arises due to their inherent properties of small size, high strength, electrical conductivity, high surface area, low power consumption, and thermal stability. Carbon nanotube-based sensors have been demonstrated for pressure (Liu and Dai, 2002; Wu, 2004), flow (Ghosh, 2003), thermal (Wong and Li, 2003), gas (Kong, 2000; Modi, 2003), strain (Dharap, 2004; Li and Chou, 2004) and biological (Sotiropoulou and Chaniotakis, 2003) sensor applications. In this chapter the focus will be mainly on the fabrication of carbon nanotube-based biological sensors, and the fabrication and testing of gas sensors comprised of carbon nanotubes.

5.2.1 Carbon Nanotube Based Biological Sensors

Carbon nanotubes (CNT) have given cell biologists and biochemists a new interface for investigating cells and important organelles (Li, 2005). The biosensor applications of CNTs include: scanning probe microscope tips used to probe single cells or molecules, field effect transistor (FET) devices used to sense specific ions, porous CNT films used as electrochemical biosensors, and CNT nanoelectrode arrays as electrochemical sensors. Recent discoveries of the electromechanical properties of CNTs may lead to their use as force sensors with piconewton sensitivity (Tombler, 2000). Nanoelectrode arrays for both electrochemical and electromechanical biosensor applications are the focus of this research work. In section 5.2 it was pointed out that the intrinsic properties of carbon nanotubes make them an ideal sensing element and their use in various types of sensors was briefly highlighted. In this section we emphasize the studies that have been conducted using carbon nanotubes to form various biological sensors.

Sotiropoulou and Chaniotakis (2003) developed an amperometric biosensor using carbon nanotubes as the immobilization matrix. Aligned MWNTs were grown on a Pt substrate which also served as the transduction platform for signal monitoring as shown schematically in Figure 5.1. The MWNT arrays were purified with acids and oxidation to remove impurities and amorphous carbon, followed by immobilization of the glucose oxidase enzyme. The response and sensitivity of the sensor was found to be very high when compared to an air-treated sensor.

Pt
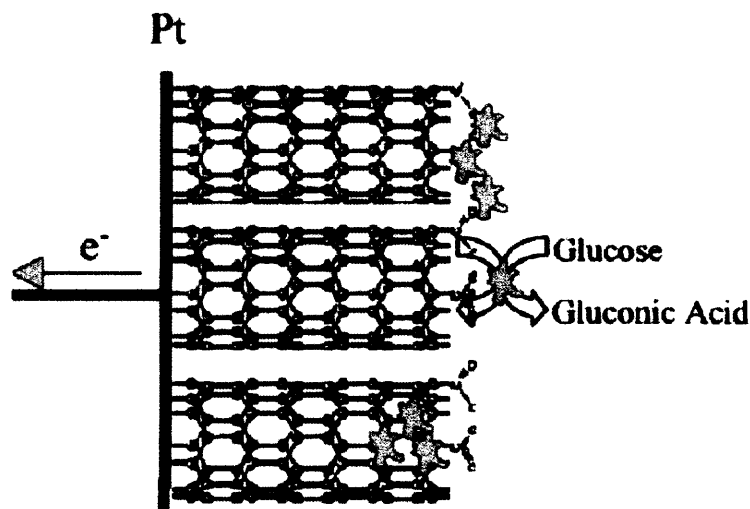
Figure 5.1 Schematic diagram of a CNT array biosensor. The enzyme immobilization allows for the direct electron transfer from the enzyme to the platinum transducer. [Source: Sotiropoulou and Chaniotakis, 2003].

Zhang and Gorski, 2005 demonstrated an electrochemical sensing platform based on the integration of redox mediators and CNTs in a polymer matrix. The incorporation of CNTs reduced the overpotential for the mediated redox process by an extra 0.30 V and reduced the response time from 70 seconds to approximately 5 seconds. This mechanism due to CNTs facilitated redox mediation in polymer matrix composite films used to study amperometric determination of $\hat{a}$-nicotinamide adenine dinucleotide (NADH). McKnight, (2003) used vertically aligned carbon nanofibers (VACNFs) grown on a Fe/Ni alloy with tungsten interconnects. VACNFs were passivated with insulating SiO_2 and the tips were exposed. The effective tip radius was calculated to be 20 nm from cyclic voltammetry measurements of 1 mM ruthenium hexamine trichloride in a 0.1 M KCl solution using Pt reference and counter electrodes. The VACNF probes were also employed to implant DNA into living cells. The cells survived the implantation and expressed the DNA in cell progeny. This study was a very important proof of several principles of intracellular

probing. However, as will be shown, the size and geometry of the VACNF (conical shaped with tip diameters of ~ 20 nm, base diameters of ~ 1 micron, and lengths of 6 – 10 microns) limit their application to biochemical and biophysical investigations involving intracellular probing.
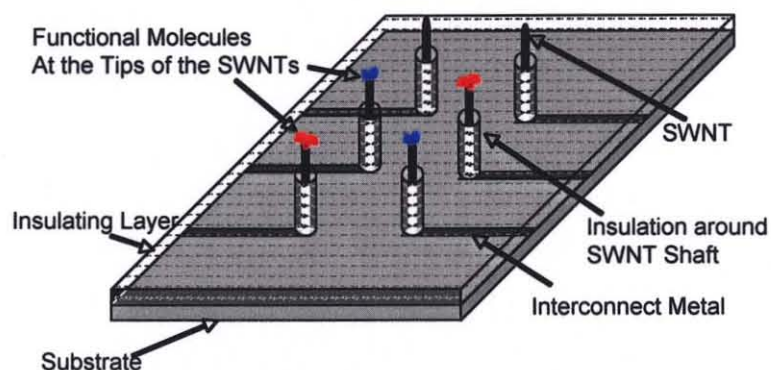
Figure 5.2 Shows a schematic drawing of a proposed SWNT array device.
[Source: Farrow, 2005, unpublished].

It consists of SWNTs grown attached to interconnects to facilitate measuring changes in their electrical characteristics. The sidewalls of the SWNT probes are passivated leaving the tips exposed to reduce the background noise and increase their electrical sensitivity. Functional molecules are bonded to the tips of the SWNTs. One variation of this device involves its use as an array of electrochemical sensors where the signal is derived from the characteristic reduction/oxidation (redox) reaction of a specific molecule in contact with one of the probes. The molecule is identified from the redox potential, which is measured from the current/voltage characteristic using cyclic voltammetry. The research conducted so far to fabricate the SWNT arrays mentioned above will be discussed below. It is important to note that such devices have broader electronic applications and their use is not just limited to biosensing devices. Graham (2004) for example has demonstrated a fabrication protocol to make vertically aligned

MWNTs (also called vias) using a process called Damscene to deposit a support metal layer (tantalum) and catalyst (Fe clusters 20 nm in size). The holes were created using focused ion beam milling to a size between 25-35 nm followed by growth of nanotubes using thermal CVD at low pressure (10 Torr) with acetylene and hydrogen as feed gases. This work made a significant contribution in realizing 3D structure transistors; however, the use of iron as catalyst and acetylene as carbon precursor limits the growth of carbon nanotubes to primarily multiwall carbon nanotubes (MWNTs). In another study by the same group (Duesberg, 2004), a process using i-line lithography to create larger holes (350-1500 nm in size) on silicon dioxide, and backfilling by depositing amorphous silicon to narrow down the holes to a size range of 20-500 nm. The holes were then filled with iron catalyst by sputtering followed by removal of excess catalyst by ion beam polishing. This study provides an alternate route to create catalyst islands in desired locations; however, once again primarily MWNTs were grown. In the third and fourth chapters of this thesis significant growth of SWNTs and MWNTs using carbon monoxide and acetylene precursors, respectively with different metal catalysts, is discussed. This experience in synthesis of SWNTs using CO and ethanol with thermal CVD will be utilized in growing nanotubes on the device structures described above. Electrophoretic deposition on device structures of pre-synthesized SWNTs using similar methods will also be discussed.

The ultimate goal was to produce an optimized CNT probe for investigating cellular signaling mechanisms with molecular sensitivity and spatial resolution on the order of nanometers. The geometry and physical properties of the CNT probe will allow it to be inserted into a living cell while maintaining cell functionality during probing.

This would not only include the electrochemical functionality but also cell motility. There would be a great technological advantage to a CNT probe array such as that shown in Figure 5.2 that cells could move over without affecting their motility while allowing the CNT probes through the plasma membrane for localized measurements of electrochemical and mechanical activity. This should be possible if the diameter of the CNT probes is of the order of the size of the phospholipids making up the cellular plasma membrane (~ 3.5 nm). Single wall carbon nanotubes would be the best choice for this application since the average diameter of an individual SWNT is ~ 1.2 nm.

The proposed SWNT probe could monitor the near-membrane intracellular signaling events (voltage, $[Ca^{2+}]$, enzymatic activity). It is, therefore, a very promising device with a multitude of applications in physiology/biophysics, cell signaling, pharmacology, neuroscience and other areas that study various forms of the interface between extracellular and intracellular signaling. Many cellular processes that are important for normal physiology occur in the vicinity of the plasma membrane. A large body of research is aimed at the coupling of electrical trans-membrane signals to intracellular events, which include important research areas such as, excitation-contraction coupling and excitation-secretion coupling. Measurement of voltage between the tip of a single SWNT electrode and the extracellular space could be very useful, especially if it could be done with nanometer spatial resolution. Previously, distribution of trans-membrane potential was simplistically inferred via theoretical modeling (Goldman, 1943; Hodgkin, 1949; Eisenberg, 2003) or calculated from molecular dynamics of membranes and channels (Roux, 1999; Jiang, 2002; Barreiro, 2003; Allen, 2004). Direct and simple measurements of voltage near functional channels have not

be therefore of great interest. The SWNT nanoprobe will permit direct measurements of charges on membrane surfaces and investigate how trans-membrane potentials change at a near-molecular scale.

5.3 Fabrication: Results and Discussions

For successful manufacturing of a MEMS/NEMS device, the fabrication process involves design, characterization, and preliminary tests. The use of new materials and device concept results in process adjustments from the existing silicon techniques and are indispensable. The use of carbon nanotubes in a vertical alignment to use as probes or as field effect transistors especially on quartz substrate has not been previously demonstrated. Many of the process steps involved in past research work had, therefore, to be modified. By means of test experiments each step is determined and well characterized.

In following section detailed studies on fabrication steps of the various layers are considered. A detailed explanation of the final working procedure is presented in the Appendix B.

Fabrication Details The development of the process steps can be divided according to the number of layers that were laid down. The following section is designed accordingly; each layer will be discussed and it's processing in detail with materials involved and challenges faced. The complete flow schematic for such a process proposed by Farrow (2005) is shown in Figure 5.3. The work presented here is limited to "Step n" shown in the process flow schematic. Following this, each sub-section will be discussed for one or

two sub-parts of the full process flow diagram. Deviation from the proposed flow diagram will also be addressed. The CNT array previously shown schematically in Figure 5.2 corresponds to the configuration shown in "Step o" (Figure 5.3). The lay out of the metal pattern and the location for nanotube deposition is shown in Figure 5.4
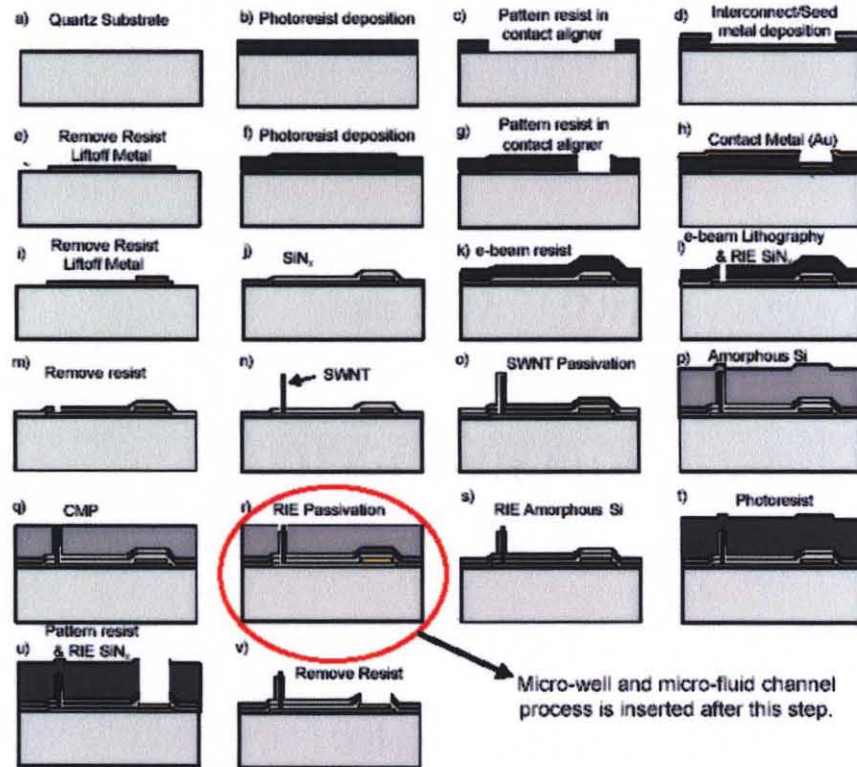
Figure 5.3 Process flow for biosensor device with carbon nanotubes as probes. [Source: Farrow (2005)].

Sites for nanotubes
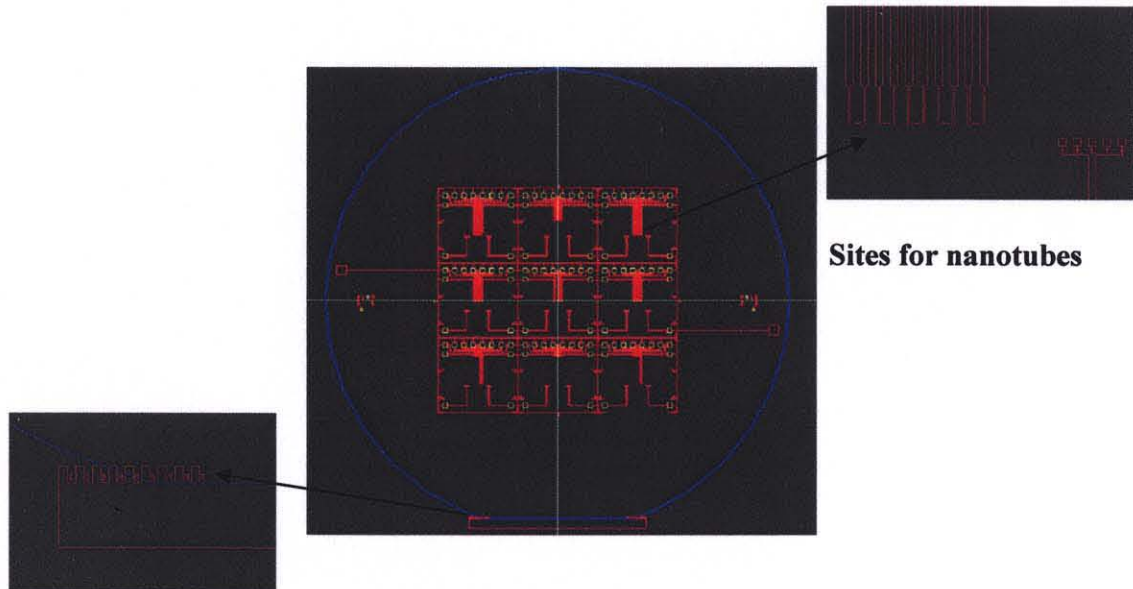
**4 inch Wafer with 9 cells
each of 14 mm X 17 mm**

Figure 5.4 Lay out of the proposed metal pattern, alignment markers, and the site for nanotube growth.

Steps a and b: Choice of Substrate and Photoresist Deposition. Quartz wafers of 100 mm diameter and 350 μm thickness were used. The quartz substrate was chosen to enable the investigation of cells from the back side using optical microscopy. Since most of the processes for photolithography were developed for silicon substrates, the process steps involved had to be modified. A standard process for cleaning wafers before deposition of resist involves rinsing of the wafers with acetone for 10 minutes, followed by rinsing with isopropyl alcohol for 10 minutes and thoroughly rinsing with de-ionized (DI) water and drying in nitrogen. The wafers are then baked at 120 °C for 10-20 minutes to remove moisture before coating with an adhesive layer of hexamethyl disilane (HMDS) – a step that is also known as wafer priming. However, initial experiments conducted using a similar protocol resulted in weak or no adhesion of photoresist on top of the HMDS prime layer. This will be discussed in more detail after consideration of the metal deposition Step e. The reason is that the quartz surface has residual adsorbed water. The

HMDS layer therefore reacts with the hydrogen atoms in the water layer and does not form the adhesive layer required for uniform photoresist deposition. There are two ways to overcome this: firstly by vapor priming, and secondly by Pirhana cleaning (P clean). P clean processing was carried out with a mixture of sulfuric acid and hydrogen peroxide at a temperature of 67 °C followed by rinsing with running DI water at the same temperature and then with running DI water at room temperature. All the steps were carried out for 5 minutes each. The P clean step requires additional safety precautions, such as the use of neoprene gloves, face shield, and an extra gown on top of the clean room lab coat. The wafers were dried by blowing N_2 and baked at 120 °C for 30 minutes to remove the moisture. The results for this protocol showed perfect adhesion of HMDS as evident after the liftoff process (Step e). HMDS was coated using a spin coater at a speed of 1200 rpm for 40 seconds with an acceleration of 500 rpm/sec.

Step b: Photoresist deposition. The wafer as discussed above has a coating of HMDS before depositing photoresist. One of the desired features for a good photoresist is its uniformity. Shipley 1813 photoresist, which is a liquid polyimide photosensitive polymer, was used. The liquid was spun onto the wafer, forming a thin sheet, and then cured in an oven to form a resistant plastic coating. Four different recipes were used to obtain the desired photoresist layer. The spin speed versus film thickness plots for dyed Shipley 1800 series resists are shown in Figure 5.5.
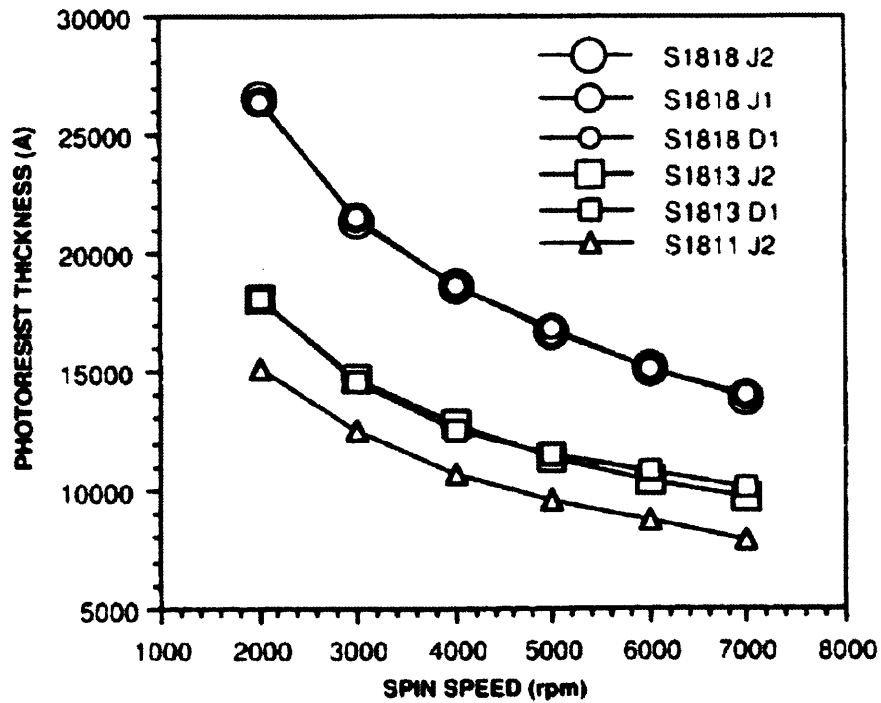
Figure 5.5 Photoresist thickness versus spin speed curves for Shipley 1800 series photoresists.

The recipes used for the photoresist layers were:

Recipe 1:
- HMDS 2000 rpm for 40 sec with acceleration of 500 rpm/sec
- S1813 4000 rpm for 60 sec with acceleration of 500 rpm/sec
- Softbake at 110 °C for 2 min on a hot plate
- Exposure 10 mW/cm^2 for 20 sec

Recipe 2:
- HMDS 1200 rpm for 40 sec with acceleration of 500 rpm/sec
- S1813 3500 rpm for 30 sec with acceleration of 500 rpm/sec
- Softbake at 110 °C for 2 min on a hot plate
- Exposure 10 mW/cm^2 for 25 sec

Recipe 3:
- HMDS 1200 rpm for 40 sec with acceleration of 500 rpm/sec
- S1813 3500 rpm for 30 sec with acceleration of 500 rpm/sec
- Softbake at 90 °C for 10 min in an oven
- Cold plate for 60 sec
- Second layer of S1813 5000 rpm for 30 sec with acceleration of 500 rpm/sec

- Second softbake at 90 °C for 2 min in an oven
- Cold plate for 30 sec
- Exposure of 10 mW/cm^2 for 35 sec

Recipe 3a
- Same as recipe 3 with exception of exposure time of 30 sec

Recipe 3b
- Same as recipe 3 with exception of exposure time of 27 sec

Recipe 4
- HMDS 1200 rpm for 40 sec with acceleration of 500 rpm/sec
- S1813 3500 rpm for 30 sec with acceleration of 500 rpm/sec
- Softbake at 90 °C for 10 min in an oven
- Exposure of 10 mW/cm^2 for 20 sec

The following briefly describes observations made to make changes in the parameters of the recipes mentioned above: The HMDS layer deposited with a spin speed of 2000 rpm and S1813 with a spin speed of 4000 rpm for 60 sec did not yield good adhesion. This was observed when the wafer was developed using MF-319 standard developer for 60 seconds. Therefore, in the second recipe both the spin speed for HMDS and S1813 was reduced to get thicker layers and the softbake protocol was kept the same in order to observe changes due to the thicker coatings. The wafers were given longer exposures because after the first process the whole photoresist was washed off due to under-exposure. Under-exposure results in a thin layer of photoresist remaining at the bottom, which is soluble in acetone and can lead to complete removal of the photoresist layer at the time of liftoff of the metal. However, this did not solve the problem and on development the pattern was still uneven and had broken edges when observed under an optical microscope. In recipe 3 a two-layer photoresist process was studied with the goal of obtaining a better undercut as shown in Figure 5.6. The undercut is required to have a good metal layer on the substrate. In the two-layer process, first layer using the same

protocol as above is deposited followed by deposition of a second thinner layer of photoresist. Since in this process the first layer is soft-baked at 90 °C for a total of 12 minutes (10 + 2 minutes in two soft-bake steps; also see recipe 3 above for a better understanding of the process), the photosensitivities of these two layers are different. The top layer is less sensitive to light than the bottom layer. These results in an inclined profile referred to as the undercut in CMOS processes. Since the thickness of the resist is now much higher compared to that for the resist from the one layer process, the exposure time was increased to 35 sec for recipe 3 and to 30 and 27 seconds, respectively (dose focus experiments) in recipes 3a and 3b. However, these process modifications did not yield a good resist pattern and the process steps involved increased. It was therefore necessary to revert back to the one photoresist layer process and reduce both the softbake temperature from 110 °C to 90 °C and exposure time from 25 sec to 20 sec. This protocol with a short development time (10~30 sec) yielded the best results and a perfect photoresist pattern was observed under an optical microscope. In the discussion here optical images after each step were not included because a camera attached to the microscope in the clean room was not available.

Step c: Pattern resist in contact aligner. The exposure was made in the contact mode with a mask aligner MA6 from Karl Suss that operates with a 350 W mercury lamp light source. The 4 inch wafers were aligned with the help of markers shown in Figure 5.6 with the help of a microscope attached to the instrument. UV-exposure test series on Shipley 1813 were required to determine the exact dose of exposure. The samples were found to be exposed for 20 sec at an energy densitiy of $E = 10.0 \text{mW/cm}^2$. This is equal to an exposure dose of $D \approx 200 \text{ mJ/cm}^2$. The energy density E was measured using a dose

measurement technique immediately before the actual exposure. The exposed samples were developed using a Microposit developer concentrate (MF319), which is a standard tetramethylammonium hydroxide phosphate developer for positive resists (95% water, <1% surfactant, and 2.2% tetramethylammonium hydroxide, with a pH of 13). The development time was determined again by means of test series and was found to be 10~30 seconds or the time until the photoresist pattern was visible to the naked eye.

Step d: E-beam evaporation for Cr/Co metal deposition. In e-beam evaporation or physical vapor deposition (PVD), the metal wafers that were exposed to UV light and hard-baked in previous steps, were mounted on a carousel and placed in the vacuum chamber. A block of the metal to be deposited was also placed in the source tray. The source tray for the model Temescal VES-2550 is designed to house more than one metal (reliable vacuum pocket crucible with 15cc and 25cc pockets) with up to 40 x 4" wafer capacity and capability to fit custom substrates. In a typical process the metal is heated by means of a highly energized electron beam (up to 10 keV) under high vacuum conditions that allow the metal atoms to evaporate freely in the chamber and subsequently condense on all the surfaces. The wafers can be mounted in two configurations. In one configuration where the wafer is perpendicular to the metal source a non-conformal coating of the metal is obtained. This process leads to deposition of metals only on flat surfaces and not on edges and edge lengths because after photolithography the wafers produced have several steep 90 degree valleys. In the second configuration the wafers are mounted on a hemispherical carousel and therefore metal vapors generated deposit on all the sides uniformly resulting in a conformal coating over the entire photoresist surface irrespective of the valleys. The two configurations are shown in Figure 5.6 below.
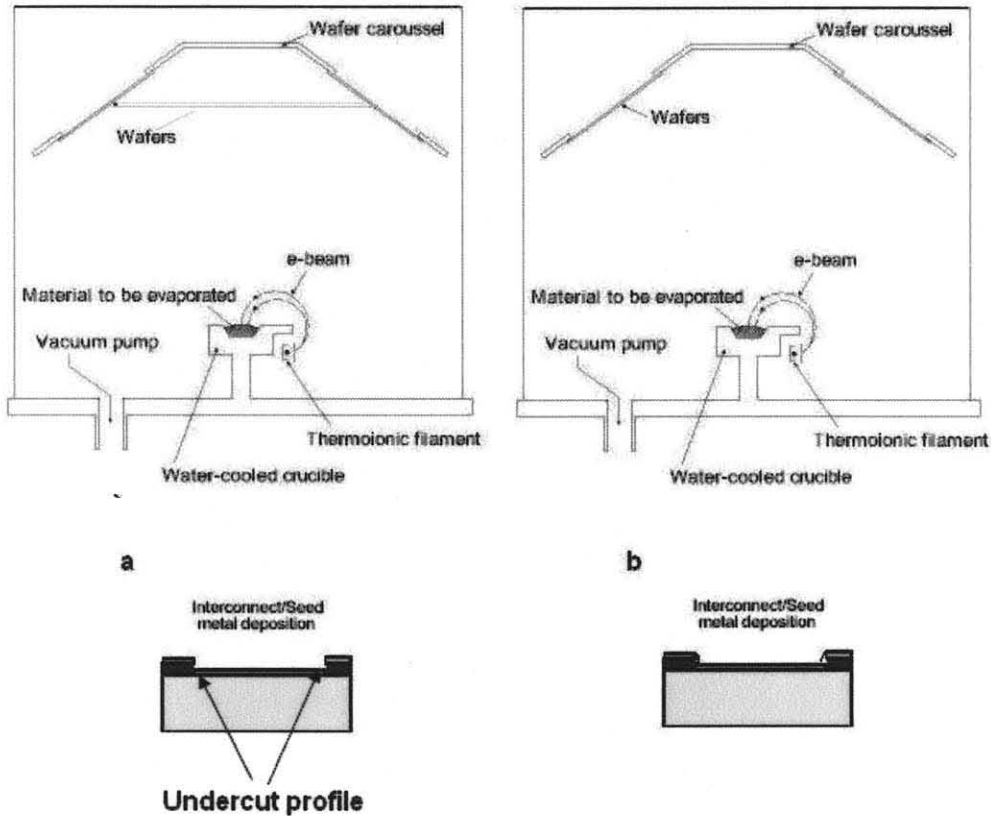
Figure 5.6 E-beam evaporation set-ups. a) Wafers mounted perpendicular to the metal source and the resulting metal profile on the photoresist pattern together with the undercut profile, and b) Wafers mounted on the hemispherical carousel for conformal deposition, and the resulting metal coating on the photoresist pattern.

Both methods were studied, poor metal pattern edges after lift off were observed using the first method. The second configuration was used after optical observation of metal patter after liftoff. The low contamination of the evaporated metal is the main advantage of this kind of evaporation. PVD leads to high quality thin films. A 20 nm thick chromium (Cr) adhesion layer that enables good cobalt (Co, which functions as the nanotube growth catalyst) adhesion on the quartz surface was evaporated at a rate of 2 Å/s. A 120 nm thick Co layer was then evaporated at a rate of 1 Å/s. The determination of the Co thickness depended on three parameters; namely the quality of the subsequently deposited silicon nitride film, the alignment markers for e-beam lithography at 100 keV,

and the catalyst/seed layer needed for nanotube synthesis or electrophoretic deposition. Thickness chosen for the chromium and the cobalt layers were 20 and 120 nm, respectively. Using these thicknesses the alignment marks were detectable in the e-beam lithography system using backscattered electron (BSE) detection with 100 keV electrons. With BSE detection the alignment mark contrast increases with the atomic number and thickness of the mark (Farrow et al, 1993). When a heavier metal such as Au is used the metal thickness can be reduced and the marks are detectable with the same e-beam energy. In another example, 42 nm thick Cr/Au layers were deposited for the gas sensors and only 30 keV for alignment and e-beam writing could be used. In addition, infrared radiation for backside alignment can be blocked thus enabling accurate backside alignment. The thickness was also sufficient for nanotube synthesis and electrophoretic deposition. The results for these processes will be shown in the later fabrication steps. Briefly, for nanotube synthesis a layer of active metal catalyst, such as cobalt of thickness above 5 nm is desired; however, in this process most of the available surface for growth was masked with a layer of silicon nitride or layers of gold and silicon nitride, thereby limiting the surface area available only through the holes. By covering the metal layer, the exposed metal area was of the order of 20 nm ~ 35nm (holes) and thickness did not play a very crucial role. For electrophoretic deposition the metal layer is a more important factor. As can be seen from the design (Figure 5.8), the sites for the nanotube deposition are connected to metal contacts. These features are 1~2 micron in size and have to be connected to a conducting contact pin while performing electrophoretic deposition. Chosen thickness of the metal layer makes the process more robust and less likely to have cracks in the metal en route to the sites of interest.
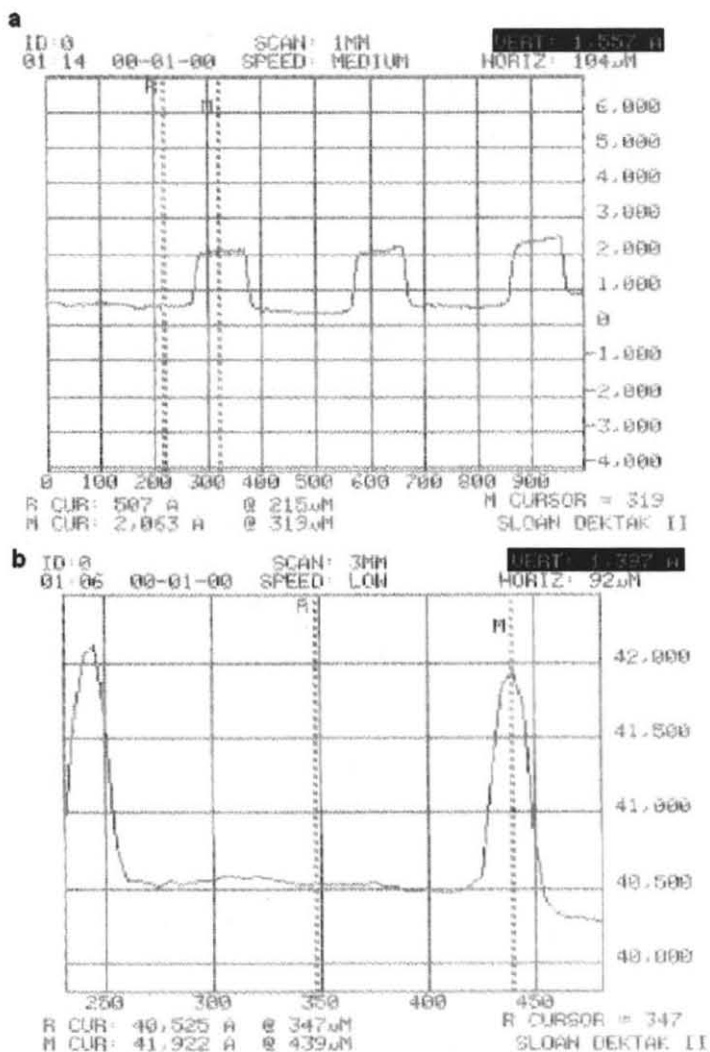
Figure 5.7 DEKTAK vertical height measurements. (a) Shows a scan for an area of 1 mm × 1 mm at medium scan speed; the vertical height is 1557 Å, and (b) scan at a different location for an area of 3 mm × 3 mm at a slow scan speed; the vertical height is 1397 Å.

Step e: Lift-Off of metal. Good lift-off results were achieved when the samples were dipped for 20 min. in acetone at room temperature in a covered container to prevent evaporation. The samples were gently sprayed with acetone using a pipette until the Cr/Co film was detached from the surface. Most often the film broke into big pieces which were sucked into the pipette and removed from the solution. If the detached pieces were small they could remain suspended in the solution and contaminate the surface by

sticking via van der Waals forces after lift-off. If this happens they cannot be removed any more. The acetone bath had to be changed two or three times and the procedure repeated until the lift-off looked good. Then the samples were bathed in isopropanol at room temperature and rinsed with DI water for 10 min. As a result the top side of the samples were structured with markers and electrode structures which were then used for the alignment and for making contacts to SWNTs. A good lift-off result for the electrode structures is shown in Figure 5.8. (a) full wafer pattern after metal lift off, (b) nanotube deposition sites, (c) gap required between two nanotube sites.

Site for nanotube growth
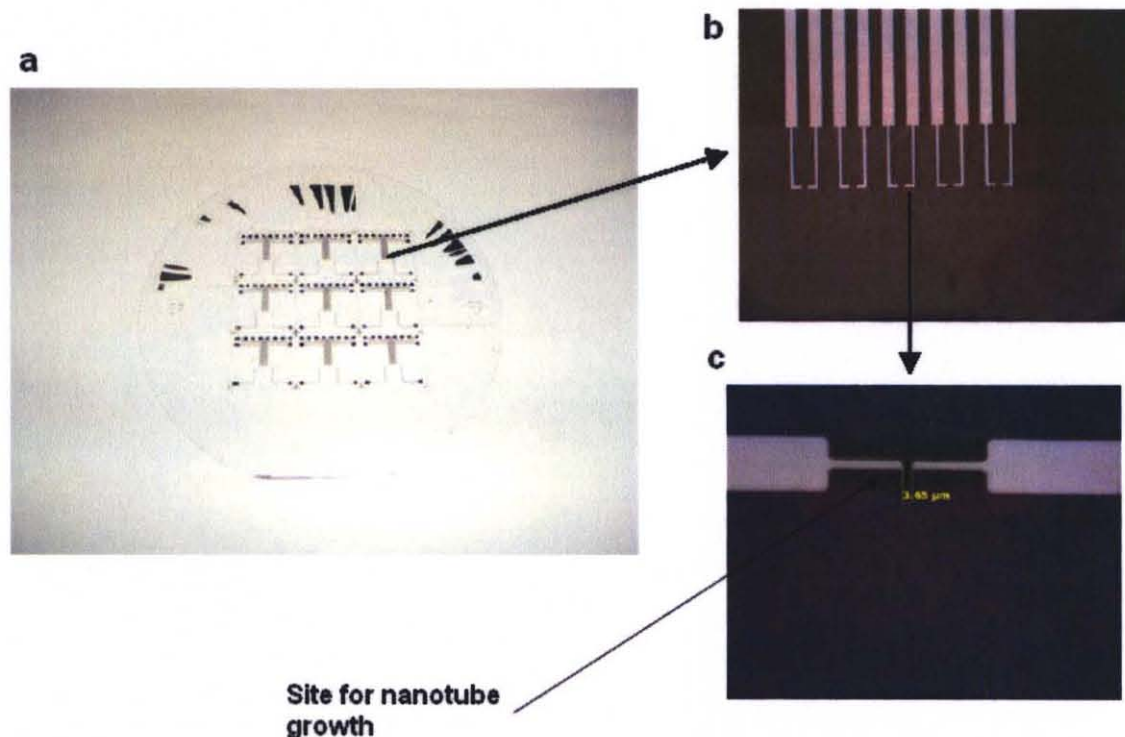
Figure 5.8 Result of a wafer after lift off. (a) Shows pattern obtained after metal lift off, (b) Shows sites for nanotube growth or deposition, and (c) Shows required gap of ~2 μm; measurements on fabricated device structure indicates a gap of 3 μm.

Step j: Silicon Nitride using Plasma Enhanced Chemical Vapor Deposition (PECVD). Silicon nitride (Si_3N_4 or SiN_x) was deposited as a film on top of the metal pattern obtained after lift off. There are two reasons for depositing a SiN_x film: firstly, SiN_x is the material on which windows can be transferred down to the metal level after e-beam lithography. These windows will then be used for SWNT growth by CVD or deposition by electrophoresis. Secondly, it provides an insulating barrier between conducting interconnect metal and the cell culture solutions on which measurements will be performed. A 50 nm thick low stress SiN_x film was deposited at low temperatures using plasma enhanced chemical vapor deposition (PECVD). PECVD was conducted at the NJIT MFC clean room facility using Plasma Therm 790 standard equipment. The system uses a capacitively-coupled 13.56 MHz source excitation to produce the plasma between two aluminum plates. The samples were placed on the anode substrate holder in order to minimize ion damage. Initially the system was cleaned using a vacuum pump and isopropyl alcohol. Before making a deposition, a cleaning cycle run was conducted using oxygen plasma to remove any residual contaminants. In addition, a passivating layer of SiN_x of 50 Å in thickness was deposited on the chamber walls before the final deposition was performed. A typical cycle used for the PECVD process after pumping down the system to 1×10^{-2} Torr was as follows:

1) Initially heat the chamber wall to a desired temperature of 20 °C and the substrate to a temperature of (300-350 °C)

2) Purge the system with nitrogen for 3 minutes at 1 liter/min

3) Using following deposition conditions:

Parameter	Set Point	Actual readout
Pressure:	900 mTorr	899 mTorr
Power:	50 W	49 W
NH_3:	45 SCCM	45 SCCM
SiH_4:	280 SCCM	280 SCCM
He:	800 SCCM	800 SCCM

4) Turn RF power on: The system is equipped with an autotuner in order to achieve the plasma and required flow rates. The system can be preset to the desired thickness.

5) Purge the system with nitrogen.

6) Evacuate gases and cool down to room temperature under nitrogen atmosphere.

7) End of cycle and samples can be taken out for measurements.

Above runs were performed at two different substrate temperatures of 300 °C and 350 °C. The observations on the SiN_x layer were made using SEM for morphology, by ellipsometry (Rudolph Research Auto EL) to obtain the thickness, and optical imaging after etching was performed with HCl to look for pinholes.

Figure 5.9 shows the SEM image after deposition at 300 °C indicating a uniform conformal coating over the entire surface at a magnification of 1300x. Since SiN_x is an insulating material it was difficult to get high resolution images at energy of 2 keV. The line visible in the image is the edge of the metal pattern below the SiN_x layer.
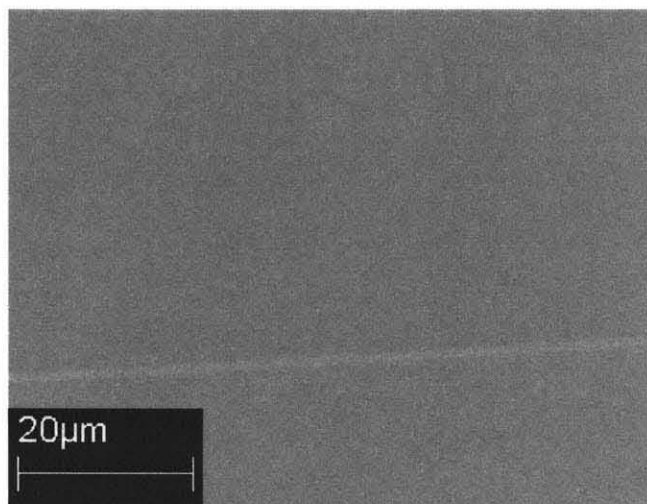
Figure 5.9 SEM image of a wafer after deposition of a 50 nm SiN$_x$ film using PECVD.

Some of the coated samples were used to grow carbon nanotubes and it was observed that the SiN$_x$ film cracked at the nanotube growth temperature. This was attributed to the presence of pinholes in the PECVD deposited layer, which functioned as crack propogation centers. The difference in the coefficient of thermal expansions between SiN$_x$ and metal layer at the interface causes the cracking of the SiN$_x$ layer (this will be discussed more in nanotube deposition step) It was difficult to observe the pinholes in the SEM images recorded. Therefore HCl was used as an etchant, which selectively removed Co metal but not SiN$_x$, by this method it was possible to locate the pinholes on the film. Figure 5.10 is an optical image after the etching process with 12 M HCl. In Figure 5.10 a color difference in the form of arrays can be observed which arises due to the presence of metal layers below the SiN$_x$ layer. The image in Figure 5.10a is a low magnification image showing the presence of pinholes over the entire area, while Figure 5.10b shows a high magnification image indicating a number of pinholes with the metal layer below. The results therefore showed that the process used did not yield the uniform coverage and this can happen because of two reasons: (1) Contamination of the

PECVD chamber with SiN_x, and (2) Use of a lower temperature process resulting in layer thicknesses that were 1.5~2 times the desired thickness of 50 nm.
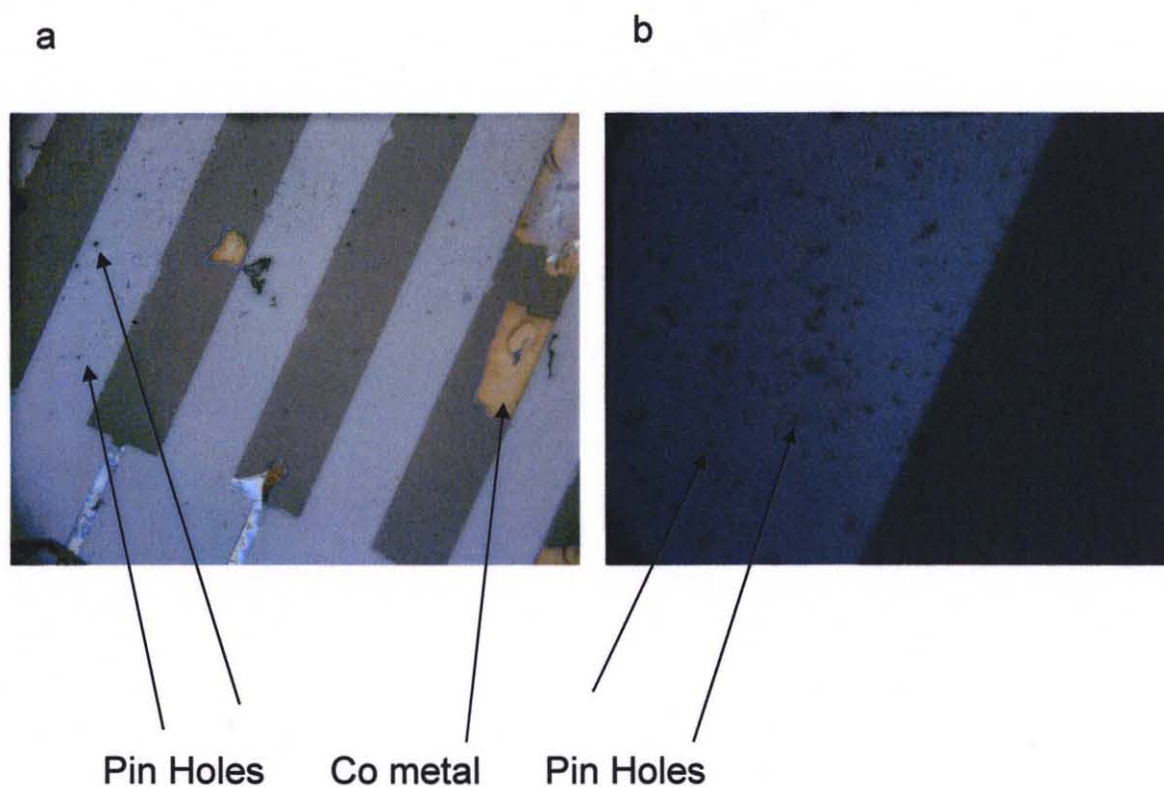
Figure 5.10 Pin holes on SiN_x deposited using PECVD visible after a 12 M HCl etch.

The SiN_x layer was then deposited at the higher temperature of 350 °C in order to get the optimal thickness and better uniformity. Higher temperature is expected to yield denser growths and thereby fewer pinholes. The SEM image shown in Figure 5.11 indicates a uniform film. Optimal film thickness is also indicated by ellipsometric measurements carried out at three locations on the film. The results are shown in Table 5.1
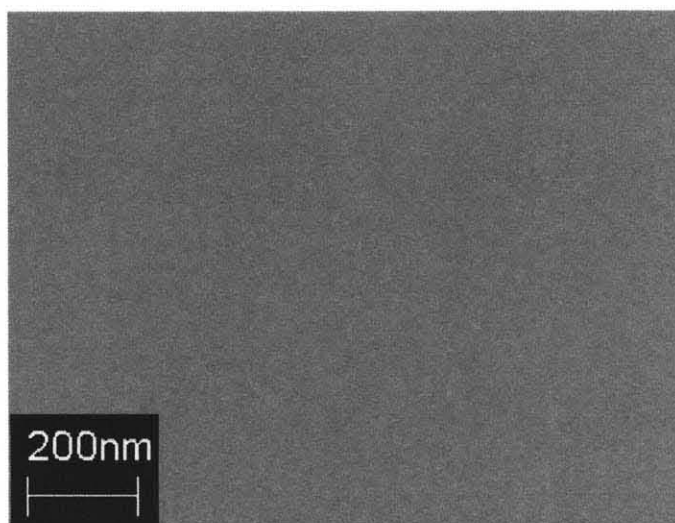
Figure 5.11 SEM image after deposition of a SiN$_x$ layer on the metal patterned quartz wafer using PECVD at 350 °C.

Table 5.1 Ellipsometric Measurement on SiN$_x$ Layer on Silicon Substrates Deposited at 350 °C

TL	NL	ORD	Thickness (Å) = M×ORD + TL
517	2.037	1751	517
509	2.045	1742	509
472	2.023	1766	472

The thickness is calculated using a standard formula M×ORD + TL = Thickness (Å). A program for two layers i.e. SiN$_x$ on top of Silicon was chosen. TL is the thickness of a layer, NL is the refractive index, ORD is a correction factor, and M is an integer multiplied by the correction factor. M is chosen depending on an initial guess of the thickness. For the above measurement M = 0 was chosen and the resulting thickness was of the order of ~ 500 Å.

Step k and l: e-beam resist, e-beam lithography. A standard procedure for e-beam resist ZEP was used. Seven different electric field doses were used as shown in Figure 5.12 to create windows from 5 nm to 100 nm. This work was carried out at the New Jersey Nanotechnology Consortium (NJNC) at Bell Laboratories located at Murray Hill, New Jersey.
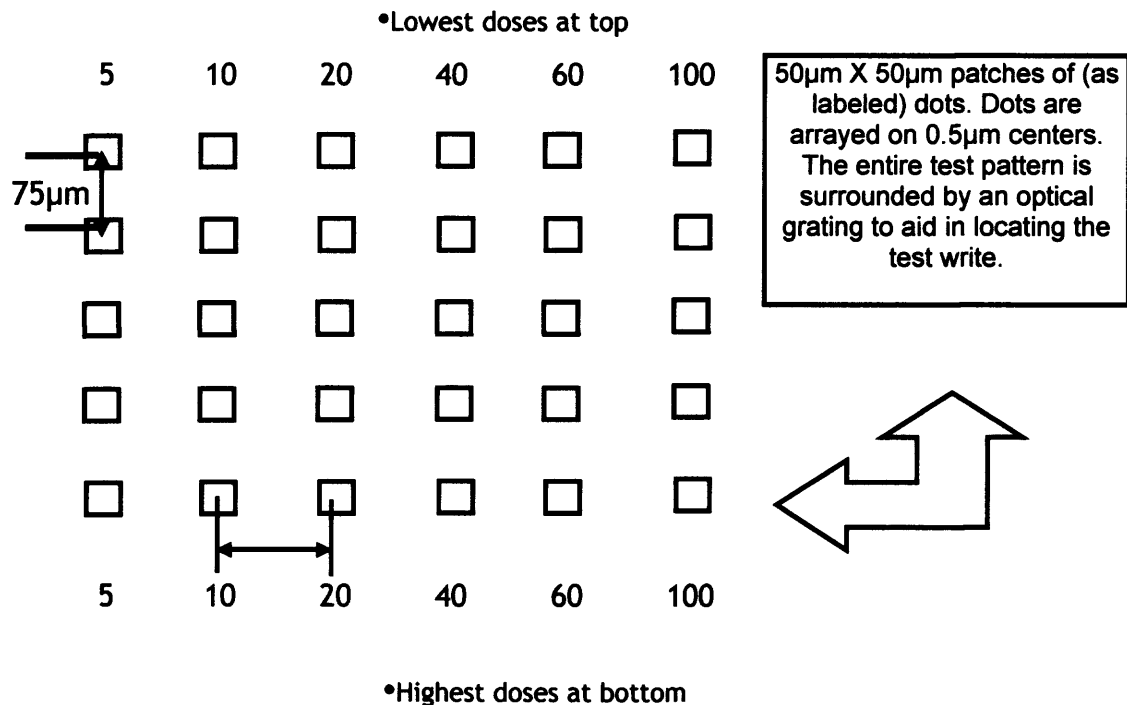
Figure 5.12 E-beam lay out: each square consists of specified (5-100 nm) size holes separated by 1 micron. Lowest dose focus is towards top and the highest dose focus is at the bottom of the lay out.
[Source: NJNC].

Step m: Reactive Ion Etch (RIE) etch to remove resist and silicon nitride. The ZEP photoresist with a thickness of 2000 Å was then the mask used for patterning the SiN_x (500 Å) layer below. A Trion Technology Phantom instrument capacitively coupled plasma reactive ion etching system was used to etch the SiN_x layer openings from the topside of the sample. In an RIE system the plasma is driven capacitively with a power

source operating at 300 Watts using a 13.56 MHz, solid state RF generator. In this case, a reactive gas species, such as CF_4, CHF_3 or SF_6 is added to the chamber. Flourine-based plasmas are generally used for isotropic etching. When the plasma is formed by the applied RF potentials, the gas molecules are broken down into a number of fragments and radicals. A significant number of these molecular fragments may become ionized in the plasma and may be accelerated to the various electrode surfaces within the discharge chamber. In the RIE system used the samples are placed on the powered electrode and exposed to the flux of ions from the plasma, as well as the more isotropic flux of gas species that may also be formed within the chamber. During reactive ion etching, gaseous species from the plasma react with the surface atoms forming compounds or molecules. These species then leave the surface thermally, if the vapor pressure is high enough, or as a result of ion bombardment. The free radical concentration controls the isotropic chemical etch rate of the system. The contribution of physical and chemical part of the plasma can be manipulated by varying the power and gas pressure.
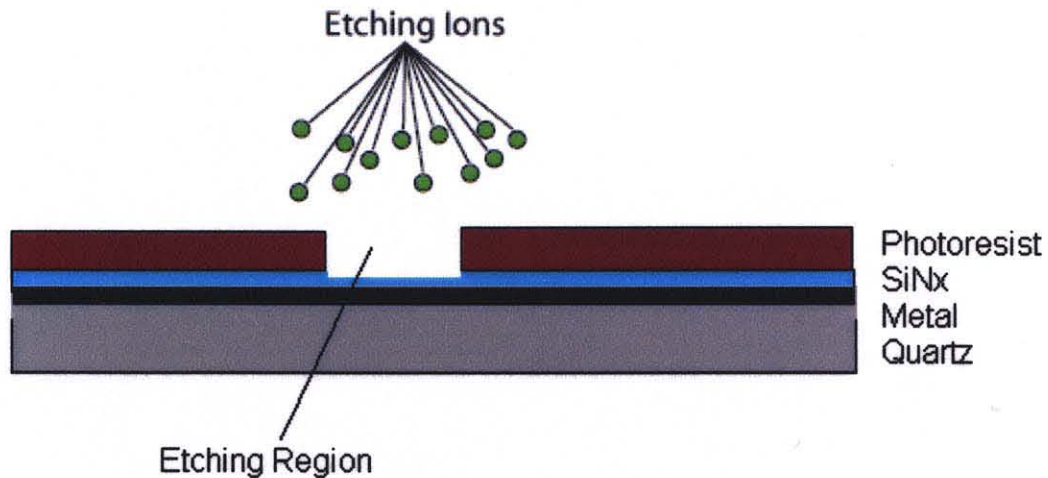
Figure 5.13 Reactive ion-etch profile after partial exposure. It shows the depletion in SiN_x layer with residual photoresist layer on top.

The tests were conducted to observe etch rates on two silicon substrates coated with with 2000 Å and 500 Å thick ZEP and SiN_x layers, respectively. The thickness of the layers chosen for the tests is the same as the layers on the device. Tests were performed with two different gases at different chamber total pressures and power. The final morphology of the holes was investigated using SEM on the quartz substrate with an array of holes created by e-beam lithography on the ZEP photoresist after the etching step.

Brief descriptions of RIE processes are given below. The respective etch rates were determined by ellipsometric measurements.

Process 1
Gas: CF_4; Flow: 10 SCCM
Pressure: 150 mTorr
Power: Set Point 15 W; Actual read out 12 W
Time 30 seconds

Two pieces of silicon one with ZEP and the other with SiN_x coating are placed on the substrate holder that is also the powered electrode. The above recipe yields an etch rate of 12.67Å/30sec for SiN_x and 431.67Å/30sec for the ZEP photoresist. The ellipsometric measurements before and after the etch process for two layers are shown below.

Before etch for 500 Å SiN_x on Silicon   After etch for 500 Å SiN_x on Silicon

TL	NL	ORD	Thickness (Å)
656	1.923	1885	656
657	1.912	1899	657
647	1.913	1898	647
			Avg. = 653.33

TL	NL	ORD	Thickness (Å)
640	1.924	1885	640
640	1.921	1888	640
642	1.920	1886	642
			Avg. = 640.667

Etch rate = <u>Avg. thickness before etch – Avg. thickness after etch</u>
<div align="center">Time of exposure</div>

Etch rate SiN_x =   (653.33 – 640.667)/30 sec   = 12.67 Å/30 sec

Before etch for 2000 Å ZEP on Silicon   After etch for 2000 Å ZEP on Silicon

TL	NL	ORD	Thickness (Å)
2967	1.364	3199	2967
2880	1.360	3010	2880
2785	1.361	2980	2785
			Avg. = 2877.33

TL	NL	ORD	Thickness (Å)
2477	1.490	2736	2477
2480	1.494	2723	2480
2380	1.520	2648	2380
			Avg. = 2445.67

Etch rate ZEP = 431.67Å/30sec

Process 2
Gas: CHF_3; Flow: 50 SCCM
Gas: O_2; Flow: 5 SCCM
Pressure: 55 mTorr
Power: Set Point 250 W; Actual read out 150 W (desired value)
Time 60 seconds

The above recipe was derived from experiments done at the Molecular Foundry in Lawrence Berkeley National Labs (Deirdre Olynick, private communication) and yields an etch rate of 244.67Å/10 sec for SiN_x and 2266Å/60 sec for ZEP photoresist. The ellipsometric measurements before and after the etch process for the two layers are shown below.

Before etch for 500 Å SiN_x on Silicon   After etch for 500 Å SiN_x on Silicon

TL	NL	ORD	Thickness (Å)
714	1.913	1898	714
649	1.927	1880	649
649	1.927	1880	649
			Avg. = 670.67

TL	NL	ORD	Thickness (Å)
440	1.84	1929	440
412	1.905	1909	412
			Avg. = 426

Etch rate SiN$_x$ = 244.67Å/10 sec

Before etch for 2000 Å ZEP on Silicon   After etch for 2000 Å ZEP on Silicon

TL	NL	ORD	Thickness (Å)
2523	1.511	2673	2523
2451	1.524	2636	2636
2692	1.451	2863	2863
2557	1.49	2736	2736
			Avg. = 2689.5

TL	NL	ORD	Thickness (Å)
446	1.442	2843	446
401	1.444	2885	401
			Avg. = 423.5

Etch rate ZEP = 2266 Å/1 min

It is desired that the etch rate of SiN$_x$ is such that the sacrificial layer of ZEP is not removed entirely before 500 Å of SiN$_x$ can be removed in order to expose the metal layer. In the first process the ratio of etch rates of SiN$_x$ to ZEP is approximately 1:40, with etch rates of 12.67 and 431.67 Å, respectively. The time required to completely remove SiN$_x$ is the total thickness of the SiN$_x$ layer divided by the etch rate, i.e., 1183 seconds, however, in the same time period the entire ZEP layer is totally removed due to the much faster (431.67 Å) etch rate. This leads to an exposed SiN$_x$ layer after 139 seconds of exposure time which under plasma conditions is then etched away leaving behind the entire metal layer exposed to the atmosphere.

In the second process, the ratio of etch rates of SiN$_x$ to ZEP is 1:1.55, with etch rates of 244.67 Å/10 sec and 2266/min Å, respectively. Therefore the time required to remove 500 Å of SiN$_x$ layer is approximately 21 (exposed for 25 seconds) seconds, for the same exposure, ZEP removed is 944.67 Å. The selectivity of this etch process towards the two layers meets the requirement, as an approximately 1050 Å thick layer of residual ZEP of a total of 2000 Å acts as a barrier and limits the total removal of SiN$_x$

below the ZEP layer. As mentioned before we performed a test run on an array of holes from 5 nm to 100 nm. Each grid consists of a 10 × 10 array of holes 1 micron apart generated with a single dose focus created by the e-beam. A total of seven such sets for each size are available and shown in Figure 5.12 and Figure 5.14. It can be noticed that the holes for 5, 10 and 20 nm are not at all visible (Figure 5.14), it is possible that either these holes were not written by the e-beam or totally wiped off during the etching process. The verification for the presence of holes was not possible before etching since the ZEP layer has to be coated with a carbon layer in order to image the morphology. The carbon coating will alter the etching process in an unknown way, possibly an oxygen plasma step has to be introduced to oxidize the carbon, but the oxygen plasma also etches ZEP. For this application the holes for 40 and 60 nm are sufficient to create windows to grow or deposit nanotubes at desired sites as shown in Figure 5.8.
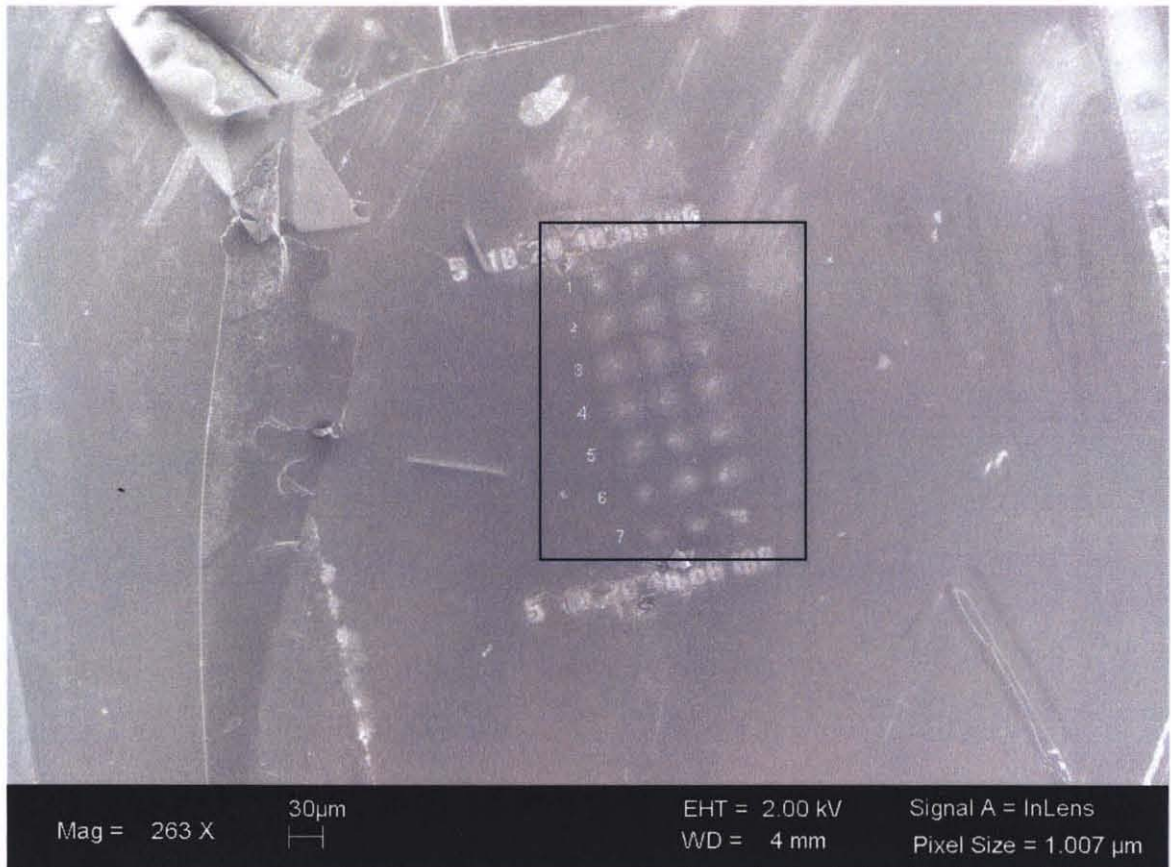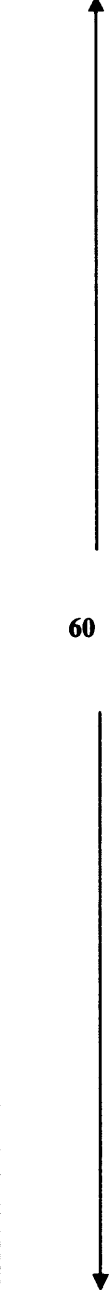
Figure 5.14 SEM image of the array of holes with sizes from 5 nm to 100 nm. Each row corresponds to a single dose focus. The numbers therefore designate a total of seven dose focus experiments.

A statistical analysis was conducted by measuring the hole diameters for all seven dose focuses for 40 nm and 60 nm grids. The smallest hole diameter achieved after the RIE etch is 145.5 nm in the case of the 3rd dose focus for the 40 nm array (refer to Figure 5.14 and Table 5.2).

Table 5.2 Hole Diameters Determined Using SEM Measurement Tool for 40 and 60 nm Grids for The Seven Dose Focuses After the RIE Etch

	File no.	Grid	Image no. on grid	Hole 1 diameter (nm)	Hole 2 diameter (nm)	Average
40 nanometer array						
	1	Numbered array				
	2		1			
	3		1	100		
	4		1	107.8		
	5		1	171.7		
	6		1	171.7		
Avg. 1				171.7		**171.7**
	7		2			
	8		2	174.9	172.9	173.9
	9		2	170	178.6	174.3
Avg. 2						**174.1**
	10		3			
	11		3	147.2	138.6	142.9
	12	40	3	142.7	153.5	148.1
Avg 3						**145.5**
	13		4			
	14		4	164.5	153.2	158.85
	15		4	131.6	158.4	145
	16		4	162.8	176.6	169.7
Avg. 4						**157.85**
	17		5			
	18		5	171.6	163.8	167.7
	19		5	173.5	165.6	169.55
Avg. 5						**168.63**
	20		6			
	21		6	175.7	183.8	179.75
	22		6	155.6	163.8	159.7
Avg. 6						**169.73**
	23		7			
	24		7	147.2	142.3	144.75

(CONTINUED)						
	25		7	157.7	171.8	164.75
	26		7	172.3	162.3	167.3
Avg. 7						**158.93**
60 nanometer arrays						
	27		1			
	28		1			
	29		1	161.8	163.2	162.5
	30		1	167.3	158.9	163.1
Avg. 1						**162.8**
	31		2			
	32		2	165.4	166.3	165.85
	33		2	169.8	162.6	166.2
Avg. 2						**166.03**
	34		3			
	35		3	180.1	181.4	180.75
	36		3	178.4	189.5	183.95
	37		3	173.8	181.4	177.6
Avg. 3						**180.77**
	38	60	4			
	39		4	195.4	197.1	196.25
	40		4	185.4	178.7	182.05
Avg. 4						**189.15**
	41		5			
	42		5	160.8	163.4	162.1
	43		5	160.2	160.2	160.2
Avg. 5						**161.15**
	44		6			
	45		6	184.9	195.1	190
	46		6	180.5	177	178.75
Avg.6						**184.38**
	47		7			
	48		7	178.8	184.6	181.7
	49		7	148	148	
	50		7	170	170	170
Avg.7						**175.85**

Step n: Carbon nanotube growth and electrophoretic deposition. The vertical growth of individual and bundled single wall carbon nanotubes (SWNTs) on silicon and quartz surface is a critical issue in nanoelectronics. Vertically aligned nanotubes have been grown recently on various substrates including silicon (Konno, 2004; Murakami, 2004; Ding, 2004; Christen; 2004; Maruyama, 2002). However, growth of nanotubes on quartz substrates has not been studied in detail simply because quartz is not typically used in nanoelectronics. In this section the methods employed to optimize vertical growth of SWNTs and the compatibility with other layers, mainly silicon nitride, will be described. In addition a method of electrophoretic deposition of carbon nanotubes on the metal surface at room temperature will be discussed.

Uniform catalyst deposition in the size regime of a few nanometers (5 -20 nm) has been found to be critical for vertical growth of carbon nanotubes. Spin coated catalyst solutions of cobalt and molybdenum, metal deposited by e-beam evaporation with a photoresist layer, metal deposited and after removal of photoresist layer, and finally, metal with a silicon nitride layer on top, will be studied. In the above-mentioned systems the effect of oxidation time/temperature, time for nanotube growth using ethanol as carbon precursor, will also be discussed.

The first step was to identify the metal catalysts that can be used to grow SWNTs on quartz. From past experience Co:Mo acetate precursor solutions aided with a polymer, polyvinylpyrollidone (PVP) (Wang, Ph.D. thesis, 2005) for better dispersion and uniform layer deposition on quartz substrate, were used. Co:Mo in a ratio of 1:1 with 1wt % of PVP in ethanol solution was spin coated at 3000 rpm for 60 seconds. The quartz pieces were placed in a clean ceramic boat, which was then positioned inside a high temperature

furnace. Oxidation at 500 C in air was carried out at the rate of 5 °C/min in order to remove PVP slowly and decompose the acetates to the corresponding oxides. This led to the formation of islands of catalyst metal oxides in the sub-micron size range, a step that is very important to grow vertically aligned SWNTs. The final temperature is 850°C and held for another 2 hrs.

The substrate was cooled to room temperature and subjected to a typical run for nanotube growth. The typical run described here will remain the same for all the metal catalyst types mentioned earlier. The quartz pieces with metal catalyst oxides are heated to 500-850°C under H_2 and held for 35 minutes to reduce the metal oxides. The chamber is pumped down to 10^{-2} Torr and back filled with carbon precursor ethanol with argon (300 SCCM) as the carrier gas to 1 atmosphere pressure; temperatures used are between 700-850°C for growth and growth time is between 2 to 30 min.

Figure 5.15 (a-i) shows Raman spectra for SWNTs grown on various substrates. Figure 5.15 (a) shows the spectrum of sample prepared using a catalyst layer from a Co:Mo acetate solution spin coated on a quartz substrate. The substrate was heated to 800°C at the rate of 5°C/min and held there for 2 hrs. Nanotube growth is also carried out at this temperature for 20 min. The Raman spectrum clearly indicates the presence of both radial breathing mode (RBM) and tangential mode (TM) lines indicating the presence of SWNTs in the sample. The peak at 463.51 cm^{-1} is associated with crystalline quartz. Using Equation 2.7, the RBM lines at 194 and 206 cm^{-1} correspond to SWNTs with average individual tube diameters of 1.25 nm and 1.17 nm, respectively. The presence of relatively narrow TM peaks at 1591 and 1580 cm^{-1} indicates that majority of the tubes are likely to be semiconducting. In addition, the higher relative intensity of the

disorder (D) mode near 1300 cm^{-1} suggests the presence of MWNTs as well as defects on the sidewalls of the SWNTs formed. The Raman spectrum is consistent with SEM images indicating vertically grown forests of SWNT together with a large number of MWNT (Figure 5.16). However this experiment suggested that cobalt can be used as catalyst for extensive SWNT growth under optimal conditions. This observation is important since a very limited number of catalyst metals for nanotube growth can be deposited using e-beam evaporation techniques. The sample for which the Raman spectrum is shown in Figure 5.15 (b) has a metal layer of 20/120 nm of Cr/Co deposited using e-beam evaporation on patterned Shipley 1813 photoresist. A very short oxidation step is performed where the substrate is heated rapidly to 800 °C from room temperature and directly reduced under H_2 for 35 min in a typical run. The presence of photoresist under the metal layer serves two purposes: (a) It functions as a secondary carbon source for nanotube growth because of its low dissociation temperature, and (b) It provides an indication of how adversely lift off affects the formation of SWNTs in later experiments. In addition, a rapid oxidation step provides a view of morphological changes in the metal layer. The Raman spectrum (Figure 5.15 b) indicates only the formation of MWNTs since lines in the RBM mode region are not observed. Also the D mode at 1327 cm^{-1} is comparable in intensity to line at at 1574 cm^{-1} which can be assigned to the graphitic G mode of MWNTs. In addition, the lower frequency TM line of SWNTs is not observed, further indicating the absence of SWNTs in the sample. This is also confirmed by the MWNT-type SEM images from the sample shown in Figure 5.16 (b) although the precursor decomposition and reduction step resulted in metal particles of 20-25 nm in size that are suitable for SWNT growth. Lack of growth of SWNTs can, therefore, be

attributed to incomplete reduction of metal oxides or the absence of initial formation of metal oxide clusters. The spectrum between 400 to 1000 cm^{-1} are not shown because of the presence of high intensity peaks from crystalline quartz in this region. Figure 5.15 (c-e) correspond to samples with an oxidation step of 30 minutes to 800°C followed by holding at constant temperature for another 30 minutes and keeping the deposition time constant at 20 minutes to observe the effect of oxidation without photoresist. Whereas in Figure 5.15 (b) growth of MWNT was observed with rapid catalyst precursor oxidation, there is substantial growth of SWNTs in samples corresponding to the spectra shown in Figure 5.15 c-e. The presence of broader peaks in the low frequency region occurs due to exposed quartz after lift off. The RBM peaks in Figure 5.15 c are at 243 and 261 cm^{-1}, in Figure 15 (d) at 261 cm^{-1} and in Figure 5.15 (e) it is hard to locate the peak due to broad high intensity quartz peak. The observation of relatively few RBM peaks suggests a narrow distribution of nanotube diameters in the sample, which is highly desired for nanoelectronic devices. On comparison of Figure 5.15 (c) with Figure 5.15 (d), it can be observed that the intensity of the TM line is lower in Figure 5.15 (d), due to the fact the Raman spectrum from this sample was taken from the back side of the quartz wafer. It also suggests that nanotube growth takes place as soon as the carbon precursor is introduced. Hence, in order to achieve low density growth one can reduce the deposition time to the order of few minutes. This was confirmed by making a series of runs for which a representative Raman spectrum is shown in Figure 5.15 (e) grown with only 3 minutes of deposition time. The SEM results shown in the Figure 5.16 (c-e) correspond to the Raman spectra shown in Figure 5.15 (c-e). Figure 5.15 c and d shows images from high density growth of SWNTs and MWNTs, where many of the tubes are oriented in the

vertical direction. The back-side Raman measurement shown in Figure 5.15 (d) shows that SWNTs are also present at the bottom-most layer and therefore low density nanotube growth was achieved for the short growth time of 3 minutes (Figure 5.15 e). However, in this case the nanotubes are not vertically aligned and grow in an inter-connected manner between the metal islands.

The Raman spectra in Figure 5.15 (f-i) were from samples grown after a 50 nm thick SiN_x layer is deposited on top of the metal layer. The spectrum shown in Figure 5.15 (f) is not a true representation of the sample since this sample was covered with a conductive carbon coating in order to perform SEM imaging. This sample does have a large density of SWNTs as can be seen from the SEM image in Figure 5.16 (f). The coefficient of thermal expansion for SiN_x is 3.3 μinch/inch K and for metal Co is 12.3 μinch/inch K; this mismatch at the interface causes the cracking of the SiN_x layer. Especially, the oxidation cycle for up to 270 minutes at a temperature of 800 °C is not conducive to the process. Therefore, in further experiments the lowest possible temperature and the shortest time required for oxidation at that temperature were determined. The sample from which the Raman spectrum in Figure 5.15 (g) was obtained was oxidized at a temperature of 700°C for 270 minutes. The sample for Figure 5.15 (h) corresponds to 60 minutes of oxidation and the sample in Figure 5.15 (i) corresponds to 30 minutes of oxidation. In Figure 5.15 (g) the RBM mode is weak, however, the presence the split TM peaks confirm the presence of SWNTs. The SEM images also support this observation. The reduction of the oxidation temperature substantially reduces the cracking of the SiN_x layer. One important observation is that the nanotubes form in a chain like fashion connecting all the exposed metal particles

emerging out of the SiN_x layer. This is a desirable feature for many electronics applications where nanotubes are used as interconnects between two metal particles as source and drain, with an oxide layer at the bottom as a back gate to form field effect transistors. The sample for which the Raman spectrum is shown in Figure 5.15 (h) was oxidized for 60 minutes. It showed the best results with minimal cracking of SiN_x and chain-like growth. A piece of the device structure was used as the substrate in this case and therefore in RBM mode region several peaks for quartz are observed. The peaks at 177 and 251 cm^{-1} are assigned to SWNTs, while peaks at 158 and 299 cm^{-1} arise due to crystalline quartz. The disorder mode is low and both G⁻ and G components of the TM mode are present, indicating the presence of SWNTs. Finally the Raman spectrum from a sample, which was subjected to e-beam and RIE etches and therefore has the specific windows where nanotubes are to be grown, is shown in Figure 5.16 (i). A very low density of nanotubes was formed in this case, since the oxidation cycle was only for 30 minutes. It was also observed that significant amounts of MWNTs are formed possibly due to lack of sufficient catalytic sites. The SEM image in Figure 5.16 (i) shows that the nanotubes are located in the holes, but the SiN_x layer was still cracked at several places. This is evident when e-beam written numbers (20, 40, 60, and 100), which are easily noticeable and have disfigured after the nanotube growth process, are examined.
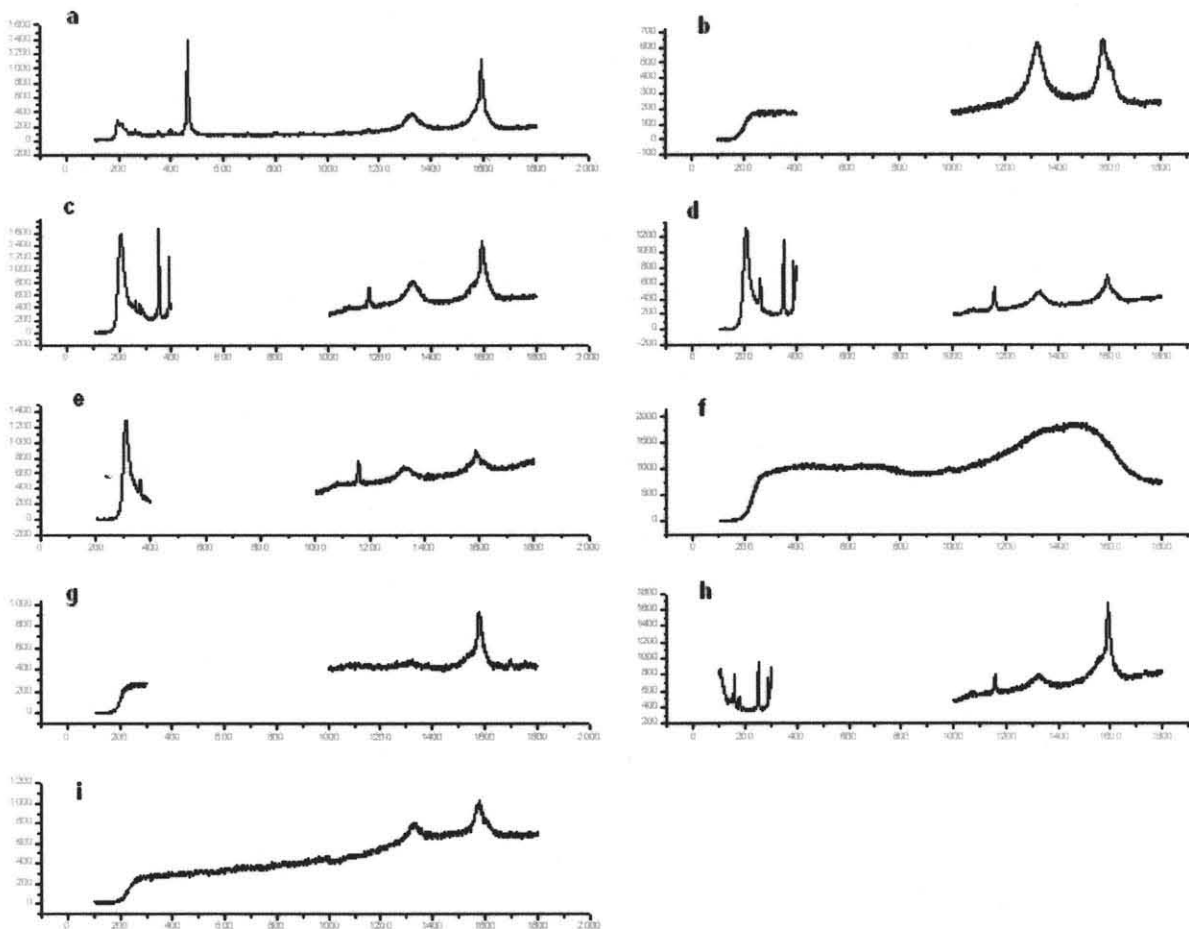
Figure 5.15 Raman spectra excited with 632.8 nm laser radiation for: (a) Sample prepared using Co-Mo acetate catalyst precursor spin-coated from solution; (b) Sample with catalyst deposited by e-beam with resist; (c) Sample with catalyst deposited by e-beam without resist followed by 60 min oxidation and reduction; (d) Same sample as (c) but taken from the backside; (e) Sample with catalyst deposited by e-beam and no resist followed by 270 min oxidation; (f) Sample with catalyst deposited by e-beam + silicon nitride and 270 min oxidation; (h) Sample with catalyst deposited by e-beam + silicon nitride and 60 min oxidation; (i) Sample with catalyst deposited by e-beam + silicon nitride and 30 min oxidation.
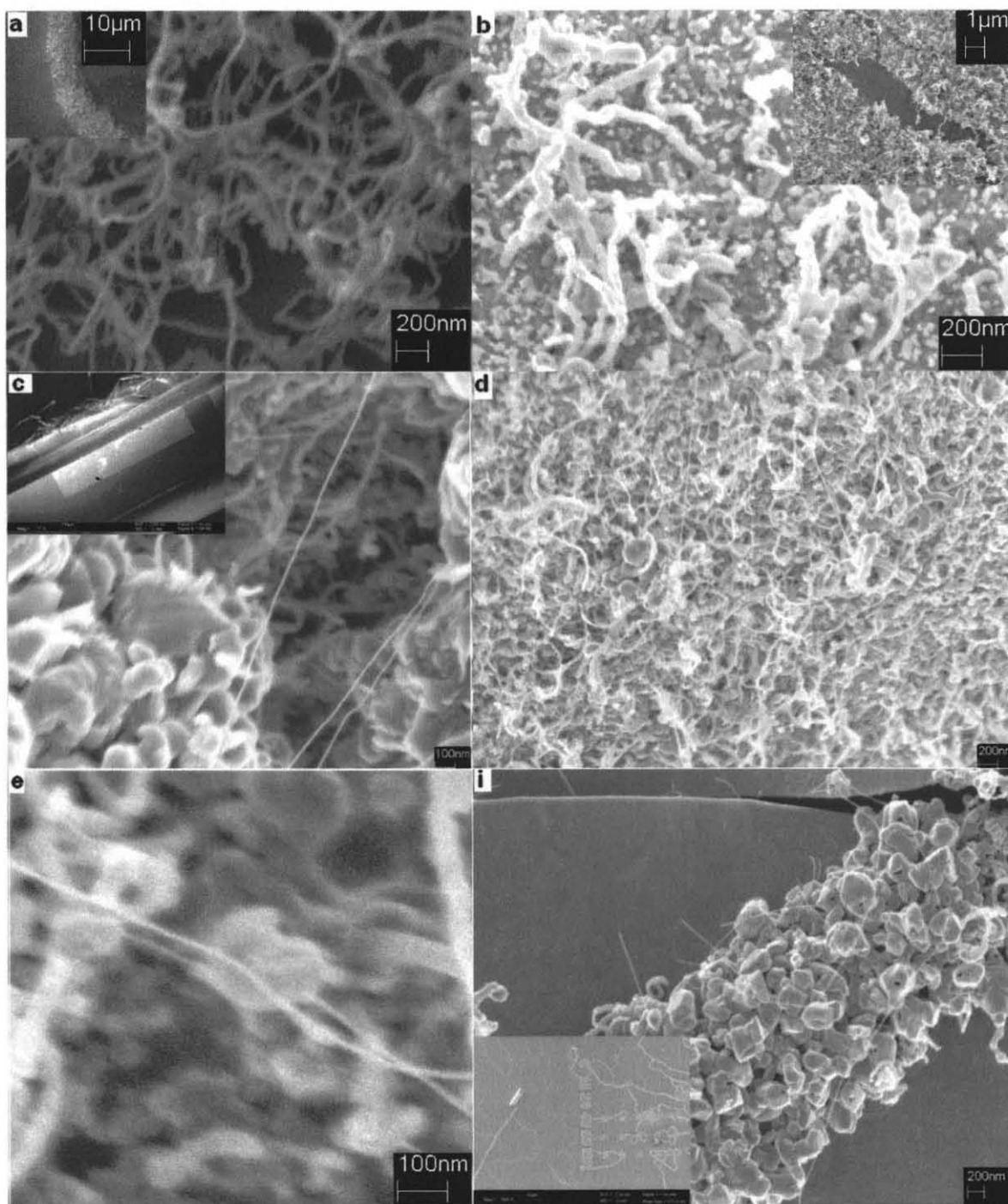
Figure 5.16 SEM images of (a) Sample prepared using Co-Mo acetate catalyst precursor spin-coated from solution, Inset shows growth of vertical nanotube forests; (b) Sample with catalyst deposited by e-beam with resist; (c) Sample with catalyst deposited by e-beam without resist followed by 60 min oxidation and reduction; aligned nanotubes are formed; (d) Same sample as (c) but taken from the backside; (e) Sample with catalyst deposited by e-beam and no resist followed by 270 min oxidation, inset shows cracking of SiNx layer and tubes are grown as interconnect between metal clusters; (i) Sample with catalyst deposited by e-beam + silicon nitride and 30 min oxidation.
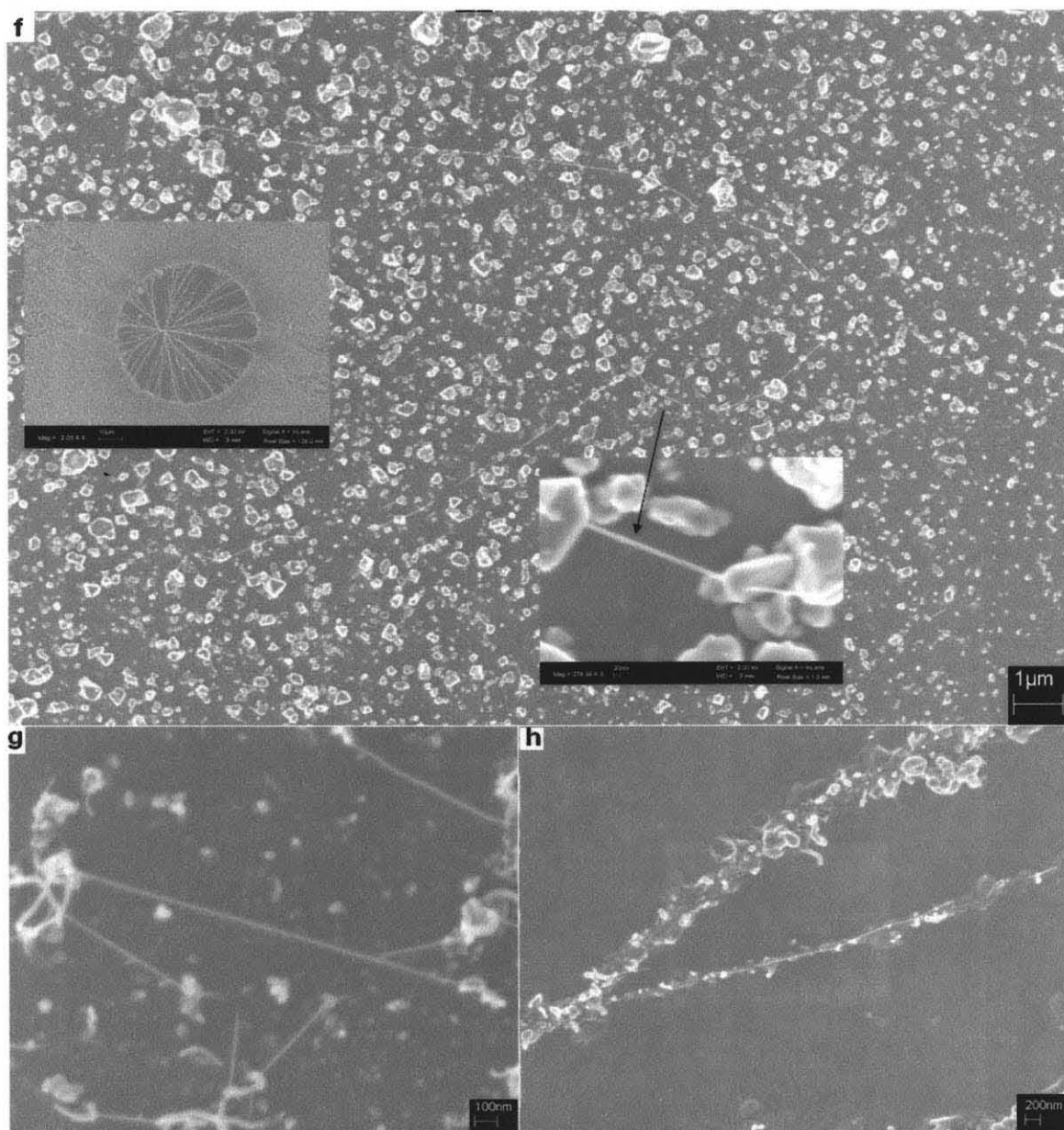
Figure 5.16 (continued) SEM images of (f) Sample with catalyst deposited by e-beam + silicon nitride and 270 min oxidation, inset shows cracking of SiNx layer and tubes are grown as interconnect between metal clusters; (g) g) e-beam metal with SiN$_X$ and 270 min oxidation; (h) Sample with catalyst deposited by e-beam + silicon nitride and 60 min oxidation.

5.4 Electrophoretic Deposition (EPD) of SWNTs

The temperature and oxidation conditions could not be further reduced to synthesize SWNTs on the metal catalyst. It was therefore necessary to find an alternative lower temperature process to deposit the nanotubes. Electrophoresis has been used in the past to deposit nanotubes on conducting surfaces at room temperature (Choi, 2001; Thomas, 2005; Gao, 2001). Electrophoresis deposition (EPD) is a very simple and cost effective method that usually requires a simple experimental setup. It is driven by the motion of charged particles, dispersed in a suitable solvent, towards an electrode under the influence of an electric field. Small particles less than 30µm size can be used in suspensions with low solid loading and low viscosity. Deposition takes place via particle coagulation. The drawback of this method is that the control of the deposition of the SWNTs in form of bundles or individual tubes depends on the nature of the suspension. As-synthesized pristine carbon nanotubes are inert, often aggregated and contain impurities such as amorphous carbon on the sidewalls and catalytic metal particles. Post synthesis treatment for purification using HCl and nitric acid imparts functional groups on side walls, such as carboxylate and oxygen-containing groups. These acidic groups electrostatically stabilize the nanotubes in water, or other polar liquids, by developing a negative surface charge. Several types of solvents have been used to prepare nanotube suspensions for EPD (Niu, 1997; Thomas, 2005; Choi, 2001; Du, 2002; Bae, 2002; Kurnosov, 2003; Ma, 2005; Nakayama, 2001). Preparation of a stable dispersion is a prerequisite for successful EPD. In general terms an electrostatically stabilized dispersion can be obtained with particles of high ζ- potential, while keeping the ionic-conductivity of the suspensions low. SWNTs have shown high ζ- potential values at low pH values

(Hu, 2005). It has also been shown that the presence of charging salts can play an important role in improving adhesion of the nanotubes to substrates and increasing the deposition rates (Choi, 2001, Bae, 2002; Kurnosov, 2003; Ma, 2005). Depending on the salt used the deposition can be performed either on the anode or cathode. For example, nanotubes have been shown to deposit on the positive electrode (anode) from suspensions in the presence of benzylalkonium (please check chemical name) chloride (Bae, 2002) while the presence of quaternary ammonium (Girishkumar, 2004) salts have been shown to deposit nanotubes on the negative electrode (cathode).

Purified SWNTs were obtained from Carbon Nanotechnologies Inc (CNI). 10 mg of nanotubes were suspended in 30 ml of distilled water. 10^{-4} moles of magnesium nitrate hexahydrate [$Mg(NO_3)_26H_2O$] was added to the suspension and sonicated for 2-3 hrs. A few drops of non ionic Triton-X surfactant were added to improve the suspension. A small piece of a patterned device on quartz with cobalt metal was used as the negative electrode, and a platinum wire was used as the positive electrode. A series of tests were performed at DC voltages in the 5V- 25V range and with different substrate structures in order to optimize the deposition. The schematic for the experimental setup is shown in the Figure 5.17. The same batch (PΦ288 from CNI) of SWNTs was used for all the EPD experiments.
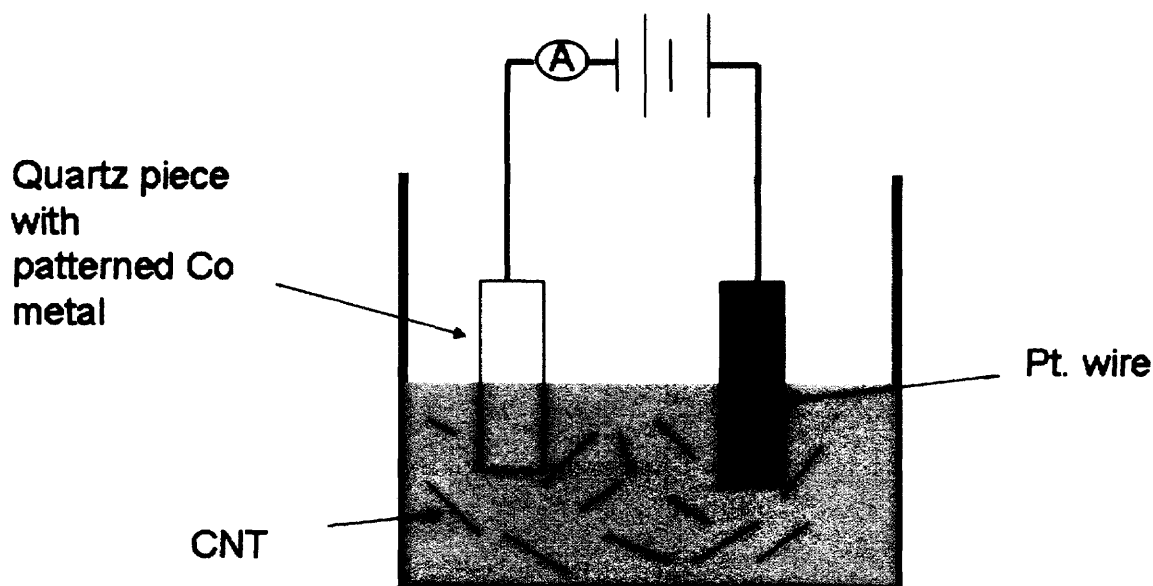
Figure 5.17 Schematic for the electrophoretic deposition of carbon nanotubes from an aqueous suspension of carbon nanotubes (CNTs). The, quartz substrate is patterned with Co metal and $Mg(NO_3)_26H_2O$ is added to the suspension.

Figure 5.18 shows a representative Raman spectrum after deposition of SWNTs on the metal patterned on the quartz substrate. The spectrum of the as-deposited SWNTs is the same as that of the as-received SWNTs from CNI.
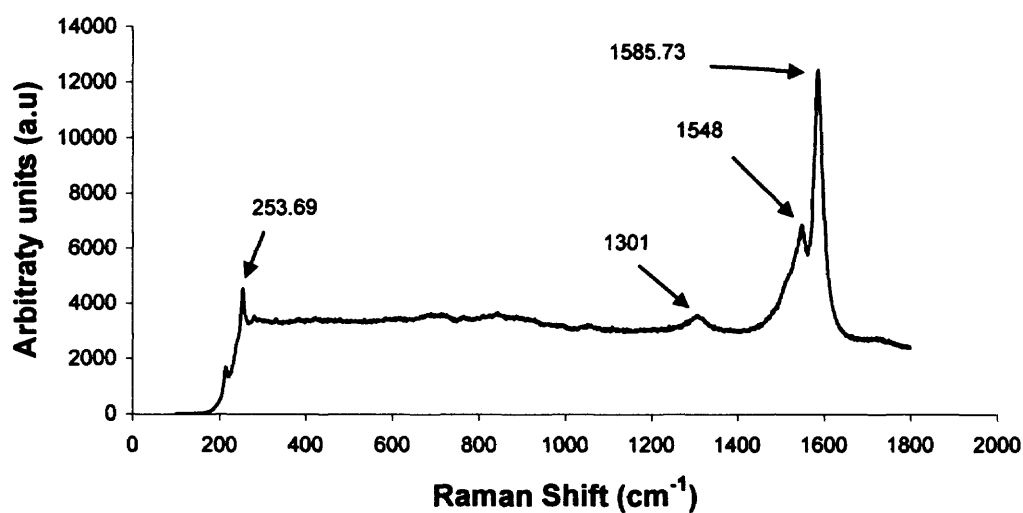
Figure 5.18 Raman spectrum excited with 632.8 nm radiation of SWNTs after electrophoretic deposition on a metal surface.

The deposition mechanism can be explained in terms of ion adsorption where Mg^{2+} ions are adsorbed by the suspended SWNTs resulting in the formation of an electrical double layer. The migration of nanotubes and final deposition under DC bias can be attributed to the preferential adsorption of ions in the nanotube suspension. The microstructure of the deposited SWNTs was determined using SEM. Figure 5.19 a-f are representative SEM images for DC biases of 5, 10, 15, 20 and 25 V, respectively. The SEM image in Figure 5.19 (a) for a sample obtained at a DC bias of 5 V shows a very low density of SWNTs. A single bundle of SWNTs was observed after surface imaging of the entire cathode surface. The images in Figure 5.19 b and c, for samples deposited at a DC bias of 10 V show very uniform and well aligned layers of SWNT bundles over the entire metal surface. A small amount of surfactant can also be observed, which can be washed away after the deposition process is completed.

The SEM image in Figure 5.19 (d) is for a sample deposited at a bias of 15 V. It shows a similar degree of alignment as for the sample deposited at 10 V. The deposition, however, is denser and forms a uniform layer. Figure 5.19 (e) shows the SEM image for a sample deposited at a bias of 20 V. The deposit is very dense but randomly oriented. SWNTs are observed right on the tip (shown as inset) where SWNT deposition would be required during device fabrication. Figure 5.19 (f) shows the SEM image for a sample deposited at a bias of 25 V. As expected a denser layer of SWNTs was observed. However, some of these samples were difficult to image because the quartz substrate is insulating and a conducting carbon layer was not deposited. Figure 5.20 is an electrophoretic deposited using optimized condition of 10 V and 10 minutes.
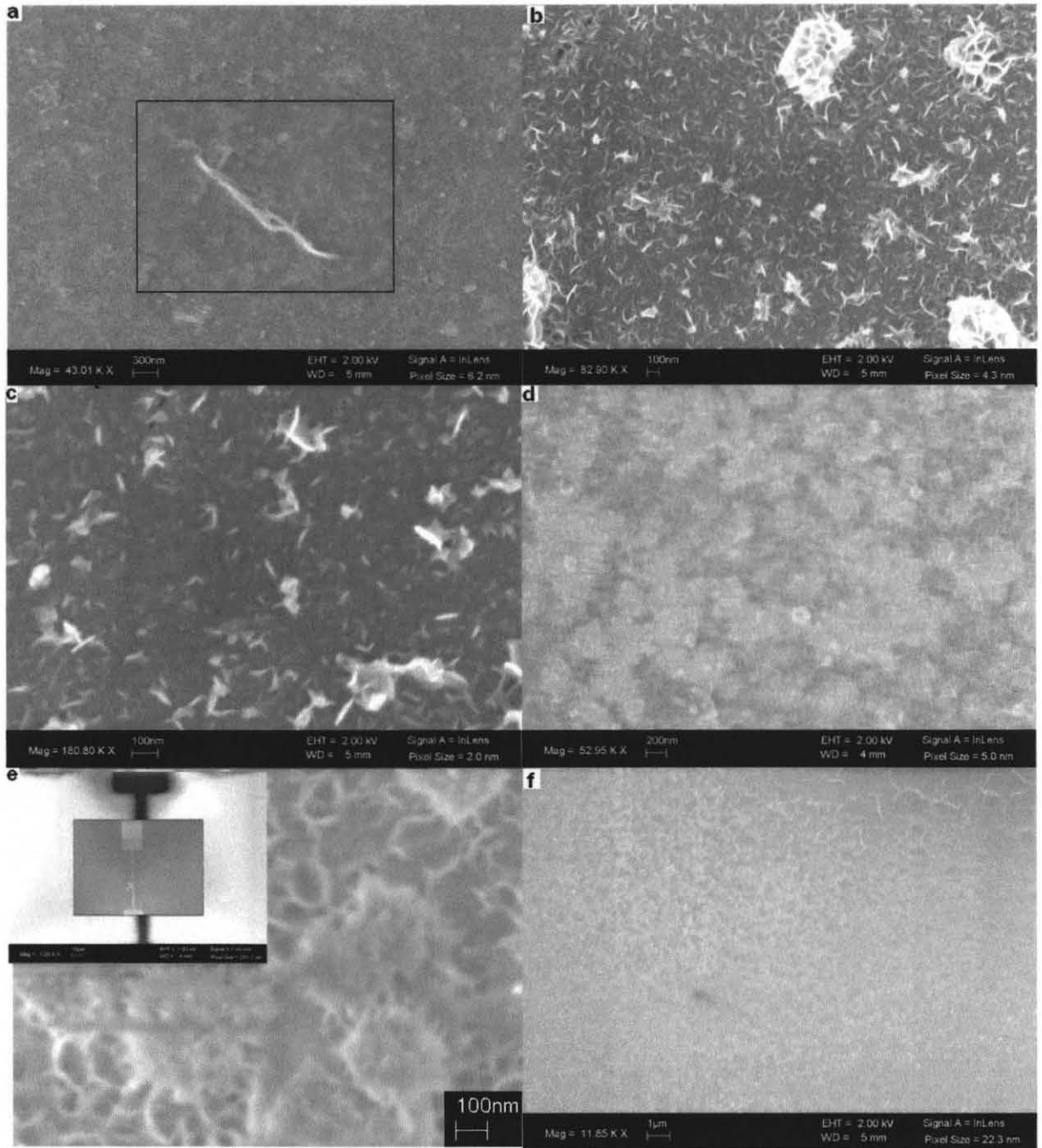
Figure 5.19 SEM images after electrophoretic deposition on metal surfaces patterned on quartz wafers for different DC biases: a) 5 V, b) and c) 10 V, d) 15 V, e) 20 V, and f) 25 V.

The images 5.20 a and b shown are from the sample that was e-beam written and etched using RIE as discussed earlier in step l and m. The sample charges under electric field of 2 keV in SEM due to the presence of top insulating silicon nitride layer. It can be noticed that all the holes are populated with nanotube bundles. A larger magnification image shown in Figure 5.20 b shows a bundle of tube in an etched hole of diameter ~100 nm. The size of the bundle is approximately 20 nm. Presence of tubes in the holes was confirmed using micro Raman (Figure 5.20 c), with a beam spot size of approximately 1 μm, it covers an array of 3×3 holes and all the features as of pristine tubes were observed. The deposition of tube is observed to occur only at the center of the hole. This can be explained by electric field distribution between two metal plates under DC bias. A finite element analysis conducted to determine the electric field distribution between the two plates, platinum and a cobalt plate which is covered with 50 nm SiN_x having 100 nm holes is shown in Figure 5.20 A. It clearly suggests that due to narrowing down of the holes below sub micron scale the field is highly localized in the center of the holes with sharp edges at corners of hole near SiN_x surface. As the hole size is increased the electric field flattens out and more tubes can deposit on the metal surface.
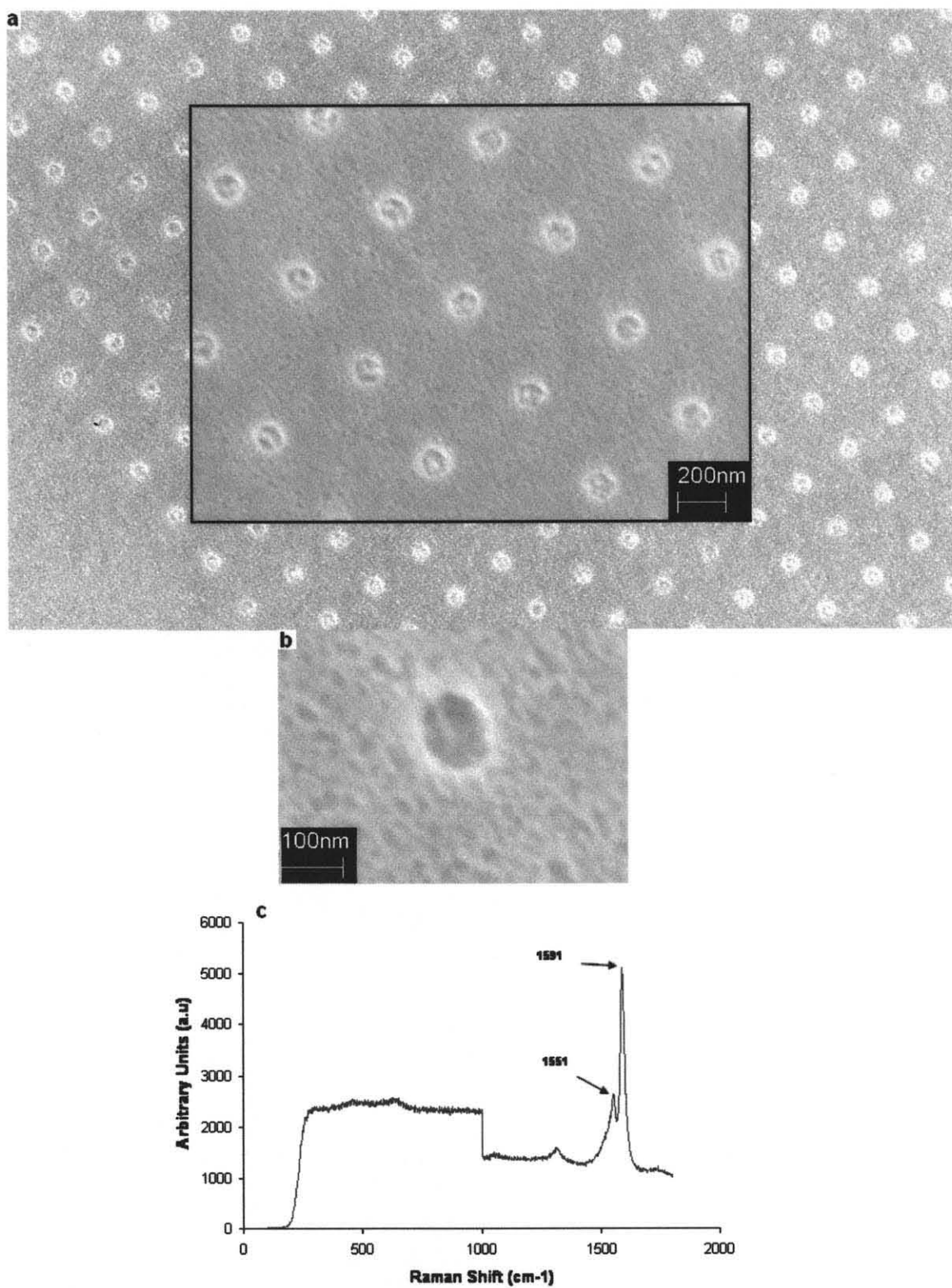
Figure 5.20 SEM and Raman of electrophoretic deposited SWNTs on e-beam written and RIE etched sample at 10 V DC bias for a period of 10 minutes. Sample has an insulating coating of SiN_x as a top layer.
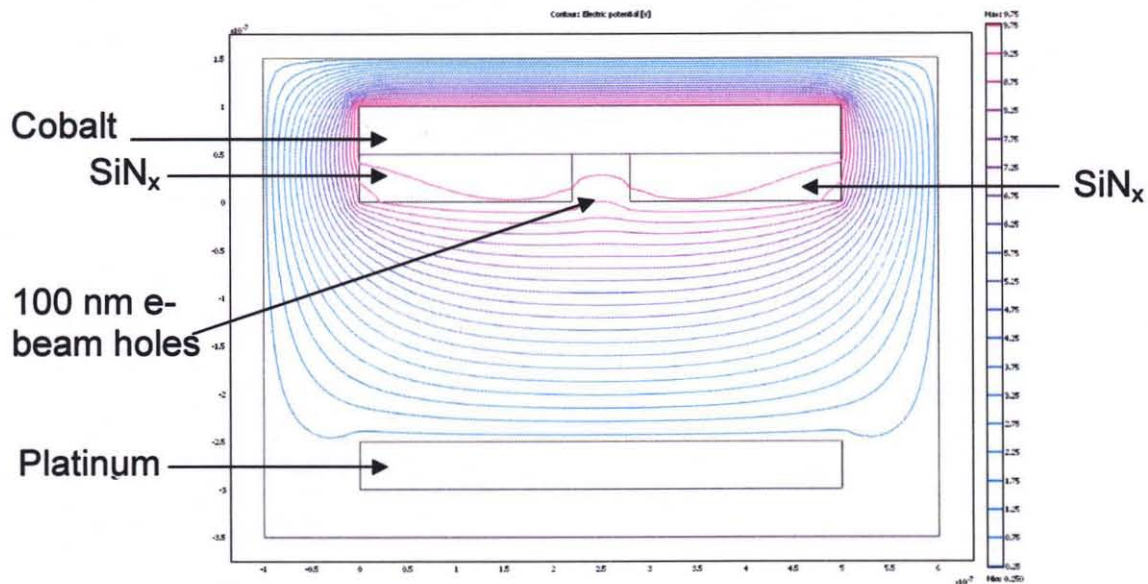
Figure 5.20 A Electric field distributions with a 10 V DC bias between a platinum and cobalt plate with 100 nm holes on a 50 nm SiN$_x$ insulating layer using finite element analysis.

5.5 Gas Sensors: Introduction

The motivation for improved gas sensing capabilities for ammonia (NH_3), carbon monoxide (CO), and nitrogen oxides (NO and NO_2) is predominantly driven by the risk of these gases to humans. Exposure to gaseous ammonia at concentrations of 50-100 parts per million (ppm) can cause severe burns to the skin, eyes, throat, and lungs. In the case of exposure at or above 5,000 ppm, blindness, lung damage, and death are possible. Even at low concentrations, ammonia exposure causes coughing and irritation. Persons with asthmatic conditions are particularly prone to these effects. At concentrations around 25 ppm, chronic exposure can lead to damage of the eyes, liver, kidneys, and lungs. The threat of exposure to carbon monoxide is considerably greater. CO is a byproduct of incomplete combustion reactions. Exposure at concentrations around 30 ppm can result in the weakening of heart contractions, reduction in ability to perform manual tasks, and general drowsiness. For individuals with heart conditions, exposure to concentrations as low as 10 ppm can cause similar effects on the body. At concentrations greater than 35 ppm for extended durations (>24 hrs), carbon monoxide exposure can result in headaches, irritability, blurred vision, lack of coordination, nausea, dizziness, and death. According to United States government regulations, the threshold level value for CO is 50 ppm for an eight hour exposure. Nitrogen oxide gas, at 1-5 ppm, is a general irritant of the respiratory system as well as the eyes. Exposure over time results in fluid build-up in the lungs, nausea, and fatigue. Higher concentration exposures cause swelling of the throat, reduced oxygenation in the blood, and in severe cases, death.

Based upon these symptoms, considerable attention has been given to the monitoring of these gases in the environment. Automotive congestion elevates the

presence of these gases in urban locations. In rural settings, gas concentrations can become elevated due to fertilizers or excessive density of livestock byproducts.

Carbon Nanotubes as Gas Sensors   Carbon nanotubes have been investigated for gas sensing applications by various groups. Sensors based on nanotubes mostly rely on direct change in their electrical properties when subjected to a chemical gas atmosphere comprising of the analyte to be studied. SWNTs with their one dimensional structure are ideal molecular wires with a highly robust chemical structure, which provides the necessary characteristics for large scale integration into advanced sensor devices. This section focuses primarily on NO_2 detection.

NO_2: First report was by Kong (2000) where semiconducting-SWNTs (S-SWNTs) grown by chemical vapor deposition on SiO_2 /Si substrates and patterned catalyst were used for NO_2 and NH_3 detection. The change in I-V_g curves after exposure to gases showed that molecular gating effects are capable of shifting the Fermi level of S-SWNTs and modulating the resistance by orders of magnitude. In this study, the lower concentration limit for NO_2 was found to be 2 ppm and 0.1 % for NH_3 with a response time of 5 min. and 10 min., respectively. The electrical conductance of the nanotubes was observed to decrease ~ 100 fold after exposure to 1% NH_3 with a response time of ~ 1-2 min. and sensitivity of ~ 10 to 100. In another study conducted at NASA (Li, 2003), purified SWNTs prepared by the HiPCO (high pressure carbon monoxide) method were used on interdigiated electrodes for NO_2 and nitrotoluene detection. The detection limits for NO_2 and nitrotoluene were observed to be 44 ppb and 262 ppb, respectively. The sensor response was on the order of seconds and recovery by UV exposure was observed

to occur in a few minutes. Suehiro (2005) demonstrated NO_2 detection using dielectrophoretic impedance measurements involving SWNTs and MWNTs trapped in a castle wall arrangement that was photolithographically fabricated. The devices were exposed to NO_2, (NH_3 was also studied) and the sensor impedance was measured at room temperature in the 1-100 KHz frequency range. It was observed that the number density of the nanotubes trapped increased the sensor sensitivity. Chemical functionalization has also been explored for NO_2 (and also for NH_3) detection. For example, Qi (2003) has demonstrated that nanotubes functionalized with polyethyleneimine (PEI) converts the as-prepared p-doped nanotubes to n-type tubes due to electron transfer doping via the amine groups on PEI. This increased the sensitivity towards NO_2 detection to a level of parts per trillion. Reproducible results showing the capability to sense NO_2 at levels that were as low as 1 ppb with 1-2 min. response times have been reported. Sensor recovery were performed by UV-exposure which results in desorption of the NO_2 molecules. Another important feature of the PEI wrapped n-doped nanotubes is that they do not show any response to NH_3, CO, CO_2, CH_4, H_2 and O_2. For selective NH_3 detection the nanotube device was coated with Nafion[®].

The sensor devices based on nanotubes described above provide evidence of their gas sensing abilities in different device setups. However, the role of a nanotube and the sensing mechanism needs further investigation. No studies have been reported for an individual nanotube without any direct contact with the substrate or gate. As it is widely known Si and its oxides can also be used as a gas sensing element, it is therefore important to study the nanotubes fabricated as a bridge rather than lying on the wafer surface. Here, a novel approach utilizing the variation of the electrical properties of

carbon nanotubes to sense a particular analyte. The choice of device configuration is based on an individual suspended S-SWNT. The fabrication process has been simplified in order to integrate it into a large scale device based on conventional CMOS methods. Several reproducible devices were made using nanotubes of different diameters. A dry gas (N_2 80% and O_2 20 %) and a humid environment (35 % relative humidity) were used to examine the gas molecule analyte in order to create successful devices for real time applications.

5.6 Experimental Section

5.6.1 Device Fabrication

This section is divided in three parts: (a) Process flow for device fabrication, (b). Chemical functionalization of the carbon nanotubes, and (c) AFM characterization used in process flow. (Experiments were conducted at ETH)

5.6.1.2 Process Flow. SWNTs made by high pressure carbon monoxide chemical vapor deposition (HiPCO) were used to fabricate the devices. For detailed description readers are referred to Stampfer (2004). A brief description is provided here for completeness. The nanotubes were mixed with sodium dodecyl sulfate surfactant, sonicated, and centrifuged at 75.60 g for 4 hours. The upper 80% supernatant was decanted while micelle suspended nanotubes were retained at the bottom. The schematic of the procedures used are illustrated in Figure 5.20. A Si substrate (4 mm × 4 mm) containing a 200 nm oxide layer was spin coated with a copolymer of methyl methacrylate and methacrylic acid [P(MMA-MAA)] as first resist layer followed by PMMA as second resist layer to enhance the lift-off process and baking at 180°C (Figure 5.21b). The reference alignment markers were defined by electron beam (e-beam)

lithography (Figure 5.21c). Development was done by a 1:3 solution of methyl isobutyl ketone (MIBK) and isopropanol (IPA). After the development process layers of 5nm Cr and 30 nm Au were deposited followed by lift-off and cleaning. Before nanotube deposition, the surface was functionalized with DAS, N-[3-(Trimethoxysilyl)Propyl]-Ethylene-Diamine (97%), molecules. This provides the advantage that Coulomb attraction between the positively charged surface due to NH_3^+ functionalization and the negatively charged carbon nanotubes with SO_3^- -groups from the SDS (sodium dodecyl sulfate) suspension, enhances the deposition. Deposited reference alignment markers served to identify the location of each SWNT which is recorded by atomic force microscopy (AFM) in the tapping mode (Figure 5.21d). The AFM image is used to orient and locate the mask of each CNT based nanodevice. After spin coating again, e-beam lithography was used to structure the individual devices (Figure 5.21f). Exposure to UV light was used for removal of residual resist in order to improve the contact resistance. Figure 5.22 shows a schematic of the proposed device consisting of a single suspended nanotube contacted with Cr/Au pads and gate oxide of SiO_2 of 200 nm thickness, which was etched to suspend the nanotubes.
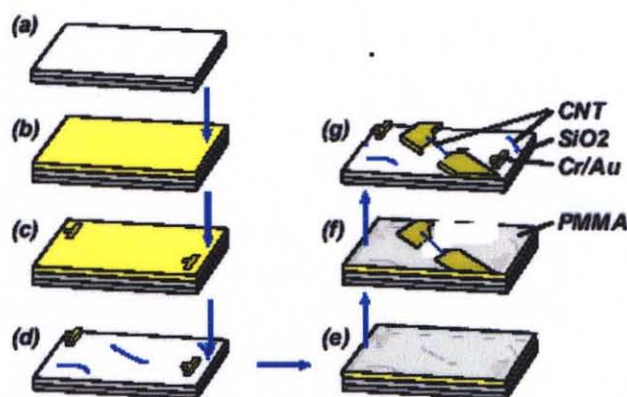
Figure 5.21 Process flow for individual SWNT based gas sensor. [Source: Stampfer et al. IEEE 2004].
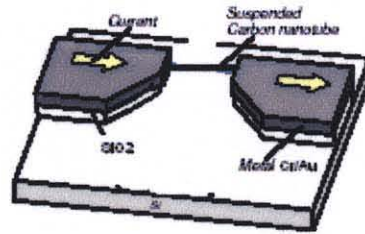
Figure 5.22 Suspended SWNT connected with Cr/Au metal contacts on 200 nm SiO_2 gate oxides. [Source: Stampfer et al. 2004].

The contacts were wire bonded with aluminum wires, and a pin assignment was performed. Two pins were assigned as gate and numbered 5 and 15 (readers should refer to left bottom image for each sample shown in Figure 5.23) and on each sample 8 SWNTs were contacted with Cr/gold pads. Figure 5.23 shows the pin diagrams for Samples A, B, C, D

Sample #A
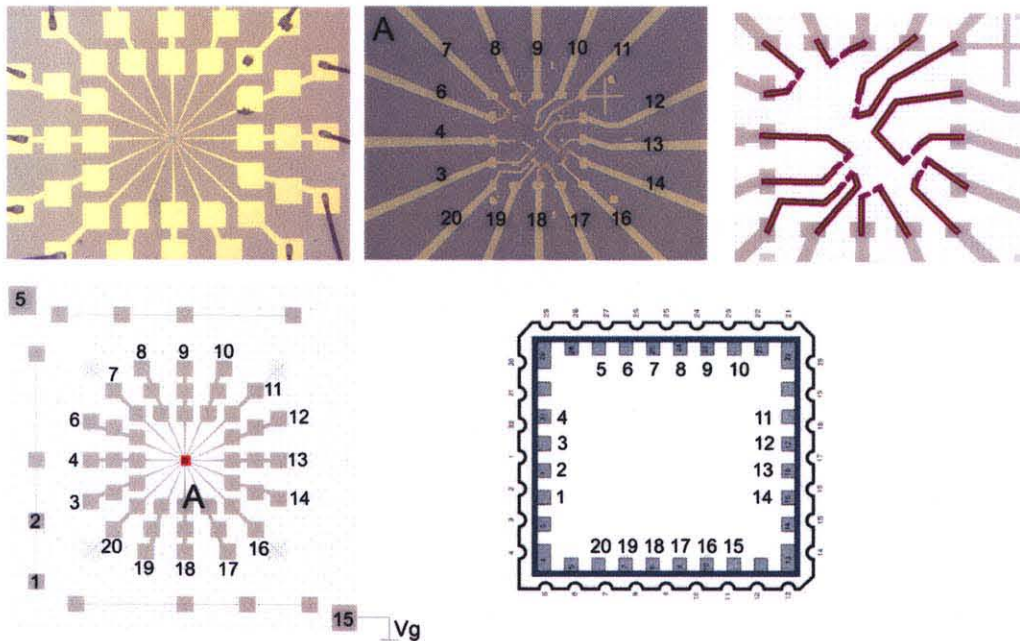
Figure 5.23 Pin assignments for Samples A.
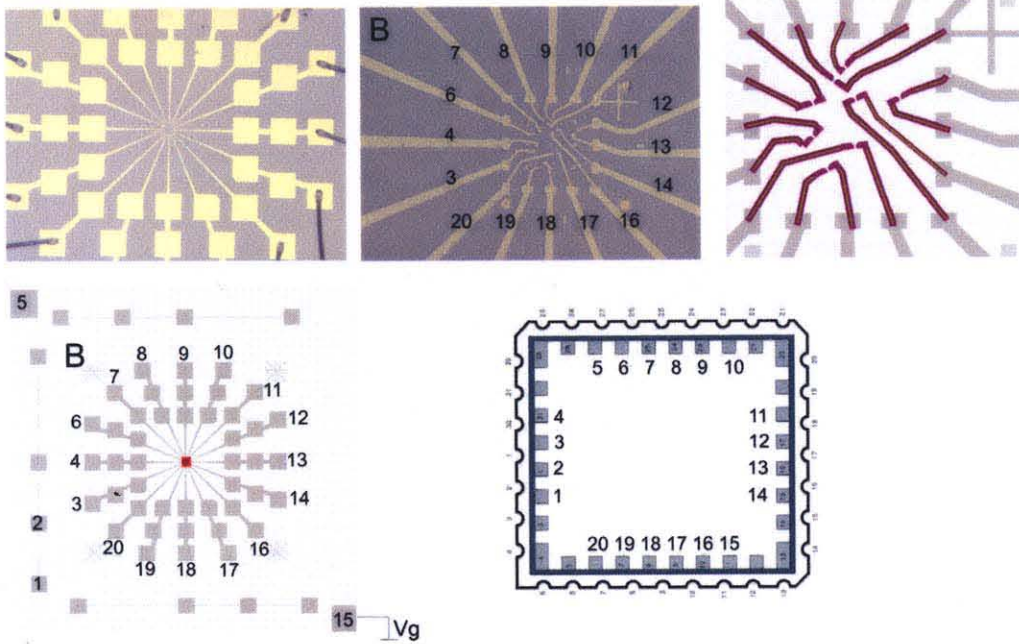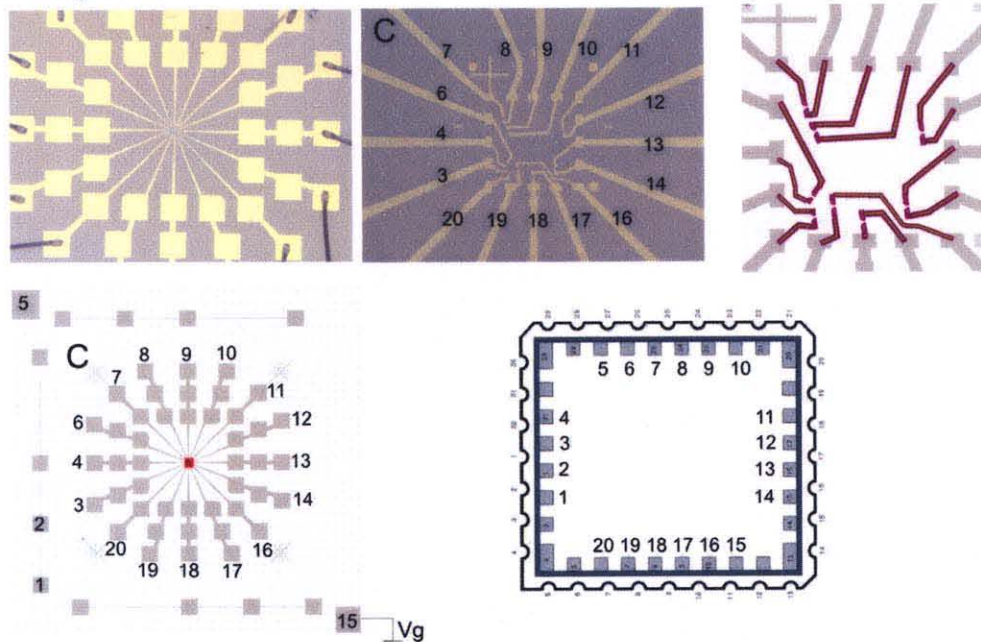
Figure 5.23 Pin assignments for Samples B, C **(continued)**.

Sample #D
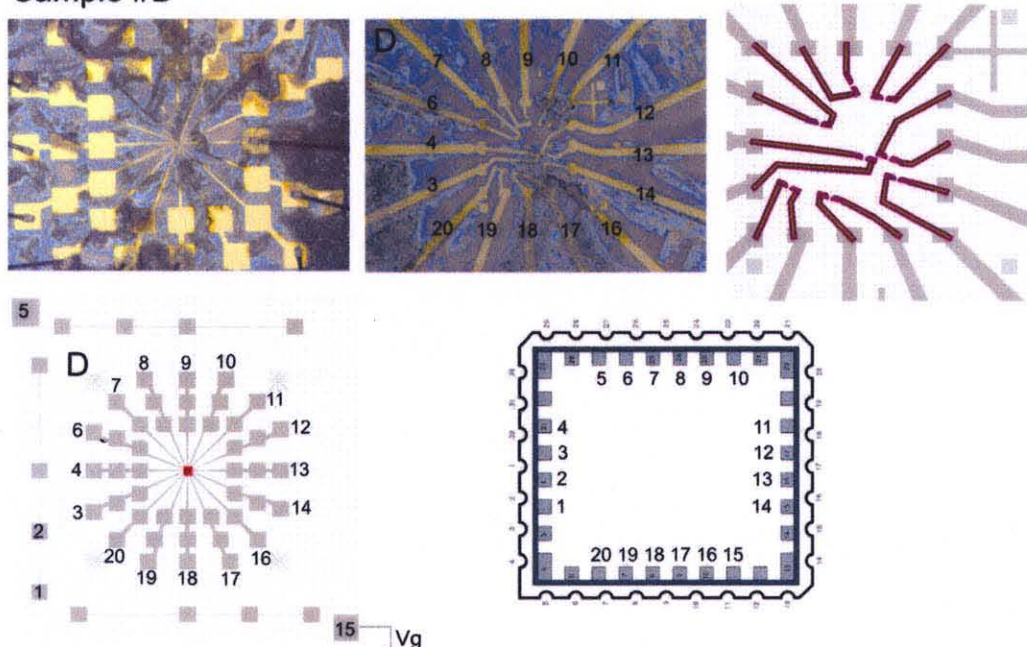
Figure 5.23 Pin assignments for Samples D (D-Functionalized with BaO) **(continued).**

5.6.1.2 Chemical Functionalization. BaO is a well known NO_2 scavenger and widely used in catalytic converters in the automobile industry (Fridell, 1999). Sample D is functionalized with BaO in order to increase selectivity and sensitivity towards NO_2. The sample was immersed in a barium nitrate solution for 24 hours at 100 °C followed by rapid thermal annealing at 600 °C in an argon atmosphere to form BaO coatings. The reaction involving NO_2 uptake is:

$$BaO + 2NO_2 + O \leftrightarrow Ba(NO_3)_2$$
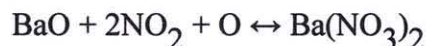
At room temperature only physiosorption of NO_2 has been reported. As catalytic converters are exposed to hot gas the regeneration of catalyst takes place continuously. Following the recovery can be achieved in two ways, either by heating the device or by using UV exposure to remove adsorbed NO_2 since the reaction is reversible.

5.6.1.3 Characterization by AFM. AFM in the tapping mode was used to determine the location and orientation of the SWNTs.

SWNT 2 on Sample #B 1.46 nm   SWNT 6 on Sample #C 1.06 nm
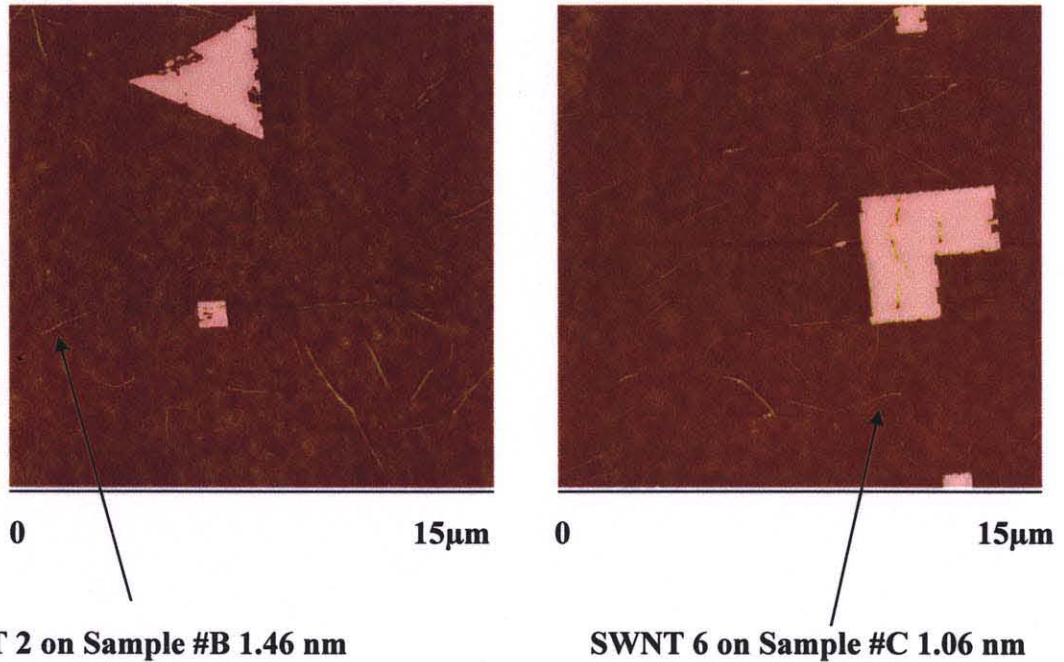
Figure 5.24 AFM images for single walled carbon nanotubes to determine location and orientation for contacting with chrome/gold pads with e-beam.

5.6.2 Electrical Measurements

Electrical measurements were performed both on gold structures used as dummy and

SWNT contacted with Cr/Au contacts.

Description of Measurement modes:

In all the modes described below the current between source-drain (I_{sd}) was measured

with a high precision current amplifier, with an amplification factor of k and converted to

voltage $V_{sd} = k$. I_{sd} I-V characteristics are plotted for each mode as described below.

Measurement Mode 1 (MM1): corresponds to a constant source drain voltage, $V_{sd} =$

constant and a constant gate voltage, $V_g =$ constant (Typical values used $V_{sd} = 150$ mV

and $V_g = 0$)

The sequence of measurements is shown in the schematic below in Figure 5.25 a: from 0 to a set point and than back to zero when measurements are aborted, both V_{sd} and V_g were measured.
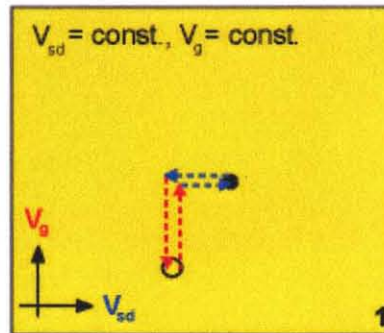
Figure 5.25 a Measurement Mode 1 sequence: results are plotted as I_{sd} vs sequence for this mode.

Measurement Mode 3 (MM3): corresponds to a constant gate voltage, V_g = constant and a source drain sweep $-V_{sd}$ to $+V_{sd}$ (Typical values used V_g = 0 V and V_{sd} = -250 mV to +250 mV)

The sequence of measurements is shown in the schematic below Figure 5.25 b: V_{sd}; zero to positive set point, from positive set point to negative set point and than back to zero value. V_g; zero to set point and back to zero when V_{sd} sweep cycle is complete.
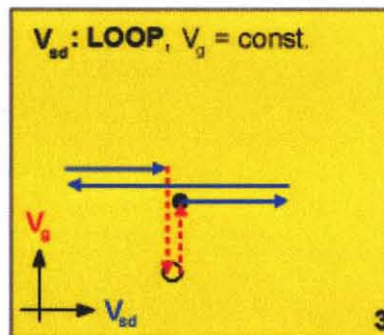
Figure 5.25 b Measurement Mode 3 sequence: results are plotted as I_{sd} vs V_{sd}.

Measurement Mode 5 (MM5): corresponds to a constant source drain voltage, Vds = constant and a gate sweep, $-V_g$ to $+V_g$ (Typical values used V_{sd}= 150 mV, V_g = -20 V to 20 V)

The sequence of measurement is shown in the schematic below Figure 5.25 c: V_{sd}; zero to set point and back to zero when V_g sweep is complete. V_g; zero to positive set point, from positive set point to maximum negative set point and finally from negative set point to zero.
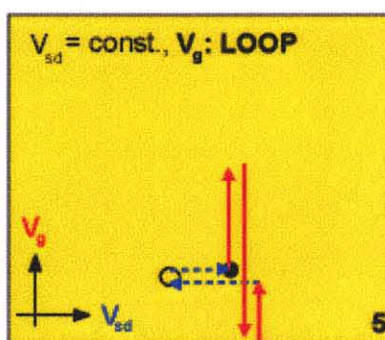
Figure 5.25 c Measurement Mode 5 sequence: results are plotted as I_{sd} vs V_g

Scheme 1: Electrical measurement for a single gas

First the device was allowed to cool to room temperature under dry gas flow. The gas test bench was programmed in the following manner e.g. Table 5.3, dry gas flow for 15 minutes, followed by flow of gas to be analyzed for a period of 1-2 hrs (sufficient enough to make measurements in all three modes), followed by purging with dry gas for 15 -30 minutes.

Table 5.3 Example for a Test Bench Program for a Single Gas Measurement in Three Electrical Measurement Modes Following Scheme 1

Gas XX

Segment no.	Gas/Gases	Time	Concentration
1	Dry Gas	15 min	Purge gas
2	Gas XX	1-2 hrs	YY ppm
3	Dry Gas	15-30 min	Purge gas

Electrical measurements under scheme 1: Firstly measurements in MM1 were carried out under dry gas flow (15 minutes) and continued under the gas to be analyzed; these measurements were typically stopped after 15-20 minutes of the analysis gas (XX) flow. A few minutes of time was used to reenter the new parameters for the MM5. Measurements were continued for MM3 and after the cycle was completed, XX gas flow was aborted (total time required for all three modes varied between 40 minutes to 1:30 minutes) and dry gas was allowed to purge the chamber. The same sequence was followed for all the gases and also for humid gas environments where dry gas was replaced by humid gas.

Scheme 2: Electrical measurements for all gases in series

Continuous measurements in MM1 were used in order to determine response of various gases. Gas test bench was programmed in the following manner (refer to Table 5.4 below). For each gas two concentration set points were used and purged with dry gas before a new gas was allowed to flow into the chamber. Same measurements were also carried out in humid gas environment where dry gas was replaced by humid gas.

Table 5.4 Example of Gas Test Bench Program for All Gases in Electrical Measurement Mode 1 Following Scheme 2

Segment No.	Gas/Gases	Time	Conc.
1	Dry Gas	15 min	Pürge
2	Methane	15 min	3000 ppm
3	Methane	15 min	6000 ppm
4	Dry Gas	15 min	Pürge
5	Hydrogen	15 min	5000 ppm
6	Hydrogen	15 min	10000 ppm
7	Dry Gas	15 min	Pürge
8	Carbon Dioxide	15 min	0.50% (5000 ppm)
9	Carbon Dioxide	15 min	2.0% (20000 ppm)
10	Dry Gas	15 min	Pürge
11	Dry Gas	15 min	Pürge
12	Ethyl acetate	15 min	24 ppm
13	Ethyl acetate	15 min	60 ppm
14	Dry Gas	15 min	Pürge
15	Carbon Monoxide	15 min	20 ppm
16	Carbon Monoxide	15 min	50 ppm
17	Dry Gas	15 min	Pürge
18	Ammonia	15 min	30 ppm
19	Ammonia	15 min	90 ppm
20	Dry Gas	15 min	Pürge
21	Nitrogen dioxide	15 min	60 ppm
22	Nitrogen dioxide	15 min	200 ppm
23	Dry Gas	15 min	Pürge

5.7 Results and Discussion

Measurements to make sure nanotube exists on device: Each tube was tested in order to make sure that the measurements were made on nanotubes and not the shorts between the tube and gate oxide.

For example, measurements on CNT 2 on sample B are shown in Figure 5.26 b. In order to make these measurements one of the contacts was used to apply the source drain voltage, and the second metal contact was grounded. In the second measurement one contact was used to apply the source drain voltage and the other one was kept floating. Similarly the second contact was used as a contact to apply the source drain voltage and the other contact was gounded and then kept floating. In total four measurements were performed (shown in Figure 5.26 a). The motive for these measurements was to find the current flow path. Of the above-mentioned verification steps, there were only two possible conduction paths (61 and 63) and makes sure that there is no current flow in the case of floating combinations (for example in 60 and 62 there is only some leakage current). In case the tube is shorted with the substrate, higher current flow must be observed in the plots for the 60 and 62 settings, which is not the case. The I-V characteristics are shown in Figure 5.26 b. The numbers 60,61,62,63 correspond to the plots in Figure 5 - for details please refer the caption for graph.
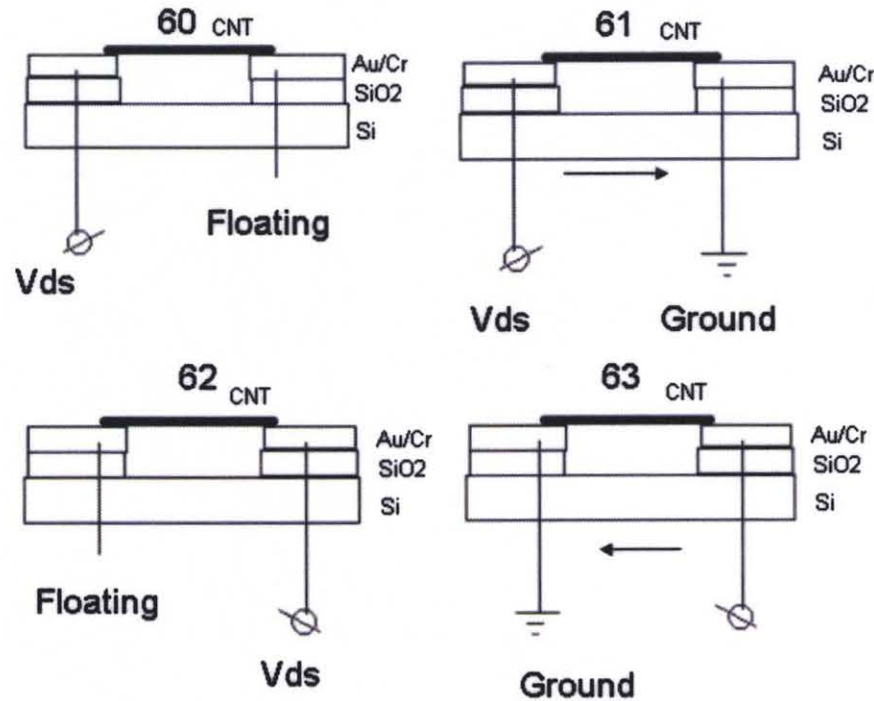
Figure 5.26 a Schematic showing connections and SWNT verification measurements.
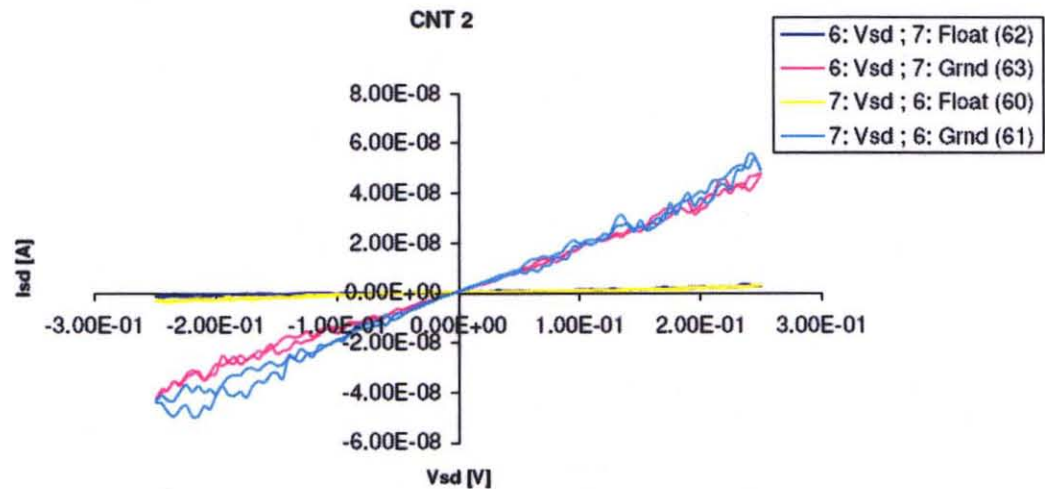
Figure 5.26 b Leakage checks: verification to check nanotube is measured and not bond shorts.

Dry Gas flow measurements to obtain transistor characteristics: Followed by these measurements devices were heated at 120 °C for 10-12 hrs in order to remove the absorbed moisture from ambient. The transistor characteristics were then recovered to

find a working point. As shown in Figure 5.27, a gate sweep from $-V_g =20$ V to $V_g = 20$

V at constant $V_{sd} = 150$mV was performed.

$$I_{on} = 37.9nA \; G_{on} = 25.3 \; \mu\Omega^{-1} \; R_{on}= 3.96M\Omega$$
$$I_{off} = 1.66nA \; G_{off} = 11.1 \; n\Omega^{-1} \; R_{off}= 90.5 \; M\Omega$$
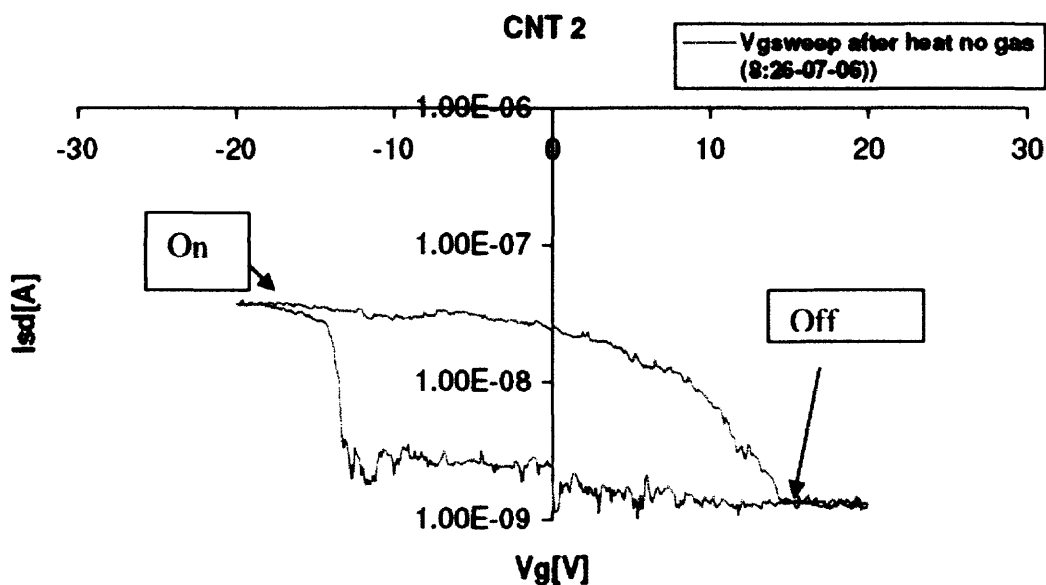
Figure 5.27 Measurement Mode 5 to determine the transistor characteristics. V_g = -20 to 20 V, V_{sd} = 150 mV.

Figure 5.28 displays the I-V bias curve for CNT2 on sample B. At $V_g = 0$, nonlinearity in

the I-V curve at room temperature and the asymmetric dependence of the conductance on

the gate voltage indicates that the nanotube is semiconducting.

CNT 2
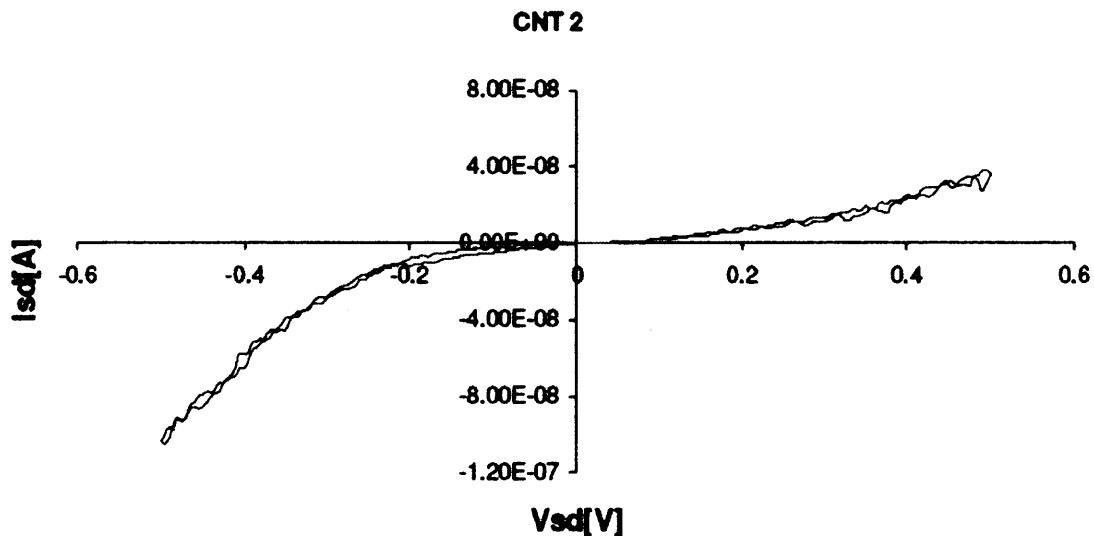
Figure 5.28 Measurement Mode 3 V_{sd} sweep from -20 V to 20 V, $V_g = 0$.

5.7.1 Electrical Measurements with Gas Flow

SWNTs were exposed to 10-300 ppm of NO_2, and representative response curves shown in Figures. 5.29 were measured. The response under gas flow was measured in three modes as described in the experimental section under scheme 1 and in MM 1 under scheme 2. Previous studies have reported a change of one order of magnitude in conductance for NO_2 concentration of 200 ppm in 2-10 seconds; 100 ppm of NO_2 were also detected in the same time scale of 2-5 seconds. There was a difference in the control gas being used because in the earlier studies nitrogen was used prior to the introduction of NO_2 at detectable concentrations. In studies where dry gas, which is a mixture of 80% N_2 and 20% O_2 was used as control gas, the baselines were higher because O_2 like NO_2 is an electron acceptor and contributes towards holes and thereby conductance. In future it is planned to make measurements with pure N_2 flow so as to compare results with previous work. In Table 5.5 shown (scheme 2) below, the time period and gas concentrations for each gas are listed for a run that was made overnight. For each gas,

two concentrations were measured and the chamber was purged for 15 minutes with dry gas before a new gas was introduced. Figure 5.29 a, and b show the I_{sd} vs sequence and gas concentration results. It can be clearly observed that there is a significant change in source drain currents with flow of NO_2 (in the last three segments). Exposure to NO_2 rapidly increased the I_{sd} or source drain current, consequently increasing the conductance. Similar behavior has been observed with the devices reported by Kong (2000). Theoretical (Kong, 2000; Peng, 2000 and Chang, 2001) and experimental studies (Kong, 2000) have attributed this phenomenon to electron donation from the carbon nanotube to the electron accepting NO_2 molecule. As-prepared SWNTs are p- or hole doped semiconductors due to their interaction with molecular oxygen. The acceptance of electrons by NO_2 increases the conductance of the SWNT structure via the creation of further holes in the valence band of the semiconducting nanotube. Figure 5.29 a and b show the response to various other gases (refer to Table 5.5), with no substantial change in source drain current observed with the exception of hydrogen at 10,000 ppm. The work reported in this thesis focuses mainly on the results for NO_2. However, the results obtained from other gases are listed in the appendices in the order of measurements conducted.

Table 5.5 Gas Concentrations for Measurement Mode 1 Run Made Overnight: $V_{sd} = 150$ mV, $V_g = 0$ V

Segment No.	Gas/Gases	Time	Conc.
1	Dry Gas	15 min	Purge
2	Methane	15 min	3000 ppm
3	Methane	15 min	6000 ppm
4	Dry Gas	15 min	Purge
5	Hydrogen	15 min	5000 ppm
6	Hydrogen	15 min	10000 ppm
7	Dry Gas	15 min	Purge
8	Carbon Dioxide	15 min	0.50% (5000)
9	Carbon Dioxide	15 min	2.0% (20000)
10	Dry Gas	15 min	Purge
11	Ethyl acetate	15 min	24 ppm
12	Ethyl acetate	15 min	60 ppm
13	Dry Gas	15 min	Purge
14	Carbon Monoxide	15 min	20 ppm
15	Carbon Monoxide	15 min	50 ppm
16	Dry Gas	15 min	Purge
17	Ammonia	15 min	30 ppm
18	Ammonia	15 min	90 ppm
19	Dry Gas	15 min	Purge
20	Nitrogen dioxide	15 min	60 ppm
21	Nitrogen dioxide	15 min	200 ppm
22	Dry Gas	15 min	Purge
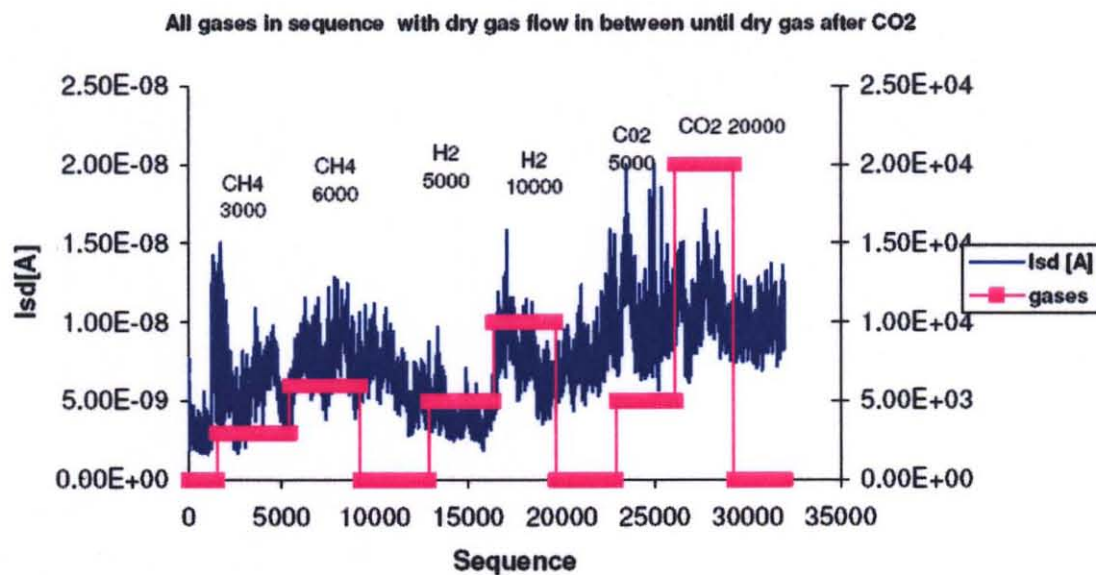
Figure 5.29 a MM 1 run, overnight, V_{sd} = 150 mV, V_g =0. Data plotted from start until the end of CO_2 flow (refer to Table 5.5).
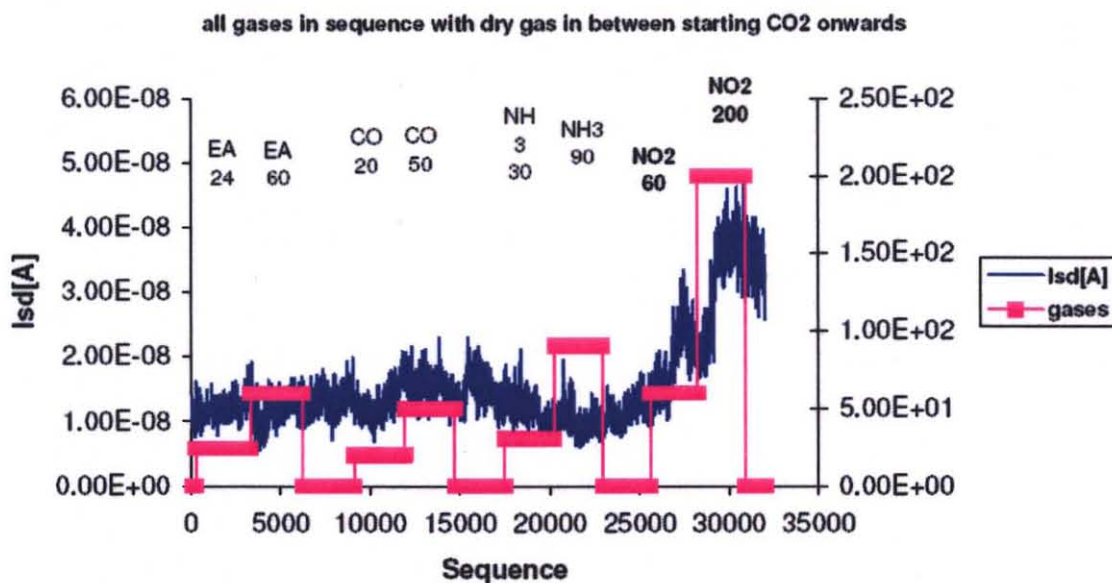
Figure 5.29 b MM1 V_{sd} = 150 mV, V_g = 0. Data plotted from dry gas purge after CO_2 flow until end of the run (refer to Table 5.5).
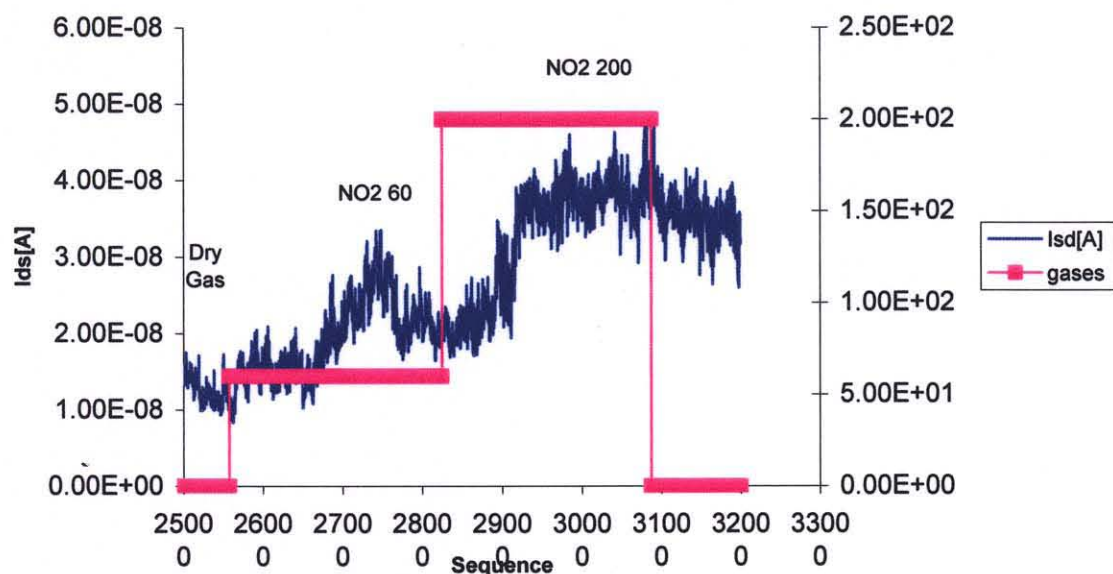
Figure 5.30 Of the above data (Figure 5.29 b) only last three segments comprising of dry gas, followed by two concentrations of NO$_2$ (60 and 200 ppm) are plotted.
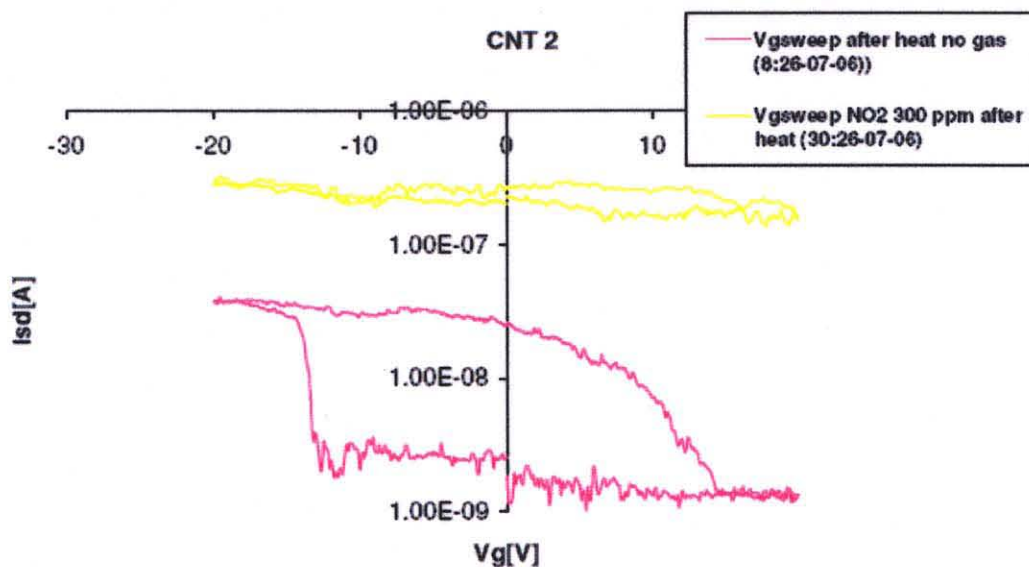
Figure 5.31 Measurement Mode 5: V$_g$ sweep = -20 V to 20 V, V$_{sd}$ = 150 mV.

Low concentration runs to check the lower onset of detection were performed after recovering the device by heating overnight at 120 °C. 10 ppm of NO$_2$ concentration was used and measurements were done in three modes (scheme 1), plots are as shown in

Figure 5.32 (MM1), Figure 5.33 (MM3), Figure 5.34 (MM5). In MM1 clear change in I_{sd} can be observed although at such low concentrations almost no change in gate sweep and source drain sweep can be observed.
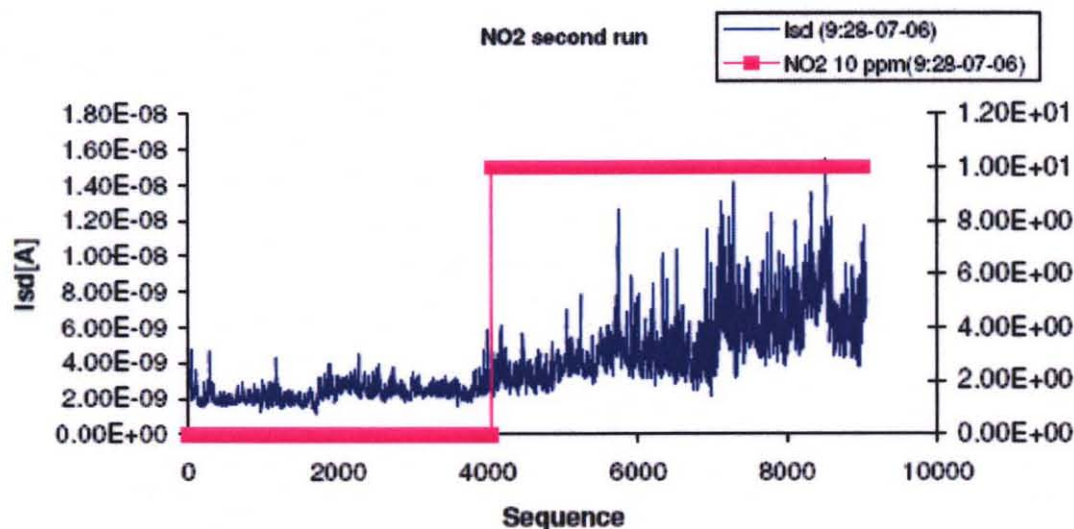
Figure 5.32 Measurement Mode 1 measurements, with 10 ppm of NO_2. $V_{sd} = 150$ mV, and $V_g = 0$ V.
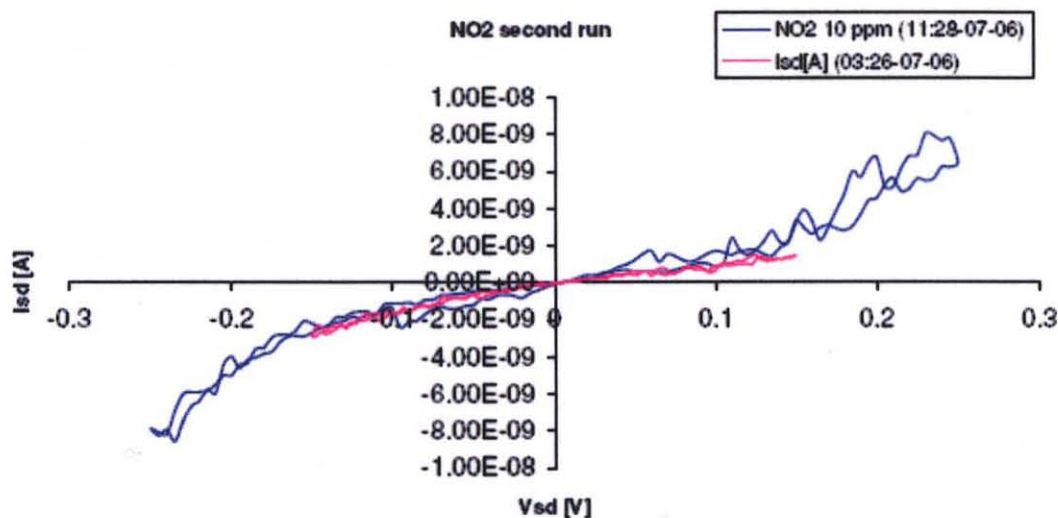
Figure 5.33 Measurement Mode 3, 10 ppm of NO_2 $V_{sd} = -250$ mV to 250 mV and $V_g = 0$.
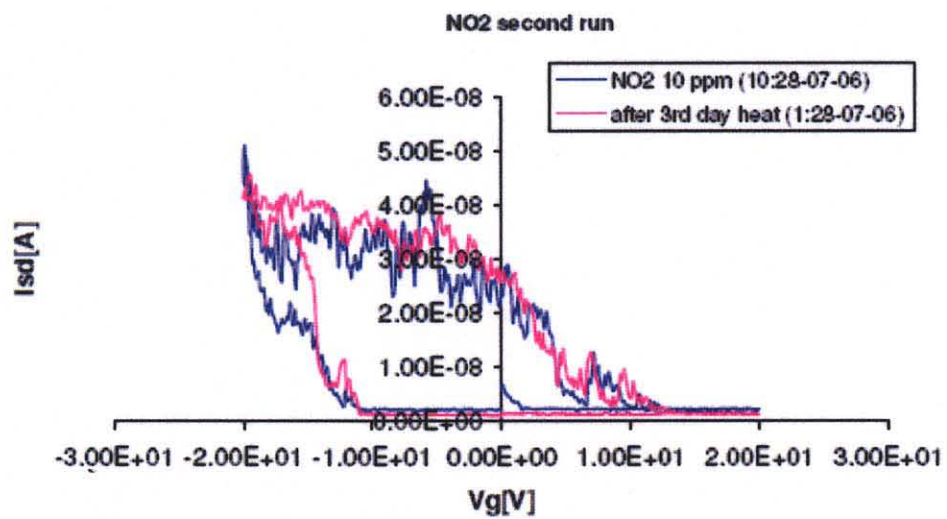
Figure 5.34 Measurement Mode 5, 10 ppm of NO_2 V_g = -20 to 20 V, V_{sd} = 150 mV.

Table 5.6 Gas Concentrations for Measurement Mode 1 run made overnight: V_{sd} = 150 mV, V_g = 0 V

Segment No.	Gas/Gases	Time	Conc.
1	Dry Gas	15 min	Purge
2	Methane	15 min	3000 ppm
3	Methane	15 min	6000 ppm
4	Dry Gas	15 min	Purge
5	Hydrogen	15 min	5000 ppm
6	Hydrogen	15 min	10000 ppm
7	Dry Gas	15 min	Purge
8	Carbon Dioxide	15 min	0.50% (5000)
9	Carbon Dioxide	15 min	2.0% (20000)
10	Dry Gas	15 min	Purge
11	HC Mix[a]	15 min	60 ppm
12	HC Mix[a]	15 min	150ppm
13	Dry Gas	15 min	Purge
14	Carbon Monoxide	15 min	20 ppm
15	Carbon Monoxide	15 min	50 ppm
16	Dry Gas	15 min	Purge
17	Ammonia	15 min	30 ppm
18	Ammonia	15 min	90 ppm
19	Dry Gas	15 min	Purge
20	Nitrogen dioxide	15 min	60 ppm
21	Nitrogen dioxide	15 min	200 ppm
22	Dry Gas	15 min	Purge

[a]HC-Mix Acetylene 0.3%
Ethane 0.3%
Propane 0.3%
Ethylene 0.3%
Nitrogen. Rest
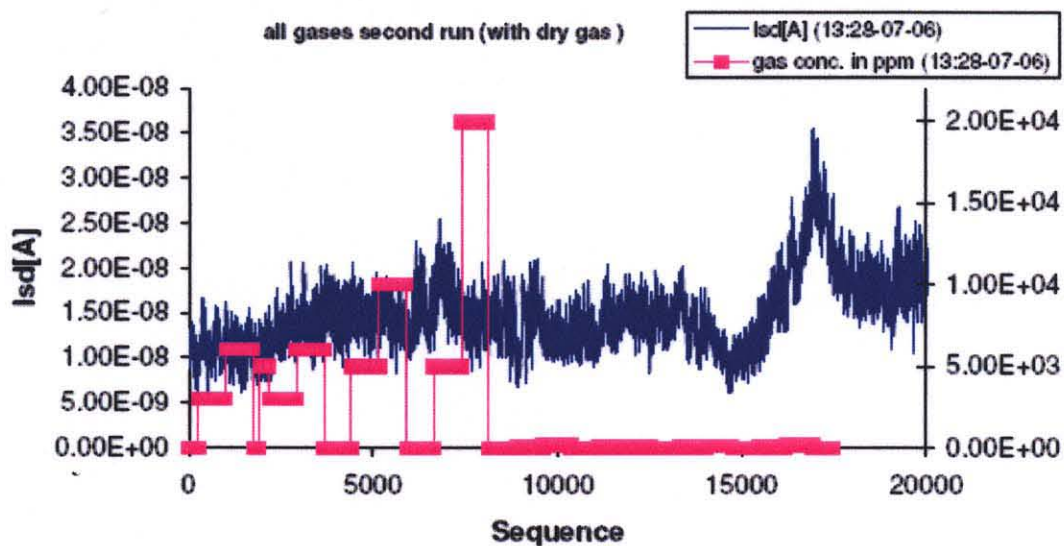
Figure 5.35 Measurement Mode 1, V_{sd} = 150 mV, V_g = 0. Nanotube was subjected to gases as shown in Table 2.

Sample C CNT6

The second device was tested for NO_2 beyond these measurements. The first two plots were under dry gas flow environment and can be used as reference for comparison when subjected to NO_2 flow. This tube showed nearly linear I-V bias characteristics as depicted in Figure 5.36
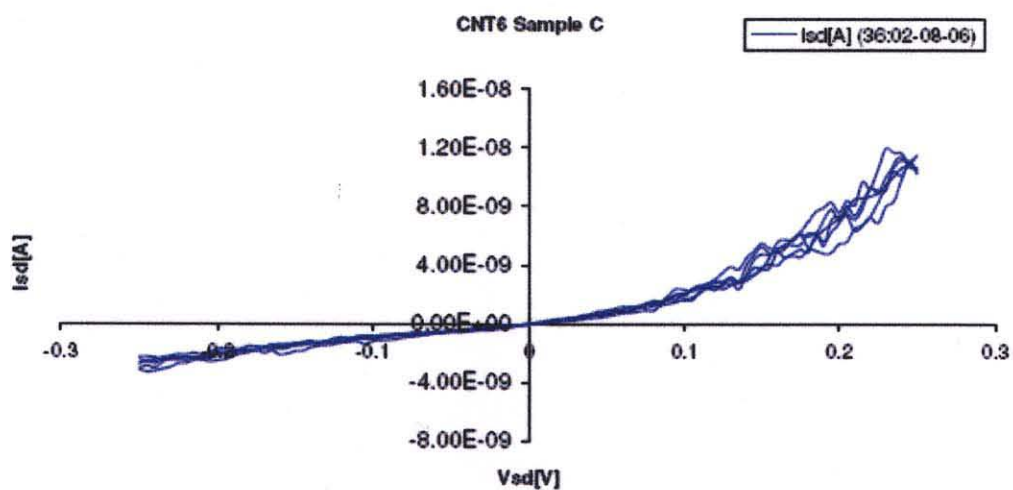
Figure 5.36 CNT 6 on sample C, measurement mode 3, V_{sd} = -250 mV to 250 mV and V_g = 0.
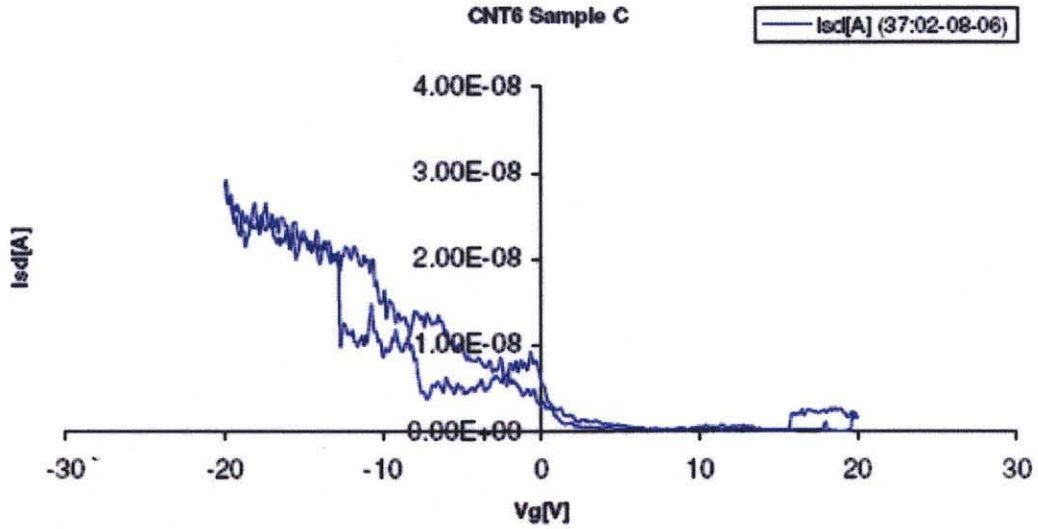
Figure 5.37 Measurement mode 5, V_g = -20 V to 20 V, V_{sd} = 150 mV.

Refer to Table 5.6 for the gas concentrations for the results shown in Figures. 5.38 and 5.39. As expected from the previous result, this device also showed a considerable change in source drain current for NO_2 gas. Same concentrations were used as before of 60 and 200 ppm. Both source drain current and gas concentration data for all the gases are shown in Figure 5.38.
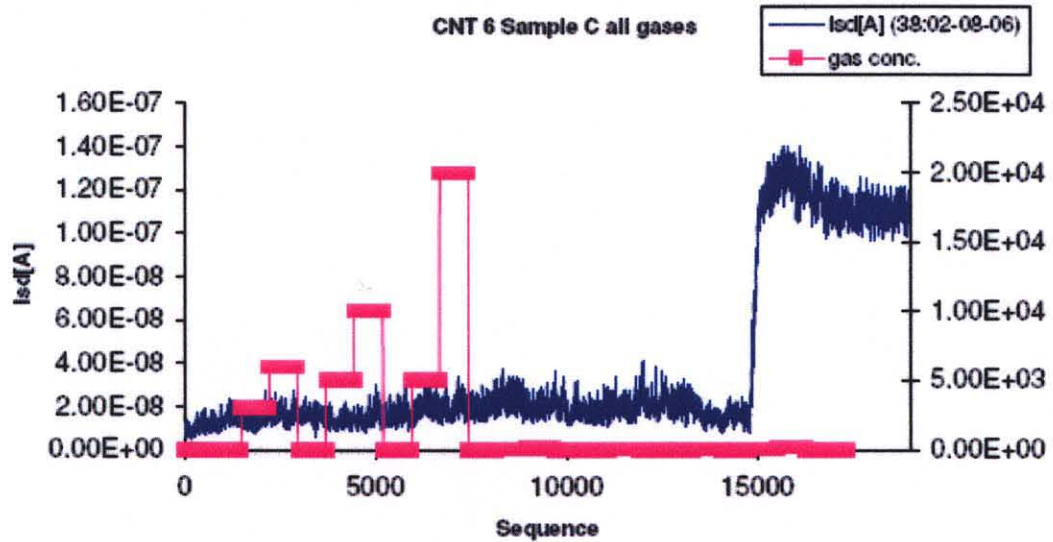
Figure 5.38 Measurement mode 1 V_{sd} = 150 mV, V_g = 0. All gases in series with dry gas used to purge.
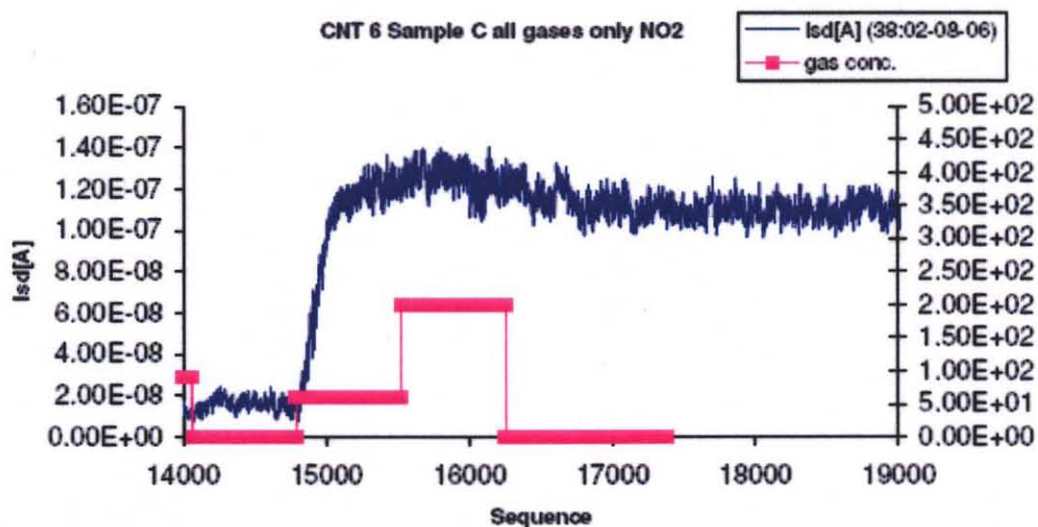
Figure 5.39 The plot shows only the last three segments from Figure 5.38. The last three segments comprise of dry gas followed by two concentrations of NO_2 (60 and 200 ppm).

Another set of measurements was performed at a fixed concentration of 100 ppm of NO_2.

Measurements were made in all the three modes as shown in Figures. 5.40 (MM1), 5.41 (MM3), and 5.42 (MM5).
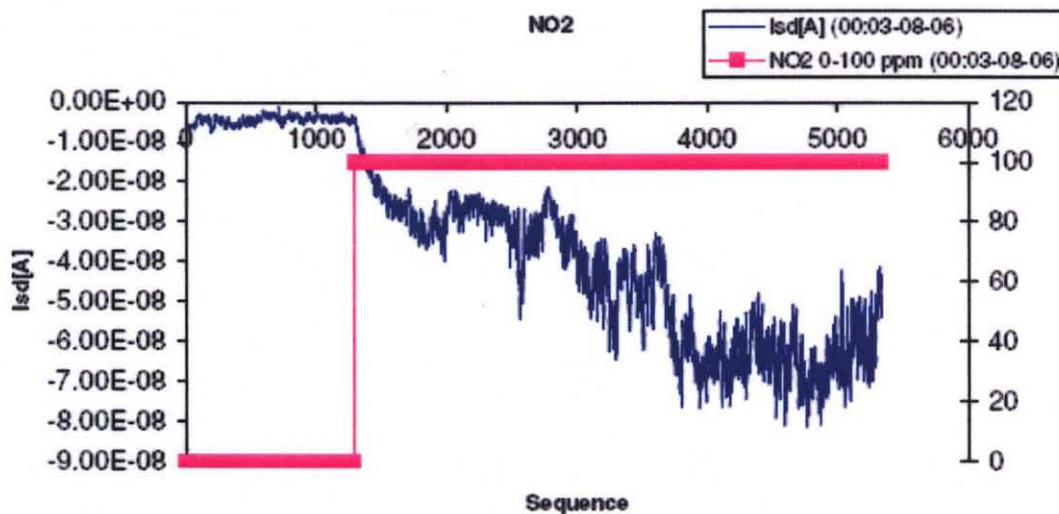
Figure 5.40 Measurement mode 1 V_{sd} = -250 mV, V_g = 0. NO_2 100 ppm.
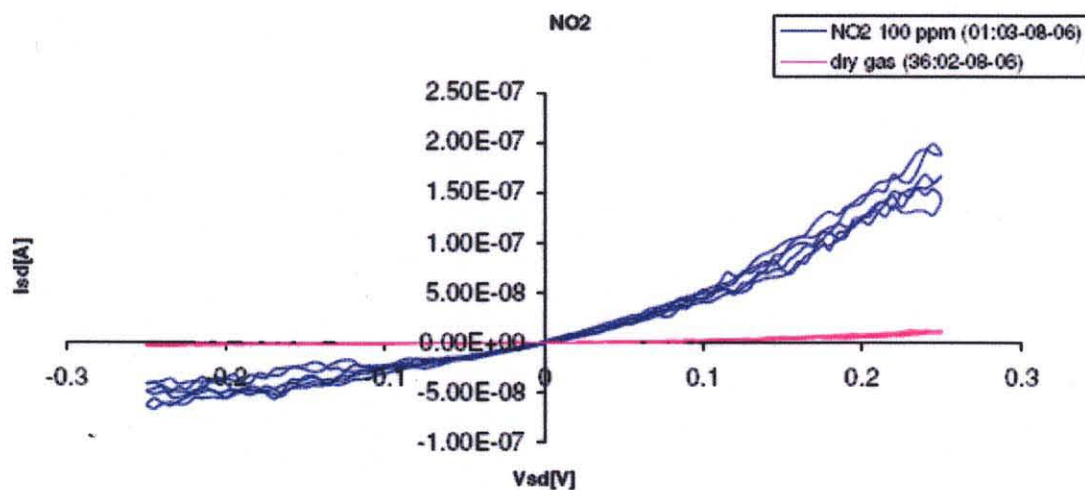
Figure 5.41 Measurement mode 3, V_{sd} = -250 mV to 250 mV, V_g = 0.
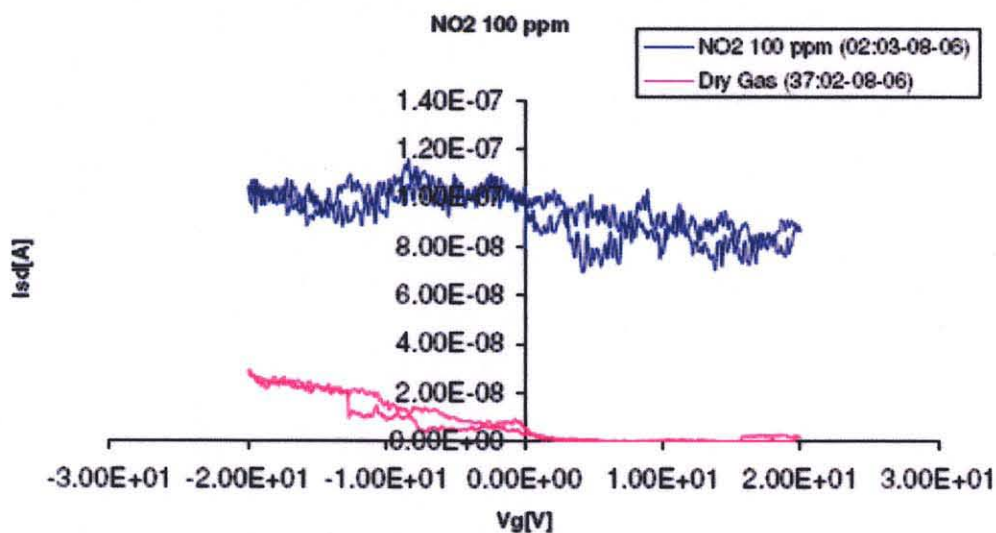
Figure 5.42 Measurement mode 5, V_g = -20 to 20 V, V_{sd} = 150 mV.

5.7.2 Device Recovery

UV exposure and thermal treatment were used to recover the device. Some results presented here to show that the device was fully recoverable by thermal treatment. Electrical measurements were performed while the device was being heated to determine the time required to reach the initial state of the device and the rate of recovery. (UV

results can be found in Appendix 1). Figure 5.43 shows the MM 5 measurements at the initial stage i.e. after heating and not subjected to any gas environment and the second plot represents the data after a whole day of measurements with various gases followed by heating overnight at 120 °C.
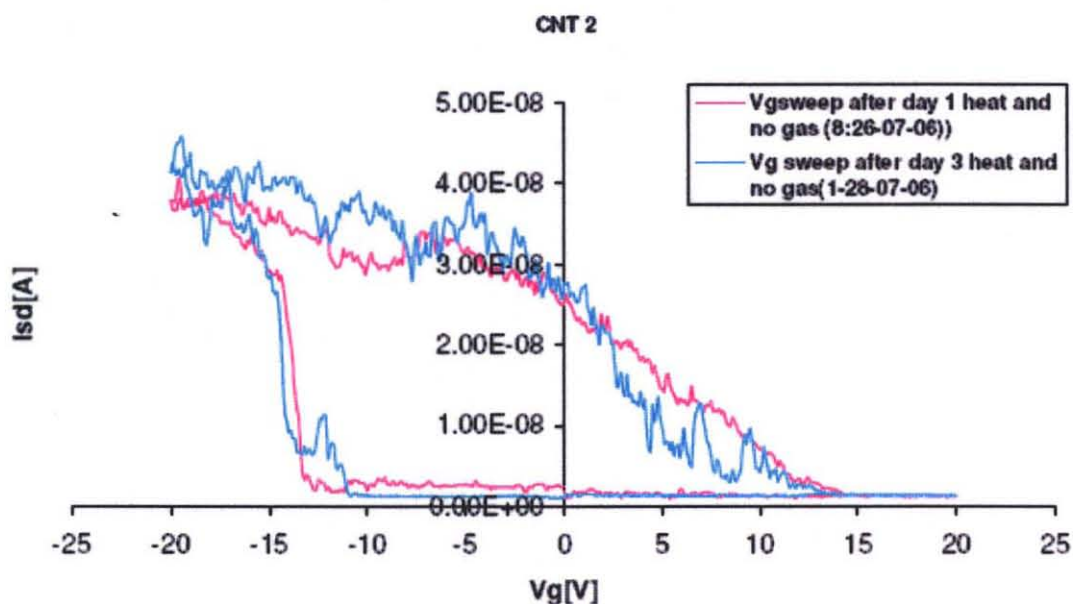
Figure 5.43 Device recovered by heating at 120 °C. Pink curve before and blue curve heated after exposure to various gases.

Results are shown in Figure 5.44 A-C, the scales on all the plots are the same so as to visually monitor the change in hysteresis. Finally, Figure 5.45 shows the source drain current at $V_g = 0$ vs. time to find the rate of recovery for the device. Seven cycles of measurements were completed and then it was stopped due to a burning smell from the other sensors placed in the same chamber. The aluminum box used to house the device was perfectly sealed and was under dry gas flow, therefore hindrance due to other gaseous or vapors has a weak possibility.
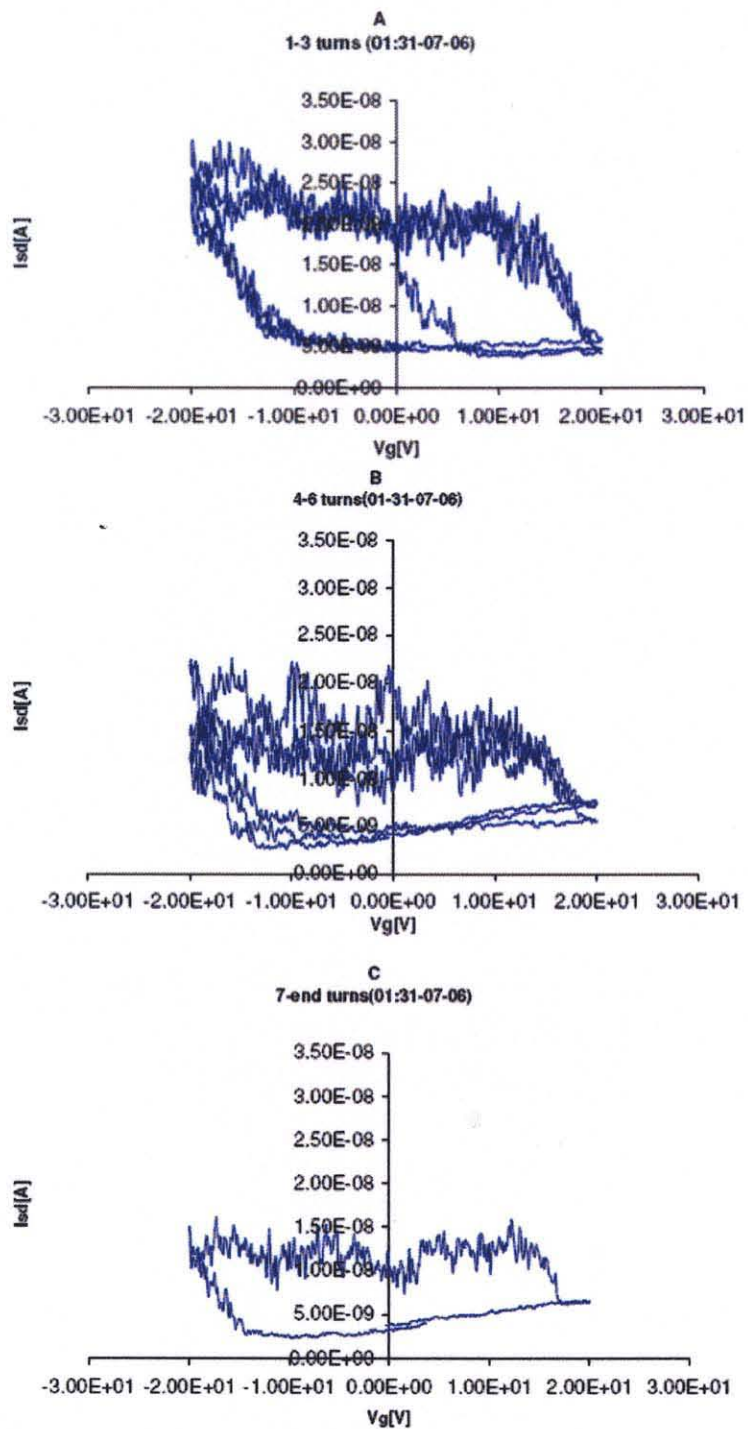
Figure 5.44 (A-C) Continuous MM 5 measurements to find the time for complete device recovery.
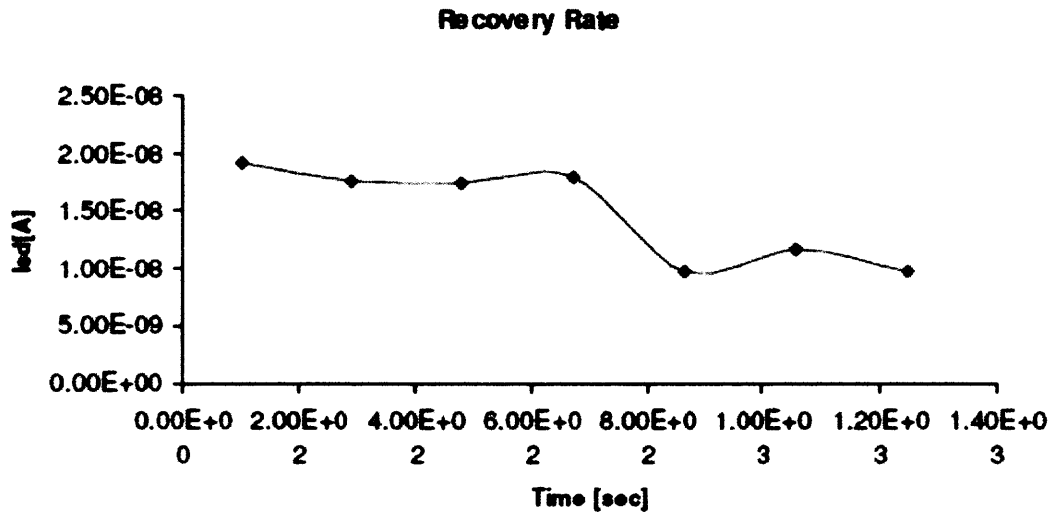
Recovery Rate

Figure 5.45 Recovery rate: I_{sd} (higher I_{sd} value from plot 27 A-C) at $V_g = 0$ vs time.

Binding energy for the NO_2 molecule at room temperature is in the range of -0.34 eV to -0.79 eV (Peng, 2004). Using these values the recovery time can be calculated using equation shown below:

$$\tau = v_0^{-1} e^{(-E_B/K_B T)}$$

where the parameters: τ = recovery time (s),

K_B = Boltzmann constant (8.62 × 10^{-5} eV K^{-1}),

E_B = Binding energy (eV),

T = Temperature (K), and

V_0 = attempt frequency (10^{12} s^{-1})

It corresponds to a recovery time of 0.5 μs to 16 s. However, from the recovery result shown above it was observed that the time needed to recover is of the order of 10-12 hrs at a higher temperature (120 °C). Conversely the binding energy of a molecule for such recovery times and under these conditions would be -1.38 eV. This indicates that the NO_2 molecule binds to the SWNTs in some other molecular arrangement, possibly as NO, NO_3 or N_2O_4 (NO_2 dimer). Further electrical measurements as shown here must be

performed to find the recovery time for NO_2 and other gases. This will give a better insight in terms of binding energy of each molecule or its derivatives.

5.8 Conclusions

In this study, a facile room temperature process was used to integrate vertically aligned SWNTs via precise deposition at desired locations. A protocol was developed and carried out to deposit various layers of metals and insulators on a quartz wafer. Initially CVD methods developed earlier and described in Chapter 3 were carried out. It was however observed that nanotube growth by CVD on catalytic metal layers covered with SiN_x resulted in cracking of the SiN_x due to thermal mismatch at the interface. A room temperature electrophoretic method was therefore developed to deposit pre-synthesized SWNTs in small holes of diameter ~100 nm. An electrostatically stable low pH suspension of SWNTs in an aqueous solution of the charging salt magnesium nitrate was prepared. Nanotubes were found to deposit at a DC electric bias of 10 V for 10 minutes and populate almost all the holes created on SiN_x using e-beam lithography. A selective etch process for removal of e-beam exposed SiN_x was developed. RIE etch rates were found for SiN_x to be 244.67 Å/10sec and for ZEP to be of 2266 Å/60 sec. Raman and SEM data revealed aligned SWNT deposits near the center of the holes. The deposition was consistent with a finite element calculation of the distribution of the electric field which was found to be localized at the center of the holes. This suggests that sub-micron dimensions lead to sharp edges of electric field at corners leaving the center of the holes as the main deposition sites.

Second part of this work demonstrates a new approach for the development of molecular sensors with reasonably reproducible performance. Several devices, each with an individually suspended single walled carbon nanotube of different diameter, were successfully fabricated. Few devices were electrically measured to gauge the response of various gases. NO_2 showed a significant response with a lower limit of 10 ppm and response time of 2 -5 seconds (100 ppm) with a sensitivity of 15-20 from the base value of the electrical conductance. Devices were found to be fully recoverable by heating at a temperature of 120 °C for a time period of 10-12 hrs. Functionalized devices did not work as the nanotubes were damaged during the process of functionalization probably due to mechanical forces and a scheme is presented here for use in further experiments. Further investigation is required to get a better understanding of the binding energy of the molecules that are physisorbed on the nanotube sidewalls and tips by making electrical measurements while recovering the devices by thermal treatment. Measurements made on other gases did not show any significant change in source drain current when subjected to various biases in different measurement modes.

CHAPTER 6

CONCLUSIONS

Scaleable Synthesis of SWNTs (Chapter 3): The carbon monoxide chemical vapor deposition (CO-CVD) method was developed and optimized for the production of SWNTs in a scalable manner. Two furnaces, one a horizontal furnace with a small scale boat type reactor and another, a large-scale vertical furnace with a fluidized bed reactor, were set up and characterized for nanotube growth. A Co-Mo/MgO catalyst/support system was studied and it was found that Co is the effective catalyst while Mo acts as co-catalyst or promoter for nanotube growth. It was also observed that if Co, is present in excess of Mo, the catalyst becomes random in shape and size. Spherical monodisperse catalyst of composition Co:Mo in the ratio of 1:4 with the remaining comprised of MgO as catalyst support, was found to be most effective for nanotube growth. The optimum conditions for growth of SWNTs using the small scale reactor were determined in this study. It was observed that nanotube growth initiates at a temperature of 675 °C and above, and the most optimum temperature is around 700 °C. The $I(D)/I(G^+)$ ratios associated with the intensities of the disorder and graphitic lines of the SWNTs, respectively, determined from the Raman data, confirmed this observation. From Co-Mo-carbon phase diagram it was inferred that the Co catalyst converts from the β to the α-phase at the nanotube growth temperature in the presence of Mo, and 0.17 wt % carbon is needed to supersaturate the catalyst metals. Purification of SWNTs was carried out using 4-6 M HCl and thin bundles of very high quality SWNTs were observed with transmission electron microscopy. XRD data revealed complete removal of MgO support

after HCl purification. Yields of 10% by weight of SWNTs were obtained in these small scale experiments. As the flow rate was increased the exit CO_2 gas concentration data revealed a shift in equilibrium suggesting that higher yields can be obtained with increasing flow rates. It was found that the partial pressure of CO above 0.2 atm is needed for nanotube growth; however, the percentage occupation of catalyst sites did not vary with the partial pressure of CO. A rate limited kinetic model with precipitation as the rate limiting step in conjunction with the observed experimental growth was proposed and fitted well with the experimental data. The SWNT formation reaction was observed to follow first order kinetics. An initial scaled up experiment carried out in a fluidized bed using the large-scale vertical furnace showed the formation of SWNTs but at low yields. More detailed optimization of the scaled up process would therefore be necessary and will be continued by new member of the group.

***In-situ* Metal-Carbon Nanotube Composites (Chapter 4):** In this chapter, an *in-situ* CVD method for metal-carbon nanotube composite developed during the course of this work, is discussed. The results indicate that acetates of iron and cobalt supported on the metal matrix particles are ideal catalyst precursors for nanotube synthesis. Several other catalysts studied also indicated the formation of nanotubes, but a layer of carbonaceous material also formed on the surface of the pellets making it difficult to conduct studies of the mechanical properties of the composite formed. Characterization by XRD revealed that no other phases of iron and carbon were formed during SWNT synthesis with CO as the carbon source. MWNT synthesis with acetylene as the carbon source on the other hand resulted in the formation of an iron carbide impurity phase. By mixing acetylene with CO as the carbon source, iron carbide formation was prevented. A

mechanism for the reaction involved is proposed in this chapter and confirmed by XRD measurements. Iron-SWNT and iron-MWNT composites prepared were found to have substantially enhanced compressive yield strength and hardness relative to specimens of similarly treated iron matrices without nanotubes. Increases of yield strength up to 45% and 36 % with ~ 1 wt % of infiltrated SWNTs and MWNTs, respectively, relative to that of similarly treated pure iron samples without carbon nanotubes of the same piece density was observed and Vickers hardness showed an increase of 74% and 96%, respectively. Iron being a very effective catalyst for carbon nanotube growth anchors the nanotube tips to the metal surfaces and creates supporting bridges in the cavities of the metal matrix as shown particularly by transmission electron microscopy. These bridges offset in part the weakening of the composites due to the presence of the cavities or pores in the matrix structure, resulting in higher mechanical strength. The enhanced mechanical strength raises the possibility of using of these nanocomposites in structural and engineering applications. It is expected that further mechanical strength enhancement and weight reduction can be achieved by increased nanotube loading using a more optimized deposition process and by controlling the porosity of the iron matrix.

Biosensor Fabrication (Chapter 5 part a): In this study, a facile room temperature process was used to integrate vertically aligned SWNTs via precise deposition at desired locations. A protocol was developed and carried out to deposit various layers of metals and insulators on a quartz wafer. Initially CVD methods developed earlier and described in Chapter 3 were carried out. It was however observed that nanotube growth by CVD on catalytic metal layers covered with SiN_x resulted in cracking of the SiN_x due to thermal mismatch at the interface. A room temperature

electrophoretic method was therefore developed to deposit pre-synthesized SWNTs in small holes of diameter ~100 nm. An electrostatically stable low pH suspension of SWNTs in an aqueous solution of the charging salt magnesium nitrate was prepared. Nanotubes were found to deposit at a DC electric bias of 10 V for 10 minutes and populate almost all the holes created on SiN_x using e-beam lithography. A selective etch process for removal of e-beam exposed SiN_x was developed. RIE etch rates were found for SiN_x to be 244.67 Å/10sec and for ZEP to be of 2266 Å/60 sec. Raman and SEM data revealed aligned SWNT deposits near the center of the holes. The deposition was consistent with a finite element calculation of the distribution of the electric field which was found to be localized at the center of the holes. This suggests that sub-micron dimensions lead to sharp edges of electric field at corners leaving the center of the holes as the main deposition sites.

Gas Sensors (Chapter 5 part b): This part of the work on nanotube-based sensors demonstrates a new approach for the development of gas sensors with reproducible performance. Several devices, each with an individually suspended SWNT of different diameter, were successfully fabricated. Some of the devices were electrically characterized in order to gauge their response to various gases. NO_2 showed a significant response with a lower limit of 10 ppm and response time of 2 -5 seconds (100 ppm) with a sensitivity of 15-20 from the base value of the electrical conductance. Devices were found to be fully recoverable by heating at a temperature of 120 °C for 10-12 hrs. Measurements made on other gases did not show any significant change in source drain current when subjected to various biases in different measurement modes. Devices with chemically functionalized SWNTs did not work as the nanotubes were mechanically

damaged during the functionalization process; a scheme is presented for use in further experiments. Further investigation is also required to get a better understanding of the binding energy of the molecules that are physisorbed on the nanotube sidewalls and tips by making electrical measurements during the thermal treatment used to desorb the gases from the sidewalls and recover the devices.

In summary, the work presented in this dissertation represents the first phase of the development of a cost-effective CVD approach to scaled up nanotubes using CO as the carbon source, and novel nanotube-based metal composites prepared by chemical vapor infiltration techniques, and nanotube-based biosensors and chemical sensors. In addition an electrophoretic technique for the deposition of vertically aligned SWNTs for biosensor probing devices was demonstrated and initially optimized. Further development of these research areas will continue in the group.

CHAPTER 7

FUTURE WORK

Suggested future work related to the research presented in this thesis can be divided into four parts: (1) Approaches to further improve the scaled up SWNT synthesis process; (2) Use of other metal matrices, particularly aluminum, for forming nanotube-filled metal composites; (3) Alternative fabrication approaches to down-size and further improve the biosensor device, and (4) Variations in electrical measurements to obtain improved understanding of the mechanism of electrical conductance changes in carbon nanotube based gas sensors.

Fluidized bed studies discussed in this thesis have revealed that a more controlled environment is required for scaled up synthesis. In order to determine the right parameters for the large scale synthesis of SWNTs, an exit gas concentration measurement will be helpful. As observed in this study, catalyst/support size and composition is most important for nanotube growth. Only small furnaces were available for catalyst/support oxidation reported in this work. However, it is important that when handling large quantities of catalyst/support mixtures furnaces should be acquired wherein hundreds of grams of mixtures can be oxidized in a safe chemical hood using the protocols developed in this work. This will result in better control of catalyst morphology similar to small scale studies.

For nanotube-based composites, the in-situ technique to make metal nanocomposites should be extended to other metal matrices, particularly aluminum and its alloys. However, in order to form porous pelletized matrices for metals other than iron and steel, special facilities may be needed. In this study room temperature hydraulic

231

compression was used to form iron pellets. For aluminum, copper, and magnesium, hot isostatic or conventional hot pressing may be necessary to consolidate the pellets. One approach attempted in this study to mitigate challenges due to poor consolidation was by mixing metal powders of two or more particle size distributions. It is therefore suggested that commercially available pellets, hot pressed pellets, melt-moulded pellets, or commercially available thin metal foils, be used as metal matrices. Thin foils with arrayed porosity fabricated using anodization techniques can also be used to grow vertically aligned pre-synthesized SWNTs via electrophoresis as discussed in Chapter 5 of this thesis. These foils containing aligned SWNTs can then be hot-pressed to form a layer by layer three dimensional composite. Such a nanocomposite structure would also be easy to model in order to understand changes in mechanical properties, since the process to make nanotubes is already optimized would use pre-synthesized nanotubes prepared by methods that have already been optimized.

For the fabrication of biosensors in this study a mixture of semiconducting and metallic nanotubes was used. Since single stranded DNA assisted technology has very recently become available to separate semiconducting from metallic SWNTs in solution form, it is recommended in future work to use a pure solution of either pure metallic or semiconducting nanotubes.

In the work on nanotube-based gas sensors the fabrication process is found to be very robust; however there is room for improvement in the measurement of the electrical properties of the devices. To determine the device recovery a heated test bench or pressure chamber is required. In the present study the climate chamber could be used only for short time periods because the polymeric wall of the chamber started to melt.

Measurements using a climate chamber with a non-polymeric wall would therefore be necessary. Also, it is recommended that measurements be made in pure N_2 as the inert gas, instead of 80 % N_2 and 20% O_2. This will give better sensitivity and comparison with existing measurements to determine the lowest detectable concentrations. The gas environment chosen for the present study was geared towards the automobile industry and showed good sensitivity and reproducible results. In addition, it would be necessary to use pre-functionalized nanotubes in order to make the device selective towards a particular gas. It was however observed that the nanotubes deposited on the silicon surface were severely damaged after functionalization. The functionalization process also led to short circuiting of the electrical contacts, since they are only 400 nm apart. More controlled electrochemical functionalization approaches may therefore be necessary in order to mitigate these challenges.

APPENDIX A

XRD DATA FOR IRON COMPOUNDS

List of the XRD data from commercially available "expert" data bank linked with Philips

XRD equipment at NJIT.

1. Aluminum 01-089-2769

2. Aluminum 00-004-0787

3. Aluminum carbide 00-001-0953

4. Iron 00-001-1252

5. Graphite 03-065-6212

6. Iron carbide 00-003-0989

APPENDIX B

FABRICATION PROCESS RECIPE FOR BIOSENSOR

Fabrication recipe for the integration of carbon nanotubes on a quartz wafer using conventional CMOS techniques.

Standard Photolithography using Shipley 1830 for Lift-off

Cleaning		
Starting material	Quartz wafers	100 mm dia and 350 μm thickness
Acetone	10 min	at 25 °C
Isopropanol	10 min	at 25 °C
D.I water rinse	10 min	at 25 °C
P-Clean: Sulfuric acid and Hydrogen peroxide mixture	5 min	at 67 °C
Hot. D.I water rinse	5 min	at 58 °C, continuous flow of D.I water
Cold D.I water rinse	5 min	at 25 °C, continuous flow of D.I water
Blow dry N_2	5-10 min	Until completely dry
Thermal drying	30 min	at 120 °C

Photolithography for lift-off using Shipley 1813		
HMDS	1200 rpm/ 40 sec at acceleration setting 5	Priming of sample surface
Shipley 1813	3500 rpm/30 sec, acceleration setting 5	
Pre bake	Oven 10 min	at 90 °C
Cooling	Cold plate 1 min	For relaxation of resist
Thickness	1.35 μm	
MA6 Contact aligner exposure	200 mJ/cm^2	At 10 mW/cm^2 for 20 sec
Microposit developer	MF319 10-30 sec	Pattern visible by bare eye
D.I water rinse	Tray 5 min, Rinse in flowing water 5-10 min	

Cr/Co Thin Film Deposition and Lift-Off

Metal Deposition		
Cr	2 Å/s	10 sec = 20 nm
Co	1 Å/s	120 sec = 120 nm

Lift-off		
Acetone	30 min	Bespatter with pipette, change acetone soften as needed
Isopropanol	30 min	Bespatter with pipette
D.I water	10 min	Bespatter with pipette
Blow dry N_2	5-10 min	Until completely dry

SiN$_x$ layer Deposition using PECVD

PECVD SiN$_x$ 50 nm using Plasma Therm 790 capacitively coupled 13.56 MHz equipment		
Clean system	Isopropanol and Vacuum Pump	To remove deposits from previous runs
Pump	1×10^{-2} Torr	
Heat	Chamber wall @ 20 °C Substrate Holder @ 350 °C	
Purge	N_2 3 min at 1l/min	
Pressure	900 mTorr	
Power	50 W	
NH$_3$	45 sccm	
SiH$_4$	280 sccm	
He	800 sccm	
RF power on		Set the required thickness of 50 nm
Purge to cool down	N_2	Cool down to room temperature

E-beam

E-beam resist and E-beam lithography		
ZEP		
Thickness	2000 Å	
Exposure		

RIE Etch

Reactive Ion Etch (RIE) etch using Trion Technology Phantom instrument		
CHF₃	50 sccm	Gas flow
O₂	5 sccm	Gas flow
Pressure	55 mTorr	
Power	250 W set point	Actual read out 150 W
Time	Exposed for 25 sec	Etch rates: SiNx 247.67 Å/10 sec; ZEP 2266 Å/60 sec

ZEP Resist Cleaning

ZEP removal		
Acetone 10 min	10 min	
Isopropanol	10 min	
D.I water	10 min	

Electrophoretic Deposition of SWNTs

SWNT suspension	10 mg HiPCO tubes;10⁻⁴ moles [Mg(NO₃)₂6H₂0] in 30 ml distilled water; few drops Triton-X surfactant	2-3 hrs sonication
DC bias	-ve electrode Quartz wafer; +ve electrode Platinum wire	10 V, 10 min

APPENDIX C

GAS SENSOR DATA FOR OTHER GASES

Electrical measurements conducted under different gas environments to test SWNT based gas sensors.

Carbon Dioxide

Mode 1: measurements at a gas conc. of 5000 ppm of CO_2 Vsd = -250 mv and Vg = 0
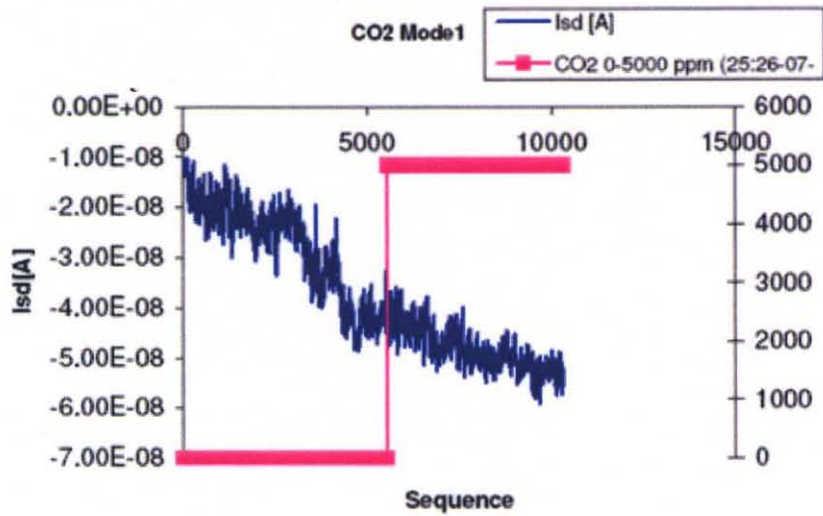
Mode 5: Gate sweep -20 V to 20 V Constant Vsd 150 mV
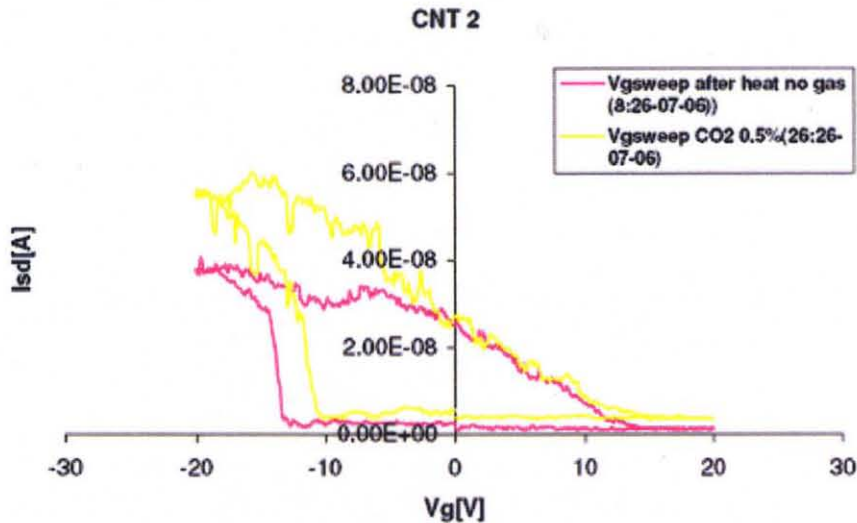
Figure C.1 Nanotube sensor response to 5000 ppm of CO_2 in Mode1 and Mode 5.

Hydrogen

Mode1: Measurement at a gas conc. of 5000 ppm, Vg = -10 V, Vsd = -250 mv
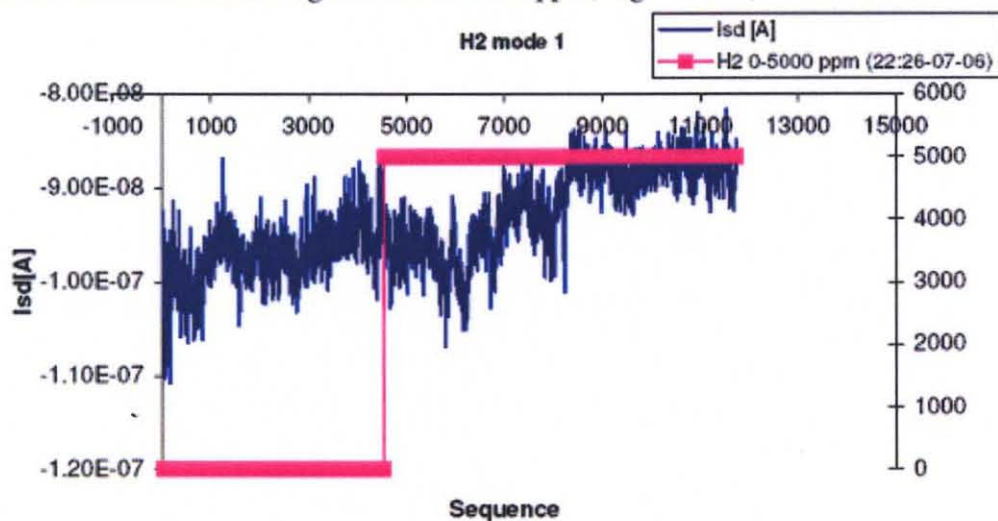
Mode 5: Vg -20 V to 20 V and Vsd constant 150 mV
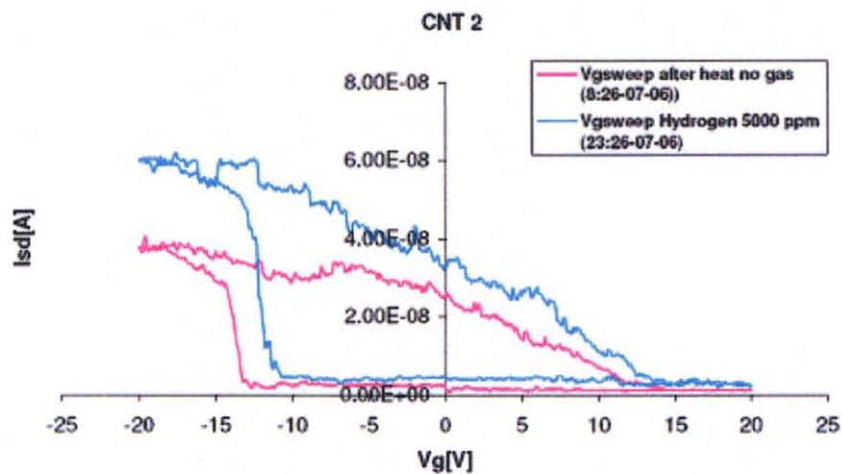
Figure C.2 Nanotube sensor response to 5000 ppm of H_2 in Mode1 and Mode 5.

Ammonia

Mode 1: measurements at a gas conc. of 50 ppm of NH3
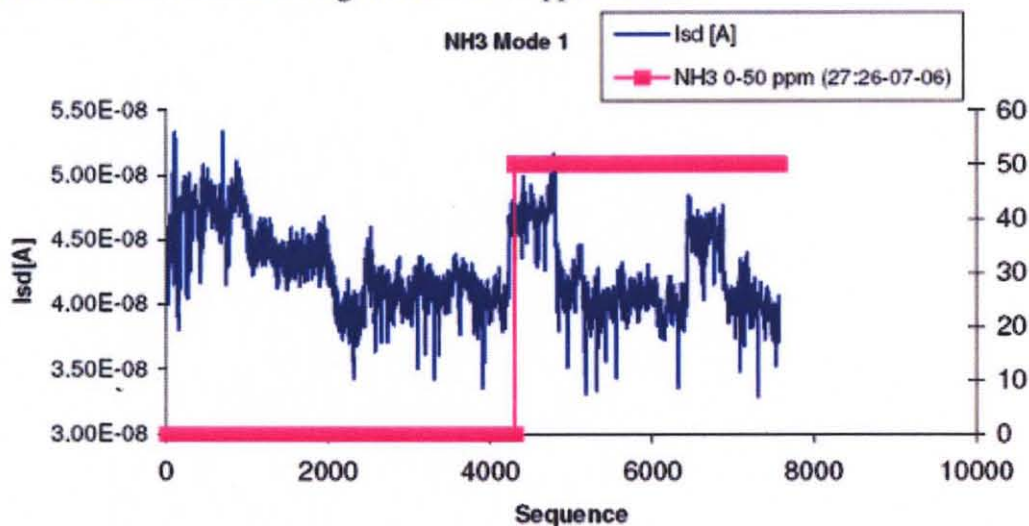
Mode 5: Gate sweep -20 V to 20 V Constant Vsd 150 mV
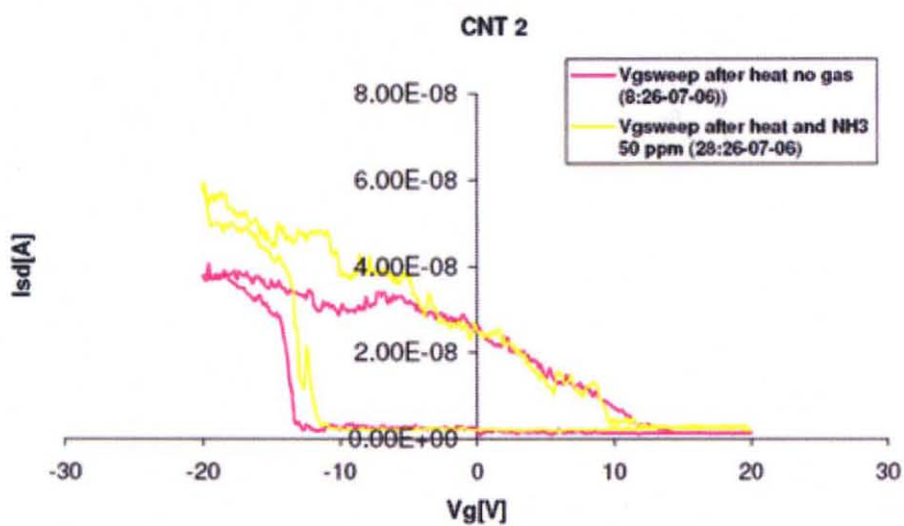
Figure C.3 Nanotube sensor response to 50 ppm of NH_3 in Mode1 and Mode 5.

REFERENCES

Allen, T., Andersen, O.S., Roux, B. (2004). On the importance of atomic fluctuations, protein flexibility, and solvent in ion permeation, *J. Gen. Physiol.*, 124, 679-690.

Alvarez, L., Righi, A., Rols, S., Anglaret, A., Suavajol, J.L., Muñoz., E., Maser, W.K., Benito, A.M., Martínez, M.T., de la Faunte, G.F. (2001), Diameter dependence of Raman intensities for single-wall carbon nanotubes. *Phys. Rev. B.*, 63, 153401-4.

Alvarez, W. E., Kitiyanan, B., Borgna, A., Resasco, D. E. (2001). Synergism of Co and Mo in the catalytic production of single-wall carbon nanotubes by decomposition of CO, *Carbon*, 39, 547-558.

An, J.-W., Lim, D.-S. (2002). Effect of carbon nanotube additions on the microstructure of hot-pressed alumina, *J. Ceram. Proc. Res.*, 3, 201-204.

An, J.-W., You, D.-H., Lim, D.-S. (2003). Tribological properties of hot-pressed alumina–CNT composites, *Wear*, 255, 677-681.

Askeland, D. R. (1989).*The Science and Engineering of Materials*, 2nd ed. Boston, MA

Bachilo, S.M., Balzano, L., Herrera, J.E., Pompeo, F., Resasco, D.E., Weisman, R.B. (2003). Narrow (n,m)-Distribution of Single-Walled Carbon Nanotubes Grown Using a Solid Supported Catalyst, *J. Am. Chem. Soc.*, 125, 11186-11187.

Bachilo, S.M., Strano, M.S., Kitrell, C., Hauge, R.H., Smalley, R.E., Weismann, R. B. (2002). Structure-Assigned Optical Spectra of Single-Walled Carbon Nanotubes, *Science*, 298, 2361-2366.

Bachtold, A., Strunk, C., Salvetat, J.P., Bonard, J.M., Forro, L., Nussbaumer, T., Schonenberger, C. (1999). Aharonov–Bohm oscillations in carbon nanotubes, *Nature*, 397, 673-675.

Bachtold, A., Hadley, P., Nakanishi, T., Dekker, C. (2001). Logic Circuits with Carbon Nanotube Transistors, *Science*, 294, 1317-1320.

Bae, J., Yoon, Y., Lee, S., Baik, H. (2002). Field emission properties of carbon nanotubes deposited by electrophoresis. *Physica B*, 323, 169-70.

Baker, R.T.K., barber, M.A., Harris, P.S., Feates, F.S., Waite, R.J. (1972). Nucleation and growth of carbon deposits from the nickel catalyzed decomposition of acetylene, *J. Catal.*, 26, 51-62.

Balázsi, Cs., Kónya, Z., Wéber, F., Biró, L.P., Arató, P. (2003). Preparation and characterization of carbon nanotube reinforced silicon nitride composites. *Mater. Sci. Eng. C.,* 23, 1133-1137.

Bandow, S., Rao, A.M., Williams, K.A., Thess, A., Smalley, R.E., Eklund, P.C. (1997). Purification of single-wall carbon nanotubes by microfiltration, *J. Phys. Chem. B,* 101, 8839-8842.

Barreiro, G., Guimaraes, C.R.W. and de. Alencastro, R.B. (2003). Potential of mean force calculations on an L-type calcium channel model, *Protein. Eng.,* 16, 209-215.

Bethune, D.S., Klang, C.H., Devries, M.S., Gorman, G., Savoy, R., Vazquez, J., Beyers, R. (1993). Cobalt-catalysed growth of carbon nanotubes with single-atomic-layer walls, *Nature,* 363, 605-607.

Brewer, L., Lamoreaux, R.H. (1980). Molybdenum: physico-chemical properties of its compounds and alloys, II Phase diagrams. In Vol. *Atomic Energy Agency Rev.,* 7, 231-234.

Bronikowski, M.J., Willis, P.A., Colbert, D.T., Smith, K.A., Smalley, R.E. (2001). Gas-hase production of carbon single-walled nanotubes from carbon monoxide via the HiPco process: A parametric study, *J. Vac. Sci. Tech. A* 19, 1800-1805.

Callister, W. D. Jr. (2002). *Materials Science and Engineering an Introduction.* New York: John Wiley & Sons, Inc. 6th Ed. 536-537.

Cao, P.G., Yao, J.L., Zheng, J.W., Ren, B., Gu, A.R., Tian, Z.Q. (2000). Two-dimensional surface Raman imaging of a roughened iron electrode in saline water in *Progress in Surface Raman Spectroscopy* edited by Z.Q. Tian, and B. Ren, (Xiamen University Press, 2000), p. 75.

Cassell, A.M., Franklin, N.R., Tombler, T.W., Chan, E.M., Han, J., Dai, H. (1999). Directed growth of free standing single-walled carbon nanotubes, *J. Am. Chem. Soc.,* 121, 7975-7976.

Cassell, A.M., Raymakers, J. Kong, J., Dai, H., (1999). Large scale CVD synthesis of single-walled carbon nanotubes, *J. Phys. Chem. B.,* 103, 6484-6492.

Chang, H., Lee, J.D., Lee, S.M., Lee, Y.H. (2001). Adsorption of NH_3 and NO_2 molecules on carbon nanotubes, *Appl. Phys. Lett.,* 79, 3863-3865.

Charlier, J.C.; Dresselhaus, M.S.; Dresselhaus, G.; Avouris, P. *Carbon Nanotubes* Springer, Berlin 2000.

Chen, J., Hamon, M.A., Hum, H., Chen, Y.S., Rao, A.M., Eklund, P.C., Haddon, R.C. (1998). Solution properties of single-walled carbon nanotubes, *Science*, 282, 95-98.

Chen, J., Rao, A.M., Lyuksyutiv, S., Itkis, M.E., Hamon, M.A., Hu, H., Cohn, R.W., Eklund, P.W., Colbert, D.T., Smalley, R.E., Haddon, R.C. (2001). Dissolution of full-length single-walled carbon nanotubes, *J. Phys. Chem. B*, 105, 2525-2528.

Chiu, P.W., Duesberg, G.S., Dettlaff-Weglikowska, U., Roth, S. (2002). Interconnection of carbon nanotubes by chemical functionalization, *Appl. Phys. Lett.*, 80, 3811-3813.

Choi, W.B., Jin, Y.W., Kim, H.Y., Lee, S.J., Yun, M.J., Kang, J.H. Choi, Y.S., Park, N.S., Lee, N.S. Kim, J.M. (2001). Electrophoresis deposition of carbon nanotubes for triode-type field emission display, *Appl. Phys. Lett.*, 78, 1547-9.

Christen, H.M., Puretzky, A.A., Cui, H., Belay, K., Fleming, P.H., Geohegan, D.B., Lowndes, D.H. (2004). Rapid growth of long, vertically aligned carbon nanotubes through efficient catalyst optimization using metal film gradients, *Nanoletters*, 4, 1939-1942.

Collins, P.G., Arnold, M.S., Avouris, Ph. (2001). Engineering carbon nanotubes and nanotube circuits using electrical breakdown, *Science*, 292, 706-709.

Cracknell, A.P., Wong, K.C. (1973). *The Fermi Surface*, London: Oxford University Press.

Curtin, W.A., Sheldon B.W. (2004). CNT-reinforced ceramics and metals. *Materials Today*, November, 44-49.

Dai, H. J., Rinzler, A.G., Colbert, D.T., Smalley, R.E. (1996). Nanotubes as nanoprobes in scanning probe microscopy, *Nature*, 394, 147-149.

Dai, H., Rinzler, A.G., Nikolaev, P., Thess, A., Colbert, D.T., Smalley, R.E. (1996). Single-wall nanotubes produced by metal-catalyzed disproportionation of carbon monoxide, *Chem. Phys. Lett.* 260, 471-475.

Dai, H., Rinzler, A.G., Nikolaev, P., Thess, A., Colbert, D.T., Smalley, R.E., (1996). Theoretical bounds for multiwalled carbon nanotube growth, *Chem. Phys. Lett.*, 296, 471-476.

De, A.K., Murdock D.C., Mataya, M.C., Speer, J.G., Matlock, D.K. (2004). Quantitative measurement of deformation-induced martensite in 304 stainless steel by X-ray diffraction. *Scripta Mater.*, 50, 1445-1449.

Delpeux, S., Szostak, K., Frackowiak, E., Bonnamy, S., Béguin, F. (2002). High yield of pure multiwalled carbon nanotubes from the catalytic decomposition of acetylene on in-situ formed cobalt nanoparticles. *J. Nanosci. and Nanotech.*, 2, 481-484.

Dharap, P., Li, Z., Nagarajaiah, S., Barrera, E.V. (2004). Nanotube film based on single-wall carbon nanotubes for strain sensing, *Nanotechnology*, 15, 379-382.

Ding, X-Z, Huang, L., Zeng, X.T., Lau, S.P., Tay, B.K., Cheung, W.Y., Wong, S.P. (2004). Catalytic chemical vapor deposition of vertically aligned carbon nanotubes on iron nanoislands formed from Fe^+-implanted SiO_2 films, *Carbon*, 42, 3030-3033.

Dresselhaus, M.S., Eklund, P.C. (2000). Phonons in carbon nanotubes, *Advances in Physics*, 49 (6), 705-814.

Dresselhaus, M.S., Dresselhaus, G., Avouris, Ph. (2001). *Carbon Nanotubes: Synthesis, Structure, Properties and Applications,* Springer, Topics in Applied Physics Vol. 80.

Du, C.S., Heldbrant, D., Pan, N. (2002). Preparation and preliminary property study of carbon nanotubes films by electrophoretic deposition. *Mater. Lett.,* 57, 434-8.

Duesberg, G.S., Graham, A.P., Kreupl, F., Liebau, M., Seidel, R., Unger, E., Hönlein W. (2004). Ways towards the scaleable integration of carbon nanotubes into silicon based nanotechnology, *Diamond and Related Materials*, 13, (2004) 354-361.

Ebbessen, T.W., Ajayan, P.M. (1992). Large-scale synthesis of carbon nanotubes, *Nature*, 358, 220-222.

Eisenberg, B. (2003). Ion channels as devices, *J. Comp. Electron.* 2, 245-249.

Endo, M., Takeuchi, K., Kobori, K., Takahashi, K., Kroto, H., Sarkar, A. (1995). Pyrolytic carbon nanotubes from vapor-grown carbon fibers, *Carbon*, 33, 873-881.

Farrow, R.C., Liddle, J.A., Berger, S.D., Huggins, H.A., Kraus, J.A., Camarda, R.M., Tarascon, R.G., Jurgensen, C.W., Kola, R.R., Fetter, L. (1993). Marks for alignment and registration in projection electron lithography, *J. Vac. Sci. Technol. B* 11, 2175.

Flahaut, E., Peigney, A., Laurent, Ch., Marlière, Ch., Chastel, F., Rousset, A. (2000). Carbon nanotube metal-oxide-nanocomposites: microstructure, electrical conductivity and mechanical properties. *Acta. Mater.*, 48, 3803-3812.

Franklin, N.R., Li, Y., Chen, R.J., Javey, A., Dai, H. (2001). Patterned growth of single-walled carbon nanotubes on full 4-inch wafers, *Appl. Phys. Lett.*, 79, 4571-4573.

Fridell, E., Skoglundh, M., Westerberg, B., Johansson, S., Smedler, G. (1999). NOx storage in Barium-containing catalysts, *Journal of Catalysis*, 1999, 183, 196-209.

Gao, B., Yue, G.Z., Qiu, Q., Cheng, Y., Shimoda, H., Fleming, L., Zhou, O. (2001). Fabrication and electron field emission properties of carbon nanotube films by electrophoretic deposition, *Adv. Mater.* 13, 1770-3.

George, R., Kashyap, K.T., Rahul, R., Yamdagni, S. (2005). Strengthening in carbon nanotube/aluminum (CNT/Al) composites, *Scripta Materialia*, 53, 1159-1163.

Gere, J. M., Timoshenko, S.P. (1990). *Mechanics of Materials*, PWS Publishing Company, Boston.

Ghosh, S., Sood, A.K., Kumar, N. (2003). Carbon Nanotube Flow Sensors, *Science* 299, 1042-1044.

Girishkumar, G., Vinodgopal, K., Kamat, P.V. (2004). Carbon nanostructures in portable fuel cells: single-walled carbon nanotube electrodes for methanol oxidation and oxygen reduction, *J. Phys. Chem. B.*, 108, 19960-66.

Goh, C.S., Wei, J., Gupta, M. (2006). Development of novel carbon nanotube reinforced magnesium nanocomposites using the powder metallurgy technique, *Nanotechnology*, 17, 7-12.

Goldman, D.E. (1943). Potential, impedance and rectification in membranes, *J. Gen. Physiol.* 27, 37-60.

Goyal, A., Wiegand, D. A., Owens, F. J., Iqbal, Z. (2006). Enhanced yield strength in iron nanocomposite with in situ grown single-wall carbon nanotubes, *Journal of Materials Science*, 21, 522-528.

Graham, A.P., Duesberg, G.S., Seidel, R., Liebau, M., Unger, E., Kreupl, F. Hönlein, W. (2004). Towards the integration of carbon nanotubes in microelectronics. *Diamond and Related Materials*, 13, 1296–1300.

Guo, T., Nikolaev, P., Thess, A., Colbert, D.T., Smalley, R.E. (1995). Catalytic growth of single-walled manotubes by laser vaporization, *Chem. Phys. Lett.* 243, 49-54.

Hafner, J., Bronikowski, M., Azamian, B., Nikolaev, P., Colbert, D., Smalley, R. (1998). Catalytic growth of single-wall carbon nanotubes from metal particles, *Chem. Phys. Lett.*, 296, 195-202.

Hamada, N., Sawada, S. and Oshiyama, A. (1992). New one-dimensional conductors: graphitic microtubules, *Phys. Rev. Lett.*, 68, 1579-1581.

Harris, P. (1999). Carbon Nanotubes and Related Structures, Cambridge University Press.

Harutyunyan, A.R., Chen, G., Eklund, P.C. (2003). Self-assembled growth of single-walled carbon nanotubes by pyrolysis of metalorganic precursor, *Appl. Phys. Lett.*, 82, 4794-4796.

Hata, K., Futaba, D. N., Mizuno, K., Namai, T., Yumura, M., Iijima, S. (2004). Water assisted highly efficient synthesis of impurity free single walled carbon nanotubes, *Science*, 306, 1362-1364.

Helbling, T., Pohle, R., Stampfer, C., Durrer, L., Goyal, A., Fleischer, M. and Hierold, C. (2007). NO_2 gas sensors based on individual suspended single-walled carbon nanotubes. Accepted (EA 0679), Transducer 2007: The 14th International Conference on *Solid-State Sensors, Actuators and Microsystems*. Lyon, France, June 10-14.

Hernandez, E., Goze, C., Bernier, P., Rubio A. (1998). Elastic properties of C and $B_xC_yN_z$ composite nanotubes. *Phys. Rev. Lett.*, 80, 4502-4505.

Hille, B. (2001). *Ion Channels of Excitable Membranes*, 3rd Edition, ed. B. Hille, Sinauer Associates, Sunderland, Mass. 646-660.

Hodgkin, A.L., Katz, B. (1949). The effect of sodium ions on the electrical activity of the giant axon of the squid, *J. Physiol.*, 108, 37-77.

Homma, Y., Koboyashi, Y., Ogino, T., Yamashita, T. (2002). Growth of suspended carbon nanotube networks on 100-nm-scale silicon pillars, *Appl. Phys. Lett.*, 81, 2261-2263.

Hone, J., Llaguno, M.C., Nemes, N.M., Johnson, A.T., Fischer, J.E., Walters, D.A., Casavant, M.J., Scmidt, J., Smalley, R.E. (2000). Electrical and thermal transport properties of magnetically aligned single wall carbon nanotube films, *Appl. Phys. Lett.*, 77, 5, 666-668.

Hu, H., Yu, A. P., Kim, E., Zhao, B., Itkis, M. E., Bekyarova, E., Haddon, R.C. (2005). Influence of the zeta potential on the dispersability and purification of single-walled carbon nanotubes, *J. Phys. Chem. B.*, 109, 11520-24.

Huang, S., Maynor, B., Cai, X., Liu, J., (2003). Ultralong, well-aligned single-walled carbon nanotube architectures on surfaces, *Adv. Mater.*, 15, 1651-1655.

http://www.cm.kyushu-u.ac.jp/dv06/images/aligned_MWNT.jpg

Iijima, S. (1991). Helical microtubules of graphitic carbon, *Nature*, 354, 56-58.

Iijima, S., Ichihashi, T. (1993). Single-shell carbon nanotubes of 1-nm diameter, *Nature*, 363, 603-605.

Iqbal, Z., Goyal A. (2005). Carbon nanotubes/nanofibers and carbon fibers in, *Functional Fillers for Plastics* edited by Xanthos, M. Berlin: WILEY-VCH Verlag GmbH & Co.175-192.

Ishida, K., Nishiwaka, T. (1991). The C-Co (carbon-cobalt) system. *J. Phase. Euqil.,* 12, 417-424.

Jiang, Y., Lee, A., Chen, J., Cadene, M., Chait, B.T. and MacKinnon, R. (2002). The open pore conformation of potassium channels, *Nature,* 417, 523-526.

Journet, C. Maser, W.K., Bernier, P., Loiseau, A., Lamy de la Chapelle, M., Lefrant, S., Deniard, P., Lee, R., Fischer, J.E. (1997). Large-scale production of single-walled carbon nanotubes by the electric-arc technique, *Nature*, 388, 756-758.

Kataura, H., Kumazawa, Y., Maniwa, Y., Umezu, I., Suzuki, S., Ohtsuka, Y., Achiba, Y. (1999). Optical properties of single-wall carbon nanotubes, *Synthetic Metals,* 103, 2555-2558.

Kataura, H., Kumazawa, Y., Maniwa, Ohtsuka, Y., Sen, R., Suzuki, S, Achiba, Y. (2000). Diameter control of single-walled carbon nanotubes, *Carbon,* 38, 1691-1697.

Kathyayini, H., Nagarajua, N., Fonseca, A, Nagy, J. B. (2004). Catalytic activity of Fe, Co and Fe/Co supported on Ca and Mg oxides, hydroxides and carbonates in the synthesis of carbon nanotubes, *Journal of Molecular Catalysis A: Chemical,* 223, 129–136.

Kitiyanan, B., Alvarez,W.E., Harewell,. J.H., Resasco, D.E. (2000). Controlled production of single-wall carbon nanotubes by catalytic decomposition of CO on bimetallic Co–Mo catalysts. *Chem. Phys. Lett.,* 317(3-5), 497-503.

Kong, J., Cassell, A.M., Dai, H. (1998). Chemical vapor deposition of methane for single-walled carbon nanotubes, *Chem. Phys. Lett.* 292, 567-574.

Kong, J., Franklin, N. R., Zhou, C., Chapline, M. G., Peng, S., Cho, K. and Dai, H. (2000). Nanotube molecular wires as chemical sensors, *Science* 287, 622-625.

Kong, J., Soh, T.H., Cassell, A., Quate, C.F., Dai, H. (1998). Synthesis of individual single-walled carbon nanotubes on patterned silicon wafers, *Nature*, 395, 878-881.

Konno, H., Sato, S., Habazaki, H., Inagaki, M. (2004). Formation of platelet structure carbon nanofilaments by a template method, *Carbon*, 42, 2756-2759.

Krishnan, A., Dujardin, E., Ebbesen, T.W., Yianilos, P.N., Treacy, M.M.J. (1998) Young's modulus of single-walled nanotubes. *Phys. Rev. B.,* 58, 14013-14019.

Kurnosov, D., Bugaev, A. S., Nikolski, K. N., Tchesov, R., Sheshin, E. (2003). Influence of the interelectrode distance in electrophoretic cold cathode fabrication on the emission uniformity, *Appl. Surf. Sci.,* 215, 232-6.

Kuzumaki, T., Miyazawa, K., Ichinose, H., Ito, K. (1998). Processing of carbon nanotube reinforced aluminum composite. *Journal of Materials Research,* 13, 2445-2449.

Lacerda, R.G., Teh, A.S., Yang, M.H., Teo, K.B.K., Rupesinghe, N.L., Dalal, K., Kosilov, K.K., Roy, D., Amaratunga, G.A.J., Milne, W.I., Chhowalla, M., Hasko, D.G., Wyczisk, F., Legegneux, P. (2004). Growth of high-quality single-wall carbon nanotubes without amorphous carbon formation, *Appl. Phys. Lett.,* 84, 269-271.

Lan, A., Zhang, Y., Zhang, X., Iqbal, Z., Grebel, H. (2003). Is molybdenum necessary for the growth of single-wall carbon nanotubes from CO? *Chem. Phys. Lett.,* 379, 395-400.

Li, C.Y., Chou, T.W. (2004). Strain and pressure sensing using single-walled carbon nanotubes, *Nanotechnology,* 15, 1493-1496.

Li, J., Lu, Y., Ye, Q., Cinke, M., Han, J., Meyyappan, M. (2003). Carbon nanotube sensors for gas and organic vapor detection, *Nanoletters,* 3, 929-933.

Li, J., Ng, H.T., Chen H. (2005) in *Protein Nanotechnology: Protocols, Instrumentation, and Applications,* ed. Tuan Vo-Dinh, Humana Press, Totowa, New Jersey. 191-224.

Li, Y., Kim, W., Zhang, Y., Rolandi, M., Wang, D., Dai, H. (2001). Growth of Single-walled carbon nanotubes from discrete catalytic nanoparticles of various Sizes, *J. Phys. Chem. B.,* 105, 11424-11431.

Liang, W., Bockrath, M., Bozovic, D., Hafner, J.H., Tinkham, M., Park, H. (2001). Fabry - Perot interference in a nanotube electron waveguide, *Nature,* 411, 665-669.

Lier, Van. G., Alsenoy, Van. C., Doren, Van. V., Geerlings, P. (2000). *Ab initio* study of the elastic properties of single-walled carbon nanotubes and graphene. *Chem. Phys. Lett.,* 326, 181-185.

Liu, B.C., Lyu, S.C., Jung, S.I., Kang, H.K., Yang, C.-W., Park, J.W., Park, C.Y. Lee, C.J. (2004). Single-wall carbon nanotubes produced by catalytic chemical vapor deposition of acetylene over Fe-Mo/MgO catalyst. *Chem. Phys. Lett.,* 383, 104-108 .

Liu, J., Dai, H. (2002). [Online].Available: http://www.nnf.cornell.edu/2002re u/ Liu.pdf

Liu, K., Avouris, Ph., Martel, R., Hsu, W.K. (2001). Electrical transport in doped multiwalled carbon nanotubes, *Phys. Rev. B*, 63, 161404-1 – 161404-4.

Lu, J.P. (1997). Elastic properties of carbon nanotubes and nanoropes. *Phys. Rev. Lett.*, 79, 1297-1300.

Ma, H., Zhang, L., Zhang, J., Zhang, L., Yao, N., Zang, B. (2005). Electron field emission properties of carbon nanotubes-deposited flexible film. Appl. Surf. Sci., 251, 258-61.

Martel, R., Scmidt, T., Shea, H. R., Hertel, T., Avouris, Ph. (1998). Single-and multi-wall carbon nanotube field-effect transistors, *Appl. Phys. Lett.*, 73, 2447-2449.

Maruyama, S., Kojima, R., Miyauchi, Y., Chiashi, S., Kohno, M., (2002). Low-emperature synthesis of high-purity single-walled carbon nanotubes from alcohol, *Chem. Phys. Lett.*, 360, 229-234.

Mauron, Ph., Emmenegger, Ch., Sudan, P., Wenger, P., Rentsch, S., Züttel, A. (2002). Fluidized-bed CVD synthesis of carbon nanotubes on Fe2O3/MgO, *Diamond and Related Materials*, 12, 780-785.

McCabe, W.L., Smith, J.C., Harriott, P. (1993). Unit Operations of Chemical Engineering, 5th ed. McGraw-Hill, Singapore.

McCrum, N.G., Buckley, C.P., Bucknall, C.B. (1997). *Principles of Polymer Engineering*. New York: Oxford University Press, 2nd Ed. 242-245.

McKnight, T.E., Guillorn, M.A., Melechko, A., Merkulov, V.I., Britt, P.F., Austin, D. W., Lowndes, D.H., Simpson, M.L. (2003). Intracellular integration of synthetic nanostructures with viable cells for controlled biochemical manipulation, *Nanotechnology*, 14, 551-556.

Mickelson, E.T. Huffman, C.B. Rinzler, A.G., Smalley, R.E., Hague, R.H., Margrave, J.L. (1998). Fluorination of single-wall carbon nanotubes, *Chem. Phys. Lett.*, 296, 188-194.

Modi, A., Koratkar, N., Lass, E., Wei, B., Ajayan, P.M. (2003). Miniaturized gas ionization sensors using carbon nanotubes, *Nature*, 424, 171-174.

Moore, G. (1965). *Electronics Magazine.*

Murakami, Y., Miyauchi, Y., Chiashi, S., Maruyama, S., (2003). Characterization of single-walled carbon nanotubes catalytically synthesized from alcohol, *Chem. Phys. Lett.,* 374, 53-58.

Murakami, Y., Chiashi, S., Miyauchi, Y., Hu, M., Ogura, M., Okubo, T., Maruyama, S. (2004). Growth of vertically aligned single-walled carbon nanotube films on quartz substrates and their optical anisotropy, *Chem. Phys. Lett.,* 385, 298-303.

Nakayama, Y., Akita, S. (2001). Field-emission device with carbon nanotubes for a flat panel display, *Synthetic Metals,* 117, 207-10.

Nicholls, D. in *Comprehensive Inorganic Chemistry,* edited by H. J. Emeleus, R. Nyholm, and A. F. Trotman-Dickenson, Pergamon, Oxford, 1973, Vol. 3, p. 990.

Nikolaev, P., Bronikowski, M.J., Bradley, R.K., Rohmund, F., Colbert, D.T., Smith, K.A., Smalley, R.E., (1999). Gas-phase catalytic growth of single-walled carbon nanotubes from carbon monoxide, *Chem. Phys. Lett.,* 313, 91-97

Nishijima. H., Kamo, S., Akita, S., Nakayama, Y., Hohmura, K.I., Yoshimura, S.H., Takeyasu, K. (1999). Carbon-nanotube tips for scanning probe microscopy: Preparation by a controlled process and observation of deoxyribonucleic acid, *Appl. Phys. Lett.,* 74, 4061-4063.

Niu, C., Sichel, E.K., Hoch, R., Moy, D. (1997).Tennent H. High power electrochemical capacitors based on carbon nanotube electrodes, *Appl. Phys. Lett.,* 70, 1480-2.

Patil, K.C. *Bull. Mater. Sci.* 1993; 16: 533.

Peng, S., Cho, K. (2000). Chemical control of nanotube electronics, *Nanotechnology,* 11, 57-60.

Peng, S., Cho, K., Qi, P., Dai, H. (2004), Ab initio study of CNT NO_2 gas sensor, *Chem. Phys. Lett.,* 387, 271-276.

Park, E., Zhang, J., Thomson, S., Ostrovski, O., Howe, R. (2001). Characterization of phases formed in the iron carbide process by x-ray diffraction, Mossbauer, x-ray photoelectron spectroscopy, and Raman spectroscopy analysis. *Metallurgical and Materials Transactions B,* 32B, 839-845.

Plöjnes, E., Palm, P., Viswanathan, G.B., Subramaniam, V.V., Adamovich, I.V., Lempert, W.R., Fraser, H.L, Rich, J.W. (2002). Synthesis of single-walled carbon nanotubes in vibrationally non-equilibrium carbon monoxide, 352, 342-347.

Qi, P., Vermesh, O., Grecu, M., Javey, Ali., Wang, Q., Dai, H., Peng, S., Cho, K. J. (2003). Toward large arrays of multiplex functionalized carbon nanotube sensors for highly sensitive and selective molecular detection, *Nanoletters,* 3, 347-351.

Qin, L.C., Zhao, X., Hirahara, K., Miyamoto, Y., Ando, Y. and Iijima, S. (2000). Materials science: The smallest carbon nanotube, *Nature,* 408, 50-51.

Raman, C.V., Krishnan, K. S. (1928). A New Type of Secondary Radiation, *Nature,* 121, 501.

Ramanathan, T., Liu, H., Brinson, L.C. (2005). Functionalized SWNT/polymer nanocomposites for dramatic property improvement, *J. Polym. Sci. B: Poly. Phys.,* 43, 2269-2279.

Rao, A.M., Richter, E., Bandow, S., Eklund, P.C., Williams, K.A., Fang, S., Subbaswamy, K.R., Menon, M., Thess, A., Smalley, R.E., Dresselhaus, G., Dresselhaus M.S. (1997). Diameter-selective Raman scattering from vibrational modes in carbon nanotubes, *Science,* 275, 187-191.

Renshaw, G.D., Roscoe, C.P.L., Walker, J. (1970). Disproportionation of CO : I. Over iron and silicon-iron single crystals, *J. Catal.* 18,164.

Roux, B., MacKinnon, R. (1999). The cavity and pore helices in the KcsA K^+ channel: electrostatic stabilization of monovalent cations, *Science* 285, 100-102.

Saito, R., Dresselhaus, G., Dresselhaus, M.S. (2000). Trigonal warping effect of carbon nanotubes, Physical Review B, 61, 2981.

Saito, R., Fujita, M., Dresselhaus, G. And Dresselhaus, M. (1992). Electronic structure of chiral graphene tubules, *Appl. Phys. Lett.,* 60, 2204-2206.

Saito, Y. (1995). Nanoparticles and filled nanocapsules, *Carbon,* 33, 979-988.

Salvetat, J.P., Bonard, J.M., Thomson, N.H., Kulik, A.J., Forró, L., Benoit, W. and Zuppiroli (1999). Mechanical properties of carbon nanotubes, *Appl. Phys. A.,* 69, 255-260.

Samuelson, L., Batra, I. P., Roetti, C. (1980). A comparison of electronic properties of various modifications of graphite, *Solid State Communications,* 33, 817-

Sanchez-Portal, D., Artacho, E., Soler, J.M., Rubio, A., Ordejon, P. (1999). *Ab initio* structural, elastic, and vibrational properties of carbon nanotubes. *Phy. Rev. B.,* 59, 12678-12688.

Schnitzler, M.C., Oliveira, M M., Ugarte, D., Zarbin, A J. G. (2003). One-step route to iron oxide-filled carbon nanotubes and bucky-onions based on the pyrolysis of organometallic precursors, *Chem. Phys. Lett.,* 381, 541-548.

Schwan, J., Ulrich, S., Batori, V., Ehrardt, H., Silva, S.R.P., (1996). Raman spectroscopy on amorphous carbon films, *J. Appl. Phys.,* 80, 440-447.

Seidel, R., Liebau, M., Duesberg, G.S., Kreupl, F., Unger, E., Graham, A.P., Hoenlein, W., Pompe, W. (2003). In-Situ Contacted Single-Walled Carbon Nanotubes and Contact Improvement by Electroless Deposition, *Nanoletters*, 3, 965-968.

Siegel, R.W., Chang, S.K., Ash, B.K, Stone, J., Ajayan, P.M., Doremus, R.W., Schadler, L.S. (2001). Mechanical behavior of polymer and ceramic matrix Nanocomposites, *Scripta Mater.*, 44, 2061-2064.

Sharma, R., Iqbal, Z. (2004). *In situ* observations of carbon nanotube formation using environmental transmission electron microscopy. *Appl. Phys. Lett.*, 84, 990-992.

Sotiropoulou, S., Chaniotakis, N.A. (2003). Carbon nanotube array-based biosensor, *Anal. Bioanal. Chem.* 375, 103-105.

Stampfer, C. Jungen, A., Hierold, C (2004). Fabrication of discrete carbon nanotube based nano-scaled force sensors, *Proceedings IEEE Sensors 2004*, T4L.F.5, 1056-1059.

Suehiro, J., Zhou, G., Imakiire, H., Ding, W., Hara, M. (2005). Controlled fabrication of carbon nanotube NO_2 gas sensor using dielectrophoretic impedance measurement, *Sensors and Actuators B*,108, 398-403.

Swanson, T. (1953). Natl. Bur. Stand. (U.S.), Circ. 539, I, 37.

Tang, S., Zhong, Z., Xiong, Z., Sun, L., Liu, L., Lin, J. (2001). Controlled growth of single-walled carbon nanotubes by catalytic decomposition of CH_4 over Mo/Co/MgO catalysts. *Chem. Phys. Lett.*, 2001, 350(1-2), 19-26.

Tang, Y., Cong. H., Zhong, R., C. H-M. (2004). Thermal expansion of a composite of single-walled carbon nanotubes and nanocrystalline aluminum, *Carbon*, 42, 3260-3262.

Tans, S. J., Devoret, M.H., Dai, H., Thess, A., Smalley, R. E., Geerlings, L. J. and Dekker, C. (1997). Individual single-wall carbon nanotubes as quantum wires, *Nature*, 386, 474-477.

Tans, S.J., Verschueren, A.R.M., Dekker, C. (1998). Room-temperature transistor based on a single carbon nanotube, *Nature*, 393, 49-52.

Thess, A., Lee, R., Nikolaev, P., Dai, H., Petit, P., Robert, J., Xu, C., Lee, Y.H., Kim, S.G., Rinzler, A.G., Colbert, D.T., Scuseria, G.E., Tomanek, D., Fischer, J.E., Smalley, R. E. (1996). Crystalline ropes of metallic carbon nanotubes, *Science*, 23, 483-487.

Thomas, B.J.C., Boccaccini, A.R., Shaffer, M.S.P. (2005). Multi-walled carbon nanotube coatings using electrophoretic deposition (EPD). *J. Am.Ceram. Soc.,* 88, 980-2.

Tombler, T.W., Zhou, C., Alexseyev, L., Kong, J., Dai, H., Liu, L., Jayanthi, C.S., Tang, M., Wu, S-Y. (2000). Reversible electromechanical characteristics of carbon nanotubes under local-probe manipulation, *Nature*, 405, 769-772.

Treacy, M.M. J., Ebbesen, T.W., Gibson, J. M. (1996). Exceptionally high Young's modulus observed for individual carbon nanotubes, *Nature,* 381, 678-681.

Wagner, R.S., Ellis, W.C. (1964). Vapor-liquid-solid mechanism of single crystal growth, *Appl. Phys. Lett.,* 4, 89-90.

Wagner, J., Wild, C., Koidl, P. (1991). Resonance effects in Raman scattering from polycrystalline diamond films, *Appl. Phys. Lett.* 59, 779-781.

Walters, D.A., Ericson, L. M., Casavant, M. J., Liu, J., Colbert, D. T., Smith, K. A., Smalley, R.E. (1999). Elastic strain of freely suspended single-wall carbon nanotube ropes, *Appl. Phys. Lett.,* 74, 25, 3803–3805.

Wang, Y., Wei, F., Luo, G., Hao, Y., Gu, G. (2002). The large-scale production of carbon nanotubes in a nano-agglomerated fluidized- bed reactor, *Chem. Phys. Lett.,* 364, 568-572.

Wang, Y. (2005).Ph.D Thesis NJIT, Department of Chemistry and Environmental Sciences.

Wang, Y., Iqbal, Z., Mitra, S. (2005). Microwave-induced rapid chemical functionalization of single-walled carbon nanotubes, *Carbon,* 43, 1015-1020.

Wang, X-T., Padture, N.P., Tanaka, H. (2004). Contact-damage-resistant ceramic/single-wall carbon nanotubes and ceramic/graphite composites, *Nature Materials,* 3, 539-544.

Weizhong, Q., Tang, L., Zhanwen, W., Fei, W., Zhifei, L., Guohua, L., Yongdan, L. (2004). Production of hydrogen and carbon nanotubes from methane decomposition in a twstage fluidized bed reactor, *Appl. Cat. A: General,* 260, 223-228.

Wiegand, D.A., Pinto, J., Nicolaides, S.J. (1991). Mechanical response of TNT and a composite (Composition B) of TNT and RDX to compressive stress, I: Uniaxial stress and fracture, *Energetic Materials*, 9, 19.

Wilder, J.W.G., Venema, L.C., Rinzler, A.G., Smalley, R.E., Dekker, C. (1998). Electronic structure of atomically resolved carbon nanotubes, *Nature,* 391, 59-62.

Wong, E.W., Sheehan, P.E., Lieber, C.M. (1997). Nanobeam Mechanics: elasticity, strength, and toughness of nanorods and nanotubes, *Science,* 277, 1971-1975.

Wong, S., Joselevich, E., Woolley, A. T., Cheung, C. L., Lieber, C. M. (1998). Covalently functionalized nanotubes as nanometre- sized probes in chemistry and biology, *Nature,* 394, 52-54.

Wong, V.T.S., Li, W.J.,(2003). Proc. IEEE of *Int. Symp. Circuit Sys.* 4, IV844.

Wu, J., Zang, J., Larade, B., Guo, H., Xong, X.G. and Liu, F. (2004). Computational design of carbon nanotube electromechanical pressure sensors, *Phys. Rev. B* 69, 153406-4.

Xu, C.L., Wei, B.Q., Ma, R.Z., Liang, J., Ma, X.K., Wu, D.H. (1999). Fabrication of aluminum-carbon nanotube composites and their electrical properties, *Carbon,* 37, 855-858.

Yakobson, B.I., Campbell, M.P., Brabec, C.J., Bernohlc, J. (1997). High strain rate fracture and C-chain unraveling in carbon nanotubes, *Comp. Mater. Sci.* 8, 341-348.

Yakobson, B.I., Smalley, R.E. (1997). Fullerene nanotubes: C-1000000 and beyond, American Scientist, 85, 4, 324-337.

Yang, J., Schaller, R. (2004). Mechanical spectroscopy of Mg reinforced with Al_2O_3 short fibers and C nanotubes, *Mater. Sci. Eng. A.,* 370, 512-515.

Yao, Z., Kane, C.L., Dekker, C. (2000). High-field electrical transport in single-wall carbon nanotubes, *Phys. Rev. Lett.,* 84, 2941-2944.

Yu, M.F., Bradley S.F., Arepalli, S., Ruoff, S.R. (2000). Tensile loading of ropes of single wall carbon nanotubes and their mechanical properties, *Phys. Rev. Lett.,* 84, 24, 5552–5555.

Yudaska, M., Komatsu, T., Ichihashi, T., Iijima, S. (1997). Single-wall carbon nanotube formation by laser ablation using double-targets of carbon and metal, *Chem. Phys. Lett.* 278, 102-106

Zeng, Z., Natesan, K., Maroni, V.A. (2002). Investigation of metal-dusting mechanism in Fe-base alloys using Raman spectroscopy, x-ray diffractiOn, and electron microscopy. *Oxidation of Metals,* 58, 147-170.

Zhan, G.-D., Kuntz, J.D., Wan, J., Mukherjee, A.K. (2003). Single-wall carbon nanotubes as attractive toughening agents in alumina based composites, *Nature Materials,* 2, 38-42.

Zhan, G.-D., Kuntz, J.D., Garay, J.E., Mukherjee A.K. (2003). Electrical properties of nanoceramics reinforced with ropes of single wall carbon nanotubes, *Appl. Phys. Lett.*, 83, 1228-1230.

Zhang, M., Gorski, W. (2005). Electrochemical sensing based on redox mediation at carbon nanotubes, *Anal. Chem.*, 77, 3960-3965.

Zhang, Y.G., Chang, A.L., Cao, J., Wang, Q., Kim, W., Li, Y.M., Morris, N., Yenilmez, E., Kong, J., Dai, H.J. (2001). Electric-field-directed growth of aligned single-walled carbon nanotubes, *Appl. Phys. Lett.*, 79, 3155-3157.

Zheng, B., Lu, C., Gu, G., Makarovski, A., Finkelstein, G., Liu, J. (2002). Efficient growth of single-walled carbon nanotubes on surfaces using carbon monoxide precursor, Nanoletters, 2, 895-989.

Zheng, L.X., O'Connell, M.J., Doorn, S.K., Liao, X.Z., Zhao, Y.H., Akhadov, E.A., Hoffbauer, M.A., Roop, B.J., Jia, Q.X., Dye, R.C., Peterson, D.E., Huang, S. M., Liu, J., Zhu, Y.T. (2004). Ultralong single-wall carbon nanotubes, *Nature Materials*, 3, 673-676.

Zheng, M., Jagota, A., Strano, M.S., Santos, A.P., Barone, P., Chou, S.G., Diner, B.A., Dresselhaus, M.S., Mclean, R.S. Onoa, G.B., Samsonidze, G.G., Semke, E.D., Usrey, M., Walls, D.J. (2003), Structure-based carbon nanotube sorting by sequence-dependent DNA assembly, *Science*, 302, 1545-1548.

Zhong, R., Cong, H., Hou, P. (2002). Fabrication of nano-Al based composites reinforced by single-walled carbon nanotubes, *Carbon*, 41, 848-851.